UNIVERSIDAD AUTÓNOMA DE MADRID
FACULTAD DE CIENCIAS
Dpto. de QUÍMICA FÍSICA APLICADA

Understanding structure-activity relationships for propane (amm)oxidation reactions over supported vanadium and phosphorus oxide catalysts

Estudios de relación de estructura-reactividad para reacciones de (amon)oxidación selectiva de propano en catalizadores soportados de óxidos de vanadio y fósforo

MEMORIA
Para aspirar al grado de

DOCTOR EN CIENCIAS QUÍMICAS
con Mención Doctor Internacional

EWELINA JOANNA MIKOŁAJSKA

Instituto de Catálisis y Petroleoquímica (CSIC)

Madrid, 2012

EWELINA JOANNA MIKOŁAJSKA

Understanding structure-activity relationships for propane (amm)oxidation reactions over supported vanadium and phosphorus oxide catalysts

Estudios de relación de estructura-reactividad para reacciones de (amon)oxidación selectiva de propano en catalizadores soportados de óxidos de vanadio y fósforo

MEMORIA
Para aspirar al grado de

DOCTOR EN CIENCIAS QUÍMICAS
con Mención Doctor Internacional

Dirigida por:

Prof. Dr. Miguel Ángel Bañares González
Profesor de Investigación
Instituto de Catálisis y Petroleoquímica (CSIC)

Dr. Søren Birk Rasmussen
Doctor
Instituto de Catálisis y Petroleoquímica (CSIC)

UNIVERSIDAD AUTÓNOMA DE MADRID
FACULTAD DE CIENCIAS
Dpto. de QUÍMICA FÍSICA APLICADA

Madrid, 2012

Understanding structure-activity relationships for propane (amm)oxidation reactions over supported vanadium and phosphorus oxide catalysts

by

EWELINA JOANNA MIKOŁAJSKA

A thesis presented to the Universidad Autónoma de Madrid
in fulfillment of the thesis requirement
for the international degree of

Doctor of Chemistry

Promotor: Prof. Dr. Miguel Ángel Bañares González
Co-promotor: Dr. Søren Birk Rasmussen

UNIVERSIDAD AUTÓNOMA DE MADRID
FACULTY OF SCIENCE
Dpt. of Applied Physical Chemistry

Madrid, 2012

MINISTERIO
DE CIENCIA
E INNOVACIÓN

CSIC
CONSEJO SUPERIOR DE INVESTIGACIONES CIENTÍFICAS

INSTITUTO DE CATALYSIS Y
PETROLEOQUIMICA

Madrid 05 de Septiembre 2012

Miguel Ángel Bañares González
Profesor de Investigación, Instituto de Catálisis y Petroleoquímica (CSIC)
Soren Birk Rasmussen
Investigador JAE-doc, Instituto de Catálisis y Petroleoquímica (CSIC)

ACREDITAN que la Memoria de Tesis titulada *"Estudios de relación de estructura-reactividad para reacciones de (amon)oxidación selectiva de propano en catalizadores soportados de óxidos de vanadio y fósforo. Understanding structure-activity relationships for propane (amm)oxidation reactions over supported vanadium and phosphorus oxide catalysts"* presentada por Ewelina Joanna Mikołajska para aspirar al grado de Doctor en Química con Mención Internacional, ha sido realizada bajo su dirección y autorizan su presentación para su defensa en el Instituto de Catálisis y Petroleoquímica (CSIC) en Madrid.

Prof. Miguel Ángel Bañares González
Instituto de Catálisis y Petroleoquímica
Consejo Superior de Investigaciones
Científicas (CSIC)
Madrid, España

Dr. Søren Birk Rasmussen
Instituto de Catálisis y Petroleoquimica
Consejo Superior de Investigaciones
Científicas (CSIC)
Madrid, España

This research project was accomplished in collaboration with the following host laboratories:

1. Süd-Chemie A.G.,
Bruckmühl, Germany,
under supervision of Dr. Gerhard Mestl

2. University of Caen
Laboratorie Catalyse et Spectrochimie,
ENSICAEN, Caen, France
under supervision of Prof. Marco Daturi

3. Lehigh University
Department of Chemical Engineering
Bethlehem, USA
under supervision of Prof. Israel E. Wachs

Süd-Chemie AG - a Group of Clariant

CE
Waldheimer Straße 13
83052 Bruckmühl
Germany

Süd-Chemie AG - a Group of Clariant - 83052 Bruckmühl - Germany

Ms. Ewelina Mikoljaska

Instituto de Catalisis y Petroleoquimica,
C/ Marie Curie 2,
Cantoblanco,
E- 28049 Madrid,
España

Dr. Gerhard Mestl
Department Manager Oxidation Catalysis
Tel.: +49 8061 4903 825
Mobil: +49 0170 7879364
Fax: +49 89 5110 73 825
Gerhard.mestl@clariant.com

Bruckmühl, 11.04.2012

To whom it may concern

This is to certify that Ms Ewelina Joanna Mikolajska (NIE Y0219434M) from the Institute of Catalysis and Petroleum Chemistry (C/ Marie Curie 2, Cantoblanco, Madrid, E-28049) stayed at Süd Chemie A. G. in Bruckmühl, Germany for a period of 92 days in dates from July 16th 2010 till October 15th 2010. During this time she worked on structural-activity relationships of dopants (Nb, W, P, Sb) on titania-supported vanadia catalysts.

Es para declarar que doña Ewelina Joanna Mikolajska (NIE Y0219434M) del Instituto de Catálisis y Petroleoquímica (C/ Marie Curie 2, Cantoblanco, Madrid, E-28049) estuvo de estancia en Süd Chemie A. G. en Bruckmühl, Alemania durante el periodo de 92 días desde 16/07/2010 hasta 15/10/2010. Durante este tiempo doña Ewelina trabajó en relación estructura-reactividad de dopantes (Nb, W, P, Sb) para catalizadores de vanadio soportado sobre titania.

20.4.12
date

SÜD-CHEMIE AG
Katalyse-Labor
Waldheimer Str. 13 · 83052 Bruckmühl

Dr. Gerhard Mestl
Department Manager
Oxidation Catalysis

Caen, le 25 avril 2012

To whom it may concern

This is to certify that Ms Ewelina Joanna Mikolajska (NIE Y0219434M) from the Institute of Catalysis and Petroleum Chemistry (C/ Marie Curie 2, Cantoblanco, Madrid, E-28049) stayed at my labolatory: Laboratorie Catalyse et Spetrochimie, ENSICAEN, CNRS and University of Caen, in Caen, France for a period of 89 days in dates from September 05th 2011 till December 2nd 2011. During this time she worked on *in situ/operando* IR study of VPO type catalysts during selective propane (ammo)oxidation reaction.

Es para declarar que doña Ewelina Joanna Mikolajska (NIE Y0219434M) del Instituto de Catálisis y Petroleoquímica (C/ Marie Curie 2, Cantoblanco, Madrid, E-28049) estuvo de estancia en mi laboratorio: Laboratorie Catalyse et Spetrochimie, ENSICAEN, CNRS y Universidad de Caen, en Caen, Francia durante el periodo de 89 días desde 05/09/2011 hasta 02/12/2011. Durante este tiempo doña Ewelina trabajó en *in situ/operando* IR de catalizadores tipo VPO para reacciones de oxidación selectiva de propano.

Firma y Sello/ Signature and stamp:

Laboratoire Catalyse et Spectrochimie
UMR CNRS 6506 - ENSICAEN
6, Boulevard du Maréchal Juin
14050 CAEN Cedex (FRANCE)
Tél. 02.31.45.28.21 - Fax 02.31.45.28.22

Professor Marco Daturi
Laboratorie Catalyse et Spetrochimie,
ENSICAEN
Caen, France

LEHIGH
UNIVERSITY

Israel E. Wachs
G. Whitney Snyder Professor
Director, Operando Molecular Spectroscopy & Catalysis Lab

Department of Chemical Engineering
Iacocca Hall, 111 Research Drive
Bethlehem, PA 18015-4791

Operando Molecular Spectroscopy and Catalysis Laboratory
Sinclair Lab, 7 Asa Drive
Bethlehem, PA 18015-3193
(610) 758-4274 Fax (610) 758-6555
e-mail: iew0@lehigh.edu

April 18, 2012

To whom it may concern:

This is to certify that Ms Ewelina Joanna Mikolajska (NIE Y0219434M) from the Institute of Catalysis and Petroleum Chemistry (C/ Marie Curie 2, Cantoblanco, Madrid, E-28049) stayed at my laboratory at Lehigh University for a period of 39 days in dates from February 06th 2012 till March 16th 2012. During this time she worked on *in situ* Raman and DRIFTS study of VPO-type catalysts for selective propane oxidation reactions.

Es para declarar que doña Ewelina Joanna Mikolajska (NIE Y0219434M) del Instituto de Catálisis y Petroleoquímica (C/ Marie Curie 2, Cantoblanco, Madrid, E-28049) estuvo de estancia en mi laboratorio en la Universidad de Lehigh durante el periodo de 39 días desde 06/02/2012 hasta 16/03/2012. Durante este tiempo doña Ewelina trabajó en el estudio *in situ* Raman y DRIFTS de los catalizadores tipo VPO para la oxidación selectiva de propano.

Firma y Sello/ Signature and stamp:

Israel E. Wachs

Israel E. Wachs

Dla Macieja

ACKNOWLEDGEMENTS

Implementation of my PhD studies has been one of the most significant challenges, not only academic, I have ever had to face. Over the past four years I have received support and encouragement from a great number of individuals.

Thus, first and foremost I would like to thank Maciej for sharing this challenge with me and for supporting my ambition. For his faith in me, his encouragement and quiet patience.

I deeply thank my parents, Ewa and Robert and my sister, Ania, who have always believed in me, for their unending encouragement and support. Mikłaki, for cheering me up during our Skype conversations dziękuję!

I would like to gratefully and sincerely thank Professor Miguel Ángel Bañares González, my supervisor, for the opportunity to gain extensive experience during my PhD studies, for his guidance, understanding and patience.

I would also like to thank Dr. Søren Birk Rasmussen, who undertook to act as the co-director of my thesis, for participation in this project with great interest and enthusiasm. Søren, for your guidance, understanding and patience tusind tak!

Many thanks to my group colleagues, Vanesa Calvino Casilda, Elizabeth Rojas García, María José Valero Pedraza, Ricardo López Medina, Manuel García Casado for their great support and friendship.

I would like to thank Susana Pérez Ferreras for her enormous help, especially during first years of my stay in Spain and for her friendship.

I thank Fernando Rubio Marcos for his support and for sharing equipments with me.

I would also like to thank to the members of Unidad de Apoyo for all the performed analysis.

My utmost gratitude to Professor Israel E. Wachs, Professor Marco Daturi, Professor Gerhard Mestl, Dr. Germán R. Castro and Dr. Ivan da Silva for hosting me at their research groups, their guidance and great interest in my scientific work. In particular, I would like to thank Professor Wachs for the significant input to my project, fruitful conversations and important advices.

I would like to thank my colleagues from Germany, France and the United States for their help and friendship.

Finally, I would like to thank DuPont for supplying the bulk VPO catalysts and the Spanish Ministry of Science and Technology, for funding this investigation (JAE-Predoc fellowship, CTQ2008-04261 and CTQ2011-25517 (MAP-IT)).

Resumen

Los modelos de relación estructura-reactividad para un mismo sistema en una misma reacción varían significativamente en bibliografía. La causa de esta discrepancia radica es que la estructura del catalizador másico se relaciona con la actividad mientras que la reacción tiene lugar en la superficie, la cual puede ser significativamente distinta de la de la masa. Pocas técnicas analíticas permiten caracterizar la superficie de los catalizadores másicos, lo cual dificulta entendimiento de naturaleza de ellos durante el proceso catalítico y la naturaleza de sus centros activos. Las técnicas de caracterización "másicas" pueden proporcionar información de la superficie si el tamaño se reduce a pocos nanómetros, donde la relación superficie-volumen se hace muy elevada.

Los fosfatos de vanadio (VPO) son los únicos catalizadores para el proceso comercial de oxidación de n-butano a anhídrido maléico pero también se emplean en los procesos de amonoxidación selectiva de parafinas a los correspondientes nitrilos (principalmente amonoxidación de compuestos aromáticos en fase liquida) y en oxidación de propano o propileno a ácido acrílico. El sistema VPO para obtención de anhídrido maléico ha sido ampliamente estudiado. Se han propuesto varios centros activos para obtención de anhídrido maléico (V^{5+}, V^{4+}, un par redox de 1 e^-, un par redox de 2 e^-, interacción entre la fase cristalina de $(VO)_2P_2O_7$ y las fases amorfas etc.). Sin embargo pocos estudios se han publicado de la amonoxidación de propano a acrilonitrilo y de la oxidación de propano a acido acético o acido acrílico sobre catalizadores tipo VPO, además la mayoría de los estudios que se encuentran en bibliografía son los estudios *ex situ.*

El presente proyecto de Tesis Doctoral incluye el análisis del proceso catalítico de oxidación selectiva de propano a acrilonitrilo (en presencia de amoniaco) y acido acrílico (en presencia de vapor de agua) sobre catalizadores de vanadio-fósforo-oxígeno soportados y sobre el catalizador tipo VPO másico y considera dos aspectos fundamentales que permiten determinar la naturaleza de los centros activos:

Ciencia de superficies: la reacción tiene lugar en la superficie, la cual es significativamente distinta de las capas interiores. La idea es estabilizar nanocristales de VPO sobre un soporte para aumentar proporción de

capas externas (la fase activa). Este proceso facilita la observación de los cambios en la superficie usando técnicas espectroscópicas al disminuir la señal de la masa. Además, el catalizador másico se caracteriza mediante técnicas "superficiales".

Técnicas operando e in situ: la estructura del catalizador depende significativamente de las condiciones del análisis. La metodología *operando* combina la espectroscopia *in situ* con las medidas cinéticas en un solo experimento y de modo simultáneo; por tanto, es muy conveniente para la comprensión de la relación estructura-reactividad.

El presente trabajo de investigación recoge el estudio de catalizadores basados en vanadio y fósforo tanto en la reacción de amonoxidación de propano como en la reacción oxidación de propano. Se han preparado y caracterizado catalizadores de óxidos de vanadio y fósforo, los cuales se han estabilizado utilizando γ-Al_2O_3 y TiO_2 anatasa como soportes. Distintas series de catalizadores soportados fueron preparadas con el objeto de estudiar el efecto en la composición en la actividad catalítica, de la relación atómica P/V y del recubrimiento de fase óxido sobre el soporte en la reacción selectiva de (amono)oxidación de propano. Los catalizadores soportados fueron comparados con un catalizador VPO másico industrial. En el presente trabajo, se describe la síntesis de impregnación incipiente y se caracteriza los catalizadores soportados tipo VPO y el catalizador VPO másico mediante distintas técnicas "másicas" y "superficiales" (DRX, Raman, UV-vis, Fisisorción de Nitrógeno, XPS, HR-TEM, TPR, TGA/DTA, XANES, EPR, FT-IR, DRIFTS, HS-LEIS) con la intención de comparar las superficies de los catalizadores soportados y los cristales del catalizador másico. Se describe también la evaluación catalítica de estos materiales tanto en la reacción de oxidación como en la amonoxidación de propano para obtener ácido acrílico y acrilonitrilo, respectivamente. Adicionalmente se realizan estudios de la estructura-reactividad, mediante espectroscopía Raman *operando*, que incluyen la caracterización de los sitios activos superficiales en condiciones verdaderas de reacción. Se estudia el efecto de fósforo como dopante y el efecto de vapor de agua para la reacción de oxidación de propano mediante espectroscopía IR.

Los resultados del presente trabajo muestran, que se ha obtenido resultados prometedores en las reacciones de amonoxidación y oxidación de propano usando catalizadores soportados (más económicos y con mejores propiedades mecánicas comparando con el catalizador másico). El catalizador tipo VPO soportado sobre γ-Al_2O_3 es más activo que el catalizador VPO másico mostrando el rendimiento a acrilonitrilo similar, aunque contiene solo ca. 50% de la fase activa (VPO). También se obtuvo por la primera vez acido acrílico utilizando catalizadores de oxido de vanadio soportados y dopados con fósforo. La ventaja de estos catalizadores es que son más económicos que los catalizadores usados para obtención de acido acrílico (los catalizadores VPO o los catalizadores con las fases M1 y M2, basados en óxidos mixtos de vanadio-molibdeno-niobio-teluro). Los centros activos fueron determinados mediante técnicas *in situ* y *operando* (Raman e IR). Se observa que las fases VPO cristalinas no son necesarias para formación de acrilonitrilo. La alúmina estabiliza las especies de V^{5+}, que es un centro responsable para activación de hidrocarburos. En los catalizadores tipo VPO soportados las especies de V^{5+} son selectivas a acetonitrilo en la reacción de amonoxidación de propano, mientras que las especies de V^{4+} (la relación de V^{4+}/ V^{5+} elevada) desplazan la selectividad hacia acrilonitrilo. Se propuso mediante espectroscopia *operando* Raman e *in situ* UV Raman que el centro activo para obtención de acrilonitrilo en la reacción de amonoxidación de propano son los grupos V-O-M (donde M = V, P o Al).

En caso de la reacción de oxidación de propano en presencia de vapor de agua se mostró que el dopaje de fósforo mejora significativamente la actividad y selectividad de catalizadores de óxido de vanadio soportados hacia ácidos carboxílicos. Se mostró qué cantidades pequeñas de fósforo cambian las propiedades de los catalizadores de oxido de vanadio. Además, la relación de acido acético a acido acrílico depende de la presión parcial de vapor de agua. Se observa mediante espectroscopia DRIFT que la interacción de los intermedios de oxidación de propano con la superficie del catalizador (con los centros activos) se debilita en presencia de vapor de agua, evitando la oxidación de los intermedios a CO_x. Acido acético se forma cuando el propileno se adsorbe sobre los grupos –OH presentes en la superficie del catalizador, formando intermedios de acetona. Mientras tanto, formación de acido acrílico requiere presencia del intermedio alílico (CH_2CHCH_2*), el cual se oxida a acroleína y a continuación a acido acrílico.

Objetivos de la investigación

1. Preparación de los catalizadores de óxidos de vanadio-fósforo soportados en alúmina y titania empleando el método de impregnación incipiente variando la relación atómica V/P y el recubrimiento V+P.

2. Caracterización de los catalizadores soportados y del catalizador tipo VPO másico usando las técnicas “superficiales” y técnicas “másicas” con la intención de comparar las superficies de los catalizadores soportados y los cristales del catalizador másico. Valorando el efecto de su encapsulamiento en sílice porosa.

3. Estudios *operando* e *in situ* para determinar la relación estructura-reactividad durante reacción de (amon)oxidación de propano y para evaluar la importancia de los estudios en condiciones reales de la reacción (estudios *in situ* versus *ex situ*).

4. Determinación de los centros activos, de la influencia de la composición de los catalizadores y de la influencia de fósforo en la actividad catalítica en la reacción de (amon)oxidación de propano.

5. Determinación de la influencia de vapor de agua para la reacción de oxidación de propano.

Abstract

This thesis is concerned with the structure-activity study of supported vanadium and phosphorus oxide catalysts in propane selective oxidation reactions. Alumina- and titania-supported vanadium and phosphorus oxide catalysts were synthesized by an incipient wetness impregnation method and compared to an industrial bulk VPO catalyst supplied by DuPont. This catalyst is nested inside a porous silica shell in order to improve the attrition resistance of the catalyst particles. Catalysis occurs at the catalyst surface, which is related to the outermost layers; before tested in propane selective oxidation reactions these catalysts were characterized using bulk and surface sensitive characterization techniques in order to determine the nature of the surface sites of bulk and supported VPO-type catalysts and to evaluate the influence of the silica shell on the structure of the industrial VPO catalyst. Alumina- supported vanadium and phosphorus catalysts are efficient materials for propane ammoxidation reaction. It has been shown that the structure of the supported VPO-type catalyst changes significantly during reaction when compared to fresh or used catalyst characterized in ambient conditions. Thus, *in situ* and *operando* techniques were applied to determining the nature of active sites under working conditions. The role of phosphorus additive was determined for the VPO-like catalysts (P/V = ca. 1.1) as well as for phosphorus-doped vanadium oxide catalysts (P/V = 0.1). Significant enhancement in activity and selectivity of propane oxidation to carboxylic acids by phosphorus doping of vanadium supported catalysts is reported. The study of the selective propane oxidation reaction in the presence and the absence of water vapour has shown that moisture plays a crucial role in formation of carboxylic acids (acrylic and acetic acids). Thus, its role was determined by *in situ* DRIFTS studies.

Chapters 1 and 2 describe a general introduction and the experimental procedures, respectively. Chapters 3-6 describe the characterization of bulk and supported catalysts. Bulk and surface sensitive techniques were used to evaluate the nature of VPO-catalysts (XRD, Raman, UV-vis, BET, (HR-)XPS, HR-TEM, TPR, TGA/DTA, XANES, EPR, FT-IR, DRIFTS, HS-LEIS). The catalyst structure, vanadium oxidation state and acidity of the bulk VPO catalyst encapsulated in the silica shell were evaluated in Chapter 3. The supported VPO-type catalysts are described in Chapter 4. Their structure, acidity, vanadium oxidation state and the nature of V^{4+} and V^{5+} surface species are also described in this chapter. Bulk and supported VPO catalysts are compared in

Chapter 5, while supported phosphorus doped vanadium oxide catalysts are characterized in Chapter 6, which also assesses the role of low concentration of phosphorus doping to vanadium oxide catalysts. *In situ* and *operando* studies during propane selective oxidation reactions are reported in Chapters 7 and 8. The structure-activity relationships of VPO-based catalysts for propane ammoxidation to acrylonitrile are determined in Chapter 7. The propane selective oxidation reaction to carboxylic acids over vanadium and phosphorus oxide catalysts was studied in Chapter 8 and the role of moisture was determined. All these results are summarized in a discussion of Chapter 9 and some concluding remarks are drawn.

Aims of this dissertation

1. Preparation of alumina- and titania-supported vanadium and phosphorus oxide catalysts, varying the atomic V/P ratio and the V + P loading, by application of the incipient wetness impregnation method.

2. Characterization of the supported catalysts and an industrial bulk VPO catalyst by application of bulk and surface sensitive analytical techniques. Comparison of surface sites of the supported and bulk VPO catalysts.

3. Application of *operando* and *in situ* studies for determination of the structure-activity relationships during propane (amm)oxidation reactions and evaluation of their importance (*in situ* vs. *ex situ*).

4. Determination of the active sites for propane (amm)oxidation reactions and evaluation of the influence of phosphorus additive on vanadium-based catalysts.

5. Evaluation of the role of moisture in propane oxidation reaction.

Table of Contents

1

General introduction

1.1 Introduction to Catalysis

The word "catalyst" was introduced by Berzelius 90 years after the first catalyst was used by J. Roebuck for a large-scale production of sulfuric acid in 1746. Berzelius defined catalysis as some kind of an unknown force by which the catalyst induces decomposition in substances, resulting in the formation of new compounds, but without being incorporated to them. According to Berzelius, the catalyst remains unchanged in each case and acts by means of the inherent force. Pure and simple compounds were under catalytic study until 1900s when the properties of multicompounds were investigated at BASF (Badische Anilin & Soda Fabrik). The real breakthrough came in 1920s when H. S. Taylor distinguished chemisorption, physical adsorption and the active site. The knowledge of the three basic phenomena has created a new, extensive and very important branch of chemistry science, which is called catalysis. Wilhelm Ostwald wrote down the definition of a catalyst in 1894:

"A catalyst is a substance that changes the rate of chemical reaction without itself appearing in the products"

and was awarded a Nobel Prize in 1909 for his work on catalysis. Ostwald's definition describes accurately what a catalyst is, the most common definition emphasizes that the catalyst does not change the thermodynamic equilibrium of a catalytic process:

"A catalyst is a substance that increases the rate of approach to thermodynamic equilibrium of a chemical reaction without being substantially consumed" [1]

However, catalysts undergo varied structural changes under reaction conditions and tend to deactivate. That is why *in situ* and *operando* techniques are applied to study the working catalysts. Thus, the Ostwald's definition seems to be less restrictive, since it applies to the effect of the catalyst, rather than to the state of the catalyst. Nowadays most chemicals are produced with the use of catalysts, which accelerate the rate or steer the chemical reaction. The role of the catalyst is to attain high selectivity to the desired product maintaining high activity. A long lifetime is its preferred feature. The value of the catalyst is typically less than 1% of the total cost of the catalytic process, but its contribution into it is very high, especially considering other cost-generating factors like raw materials, energy consumption or environmental pollution preventions [2].

Many factors must be tuned to reach the right catalytic process conditions. It is because in the majority of the cases needing a catalyst, the desired products are far less favored than the end-products (i.e. CO_x for oxidation reactions) or even the by-products. High selectivity to the desired product is the main factor determining the catalyst properties, so in some cases a decrease in the reaction rate is acceptable as long as it helps to keep high product yield [3]. This scenario often happens in the selective oxidation reactions over heterogeneous catalysts. The advantage of the heterogeneous catalytic systems over the homogeneous ones is that the catalysts can be rapidly and effectively separated and recovered from the reaction products. It is also possible to design various catalytic beds (which differ in active phases) in one simple reactor, directing not only the formation of the desired product but as well the formation of byproducts. Various reaction mechanisms take place on the catalysts surface. They strongly depend on the adsorption process of at least one of the reactants. The adsorption step is of a key importance for the heterogeneous catalysts and makes the reaction mechanism conditional. One of the most important mechanisms characteristic of supported and bulk catalysts is the Mars van Krevelen mechanism, where the hydrocarbon molecule is oxidized by lattice oxygen, which is subsequently restored from the gas phase or by migration of oxygen ions from the deepen lattice fraction [4,5,6]. The Langmuir-Hinshelwood and the Eley-Rideal mechanisms should be mentioned as well. They propose that both reactant molecules are adsorbed on the catalyst surface and undergo a bimolecular reaction (Langmuir-Hinshelwood mechanism) or that only one molecule is adsorbed on the catalyst surface and reacts with the other molecule from the gas phase (Eley-Rideal mechanism). However different reaction mechanisms may combine each other giving different reaction products or hindering the expected catalytic process. Zhao and Wachs reported using an *operando* Raman/IR/MS and TPSR spectroscopic study that a combined

Langmuir-Hinshelwood-Mars-van Krevelen mechanism takes place for a selective oxidation reaction of propylene to acrolein over a model supported V_2O_5/Nb_2O_5 monolayer-type catalyst [7]. Even if their previous TPSR study did not confirm that acrolein was formed in absence of gas phase oxygen [8] the $^{18}O_2$ labeled studies demonstrated that only lattice oxygen is incorporated into the acrolein according to the Mars-van Krevelen mechanism, while gas phase oxygen is required in order to oxidize surface H* and to prevent the hydrogenation of the surface allyl ($H_2C=CHCH_2$*) intermediate back to propylene (the Langmuir-Hinshelwood mechanism). Many times the role of Mars van Krevelen mechanism in a catalytic process is examined by running the specific test in absence of gas phase oxygen (TPSR study). Unfortunately, in many cases, when model near-monolayer supported catalysts are tested, the sensitivity of mass spectrometers or gas chromatographs is not high enough to give an evidence for participation of lattice oxygen in product formation. That is why the $^{18}O_2$ labeled studies are required for qualitative or even quantitative determination of reaction mechanism.

1.2 The Surface: where heterogeneous catalysis occurs

Many analytical techniques are applied to characterize catalysts nature and their active sites. However, since the catalytic process takes place at the outermost surface layer and the reactant molecule cannot diffuse into the bulk phase (except for the case when molecular sieves or zeolites are used as catalysts), the real characterization of the active phase becomes complicated [9]. Many widely used characterization techniques like Raman and IR spectroscopy, XRD, TGA XANES/EXAFS, EPR, NMR or even XPS (an escape depth of ~1-3 nm) involve an interference of the bulk phase and the signal of the bulk prevails over the outermost layers signal [9]. The lack of surface information about bulk mixed oxides and the correlation of bulk characteristics with activity often create confusion in the literature. Early studies considering the role of the catalyst surface in a catalytic process assumed that the bulk mixed oxides terminate with one of their crystallographic planes [10, 11, 12], and did not take into account that the outermost layer might be amorphous [13, 14, 15], neither that the metal ratio of the outer layer not necessarily is the same as for the bulk phase, since a surface enrichment may take place [16]. The discrepancy in a structure-activity relationships study of bulk catalytic systems has provoked a dynamic progress in surface science, which shows that new catalysis models should base on the actual surface features of bulk mixed oxide catalysts [17, 18].

Analytical techniques are developed or improved for providing more information about the surface chemistry of bulk catalysts. (1) Low energy ion scattering spectroscopy (LEIS) is a very powerful technique, unique in its sensitivity to structure and composition of the catalyst surface (escape depth of ~0.3 nm). It enables obtainment of depth profiles, which provides information of any possible changes in elemental composition. (2) High resolution transmission electron microscopy (HR-TEM) might be able to examine the amorphous surface layers supported on bulk mixed oxide catalysts. (3) Temperature programmed surface reactions (TPSR) gain increased interest because they are extremely informative about the mechanistic details of a reaction, while combined with IR spectroscopy and with a "smart" probe molecule (i.e. CH_3OH) provides an extensive information about the number and the nature of surface active sites (redox, acidic or basic sites), surface composition (methoxy species coordinated to different surface sites), kinetics, and oxidation states of the active sites [19, 20]. However, caution should be taken if this technique is applied for supported catalysts, since the probe molecule may easily adsorb on an exposed support skewing the obtained results.

Another way to learn about the surface active sites includes a synthesis of model supported monolayer-type catalysts. This variant allows the use of traditional "bulk" analytical techniques, since it is possible to distinguish between the signals of the support and the active monolayer and usually consists in mimicking the amorphous outer layer of the bulk catalysts. Moreover, if nanocrystallites of an active phase are formed on a support, the surface to bulk ratio increases significantly (comparing to crystallites of bulk catalysts), and the surface signal is not overlapped by the bulk any longer. This makes the spectroscopic study very accurate [21,22]. Furthermore these procedures allow the verification of the active phase by comparison of the activity tests of bulk and supported catalysts. It often happens that the supported mixed oxides, which posses amorphous phases show the same (or even higher) conversions than their bulk counterparts, even though they contain less active phase. It is often related to higher accessibility of the active sites dispersed on the support with high surface area.

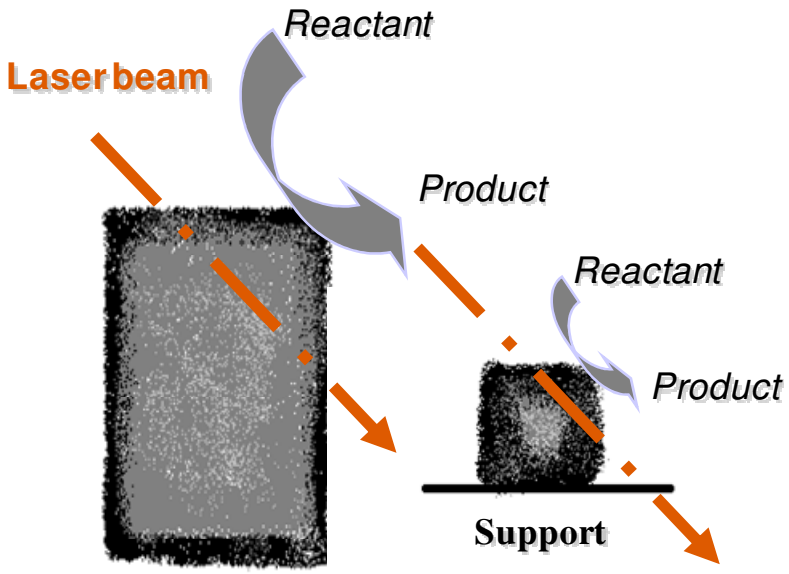

Figure 1.1 Spectroscopic advantage of analysis of supported nanocrystallites over bulk phases, which originates from the increase of surface to bulk ratio

For this study it is convenient to compare the turn over frequencies (TOF – molecules converted per second per active site [23]) rather than conversions in order to take into consideration much higher BET areas of the supported catalysts. From the industrial point of view; it is worth to entertain the space, which is occupied by the catalyst bed in the reactor. As long as the total volume is similar in case of bulk and supported catalysts (despite of the higher BET area) it may be profitable to use supported catalyst even if it contains more active phase. However, as mentioned above, very often the mass of the active phase is much lower for supported catalysts; thus decreasing significantly the cost of catalyst production and delivering similar product yields.

1.3 Structure-Activity Relationships

The goal for finding the active and selective catalyst is to understand the nature of its active site, which in theory is a site participating in the catalytic reaction, but its number is strictly limited comparing to the surface atoms. It extorts

investigation of the catalysts under real reaction conditions, because as it was already reported the *ex-situ* measurements do not reflect the real state of the catalyst nor its dynamic changes under process conditions [24]. Post mortem analysis prevent study of reduced states, which are stable only under reducing environment and at high temperatures (e.g. V^{3+} phases), also metastable phases may be observed only thanks to *operando* techniques. The *operando* methodology combines *in situ* spectroscopy and kinetic measurement in a single experiment and thus is very convenient for fully understanding the structure-activity relationships of any catalyst during catalytic processes [25,26]. Recently *operando* techniques have received increased interest, which provokes a development of new *operando* methodologies. Nowadays spectroscopic techniques as Raman, IR, UV-vis, XAFS, [27,28,29,30,31,32,33,34] become a widely used tools in catalysis, but also techniques as NMR, ESR or microscopic techniques are available for the *operando* approach [35,36,37,38], while combined with gas chromatographs or mass spectrometers. However using analytical techniques as *in situ* or all the more as *operando* methodology requires a specific design of reactors and cells, which allow gas, temperature and/or pressure treatment. Those catalytic systems should give the same activity results as the conventional catalytic test (i.e. gas chromatography) [39,40].
Operando techniques are not only limited to gas phase reactions [41,42]. A real time spectroscopic monitoring of liquid phase reactions enables monitoring the reaction progress [43,44,45], which in case of liquid phase catalytic tests is often more reliable than the use of chromatography analyses [46]. It is because in contrast to the gas phase catalytic processes, there is no on-line product outlet analysis. Samples need to be taken and analyzed off-line, which may cause problems of different nature (i. e. timing, environment or temperature changes), In general, the *operando* technique makes monitoring more complex.

1.4 Selective oxidation reactions

Selective oxidation reactions are of constant interest not only in academia but also especially in industry, which results in continuous effort to understand the fundamental principles of catalysis. This knowledge is necessary for inventing of more effective catalysts and new technologies. Many of these processes, although affording economical and environmental advantages, are limited by low selectivity to desired product. The low selectivity to partial oxidation products is the main reason why despite of the great effort that has already been done, new effective catalysts are still required to be found. Also, an attempt is

being made in order to replace olefins by alkanes as raw materials for selective oxidation reactions due to their low cost and abundance. Unfortunately, higher activation energy of the C-H bond in alkanes comparing to the C=C bond of olefins is usually connected to lower activity or to an increase of the temperature of the catalytic processes [47]. The reaction mechanism strongly depends on the nature of the catalyst and on reaction conditions. For the high efficiency of Mars van Krevelen mechanism, characteristic of oxidation reactions, acid-base and redox sites are required. Most of the catalysts used for propane oxidation are based on vanadium, which exhibits both redox and acidic properties. Vanadium (V^{5+}) cation, an acidic site is an active site for alkanes activation [48,49,50] but, depending on its oxidation state, it is also a selective site for a number of desired products of alkane partial oxidation, such as: acrylonitrile and acetonitrile [51], acrolein [52,53,54], acrylic acid [55,56], or maleic anhydride [57,58,59] among others. For the purpose of this dissertation, selective oxidation reactions of propane will be considered.

1.4.1 Propane oxidation reaction

1.4.1.1 Mechanism of propane oxidation over vanadium based oxide catalysts

The process of selective oxidation of propane leads to formation of acrylic acid in a two-step reaction with acrolein as an intermediate, or to formation of isopropyl alcohol, then acetone and its subsequent cracking to acetic acid and CO_x according to Figure 1.2.

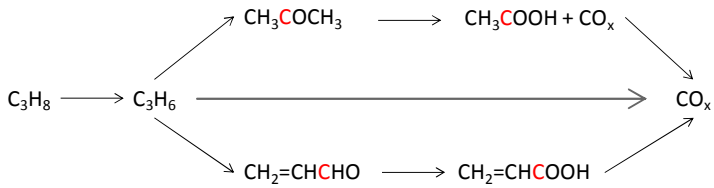

Figure 1.2 Paths of selective propane oxidation reaction to acrylic and acetic acids. Red carbon (C) indicates oxidation position

The selectivity of this reaction probably depends on the propane adsorption position (C_x position, x = 1 or 2) on the catalyst surface. Thus, in order to shift the selectivity to acrylic acid and to avoid cracking of propane molecule to acetic acid and CO_x - formation of isopropyl alcohol should be hindered. Isopropoxide

species form when propylene adsorbs on the catalysts surface undergoing an electrophilic attack at its C_2 position by a proton of surface -OH groups. Formation of acrylic acid requires an attack at the C_1 position and formation of an allyl intermediate (CH_2=CH-CH=O*, where * indicates the catalyst surface).

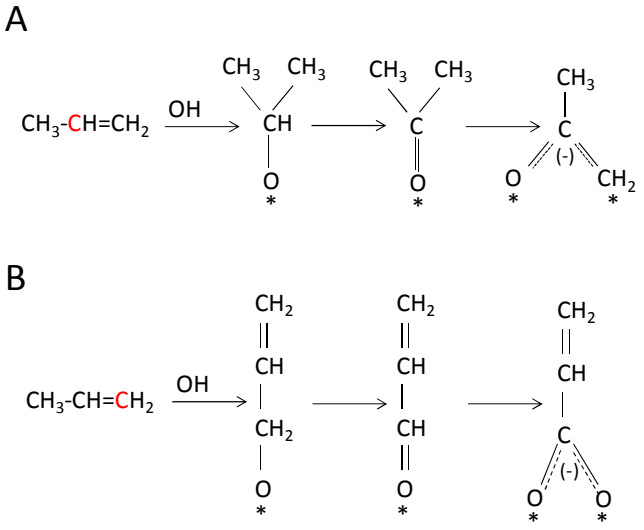

Figure 1.3 Propylene transformation on a surface of vanadium based catalysts [60]. Attack at C_2 position (A) and at C_1 position (B). Red carbon (C) indicates the C_x position of an electrophilic attack by a proton of surface OH groups

The Mo-V-Te [61,62,63] and Mo-V-Sb [64,65] based oxide catalysts were widely investigated for acrylic acid production, while the V-P-O based catalysts were also reported in the literature [66,67].

1.4.1.2 Influence of water vapor

The lattice oxygen in vanadium oxide catalysts, the base site [68] plays an important role in the oxidation of adsorbed molecules. According to Ai [69], the control of basic properties is critical to obtain a good catalyst for propane oxidation to acrylic acid. It is also believed that a decrease in surface acidity, provoked by presence of moisture in the reaction flow avoids the propane oxidation to CO_x and shifts the selectivity to acrylic acid, thus water vapor in

reaction flow is required to achieve good selectivity in propane oxidation reaction. However, the role of water is not fully understood yet. It was reported that steam entails a significant increase of crystallization of the catalyst and the decrease of its surface acidity [70]. Wachs et. al. demonstrated by oxygen-18 isotopic labeling experiments that surface vanadia species undergo oxygen exchange with steam much more efficiently than with O_2 (8% of H_2O in O_2 at 300 °C). This is caused by ability of moisture to hydrogen bond to the oxygen of vanadia surface species [71], modifying the molecular structure of supported vanadium oxide species and the interaction with the oxide support [72]. Redox properties may strongly be influenced by presence of water since it enhances significantly the vacancy formation [73]. The presence of defects related to the red-ox properties of the catalyst has been reported to activate alkanes [74,75]. Landi et al. investigated vanadyl phosphate in propane oxidation to acrylic acid [70,76]. The catalyst was strongly modified by water vapor during activation process. No vanadium (V) containing phases were detected in the active, highly crystalline $(VO)_2P_2O_7$ catalyst, while NH_3 TPD analyses confirmed the decrease in the surface acidity. This suggests the V^{4+} to be the selective site to acrylic acid for the vanadium and phosphorus containing catalysts. However, other studies show that TiO_2-SiO_2 supported VPO are more active and selective to acrylic acid [77].

1.4.1.3 Industrial process of propylene oxidation to acrylic acid

Industrial process of acrylic acid production is divided in two steps [78,79,80,81]. The reason of that is a lack of an efficient catalytic system, showing satisfying catalytic properties in propylene oxidation reaction to acrylic acid. Thus, in the first step propylene is selectively oxidized to acrolein in presence of moisture at 330-370 °C over Mo-Bi-O oxide catalysts [82]. Subsequently acrolein is oxidized to acrylic acid at ca. 210-300 °C over Mo-V-O catalysts with additives like Mg, W, Ni, Cu [83,84]. This two-steps propylene oxidation process gives the selectivity to acrylic acid of ca. 90% at ca. 95% of propylene conversion and is used by SOHIO, Nippon Shokubai, Mitsubishi Chemical, BASF, Rohm and Haas and Elf Atochem (ATO) [85]. Activation of propylene requires higher temperatures than activation of acrolein, thus the one-step propylene oxidation reaction is carried out at ca. 350 °C. Higher reaction temperature leads to overoxidation of reaction products decreasing selectivity to acrylic acid [86].

1.4.2 Propane ammoxidation reaction

1.4.2.1 Mechanism of propane ammoxidation over vanadium based catalysts

Acrylonitrile is the product of propane ammoxidation reaction. According to Grasselli et al. propylene forms an allyl intermediate in contact with catalyst active centers (VO*) by losing an α hydrogen atom. This step is followed by insertion of nitrogen atom to the activated molecule from ammonia adsorbed on the catalyst surface [87]. Similarly to the selective oxidation reactions, propane molecule may crack. Nitrogen insertion at the C_2 position leads to formation of acetonitrile and CO_x. As a result of these processes the catalyst surface is reduced and subsequently reoxidized by the gas phase oxygen. However, the mechanism of this reaction leads not only to formation of acrylonitrile and acetonitrile, but to formation of various sites products as HCN, NO_x and CO_x [88]. Recently a new method was discovered of acrylonitrile production from glycerol in only one-step reaction [89].

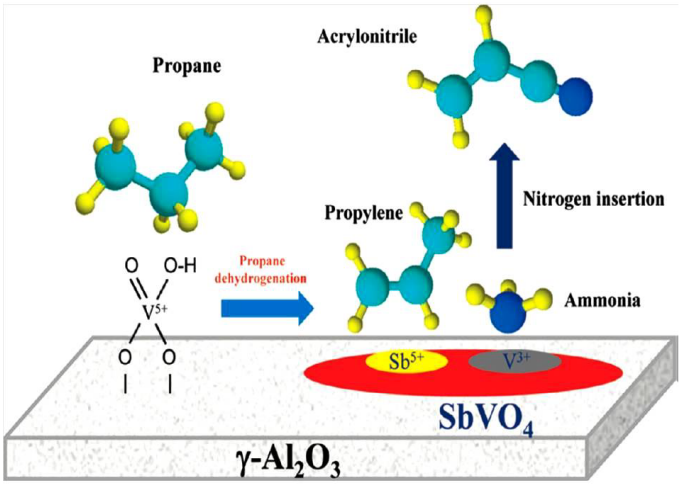

Figure 1.4 Mechanism of propane ammoxidation reaction over supported V-Sb-O catalyst [90]

1.4.2.2 Industrial process of propylene ammoxidation to acrylonitrile

Ammoxidation of propylene is the most important process for acrylonitrile production. Bp America (Sohio) apart from Taekwang Industrial CO., LTD. (using Monsanto process) is the exclusive licensor of this process technology. This strongly exothermic process includes reaction between propylene, ammonia and oxygen in a fluidized bed reactor at ca. 400-450 ^{o}C. Ammonia, which did not react, is neutralized with sulfuric acid, while the reaction products are adsorbed in water. Acetonitrile and other site products are separated from acrylonitrile by distillation [91].
Acrylonitrile is produced in ammoxidation reaction of propylene using Fe-Bi-Mo-O and Fe-Sb-O systems as catalysts but recently propane due to lower cost and abundance became a very competitive raw material for oxidation reactions in general. Ammoxidation of propane includes multifunctional molybdates [92,93,94] and antimonates [95,96,97,98] as catalysts. The new technology to produce acrylonitrile from propane is based on recent patents issued to Mitsubishi Kasei Corporation (MKC), which reports a high conversion, over 90%, with a selectivity of ca. 70% acrylonitrile. In some circumstances, this process may replace the conventional ammoxidation of propylene to acrylonitrile, i.e. when the price of propane is lower in comparison to propene or when propylene supplies are extremely restricted. Otherwise propene ammoxidation is still more convenient for acrylonitrile production. Propane conversion is lower than conversion of propylene because the activation energy of the C-H bond is higher and propane adsorption occurs more slowly. As a matter of fact, propane ammoxidation on vanadium antimonates requires the conversion of propane on dispersed vanadia sites into propene, prior to its reaction with ammonia on the vanadium antimonate sites [90].

1.5 Supported metal oxide catalysts

The monolayer type catalysts possess oxo-anions anchored to the support. These anions contain usually one or more transition metals as the active components (V, Pt, Pd, W, Ag, Cr, Mo, Nb, Ni etc.). They often appear with addition of other promoters from the main groups of periodic table. The active phase may be supported on various supports. The most common ones are bulk oxides (TiO_2, Al_2O_3, ZrO_2, Nb_2O_5, SiO_2, MgO) other popular supports include bulk mixed oxides, zeolites, molecular sieves, activated carbons etc. The last three mentioned supports possess very high surface areas, but unfortunately are

unstable at elevated temperatures. Supported catalysts are widely used in oxidation reactions and are characterized by high oxygen mobility and high oxygen deficiency tolerance. These characteristics are particularly required for Mars van Krevelen mechanism. Oxygen vacancies may be responsible for the selectivity of the reaction. An isotopic study has proved that the diffusion of oxygen is limited in bulk catalysts to only a few surface layers. It takes place rapidly on the surface, but very slow between the surface and the solid bulk [99], which indicates that even in case of bulk catalyst the Mars van Krevelen mechanism relates to the catalyst surface. That was the reason why the bulk VPO catalysts did not give satisfying catalytic properties in maleic anhydride production in absence of oxygen, which was applied at constructed by DuPont Asturias Factory in Spain. In order to decrease the overoxidation to CO_x the reactor for maleic anhydride production was designed with separate reduction and oxidation chambers [100]. The reaction was performed in a reduction chamber, and subsequently the catalyst was circulated to the oxidation chamber for regeneration of lattice oxygen. Unfortunately, the lattice oxygen mobility of the bulk VPO catalyst is not fast enough to ensure satisfying catalytic properties in absence of molecular oxygen.

The use of a support usually enhances catalyst activity [101] (e. g. by increasing the surface area or facilitating the redox processes), minimizes cost of the catalysts production, and improves mechanical strength, thermal stability and lifetime of the catalyst [102]. However, in most of the cases the support interacts with the active phase and affects the catalytic properties, which is why it should be carefully chosen for any specific kind of reaction. The support effect appears to be related with electronegativity of the support cation and thus to influence reaction steps like: adsorption, desorption or the molecule decomposition on the support surface by changes in the basicity of the bridging M-O-support bond (lower electronegativity increases the basicity or electron density of the M-O-support bond). Supported oxide catalysts are applied in petroleum, chemical and environmental pollution control industries [103]. They are widely studied as model catalysts for several reactions: alkane oxidative dehydrogenation reactions [104,105], selective catalytic reduction of NO_x in presence of ammonia [106,107], olefin metathesis [108], selective oxidation and ammoxidation reactions [109,110,111]. The possibility of controlling the support coverage gives opportunities for evaluation of active sites. Some reactions involve single active site [112], while others require two or more active sites [113]. This phenomenon may be easily evaluated using supported metal catalysts with increasing coverage of the active metal (M). Isolated species usually are present on the support surface when the coverage does not exceed 1 atom of the active metal

per nm^2 of the support. Increasing the loading, polymerized species are formed until the support surface gets saturated and a two-dimensional monolayer of the active metal oxide is formed. Additional amount of the metal oxide leads to formation of crystallites on the support surface [114,115].

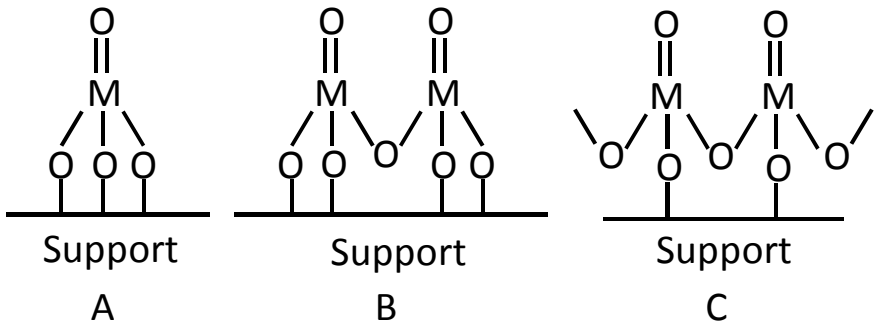

Figure 1.5 Isolated surface species (A), polymerized surface species (B) and monolayer coverage (C) at perfectly dehydrated conditions. M: active metal cation

The dispersion limit loading strongly depends on the support nature, mainly on the amount and character of its -OH groups and on the size of the supported metal, such a value on most oxides (ceria, alumina, zirconia, titania, etc.) is nearly 6 atoms per nm^2 of support. Silica support is different since it dispersion limit loading is at nearly 1 atom per nm^2 of the silica support. Some commercial silica supports contain an extremely low number of surface -OH groups, which results in formation of only isolated species up to the maximum dispersion on the silica surface.

The state of supported oxides is also affected by environmental conditions, which is hydrated under ambient conditions. In such a case, liquid phase chemistry rules behavior of supported oxides, like for supported vanadia [116]. At high temperatures in dry air or at room temperature under dehydrated conditions, supported oxides are in "dehydrated" state [117]. In general various surface species can be distinguished under dehydrated conditions for supported metal oxide catalysts:

- Isolated surface species – with terminal M=O bond and bridging M-O-support bonds
- Polymeric surface species – with terminal M=O bond and bridging M-O-M or M-O-support bonds
- Crystalline nanoparticles
- Mixed oxide compounds or solid solutions with a support – may occur at elevated temperatures when supports like ZrO_2, Al_2O_3, TiO_2, Nb_2O_5, MgO are used.

Table 1.1 Monolayer surface coverages of supported metal oxide catalysts [118], χ: Sanderson electronegativity (at the highest oxidation state) and Cov. Rad.: covalent radius [Å], n.r. – not reported

			Support	**Al_2O_3**	**TiO_2**	**SiO_2**	**ZrO_2**	**Nb_2O_5**
			χ	1.71	1.50	2.14	0.90	1.42
			At. Rad.[Å]	1.21	1.36	1.11	1.75	1.64
			Dispersion limit loading					
Metal	χ	At. Rad.[Å]						
V	2.51	1.53		7.3	7.9	0.7	6.8	8.4
Cr	3.37	1.27		4.0	6.6	0.6	9.3	-
Mo	2.20	1.54		4.6	4.6	0.3	4.3	4.6
W	1.67	1.62		4.0	4.2	0.1	4.0	3.0
Nb	1.42	1.64		4.8	5.8	0.3	5.8	-
Re	n.r.	1.51		2.3	2.4	0.5	3.3	-

The possible structures for dehydrated molecularly dispersed isolated species may be monoxo, dioxo or trioxo species. Their form may be distinguished using e. g. Raman spectroscopy. Monoxo species give a rise to one symmetric vibration; the dioxo species show both: one symmetric and one asymmetric bands, while for trioxo species one symmetric and a few asymmetric Raman vibrations appear. The number of terminal M=O bonds in isolated surface species depends on group number or the oxidation state of the metal. On silica support investigated metals from group 5 (V, Nb, Ta) show monoxo structures,

group 6 metals (Cr, Mo, W) show dioxo structures and group 7 metals (Re) posses trioxo structure [119].

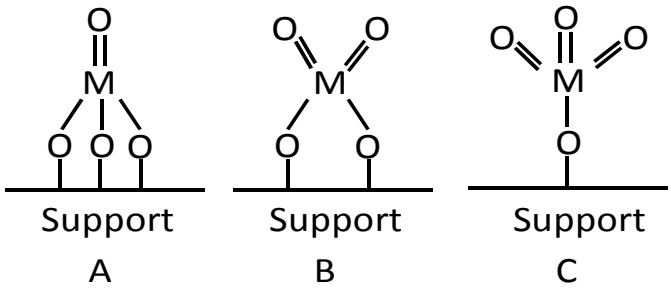

Figure 1.6 Totally dehydrated supported monoxo species (A), dioxo species (B) and trioxo species (C)

The structures of molecularly dispersed oxides presumes that these are absolutely dehydrated, however, this is not a realistic case, since environmental water molecules will coordinate to surfaces, dissociating into H^+ and -OH species, being the proton coordinated to the oxygen sites of the supported oxides. At low partial pressure of water (e.g., ambient humidity) and at high temperatures, the catalysts will possess some protons bond to the supported oxide phase, hydrolyzing some of the M-O-support bond, and creating M-O-H sites.

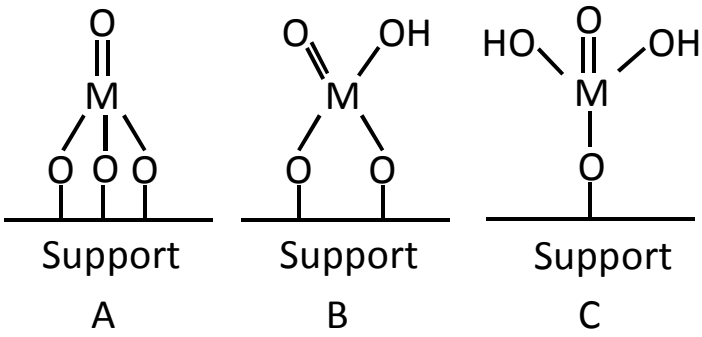

Figure 1.7 A totally dehydrated supported monoxo species (A) and its exemplary realistic structures of supported oxides under ambient conditions (B and C) [120]

The UV-vis edge energy (Eg) can quantitatively monitor the ratio of vanadia polymerization. In polymerized structures the electron delocalization is greater, when compared to isolated species, which leads to shift of V^{5+} LMCT to lower energy values [121,122].

When nanocrystallites are observed on the support surface, a spontaneous dispersion may occur at elevated temperatures in oxidizing conditions and reversebly, dispersed oxides may aggregated into nanocrystals in reducing or oxidizing environments [123]. The dispersion effect may be confused with a thermal broadening, which has to be taken into account, when spectroscopic study at elevated temperatures is performed on catalysts containing more than one monolayer of an active phase.
Mixed oxide phases formation from the active phase and the support is correlated with the difference in their acid-base properties. It also takes place when the size of metal cation of supported oxide and the support are similar (the same oxidation state is a favorable factor). In this case at elevated temperatures the metal from the supported layer may migrate to the support lattice. It is a well-known example of deactivation process of titania (anatase)-supported vanadium catalysts, when incorporating vanadium to the anatase structural transformation to rutile takes place [124]. Similar phenomena are described for supported oxides like ceria-supported vanadia [125] or other systems.

1.6 Bulk oxide catalysts

Bulk oxide catalysts are widely used in petroleum, chemical, energy and pollution control industries. They are characterized by fact that their active phase is distributed throughout the entire catalyst. Bulk catalysts may be composed from only one active cation, but usually they contain two or more active metals. This, inter alia, was explained to be due to the contact synergy, i.e. promotion of one phase in presence of the other by modifying the electronic density of the active phase. Recently, a number of articles have appeared indicating that structure-activity relationships related to interactions of these active sites are limited only to the amorphous phases present on the surface of bulk catalysts [126,127,128]. Common bulk catalytic systems used in catalysis are presented in Table 2. Different cations may play different role in the reaction mechanism, like it was proposed for the ammoxidation reaction mechanism over V-O-Sb catalytic system, where molecularly dispersed vanadium activate of hydrocarbons to olefins (dehydrogenation process), while the Sb site activates

the olefin, which coordinated with ammonia adsorbed at lattice reduced vanadium oxide site, leading to N insertion [[90]]. An increase of catalytic activity may be caused by presence of an additional metal cation or dopants, which generate defects in the catalyst lattice.

Table 1.2 Exemplary bulk oxide catalytic systems. C_x states for an alkane and alkene with x carbon number

Catalyst	Reaction	Product	Reference
V-P-O	C_4 oxidation	$C_2H_2(CO)_2O$	[[129]]
V-P-O	C_5 oxidation	$C_6H_4(CO)_2O$	[[130]]
V-Sb-O	C_3 ammoxidation	C_3H_3N	[[131]]
Bi-Mo-O	C_3 ammoxidation	C_3H_3N	[[132]]
V-Mo-O	Benzene oxidation	$C_2H_2(CO)_2O$	[[133]]
MoVTeO	C_3 oxidation	$C_3H_4O_2$	[[134]]
Fe-Mo-O	Methanol oxidation	CH_2O	[[135]]

1.7 Bulk *vs*. Supported catalysts

The catalytic process takes place on the catalyst surface in case of both, bulk and supported catalysts. This theory suggests that only the active sites on the catalyst surface are actually active in a reaction. The bulk phase in selective oxidation reactions was proposed to play a role of an oxygen store. Surface lattice oxygen consumed in Mars van Krevelen mechanism is subsequently restored by deeper lattice oxygen sites. However, in many cases the oxygen diffusion from the bulk to the surface is slower than the reaction rate and thus it is replaced by gas phase molecular oxygen. Another hypothesis of the role of bulk phase states that the surface of bulk catalysts terminates with one of their crystallographic planes, which possesses specific active sites, but is difficult to recreate on a support. However, most likely the bulk phase plays a role of a support for the active outer-layers stimulating the importance of the M-O-support bond. Recently much attention has been paid to the surface of bulk catalysts [[9 and references therein]]. It was caused by the discrepancy in literature when the structure of bulk catalysts is correlated with their activity. Use of methods and techniques, which allow for detailed surface analysis of bulk catalysts (spectroscopic study of model supported catalysts, HS-LEIS, HR-TEM) provided information that the surface

differs significantly from the bulk. In case of vanadate or molybdate bulk catalysts, an enrichment of the surface in VO_x and MoO_x is apparent [19]. Surface enrichment with amorphous VO_x and MoO_x may reach few topmost layers. This phenomenon is related to the Tamman temperature ($T_{Tamman} = 0.5\ T_{melting\ (K)}$) of the metal cation, the temperature at which the solid phase becomes mobile [136]. It depends on several factors such as texture, size and morphology. However, it was reported that even for one-component bulk oxides (V_2O_5, Nb_2O_5, WO_3) exhibit amorphous surface layers, like those present in supported catalysts [137,138,139]. In order to investigate the surface amorphous layer phenomenon in bulk mixed $MoO_3/Fe_2(MoO_4)_3$ system, a model supported MoO_3/Fe_2O_3 catalyst was examined in methanol oxidation reaction by Routary et al. [140]. It is a well-known procedure (comparison of model supported catalyst with its bulk equivalent) for confirmation of catalytic importance of an amorphous surface layer detected by surface sensitive techniques (HS-LEIS, HR-TEM) over a bulk crystalline structure. The amorphous surface MoO_x monolayer phase, was found to exhibit the same catalytic performance for methanol oxidation reaction as the bulk $MoO_3/Fe_2(MoO_4)_3$ catalyst. Moreover, LEIS analysis of the MoO_3-free $Fe_2(MoO_4)_3$ surface shows that it is completely covered with MoO_x. This proves that only amorphous MoO_x in contact with Fe_2O_3 is required for good activity in methanol oxidation reaction, and reveals the importance of Mo-O-support bond (Mo-O-Fe in this case) as the active site.

1.8 VPO catalysts

1.8.1 Nature of VPO catalysts

Vanadium phosphate (VPO) catalysts have excited researchers for over four decades, since Bergman and Frisch used them for the first time in a selective oxidation of *n*-butane in 1966 [141]. Today, they are known as the only catalysts for industrial process of *n*-butane oxidation to maleic anhydride [142,143]. The typical industrial conditions (2 mol. % n-butane in air, 400-450 ^oC, GHSV 1100-2600 h^{-1}) lead to the 65-75 mol. % of selectivity to maleic anhydride at 70-85 % conversion [144]. However, the multitude of crystalline phases present in bulk VPO combined with its disordered, glass-like phases makes it difficult understanding the nature of these catalysts during reaction [145,146,147]. The population ratio of VPO phases depends on preparation methods and catalyst precursors, but it is further shaped by reaction and reactive conditions, which makes the catalytic system even more complex.

VPO phases may contain V^{4+} and V^{5+} species like $(VO)_2P_2O_7$ and $VOPO_4$ (α_I, α_{II}, β, γ, δ, ε, metastable ω) respectively. The ω-$VOPO_4$ phase is stable only at elevated temperatures and appears very sensitive to reactants and products of butane oxidation; it transforms rapidly to δ-$VOPO_4$ phase upon butane exposure and reaction conditions [148]. However, the industrial VPO catalyst contains mainly the vanadyl pyrophosphate phase, $(VO)_2P_2O_7$ reported as the active phase for *n*-butane oxidation. Phase transformations in the VPO system under different conditions are present in Figure 1.7. Many attempts were made to understand the structure-activity relationships of bulk VPO catalysts in *n*-butane oxidation reaction. Literature presents several theories about the nature of the active site of bulk VPO catalysts and also about the reaction mechanism of *n*-butane oxidation. It was believed that Mars van Krevelen is applied in the *n*-butane oxidation, but the bulk VPO catalyst has a very limited ability to O-insertion reaction in comparison to vanadium containing supported catalysts, this probably is one of the reasons of high selectivity of bulk VPO system in *n*-butane oxidation reaction. It was recently reported that the involvement of the lattice oxygen of bulk VPO catalyst is limited only to the top layers of the catalyst structure [149,150].
In contrast to the *n*-butane oxidation reaction other catalytic reactions performed over VPO-type catalysts, like selective (ammo)xidation reactions of propane or propylene were not studied so precisely.

1.8.2 Preparation of bulk vanadyl pyrophosphate catalyst

Vanadyl pyrophosphate forms during dehydration process of the vanadyl hydrogen phosphate hemihydrate precursor: $V^{4+}OHPO_4 * 0.5\ H_2O$. The morphology of the precursor depends on many factors, i.e. (1) the nature of solvent, (2) on the reducing agent, (3) amount of water present in the synthesis, (4) synthesis temperature, (5) activation process and (6) on the P/V ratio. Reduction deficiency of vanadium species and co-formation of $V^{5+}OPO_4 * 2H_2O$ increases the V^{5+}/V^{4+} ratio. The synthesis of the precursor usually proceeds during precipitation process in aqueous solution (aqueous synthesis) of vanadium and phosphorus sources (usually V_2O_5 and H_3PO_4) or in presence of an anhydrous alcohol (organic synthesis). There is a general agreement that the organic synthesis leads to the most active and selective catalyst [151,152,153], through the significant increase in V^{4+}/V^{5+} ratio. V_2O_5 in the solution forms V^{5+}-alcoholate species, which are subsequently reduced to solid V_2O_4. The V_2O_4 reacts with the H_3PO_4 and forms the $VOHPO_4 * 0.5\ H_2O$ precursor.

The precursor usually has a P/V ratio higher that the stoichiometric ratio for vanadyl pyrophosphate (i.e. P/V = 1.1). The role of phosphorus is to prevent the overoxidation of vanadium and stabilization of V^{4+} [154,155,156]. In case of P/V ratio greater than 1.0 it is believed that the excess of phosphorus appears on the catalyst surface (phosphorus enrichment) [157]. However high surface phosphorus concentration leads to low redox properties (low reducibility of V^{4+}) and to decrease of the catalyst activity, which is why a compromise in phosphorous amount should be found.

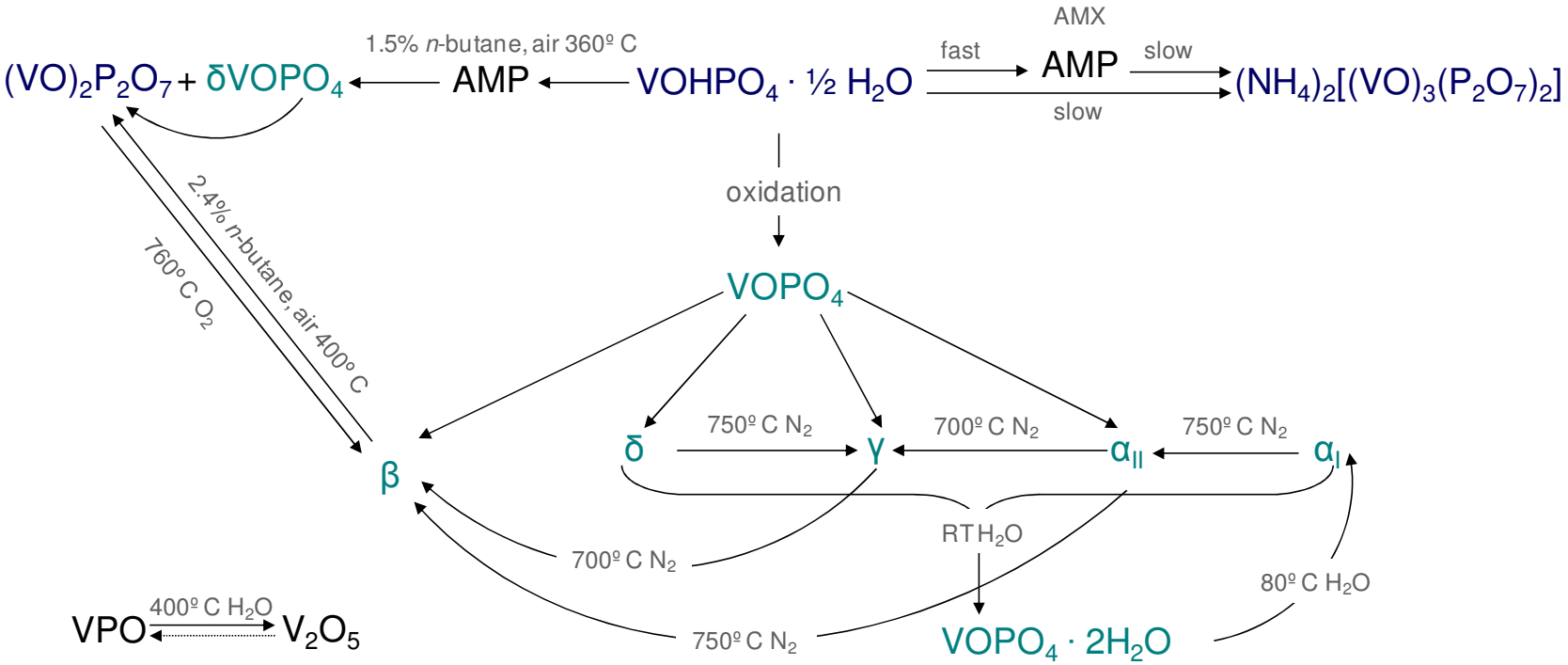

Figure 1.7 VPO phase transformations, V^{4+} containing phases, V^{5+} containing phases, AMP – amorphous phases [24]

1.8.3 Active sites in VPO catalytic systems

The $(VO)_2P_2O_7$ phase was reported as the active phase for *n*-butane oxidation. However, many studies reveal the presence of small amount of $VOPO_4$ phases, probably as amorphous $(VO)_2P_2O_7$ overlayer to be necessary for increasing the catalyst activity and selectivity to maleic anhydride [158]. These phases are present in fresh VPO catalyst. However, Guliants et al. reported that this interpretation has its origin in a study of a non-equilibrated catalyst. He stated, that because of a very long activation time, VPO catalysts are usually studied as non-equilibrated, while the best catalyst (after ca. 30 days of activation under catalytic reaction conditions) does not contain V^{5+} phases [159]. In other studies vanadium (V^{5+}) was reported to be responsible for formation of maleic anhydride and to be involved in the selective oxidation reaction of *n*-butane, while vanadium (V^{4+}) was characterized as an active site in the formation of by-products [160]. Cavani et al. described that the active surface made of vanadium oxide and polyphosphoric acids forms on VPO catalysts containing P/V > 1.0 while at P/V < 1.0 ratios, $VOPO_4$ phase forms and the catalyst becomes very active but unselective [161]. Many active sites have already been proposed for *n*-butane oxidation reaction over bulk VPO catalysts [162] i.e.:

- Terminal oxygen V=O
- Bridging oxygen V-O-V
- Bridging oxygen V-O-P
- Brønsted acid sites (probably P-OH groups)
- Lewis acid sites (probably V^{5+} or V^{4+})
- One electron redox couple V^{5+}/V^{4+}
- Two electron redox couple V^{5+}/V^{3+}
- Peroxo species

Schrader et al. investigated vacancy-induced disorder in the VPO phases [163]. They reported that *n*-butane induced higher number of vacancies than N_2 or H_2, while the presence of steam intensified significantly their formation. Presence of oxygen in a flow of *n*-butane prevents vacancies formation, since they form as a result of oxygen loss from the V-O-P bonds. A small amount of oxygen vacancies may improve catalytic properties by intensifying the redox cycles, while a high number would lead to the segregation of vanadium and phosphorus species, which would decrease activity and selectivity to maleic anhydride. This could suggest that bridging oxygen, V-O-V and V-O-P, are active sites for the *n*-

butane oxidation reaction. Disorganization of VPO phases is related to the red-ox properties of these catalysts and facilitates activation process of alkanes; however, Abon et al. reported that an amorphous catalyst is not able to form maleic anhydride [164] while Wachs et al. proved that both isolated and adjacent surface vanadia species are able to oxidize butane to maleic anhydride, and selectivity increases with polymerization of vanadia species [165]. This experiment rules out the need of crystalline VPO phases to form maleic anhydride. Moreover, supported vanadia catalysts were active and selective in this reaction in absence of phosphorus (even though in case of titania-supported vanadium catalyst the phosphorus addition increased the maleic anhydride TOF by more than a factor 5). It was reported that the selectivity to maleic anhydride increases when approaching monolayer coverage. In general from the experiment performed by Wachs et al. relevant conclusions come out:

- No correlation between the butane oxidation TOF and the corresponding extent of surface vanadium species reduction was observed
- Experiments with oxygen-18 labeling show that the terminal V=O bond is too stable to be involved in the reaction mechanism
- Oxide supports influence significantly the *n*-butane oxidation TOF (by a factor of ca. 50) indicating the importance of the V-O-support bond
- Selective *n*-butane oxidation may occur as on the isolated vanadium species as well as on the polymerized vanadium species
- Brønsted acid sites increase the *n*-butane conversion, while Lewis acid sites increase both, *n*-butane conversion and selectivity to maleic anhydride (experiment stimulated by addition of W as Brønsted acid sites and Nb as Lewis acid sites)

These authors do not compare the activity of supported catalysts with the bulk VPO, because quantification of surface active sites of bulk VPO catalysts was impossible. Anyway, their work has brought an important insight to catalysis about the structure-activity relationships of VPO-type catalysts. Also Overbeek has shown that the active phase for *n*-butane oxidation in bulk VPO catalysts is probably an amorphous phase [166], while Ruitenbeek reported in his PhD thesis that silica supported VPO catalysts show comparable selectivity to maleic anhydride to a home-made bulk VPO catalyst (yield of 26%) [167].

1.8.4 VPO in other selective oxidation reactions

Bulk VPO catalysts are also used for conversion of propane into acrylonitrile [144]. The structure of VPO-based catalysts during propane ammoxidation depends on reaction conditions and is affected not only by the presence of the hydrocarbon and its interaction with oxygen, but also by the presence of ammonia in the feed and water. The presence of steam has an effect on VPO catalysts. In the case of propane or propylene oxidation reaction, steam addition improves activity and selectivity to acrylic acid, but propane conversion decreases due to increase of the crystallinity and decrease of number of acid sites on the surface of the catalyst [76]. Centi et al. based on IR experiments suggested that an incorporation of ammonia to the gas flow of propane oxidation reaction might cause competitive adsorption phenomena between ammonia and oxygen during ammoxidation reaction on VPO catalysts [168]. It leads to shift in selectivity, depending on NH_3/O_2 surface coverage. High amount of ammonia on the catalyst surface leads to propane dehydrogenation, but not to acrylonitrile formation, while at low ammonia coverage mainly carbon oxides are formed. In further work Centi et al. proposed two pathways of formation of acrylonitrile on bulk VPO catalysts [169], an anaerobic and a more rapid one, in presence of O_2. In the first case acrylonitrile is formed by an intermediate as propylamine, while the process in presence of oxygen involves reaction between surface acrylate species and adsorbed ammonia species.

Centi et al. obtained 25% selectivity to acrylonitrile at 75% of propane conversion over bulk VPO catalyst [170], while Landi et al. reported that in propane oxidation reaction to acrylic acid over bulk VPO catalyst the catalytic properties strongly depend on presence of moisture. In absence of water vapor 80% of propane conversion was reached, but the total combustion occurred giving only 4% selectivity to acrylic acid. However, in presence of 25% of water vapor in the reaction flow, the activity decreased to 55% of propane conversion but the selectivity to acrylic acid increased significantly, up to 30%.

Kalevaru et al. studied VPO catalysts for ammoxidation reaction of cyclic compounds, like 2,6-dichlorotoluene, 3-picoline or *o*-xylene [171,172,173]. They obtained high yields of the desired products (ca. 80%) and stated that supported catalysts were always more active than the bulk VPO. Also P/V ratio and oxidation state of vanadium were found to influence the catalytic properties. However V^{5+} was detected only for a catalyst with the P/V ratio = 0.5. At higher P/V ratios only V^{4+} and V^{3+} are present, while the amount of V^{3+} increases with the P/V ratio.

References

[1] B. C. Gates, *Catalytic Chemistry*, John Wiley & Sons Inc. New York, 1992

[2] H. H. Brongersma (Ed), R. A. Van Santen (Ed), H. Knözinger, *Fundamental Aspects of Heterogeneous Catalysis Studied by Particle Beams*, Series B: Physics, Vol. 265, 1990 p. 7, ISBN 0-306-44002-4

[3] B. E. Leach (Ed), *Applied Industrial Catalysis*, New York, Academic press, Inc. (1983), vol 1

[4] P. Mars, D. W. van Krevelen, *Chem. Eng. Sci*. (Spec. Suppl) 3 (1954) 41

[5] H. Over, Y. D. Kim, A. P. Seitsonen, S. Wendt, E. Lundgren, M. Schmid, P. Varga, A. Morgante, G. Ertl, *Science* 287 (2000) 1474

[6] A. M. Khenkin, L. Weiner, Y. Wang, R. Neumann, *J. Am. Chem. Soc*. 123 (2001) 8531

[7] C. Zhao, I. E. Wachs, *J. Phys. Chem*. C 112 (2008) 11363

[8] C. Zhao, I. E, Wachs, *Catal. Today* 118 (2006) 332

[9] I. E, Wachs, K. Routary, *ACS Catal*. 2 (2012) 1235

[10] E. Bordes, *Catal. Today* 1 (1987) 499

[11] G. Hutchings, *Appl. Catal.* 72 (1991) 1

[12] G. Centi, *Catal. Today* 16 (1993) 5

[13] K. Routary, W. Zhou, C. J. Kiely, I. E. Wachs, *ACS Catalysis* 1 (2011) 54

[14] A. C. Sanfiz, T. W. Hansen, F. Grigsdies, O. Timpe, E. Rodel, T. Ressler, A. Trunschke, R. Schlogl, *Topics Catal*. 50 (2008) 19

[15] V. V. Guiliants, J. B. Benziger,S. Sundaresan, N. Yao, I. E. Wachs, *Catal. Letters* 32 (1995) 379

[16] S. V. Merzlikin, N. N. Tolkachev, L. E. Briand, T. Strunskus, C. Woll, I. E. Wachs, W. Grunert, *Angew. Chem*., Int. Ed. 49 (2010) 8037

[17] G. A. Somorjai, *Introduction to Surface Chemistry and Catalysis*, Wiley Interscience, New York, 1994 p. 271

[18] J. M. Thomas, W.J. Thomas, *Principles and Practice of Heterogeneous Catalysis*, VCH: New York, 1997, p. 159

[19] W. E, Farneth, R. H. Staley, A. W. Sleight, *J. Am. Chem. Soc*. 108 (1986) 2327

[20] I. E. Wachs, J.-M. Jehng, W. Ueda, *J. Phys. Chem. B* 109 (2005) 2275

[21] M. A. Bañares, *Catal. Today* 100 (2005) 71

[22] M. A. Bañares, *Adv. Mater*. 23 (2011) 5293

[23] M. Badlani, I. E. Wachs, *Catal. Letters* 75(2001) 137

[24] E. Mikolajska, S.B. Rasmussen, A.E. Lewandowska, M.A. Bañares, *Phys. Chem. Chem. Phys*. 14 (2012) 2128

[25] B. C. Gates, H. Knözinger (Eds.), M. A. Bañares, G. Mestl, *Adv. Catal.* 52 (2009) 43

[26] M. A, Bañares, *Adv. Mater.* 23 (2011) 5293

[27] F. Romero Sarria, J. Saussey, J.-P. Gallas, O. Marie, M. Daturi, *Studies in Surf. Sci. and Catal*. 158 (2005) 821

[28] P. Pietrzyk, C. Dujardin, K. Gora-Marek, P. Granger, Z. Sojka, *Phys. Chem. Chem. Phys*. 14 (2012) 2203

[29] G. Tsilomelekis, S. Boghosian, *Phys. Chem. Chem. Phys*. 14 (2012) 2216
[30] M. O. Guerrero-Pérez, M. C. Herrera, I. Malpartida, M. A. Larrubia, L. J. Alemany, M. A. Bañares, *Catal. Today*, 126 (2007) 177
[31] A. Brückner, E. Kondratenko, *Catal. Today*, 113 (2006) 16
[32] F. J. Garcia, S. Guerrero, E. E. Wolf, J. T. Miller, A. J. Kropf, *J. Catal*. 233 (2005) 372
[33] A. Brückner, *Chem. Comun*. (2005) 1761
[34] M. H. Groothaert, K. Lievens, H. Leeman, B. M. Weckhuysen, R. A. Schoonheydt, *J. Catal.* 220 (2003) 500
[35] V. Sundaramurthy, J-P. Cognec, K. Thomas, B. Knott, F. Engelke, C. Fernandez, *Comptes Rendus Chimie* 9 (2006) 459
[36] P. Dhage, A. Samokhvalov, D. Repala, E. C. Duin, B. J. Tatarchuk, *Phys. Chem. Chem. Phys.* 13 (2011) 2179
[37] P. Dhage, *Dissertation: Promoted ZnO Sorbents for Wide Temperature Range H_2S/COS Removal for Applications in Fuel Cells,* Auburn University, 2011, DAI/B 73-01, p. , Nov 2011, Publication Nr 3480670
[38] Y. Chen, J. L. Fulton, J. C. Linehan, S. T. Autrey, *J. Am. Chem. Soc.* 127 (2005) 3254
[39] M. A. Bañares, M. O. Guerrero-Pérez, J. L. G. Fierro, *J. Mater. Chem*.12 (2002) 3337
[40] M. O. Guerrero-Pérez, M. A. Bañares, *Chem. Commun*. (2002) 1292
[41] G. Mul, G. M. Hamminga, J. A. Moulijn, *Vib. Spectrosc.* 34 (2004) 1009
[42] A. F. Lee, P. J. Ellis, I. J. Fairlamb, K. Wilson, *Dalton Trans.* 39 (2010) 10473
[43] D. E. Pivonka, J. R. Empfield, *Appl. Spetrosc*. 58 (2001) 41
[44] D. Pivonka, *Appl. Spectrosc*. 58 (2004) 323
[45] N. E, Leadbeater, J. R. Schmink, *Nature Protocols* 3 (2008) 1
[46] E. Mikolajska, V. Calvino-Casilda, M. A. Bañares, *Appl. Catal*. A, 421 (2012) 164
[47] Y. C. Kim, W. Ueda, Y. Moro-oka, *Catal. Today* 13 (1992) 673
[48] X. Gao, J. M. Jehng, I. E. Wachs, *J. Catal.* 209 (2002) 43
[49] R. López-Medina, H. Golińska, M. Ziólek, M. O. Guerrero-Pérez, M. A. Bañares, *Catal. Today* 158 (2010) 139
[50] P. Concepción, P. Botella, J. M. López Nieto, *Appl. Catal. A* 278 (2004) 45
[51] E. Mikolajska, E. Rojas Garcia, R. López Medina, A. E. Lewandowska, J. L. G. Fierro, M. A. Bañares, *Appl. Catal. A* 404 (2011) 93,
[52] H. Jiang, W. Lu, H. Wan, *J. Mol. Catal. A* 208 (2004) 213
[53] X. Li, *Selective Oxidation of Propylene to Acrolein Over Vanadium and Niobium Doped Bismuth Molybdates*, University of Delaware, 2008, ISBN 0549926690, 9780549926696
[54] T. V. Andrushkevich, L. M. Plyasova, G. G. Kuznetsova, V. M. Bondareva, T. P. Gorshkova, I. P. Olenkowa, N. I. Lebedeva, *React. Kinet. Catal. Lett*. 12 (1979) 463
[55] Z. Wang, W. Wei, G. Liu, G. Mao, D. Kuang, *Acta Petrolei Sinica* 14 (1998) 21
[56] Mitsubishi Chemical Corp., US Patent 5,380,933 (1995)
[57] T.P. Moser, R.W. Wenig, G.L. Schrader, *Appl. Catal*. 34 (1987) 39

[58] H. Bosh, A. A. Bruggink, J. R. H. Ross, *Appl. Catal.* 31 (1987) 323
[59] A. Cruz-López, N. Guilhaume, S. Miachon, J.-A. Dalmon, *Catal. Today* 107 (2005) 949
[60] V. S. Escribano, G. Busca, V. Lorenzelli, *J. Phys. Chem*. 94 (1990) 8939
[61] V. V. Guliants, R. Bhandari, J. N. Al-Saeedi, V. K. Vasudevan, R. S. Soman, O. Guerrero-Pérez, M. A. Bañares, *Appl. Catal.* 274 (2004) 123
[62] R. K. Grasselli, C. G. Lugmair, A. F. Volpe Jr., A. Andersson, J. D. Burrington, *Cat. Today* 157 (2010) 33
[63] B. Deniau, J. M. M. Millet, S. Loridant, N. Christin, J. L. Dubois, *J. Catal*. 260 (2008) 30
[64] T. Blasco, P. Botella, P. Concepción, J. M. López-Nieto, A. Martinez-Arias, C. Prieto, *J. Catal*. 228 (2004) 362
[65] V. H. Rane, U. Rodemerck, M. Maerns, *J. Mol. Catal. A* 245 (2006) 161
[66] M. Ai, *J. Catal.* 101 (1986) 389
[67] Y. Han, H. Wang, H. Cheng, J. Deng, *J. Chem. Soc., Chem. Comm*. (1999) 521
[68] J. C. Vedrine, J. M. M. Millet, J. C. Volta, *Catal. Today* 32 (1996) 115
[69] M. Ai, *Catal. Today* 42 (1998) 297
[70] G. Landi, L. Lissi, J-C. Volta, *J. Mol. Catal. A* 222 (2004) 175
[71] J-M. Jheng, G. Deo, B. M. Weckhuysen, I. E. Wachs, *J. Mol. Catal. A* 110 (1996) 42
[72] A. E. Lewandowska, M.Calatayud, F. Tielens, M. A. Bañares, *J. Phys. Chem. C* 115 (2011) 24133
[73] Z.-Y. Xue, G. L. Schrader, *J. Phys. Chem. B* 1999, 103, 9459
[74] G. W. Clouston, S. R, Bare, H. Kung, K. Birkeland, G. K. Bethke, R. Harlow, N. Herron, P. L. Lee, *Science* 275 (1997) 191
[75] V. V. Guliants, J. B. Bezinger, S. Sundaresan, I. E. Wachs, J. M. Jehng, J. E. Roberts, *Catal. Today* 28 (1996) 275
[76] G. Landi, L. Lisi, G. Russo, *J. Mol. Catal. A* 239 (2005) 172
[77] Y. Han, H. Wang, H. Cheng, R. Lin, J. Deng, *New J. Chem*. (1998) 1175
[78] N. Nojiri, Y. Sakai, Y. Watanabe, *Catal. Rev*. 37 (1995) 145
[79] J. M. Oliver, J. M. López Nieto, P. Botella, *Catal. Today* 96 (2004) 241
[80] J. M. López Nieto, *Top. Catal*. 41 (2006) 3
[81] H. G. Lintz, S. P. Müller, *Appl. Catal.* 357 (2009) 178
[82] S. Umemura, K. Odan, H. Asada, Y. Nakamura, M. Tsuruoka, JP Patent 58-49535B (1983)
[83] Petrotex, US Patents 3607966 (1971), 3666687 (1972)
[84] M. Ogawa, JP Patent 62-34742B (1987)
[85] P. Kampe, L. Giebeler, D. Samuelis, J. Kunert, A. Drochner, F. Haab, A. H. Adams, J. Ott, S. Endres, G. Schimanke, T. Buhrmester, M. Martin, H. Fuess, H. Vogel, *Phys. Chem. Chem. Phys.* 9 (2007) 3577
[86] M. M. Lin, *Appl. Catal*. 207 (2001)1
[87] R. K. Grasselli, *Catal. Today* 49 (1999) 141

[88] N. Ballarini, F. Cavani, S. D. Memmoa, F. Zappoli, P. Marion, *Catal. Today* 141 (2009) 264

[89] M. O. Guerrero–Pérez, M. A. Bañares, *ChemSusChem* 1 (2008) 511

[90] E. Rojas, M. Calatayud, M. A. Bañares, M. O. Guerrero-Pérez, *J. Phys Chem*. C 116 (2012) 9132

[91] R. López-Medina, *Dissertation: "Estudio de la oxidación parcial de propano para la obtención de ácido acrílico utilizando catalizadores nanoestructurados MoVNbTeO/γ-Al_2O_3"*, Universidad Complutense de Madrid 2012

[92] B. Kilos, M. Aouine, I. Nowak, M. Ziolek, J. C. Volta, *J. Catal*. 224 (2004) 314

[93] J. S. Kim, S. I. Woo, *Appl. Catal.* 110 (1994) 207

[94] M. O. Guerrero-Pérez, J. L. F. Fierro, M. A. Vicente, M.A. Bañares, *J. Catal*. 206 (2002) 339

[95] G. Centi, S. Perathoner, F. Trifiro, *Appl. Catal.* 157 (1997) 143

[96] A. T. Guttmann, R. K. Graselli, J. F. Brazdil, US Patent: 724226 [US4746641] 1988

[97] Y. Li, J. N. Armor, *J. Catal.* 176 (1998) 495

[98] M. O. Guerrero-Pérez, J. L. G. Fierro, M. A. Bañares, *Catal. Today* 78 (2003) 387

[99] M. Pepera, J.L. Callahan, M.J. Desmond, E.C. Milberger, P.R. Blum, N.J. Bremer, *J. Am. Chem. Soc.* 107 (1985) 4883

[100] R. M. Contractor, A. W. Sleight, *Catal. Today* 3 (1988) 175

[101] M. O. Guerrero-Pérez, M.A. Bañares, *J. Phys. Chem.* 111 (2007) 1315

[102] G. C. Bond, S. Flamerz Tahir, *Appl. Catal.* 71 (1991) 1

[103] I. E. Wachs (Ed.), K. Segawa, *Characterization of Catalytic Materials*, Butterworth-Heinemann, Boston 1992, Chapter 4

[104] L. Owens, H. H. Kung, *J. Catal.* 144 (1993) 202

[105] J. Le Bars, J. C. Vedrine, A. Auroux, S. Trautmann, M. Baerns, *Appl. Catal. A* 88 (1992) 179

[106] J. Due-Hansen, S. B. Rasmussen, E. Mikolajska, M. A. Bañares, P. Ávila, R. Fehrmann, *Appl. Catal. B* 107 (2011) 340

[107] M. de Boer, *Dissertation: On the design and properties of silica-supported molybdenum oxide catalysts*, Utrecht University 1992, ISBN 90-393-0384-3

[108] J. R. Anderson, M. Boudart (Eds.), Mel, J. C.; Moulijn, J. A., *Catalysis: Science and Technology,* Springer-Verlag: Heidelberg, Germany, 1987; Vol. 8, p 69.

[109] A. K. Bhattacharya, J.A. Breach, S. Chand, D.K. Ghorai, A. Hartridge, J. Keary, K.K. Mallick*, Appl. Catal. A* 80 (1992) L1-L5

[110] R.J.H. Griseland, B.E. Nieuwenhuys, *J. Catal.* 199 (2001) 48

[111] O. M. Guerrero-Pérez, M. A. Bañares, *Chem. Commun.* (2002) 1292

[112] H. Tian, E. I. Ross, I. E. Wachs, *J. Phys. Chem.* 110 (2006) 9593

[113] C. Zhao, I. E. Wachs, *J. Catal*. 257 (2008) 181

[114] M. V. Martínez-Huerta, X. Gao, H. Tian, I. E. Wachs, H. L. G. Fierro, M. A. Bañares, *Catal. Today* 118 (2006) 279

[115] M. V. Martínez-Huerta, G. Deo, H. L. G. Fierro, M. A. Bañares, *J. Phys. Chem.* 111 (2007) 18708
[116] G. Deo, I. E. Wachs, *J. Phys. Chem*. 95 (1991) 5889
[117] M. A. Bañares, I. E. Wachs, *J. Raman Spetrosc*. 33 (2002) 359
[118] I. E. Wachs, *Catal. Today* 27 (1996) 437
[119] E. L. Lee, I. E. Wachs, *J. Phys. Chem*. C 111 (2007) 14410
[120] A. E. Lewandowska, M. Calatayud, F. Tielens, M. A. Bañares, *J. Phys. Chem*. C 115 (2011) 24133
[121] X. Gao, M. A. Bañares, I. E. Wachs, *J. Catal.* 188 (1999) 325
[122] M. D. Argyle, K. Chen, C. Resini, C. Krebs, A. T. Bell, E. Iglesia, *J. Phys. Chem. B* 108 (2004) 2345
[123] M. A. Bañares, J. H. Cardoso, F. Agulló-Rueda, J. M. Correra-Bueno, J. L. G. Fierro, *Catal. Lett*. 64 (2000) 191
[124] M. V. Martínez-Huerta, H. L. G. Fierro, M. A. Bañares, *Catal. Commun*. 11 (2009) 15
[125] M. V. Martínez-Huerta, G. Deo, J. L. G. Fierro, M. A. Bañares, *J. Phys. Chem*. 112 (2008) 11441
[126] L. E. Briand, A. M. Hirt, I. E. Wachs, *J. Catal.* 202 (2001) 268
[127] L. E. Briand, J.-M. Jehng, L. Cornaglia, A. M. Hirt, I. E. Wachs, *Catal. Today* 78 (2003) 257
[128] C. Zhao, X. Gao, I. E. Wachs, *J. Phys. Chem. B* 107 (2003) 6333
[129] Y. Zhang-Lin, M. Forissier, J. C. Védrine, J. C. Volta, *J. Catal.* 145 (1994) 267
[130] Z. Sobalik, S. Gonzalez, P. Ruiz, B. Delmon, *Stud. Surf. Sci. Catal.* 110 (1997) 1213
[131] H. W. Zanthoff, S. A. Bichholz. O. Y. Ovsitzer, *Catal. Today* 32 (1996) 291
[132] R. K. Grasselli, J. D. Burrington, D. J. Buttrey, P. DeSanto Jr., C. G. Lugmair, A. F. Volpe Jr., T. Weingand, *Topics in Catal.* 23 (2003) 5
[133] G. Centi, F. Trifiro (Eds.) M. Najbar, W. Wal, J. Chrząszcz, *New Developments in Selective Oxidations,* Elsevier Science Publishers B. V., Amsterdam 1990, p. 779
[134] J. N. Al-Saeedi, V. K. Vasudevan, V. V, Guliants, *Catal. Commun*. 4 (2003)537
[135] G. Liberti, N. Pernicone, S. Soattini, *J. Catal.* 27 (1972) 52
[136] J. A. Moulijn, A. E. van Diepen, F. Kapteijn, *Appl. Catal.* 212 (2001) 3
[137] G. Busca, *J. Mol. Catal.* 50 (1989) 241
[138] J.-M. Jehng, I. E. Wachs, *Chem. Mater.* 3 (1991) 100
[139] E. I. Ross-Medgaarden, W. V. Knowles, T. Kim, M. S. Wong, W Zhou, C. J. Kiely, I. E. Wachs, *J. Catal.* 256 (2008) 108
[140] K. Routray, W. Zhou, C. J. Kiely, W. Gruenert, I. E. Wachs, *J. Catal.* 275 (2010) 84
[141] R. I. Bergman, N. W. Frisch, US Patent 3 (1966) 293, 268
[142] Y. H. Taufiq-Yap, F. Rezaei, A. A. Rownaghi, *Ind. Eng. Chem. Res*. 48 (2009) 7517
[143] M. T. Sananes, G. J. Hutchings, J. C. Volta, *J. Catal*. 154 (1995) 253
[144] G. Centi, F. Trifiró, J. R. Ebner, V. M. Franchetti, *Chem. Rev.* 88 (1988) 55

[145] Y. Z. Lin, M. Forissier, R. P. Sneeden, J. C. Vèdrine, J. C. Volta, *J. Catal*. 145 (1994) 267

[146] F. B. Abdelouahab, R. Olier, N. Guilhaume, F. Lefebvre, J. C. Volta, *J. Catal*. 134 (1992) 151

[147] C. J. Kiley, G. J. Hutchings, *Appl. Catal.* A: General, 325 (2007) 194

[148] F. Girgsdies, M. Schneider, A. Brückner, T. Ressler, R. Schlögl, *Sol. St. Sci.* 11 (2009) 1258

[149] D. Wang, H. H. Kung, M. A. Barteau, *Appl. Catal.* 201 (2003) 203

[150] L. Lopez Soto, *Dissertation: Studies of the Mars van Krevelen Mechanism in Hydrocarbon Selective Oxidation*, University of Delware, DAI/B 68-05, p. , Oct 2007, Publication number: 3267153

[151] H. S. Horowitz, C. M. Blackstone, A. W. Sleight, G. Teufer, *Appl. Catal.* 38 (1988) 193

[152] L. M. Cornaglia, C. A, Sanchez, E. A. Lombardo, *Appl. Catal.* 95 (1993) 117

[153] R. K. Graselli, A. W. Sleight (Eds.), J. R. Ebner, M. R, Thompson, *Structure-Activity and Selectivity Relationships in Heterogeneus Catalysis*, Elsevier, Amsterdam (1991) 31

[154] F. Cavani, F. Trifiró, *Catalysis* 11 (1994) 246

[155] P. Ruiz, B. Delmon (Eds.), M. Guilhoume, M. Roullet, G. Pajonk, B. Grzybowska, J. C. Volta, *New Developments in Selective Oxidation by Heterogeneous Catalysts*, Elsevier, Amsterdam (1922) 255

[156] M. O'Connor, F. Dason, B. K. Hodnett, *Appl. Catal.* 64 (1990) 161

[157] L. M. Cornaglia, C. Caspani, E. A. Lombardo, *Appl. Catal.* 74 (1991) 15

[158] L. DeCaul, R. K. Grasselli, *Catal. Lett*. 23 (1994) 339

[159] V. V. Guliants, M. A. Carreon, *Catalysis* 18 (2005) 1

[160] M. Conte, G. Budroni, J. K. Bartley, S. H. Taylor, A. F. Carley, A. Schmidt, D. M. Murphy, F. Girgsdies, T. Ressler, R. Schlögl, G. J. Hutchings, *Science* 313 (2006) 1270

[161] N. Ballarini, F. Cavani, C. Cortelli, M. Ricotta, F. Rodeghiero, F. Trifiró, C. Fumagalli, G. Mazzoni, *Catal. Today* 117 (2006) 174

[162] F. Cavani, F. Trifiró, *Chemtech* 24 (1994) 18

[163] Z-Y. Xue, G. L. Schrader, *J. Phys. Chem. B* 103 (1999) 9459

[164] M. Abon, K. E. Bere, A. Tuel, P. Delichere, *J. Catal.* 156 (1995) 28

[165] I. E. Wachs, J.-M. Jheng, G. Deo, B. M. Weckhuysen, V. V. Guliants, J. B. Bezinger, *Catal. Today* 32 (1996) 47

[166] R. A. Overbeek, *Dissertation: New aspects of the selective oxidation of n-butane to maleic anhydride: The development of a novel catalysts.*, Utrecht University 1994, ISBN 90-393~0993-0

[167] M. Ruitenbeek, *Dissertation: Characterization of vanadium-based oxidation catalysts,* Utrecht University 1999, ISBN 90-393-2051-9

[168] G. Centi, T. Tosarelli, F. Trifiró, *J. Catal.* 142 (1993), 70

[169] G. Centi, S. Perathoner, *J. Catal.* 1993, 142, 84

[170] G. Centi, D. Pesheva, F. Trifiro, *Appl. Catal*. 33 (1987) 343

[171] V. N. Kalevaru, B. Lücke, A. Martin, *Catal. Today* 142 (2009) 158
[172] V. N. Kalevaru, N. Madaan, A. Martin *Appl. Catal.* 391 (2011) 52
[173] V. N. Kalevaru, A. Martin, U. Bentrup, B. Lücke, J. Sans, *Appl. Catal.* 270 (2004) 59

2

Experimental procedures

2.1 INTRODUCTION

In this chapter the catalyst preparation, applied characterization techniques and the experimental set-up for the catalytic test reactions are described. In all cases a short description of the used methodology is included to reveal the suitability of chosen techniques and methods. Unless stated otherwise, the results presented in subsequent chapters are obtained as described in this chapter.

2.2 Preparation methods

2.2.1 Preparation of supported catalysts

The catalysts used in this study were alumina- or titania-supported vanadium and phosphorus oxides. They were all prepared by the incipient wetness impregnation method varying the P/V ratio (0.1-1.1) and the loading (1 – 4 V+P monolayers). Supported vanadium or phosphorus oxide catalysts were prepared as references. This impregnation method is widely used for preparation of monolayer-type catalysts [[1,2,3]]. It denotes a procedure where a solution containing the active element is completely absorbed in the pores of the support [[4]]. The procedure used for synthesis of vanadium based supported catalysts is well known. It includes dissolving NH_4VO_3 in an aqueous solution of $(COOH)_2$, which leads to reduction of vanadium ($V^{5+}_{yellow} \rightarrow V^{4+}_{blue}$) and formation of the $(NH_4)_2[VO(C_2O_4)_2]$ complex as a deep blue solution, according to the procedure described below.

Oxalic acid (Panreac Química S.A.) and ammonium metavanadate (99%, Sigma Aldrich) were dissolved in distilled water. The solution was stirred one hour at 70 ^{o}C, while its color has changed from orange through green to deep blue. At this stage the phosphoric acid (85%, Panreac Química S.A.) was added. The final solution was stirred at 70 ^{o}C and, after one hour, impregnated onto γ-Al_2O_3 (Sasol, Puralox SCCa-5/200, ca. 200 m^2/g) or TiO_2-anatase (Cymit Química CEE 215-280-1, ca. 150 m^2/g) by the incipient wetness impregnation method. The catalysts were dried in the air at room temperature and afterwards treated at 400 ^{o}C during 19 hours in a flow of nitrogen in order to avoid the total oxidation of vanadium. The color of the catalyst precursor was blue and became dark green or brown after N_2 treatment, which suggests, that indeed, vanadium was not completely oxidized.

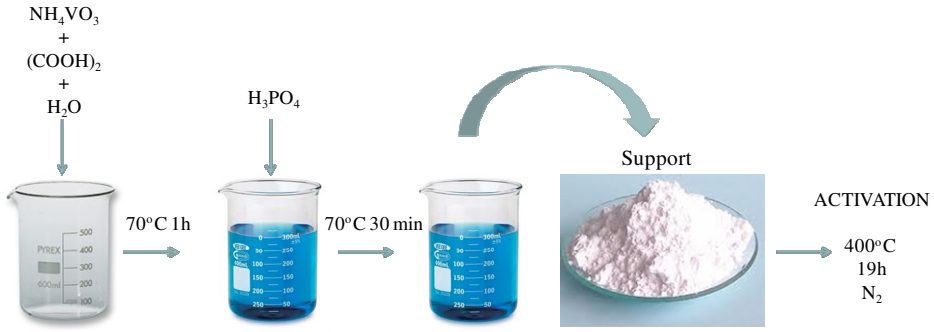

Figure 2.1 Scheme of a preparation method of supported vanadium and phosphorus oxide catalysts

The V-P-O supported catalysts were compared to vanadium supported catalysts in order to evaluate the role of phosphorus in VPO-type materials and to bulk industrial VPO catalysts (supplied by DuPont) for evaluation of the support role.

2.2.2 Bulk VPO catalyst supplied by DuPont

DuPont has performed specialized modifications of the VPO catalyst for the tetrahydrofuran (THF) manufacture. This process was carried out in a fluidized bed reactor, to overcome the potential problem of hotspots [5,6]. In this reactor type the catalyst particles collide continuously with each other and for this reason a high attrition resistance of the catalyst particles is required. Various more or less successful attempts have been reported previously in literature [7,8,9,10], while DuPont has developed a new method of imparting the resistance of bulk VPO catalyst without decrease of selectivity to maleic anhydride [11,12]. The modified VPO catalyst consists of ca. 150 μm of a V-P-O core encapsulated in a porous silica shell of ca. 2 μm and was prepared as described below.

The VPO precursor was prepared in an organic medium with *iso*-butanol and benzyl alcohol and subsequently spray-dried with polysilicic acid to form a porous silica shell. The precursor was then calcined at 390 °C and the silica-surrounded $VOHPO_4*0.5H_2O$ material was transformed to $(VO)_2P_2O_7$ [13]. Silica content ranges from 5 to 20 wt. % of bulk VPO catalyst. DuPont supplies these silica-shelled bulk VPO catalysts to laboratories worldwide for their analysis in order to further understand the functionality of these catalysts.

Supported catalysts were marked as xVyPSu, where x and y are numbers of atoms of vanadium and phosphorous per nm^2 of the support (Su), while VPO corresponds to the commercial bulk VPO catalyst (DuPont, vanadyl pyrophosphate, calcined catalyst).

2.3 Nitrogen Physisorption Measurements

N_2 physisorption measurements provide information on sample texture and porosity. The higher is the surface area, the more gas is adsorbed; which inherently induce either greater number of active sites or better dispersion. In case of supported metal oxide catalysts, the surface area decreases with increasing loading of the active phase which can partly be due to closing of the support pores with the embedded active phase, but also due to the introduction of non-porous active material, often with higher atomic mass, which diminishes the volume fraction of porous material per gram of sample. The Brunauer, Emmett and Teller model (BET) provides a mathematical approach to gas adsorption over an entire exposed surface and of a material and its pores [14]. It is used for measuring the total surface area and for determination of the pore size, e. g. micropores (<2 nm), mesopores (2-50 nm) and macropores (>50 nm). Nitrogen adsorption at -196 ^oC is the most conventional technique for surface area analysis, as the molecular size of N_2 is well established (0.164 nm^2), and additionally it is inert and inexpensive. This technique includes determination of the extent of N_2 adsorption at relative pressures from 0 to 1, since the shape of the isotherm depends strongly on the texture of the analyzed material. Nitrogen may be replaced with smaller argon molecule for materials with very low surface areas. The model developed by Brunauer, Emmett and Teller (BET) determines the monolayer volume (V_m) of the adsorbate as the surface area (S_{BET}) according to the equation 2.1 [15]:

$$S_{BET} = \frac{V_m}{22414} N_a \sigma \qquad \text{(eq. 2.1)}$$

Where V_m is the monolayer volume, N_a is Avogadro number, and σ states for the area occupied by one N_2 molecule (0.164 nm^2).

The BET surface area values of the catalysts and the adsorption/desorption isotherms were determined with a Micromeritics TriStar-3000 analyzer with N_2 as the adsorbate at -196 ^oC. Degasification was performed at 140 ^oC for 2 hours. The estimated error is ca 5-10%.

2.4 Powder X-Ray Diffraction

Powder X-ray diffraction (XRD) is a widely used for characterizing materials in catalysis due to the huge data bank available covering virtually every phase of every known material. It is a non-destructive technique and does not require any special sample treatment. The ideal sample is homogeneous and the crystallites are randomly distributed. The sample is pressed into a self-supporting disc to obtain a smooth, flat surface. The X-rays penetrate deep into the analyzed material and their diffraction provides information about the bulk structure. A characteristic pattern of the sample is produced when plotting the angular positions and intensities of the resulting diffracted peaks. The X-ray diffraction pattern of a pure substance is like its fingerprint and when a mixture of different phases is present, the resultant diffractogram is formed by their linear combination. Based on the principle of X-ray diffraction, a wealth of structural, physical and chemical information about the material investigated can be obtained.

During this analysis, the X-ray photons collide with the atoms. As a result some photons from the incident beam are scattered away without changing their energy (elastic scattering,), while others have different wavelength than the incident X-rays after collision with the electrons (inelastic scattering). The elastic scattering provides information about atomic distribution in materials. Scattered photons may interfere with each other either destructively or constructively. When they undergo a constructive interference according to Bragg's law, a diffraction pattern is produced. The interference is constructive when the phase shift is a multiple of 2π. Bragg peaks are obtained when scattered waves satisfy the Bragg condition:

$$2d\sin\theta = n\lambda \quad \text{(eq. 2.2)}$$

In which n is an integer determined by the order given, λ is the wavelength of incident wave, d is the spacing between the planes in the atomic lattice, and θ is

the angle between the incident ray and the scattering planes. So that the path difference between two waves undergoing constructive interference is given by *2dsinθ*.

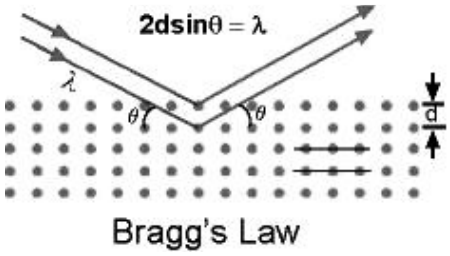

Figure 2.2 Graphical description of the Bragg's Law

The possible *d*-spacing defined by the indices *h*, *k*, *l* are determined by the shape of the unit cell. Rewriting Bragg's law we get:

$$\sin \theta = \lambda/2d \quad \text{(eq. 2.3)}$$

Therefore the reflections at *2θ* values are determined by the unit cell dimensions. However, the intensities of the reflections are determined by the distribution of the electrons in the unit cell. Since the highest electron densities are found around atoms the intensities depend on what kind of atoms are present and where in the unit cell they are located.

XRD analyses were performed with an X-Ray Diffractometer PANanalytical PW3040/60 using Cu Kα, 1.5406 Å, equipped with a Ni filter and X'Celerator RTMS detector. The voltage of the X-ray tube was 45 kV and the current 40 mA. The sample was pressed into a self-supporting disc of 14 mm diameter and the XRD spectra were taken in 4 – 90^{o} range, with 0.4^{o} degree soller-slit collimator.

2.5 Ultraviolet-visible Spectroscopy

The UV-Vis spectrometry is a spectroscopic technique involving the use of light in the visible, near ultra-violet and near infrared regions in order to cause electronic transitions in the target material. When a sample is exposed to light having an energy that matches the possible electronic transition within the molecule, the electron is promoted to a higher energy orbital. Molecules absorb some of the light, accommodate the additional energy and in consequence promote electrons to higher energy atomic or molecular orbitals. The d-d transitions, ligand-to metal, metal-to-ligand, $n \rightarrow \pi^*$ and $\pi \rightarrow \pi^*$ transitions are possible in transition metal ions, inorganic and organic molecules. An optical spectrometer records the wavelengths at which the absorption occurs, together with the degree of the absorption at each wavelength. The resulting spectrum is presented as a graph of absorbance (*A*) versus wavelength. The absorbance usually ranges from 0 (when no absorption occurs) to 2 (ca. 99% absorption), and is precisely defined in context with spectrometer operation.
Since transmission experiments of solids are almost impossible, a diffuse reflectance spectroscopy based on the reflection of light by a sample becomes an alternative. This technique provides information about the electronic structure, oxidation states and coordination environment of transition metal ions and adsorbed species. It is a "bulk" technique but may be used in determining the local structure of supported metal oxides (e. g. isolated monomers, dimmers, polymeric species, clusters or 3D structures) by comparison with electronic structures of well defined metal oxide reference compounds [16]. In this case the support may be usually used as a baseline standard due to its low absorbance.

Kubelka-Munk theory is universally used for modeling optical properties of light scattering materials. It is generally used for the analysis of diffuse reflectance spectra obtained from weakly absorbing samples and provides a correlation between reflectance and concentration. A common problem for powder samples in a diffuse reflectance spectroscopy is that the scattering effect is strongly enhanced, since high superficial area is exposed. This causes problems of technical nature (dispersed light may be counted as absorbed light). The Kubelka Munk formula $F(R_\infty)$ is used to avoid these complications [17]:

$$F(R_\infty) = \frac{(1-R_\infty)^2}{2R_\infty} = \frac{k}{s} = \frac{Ac}{s} \quad \text{(eq. 2.4)}$$

$$\text{where } R_\infty = \frac{R_{sample}}{R_{standart}} \quad \text{(eq. 2.5)}$$

The equation 2.4 is used in the infinitely thick sample, when the thickness and the sample holder have no influence on the value of *R*. In equations 2.4 and 2.5 *R* states for reflectance, *k* for absorption coefficient, *s* is a scattering coefficient, *c* is concentration of the absorbing species and *A* is the absorbance (*log1/R*).

Obtaining $F(R_\infty)$ from the equation 2.4 and plotting the $[F(R_\infty)hv]^{1/n}$ against *hv*, where *hv* is the photon energy, and *n* depends on the type of transition, the band gap, *Eg* of powder samples may be easily determinate. The *Eg* of a material is defined as the energy distance between the valence and conduction bands. The smaller is the band gap, the more electrically conductive is the material. The *Eg* of insulators is large (> 4eV), which explains why there are so few electrons found in their conduction bands. The *Eg* for semiconductors is lower (< 3eV) but it may be increased by dopant addition (e.g. cadmium) by introducing additional energy levels within the band gap.
UV-Vis spectra were run with an Avantes spectrophotometer, model AvaSpec2048-TEC equipped with an optic fiber FCR-7xx200-2, a refrigerated CCD detector (-30 ^{o}C) and a UV and visible light source, AvaLight-DHS. UV–vis spectra were collected in reflectance mode in a 200-1100 nm range and converted into Kubelka–Munk (KM) function. For each spectrum, 11 accumulations of 50 milliseconds were made and a Halon white disc was used as a reference standard.

2.6 Temperature Programmed Reduction Analysis

The method of temperature programmed reduction (TPR) is widely used for measurements of reduction kinetics of metal oxides. The reducing agent continuously flows over a surface of a sample at low temperature, so that the

reduction rate is close to zero. Subsequently the temperature is increased linearly and the reaction rate increases depending on the catalyst activity and the actual degree of reduction of the material until it is completely reduced. The reactant consumption is measured at the outlet with a high sampling rate, thus the TPR curves deliver information on the whole spectrum of reduction reactions that occur in the examined system.

Mettler Toledo (TGA/SDTA 851^e) analyzer with a mass detector (Pfeiffer model Thermostar) was used for determination of these analyses. Samples were activated in N_2 flow (50 ml min^{-1}) at 200 ^oC for 30 minutes. Subsequently 10% of H_2 in N_2 was used with a flow of 50 ml min^{-1} for the TPR study at 25-950 ^oC temperature range.

2.7 Thermal Gravimetric Analysis and Differential Thermal Analysis

Thermal gravimetric analysis (TGA) analysis determinates with precision changes in sample weight in relation to temperature in a controlled atmosphere. The analyzed material is heated to high temperatures so that a decomposition of the solid sample into a gas occurs. The composition and purity of analyzed material may be determined as well as its temperature of decomposition. The complementary information obtained by differential thermal analysis (DTA) allows differentiation between endothermic and exothermic events.

TGA/DTA spectra were run with a Thermo Gravimetric Mettler Toledo TGA/SDTA 851^e analyzer equipped with a balance sensitive up to 1 μg and with an oven, which allows heating the sample up to 1100 ^oC. Spectra were registered up to 650 ^oC with a temperature ramp of 10 ^oC min^{-1} in a flow of N_2.

2.8 X-Ray Photoelectron Spectroscopy

X-ray photoelectron spectroscopy (XPS) is widely used for detection and quantification of elements present in the analyzed material and for the determination of their oxidation states and coordination. Generally, all elements except hydrogen and helium can be analyzed. When a photon with definite energy hv is absorbed by an atom an ejection of a core or valence electron occurs. The energy of this electron is changed from binding energy E_{bin} to the kinetic energy E_{kin} at the time when the electron leaves the sample. Then it may

be easily analyzed by a detector and since kinetic energies of the emitted electrons depend on their bindings energies, which are characteristic of specific elements, the composition of the sample may be analyzed.

$$E_{kin} = h\nu - E_{bin} - e\varphi_{Spec} \quad \text{(eq. 2.6)}$$

In the equation 2.6 E_{kin} states for the kinetic energy of the photoelectron, h is the Plank's constant, υ is the frequency of the exciting radiation, E_{bin} represents the binding energy of the photoelectron with respect to the Fermi level of the sample and $e\varphi_{Spec}$ is the work function of the spectrometer. The binding energies are element specific, but also provide information of differences in oxidation states, molecular environment and lattice site.
However, due to the escape depth of (usually 1-3 nm, which corresponds up to ca. 15 monolayers, but penetration even up to 10 nm is possible) this technique is not purely surface sensitive. One solution for performing more adequate surface study seems to be the new Energy Resolved-XPS methodology (ER-XPS). This method enables tuning of the excitation energy to control the depth from which the measurement is performed and provides depth profile elemental composition information [18,19,20]. However, conventional XPS (with $AlK\alpha$ or $MgK\alpha$ sources) is not able to provide reliable information on the composition of the outermost surface layer. The intensity contribution from a depth z may be calculated for homogeneous materials according to equation 2.7:

$$I(z) = I(z = 0)\exp(-z/\lambda \cos\theta) \quad \text{(eq. 2.7)}$$

Where θ is the emission angle, and λ states for the inelastic mean free path of the photoelectrons (IMFP) [21]. The dependence of the inelastic mean free path of photoelectrons on the kinetic energy is shown in Figure 2.3. The diagram illustrates that in the 20-100 eV range the majority of photoelectrons come from the outermost layer and that the XPS technique used in this work gives the escape depth of ca. 2 nm. There are various methods for the calculation of the IMFP [22,23,24] and values may be find in tables or data bases [25].

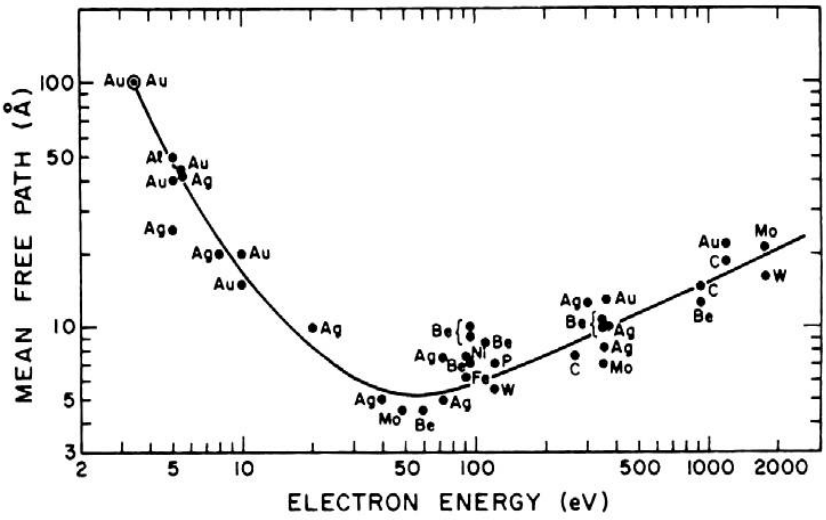

Figure 2.3 Empirical diagram of the inelastic mean free path of photoelectrons according to Delgass et al. [26]

The X-ray beam and the photoelectron emission may cause changes of the analyzed sample, e. g. changes in the sample composition or in the oxidation state, defects or vacancies formation, destruction of crystal order etc. The beam damage mostly depends on the X-ray beam, vacuum conditions, thermal and electric properties of the sample, surface roughness and incorporated contaminations. Charging effect occurs in case of poorly conducting samples. It relates to electron emission and formation of positive charge at the sample surface. It leads to broadening of the photoemission line and causes difficulties in data analysis.

XPS Spectra were recorded on a VG Escalab 200R electron spectrometer equipped with a X-ray source, hemispherical analyzer and a twin anode (where Mg K_α = 1254.6 eV, 1eV = 1.6302×10^{-19}J) working at 120 W.

High Resolution X-ray Photoelectron Spectroscopy (HR-XPS) of bulk VPO catalyst was performed at Lehigh University in Bethlehem PA, in the USA during a short-term stay in a group of prof. I. E, Wachs. Spectra were recorded on Scienta ESCA-300 High Resolution-X-ray Photoelectron Spectroscopy, which is currently a cutting-edge XPS instruments. Monochromatic Al Kα X-rays were generated from a rotating anode which can operate at power levels of up to 7.5 kW. The apparatus is equipped with a detector: a multi channel

microchannel plate-CCD camera combination and a non-line-of sight monochomatic low energy electron flood gun for charge compensation. The nominal analyzed area is rectangular with approximate dimensions of 4 mm x 0.2 mm for a total area of about 0.8 mm², while the depth resolution is 1-3 nm. The pressure of the XPS system was ca. $1*10^{-8}$ mbar.

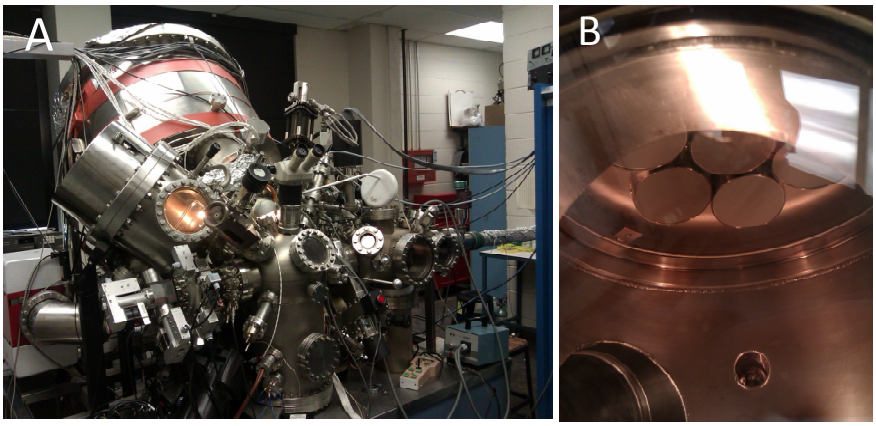

Figure 2.3 Scienta ESCA 300 XPS Spectrometer at Lehigh University (A), The monochromator of seven crystals mounted on three Rowland circles (B)

For alumina-supported catalysts, charge correction was done by taking the Al 2p peak at a binding energy of 74.5 eV. For unsupported VPO catalyst, the C 1s peak arising from contamination was fixed at a binding energy of 284.6 eV. These references gave an accuracy of ± 0.1 eV. A caution was taken for all XPS analysis in order to avoid the surface-damage problems, i. e. a couple of fast preliminary scans were taken before the analysis, while both, monochromatic and non-monochromatic X-ray sources were tested.

2.9 High Sensitivity Low-Energy Ion Scattering

"Whether you are trying to develop a new catalyst, fabricate a smaller transistor, or improve the adhesive properties of a polymer surface, it is extremely important to be able to control surface properties at the atomic level. (…) In order to do this, you must be able to analyze the surface composition with the same precision" said prof. H. Brongersma, who developed the world's most

sensitive spectrometer for identifying atoms on a target's surface (Lehigh University Surface Analysis Symposium) [27].

Low-energy ion scattering is the only technique that can identify atoms present at the outermost layer of a solid surface (~0.3 nanometer depth resolution) with no matrix effects taking place; there are no contributions from deeper layers. Additionally, it is one of the very few surface-sensitive techniques capable of directly observing hydrogen atoms. The LEIS spectroscopy is referred to primary energies in the range of 100 eV to 10 keV.

When a beam of an ionized noble gas (He, Ar, or Ne) hits the surface of analyzed material, it may either bounce straight back or it may be deflected. During this interaction a fraction of the momentum or energy of the gas ion is transferred to the surface atom. The energy loss is related directly to the atomic weight of the surface atom, so that by measuring the energy of the rebounded ion this technique enables determination of the atom from which the ion was scattered as well as the relative positions of atoms of the surface lattice. A detector is sensitive only to ions of the same type as those in the incident beam, that have had only one collision with a target atom (collision with the surface atom). After two or more collisions (penetration beyond the first surface layer) the noble gas ion is neutralized and thus is not measured by the detector. The energy of 1keV He^+ is high enough to penetrate deeper than only the first layer, but there is a possibility of ca. 99% of neutralization of He^+ when passing through one layer of surface atoms. Moreover the fraction of He^+ that survives the single collision without being neutralized is only between 10^{-4} and 10^{-2} [28,29]. For this reason the majority of the ions that reach the analyzer come scattered from the outermost layer. However, some ions neutralized in deeper layers may undergo ionization at the surface and, because of that, the LEIS spectrum might contain some information from a subsurface layer.

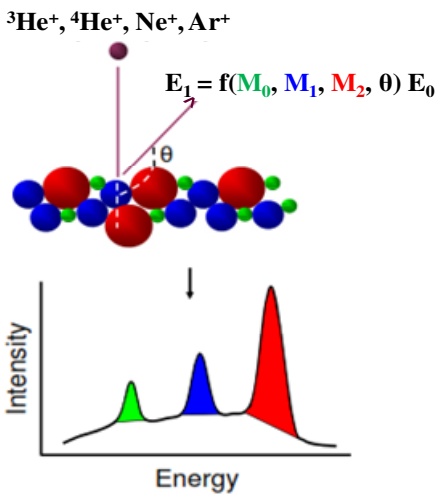

Figure 2.4 The collision model and its spectroscopic representation [30], E_1 – final energy, E_0 – initial ion energy, M – ion mass, θ – scattering angle

The kinetic energy of scattered ions (E_1) depends on the kinetic energy of the incident ion (E_0), on the mass of the ion (M_1) and of the mass of the scattering in the angle θ atom (M_2):

$$\frac{E_1}{E_0} = \frac{M_1^2}{(M_1 + M_2)^2}\left\{\cos\Theta_L + \left(\frac{M_2^2}{M_1^2} - \sin^2\Theta_L\right)^{\frac{1}{2}}\right\}^2 \quad \text{(eq. 2.8)}$$

While the intensity of the signal (I) can be expressed as:

$$I = I_p\, N_k\, \sigma\ P_k\, W \quad \text{(eq. 2.9)}$$

Where I_p states for the incident beam current, N_k for the surface atomic density, σ is the differential scattering cross-section (the probability that an incident ion will be scattered towards the detector, after a collision with an atom of species k), P_k – the probability that an ion remains un-neutralized after a collision, W – entrance solid angle of the detector.

The differential scattering cross section can be calculated from the interaction between the ion (Z_{ion}) with the atom (Z) according to the equation 2.10, which combines the Coulomb potential and screening function (a_0 states for the Bohr radius of the scattering atom):

$$V(r) = \frac{Z_{ion} e \cdot Ze}{r} \frac{0.85 a_0}{2r(\sqrt{Z_{ion}} + \sqrt{Z})^{2/3}} \quad \text{(eq. 2.10)}$$

However, the use of the equation 2.9 in quantitative analysis is limited, because the P_k parameter is hardly know, as the LEIS sensitivity varies with analyzed element. Since for elements like vanadium and phosphorus, the reference samples (exposing well defined and stable surface structures) are not available, the quantitative analysis becomes more complicated [31].

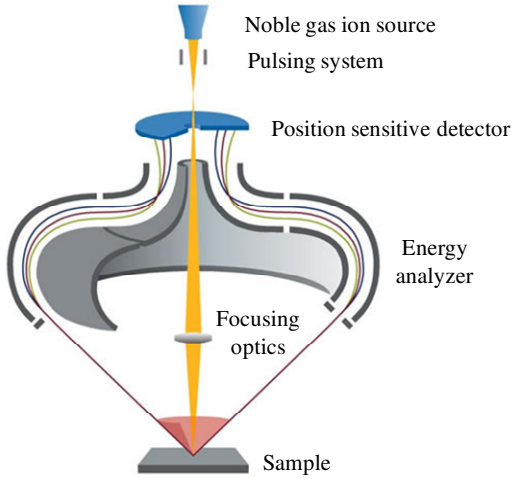

Figure 2.5 High-Sensivity Low Energy Ion Scattering analyzer (Qtac 100)

LEIS can analyze not only the surface; sputtering may be performed, which allows for the determination of the in-depth distribution of the elements present in the analyzed material. Because of the ion bombardment, atoms are sputtered

from the target surface exposing subsequent layers. A sputter dose of ca. 10^{15} ions cm^{-2} equals about one monolayer.
Unfortunately, the LEIS technique does not provide information about the oxidation state of the elements and the XPS gives an average oxidation state of even 10 nm depth. To learn about the oxidation state of the surface elements of a bulk material, a combination of LEIS and chemical titration methodologies is required. It consists in a titration of the metal cation by oxygen atoms and examines a decrease of a signal of the titrated metal.

HS-LEIS experiment was performed at Lehigh University using the ION-TOF Qtac 100 High Sensitivity-Low Energy Ion Scattering Spectrometer. The HS-LEIS system utilizes a unique double toroidal electrostatic energy analyzer that provides 3000 times higher sensitivity than a conventional ion scattering spectrometer. The base pressure was $1*10^{-9}$ mbar. $^{4}He^{+}$ ions were used as incident beam with energy of 4 keV for analysis beam. Sputtering was performed with Ar^{+} ions (1 keV). A sputter dose of ca. 10^{15} ions cm^{-2} equals about one monolayer. The total dose was $4*10^{16}$ ions cm^{-2}, which gives ca. 40 monolayers removed during the sputtering process.

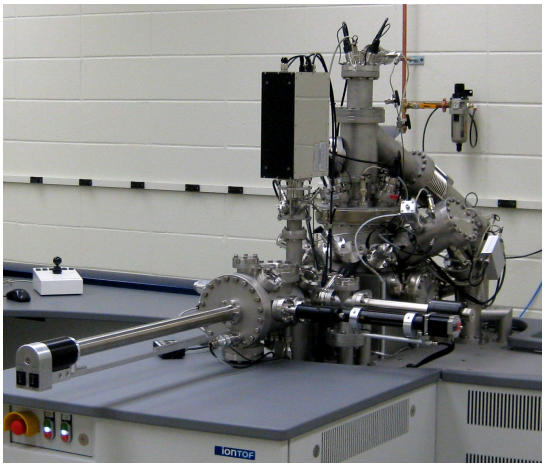

Figure 2.6 ION-TOF Qtac 100 High Sensitivity-Low Energy Ion Scattering Spectrometer at Lehigh University

2.10 X-ray Absorption Spectroscopy

X-ray absorption fine structure (XAFS) methodology relates to X-ray (ca. 500 eV to 500 keV) absorption by an atom at energies near and above its core level binding energies. It provides information about chemical and physical state of the atom, like: oxidation state, coordination and chemical environment. Essentially all elements may be analyzed, since all atoms have core level electrons with well defined binding energies it is possible to analyze different elements by tuning the X-ray energy to the appropriate absorption edge. Not only crystalline materials but also highly disordered materials (including solutions) are available for XAFS technique.

Figure 2.7 European Synchrotron Radiation Facility at Grenoble, France

Absorption of the radiation takes place when X-rays hits an atom with photon energy equal or higher than the binding energy of a core electron. It results in excitation of the electron and formation of a photoelectron, while an adsorption edge is observed in the XAFS spectra. The ejected photoelectrons are considered as spherical waves, which are subsequently reflected from neighbouring atoms. This causes modulation of the outgoing wave and results in a fine structure of the absorption spectrum. The spectrum is typically divided in two regions:

- The X-ray absorption near edge spectroscopy, XANES or NEXAS – the kinetic energy of the electron is small and the scattering on the neighboring atoms is strong, because the corresponding wave vector of the photoelectron is large enough to be comparable to the inter-atomic distances between the absorber and its neighbors. XANES is sensitive to the oxidation state and coordination chemistry.

- The extended X-ray absorption fine structure spectroscopy, EXAFS – the kinetic energy of the electron is smaller, so that the scattering is smaller, because the absorption of X-ray is decreasing with the increasing energy of the X-ray photons. It is sensitive to the environment of the absorbing atom, distances and coordination numbers.

However, in this work we will focus only on XANES spectra, the region of X-ray absorption spectrum within ca. 50 eV of the absorption edge. Even though XANES provides much chemical information (K-edges XANES show dependence on local coordination chemistry), its interpretation is complicated. The reason is that this technique is quite new and no simple description of XANES is yet available. Also, there are still no equations useful for quantification of XANES spectra. However, a significant progress has been done in the last decade. XANES may be used as fingerprint to identify phases of the analyzed material. Moreover, this technique is very useful for determination of oxidation states and coordination chemistry and enables a wide range of in situ experiments at elevated pressures and temperatures. In many cases a linear combination of spectra of well-known references with the analyzed compound is enough for determination of valence states and phases.

V K-edge absorption spectra were performed at SpLine BM25A (Spanish CRG Beamline for Absorption and Diffraction) at European Synchrotron Radiation Facility (Grenoble, France), one of the largest synchrotrons in the world. Electrons are emitted by an electron gun, and accelerated first in a linear accelerator and then in a circular accelerator. When they reach the required speed are injected to the storage ring where are circulating in vacuum for hours passing through different type of magnets.

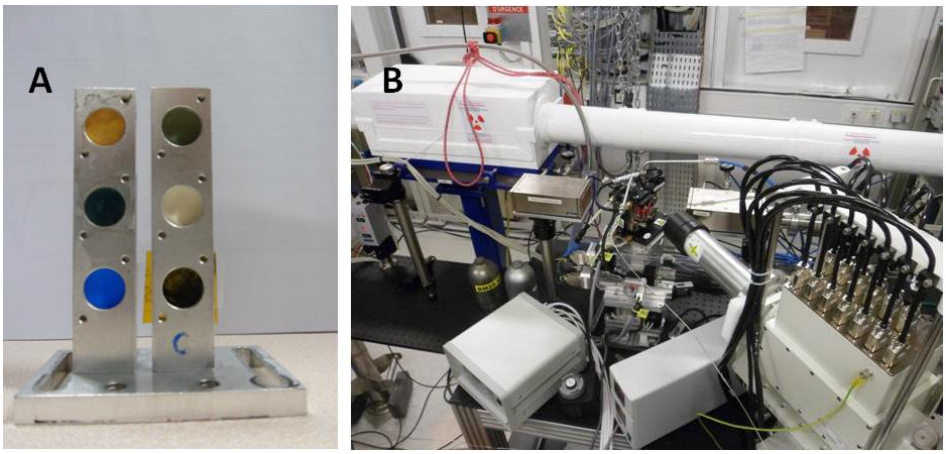

Figure 2.8 XAFS sample holder (A), operating system during XANES analyses (B), ESRF, Grenoble, France

The electron energy of the storage ring of 844 m was 6.0 GeV and the ring current varied between 150 and 200 mA, 13-element Si(Li) detector from e2v Scientific Instruments was used. The incident energy range of SpLine BM25A was 5-45 keV, were the highest value is actually at the boarder of detection of vanadium atoms (V K-edge = 5465 eV). The measurements were performed in reflectance mode because of a low transmission capacity of analyzed samples. The samples were pressed into self-supporting discs without dilution (ca. 40 mg) and placed in a sample holder. Spectra were taken in reflectance mode. For each spectra 1 accumulation of 15 s was taken. A vanadium metal foil was used for calibration of the edge position. The spectra were normalized using Athena software.

2.11 Electron Paramagnetic Resonance

The electron paramagnetic resonance (EPR) spectroscopy is a technique for studying molecules with one or more unpaired electrons. It employs magnetic fields in combination with microwave excitation in a range between 1-500 GHz, since electrons can be turned and twisted in a magnetic field by microwaves. EPR spectrometers work by generating microwaves from a radiation source (e. g. originally klystrons, but nowadays gunn diodes). The radiation passes through

an attenuator to the sample located in a microwave cavity. The frequency of the radiation is held constant while the magnetic field is varied in order to obtain the situation where the energy of the electromagnetic wave match the energy gap created between the two spin states by the electromagnetic field. Thus energy absorption occur, which essentially yields an absorption spectrum. Microwaves reflected back from the cavity are routed in a circulator to the detector. When absorption of the radiation takes place ($\Delta E = h\nu$), a spectrum is produced and presented as the first derivative. In absence of a magnetic field applied, B_0 two spin states have the same energy, but two states with different energies are possible for an electron when magnetic field is applied.

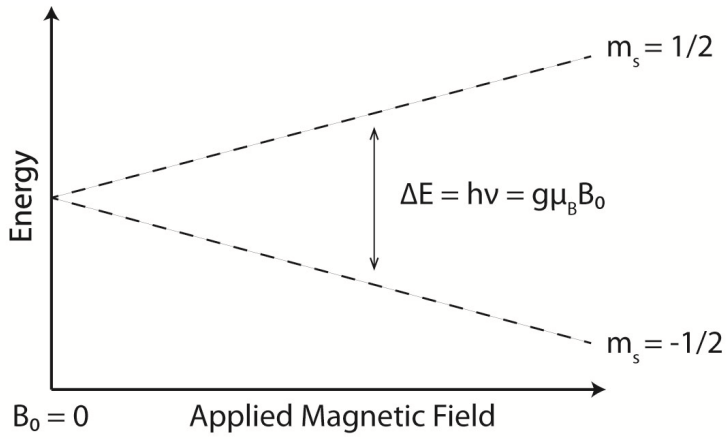

Figure 2.9 Diagram of the Zeeman splitting effect

The lower energy state occurs when the magnetic moment of the electron (μ) is aligned with the magnetic field, otherwise when μ is aligned against the magnetic field the higher energy state occurs. The difference in energy is a result of the Zeeman effect and increases with increasing magnetic field strength (see Fig. 17). Equation 2.11 defines the energy states of the electron:

$$E = g\mu_B B_0 Ms = \pm 1/2 g\mu_B B_0 \quad \text{(eq. 2.11)}$$

Where g is the proportionality factor (g-factor), μ_B is the Bohr magneton, B_0 is the applied magnetic field and Ms states for electron spin quantum number. The

g-factor, a unitless measurement of the intrinsic magnetic moment of the electron, for a free electon is equal to 2.00232, but it differs from 1.4 to 3.0 in case of transition metals due to spin-orbit coupling and zero-field splitting. It can be calculated from equation 2.12:

$$g = \frac{h\nu}{\mu_B B_0} \quad \text{(eq. 2.12)}$$

The *g*-factor as well as hyperfine interactions yield an important information about the sample. The hyperfine interaction (hyperfine coupling) is an interaction between the magnetic moments of the electron and its own nucleus or with nucleus of another atom. It results in a splitting of the spectral lines according to Pascal's triangle. The hyperfine coupling constant *A* is related to a distance between hyperfine lines (*a*).

$$A = g\mu_B a \quad \text{(eq. 2.13)}$$

The EPR experiments were run as a result of a collaboration with prof. Rasmus Fehrmann from the Technical University of Denmark in Copenhagen. A Bruker EMX equipped with a Bruker ER 4114HT X-band cavity was used for *in-situ*/high temperature EPR measurements. The crushed catalyst samples (around 100 mg) were contained in the inner tube of a reactor cell consisting of two concentric quartz tubes (i.d. 1.8 and 3 mm, respectively). The reactor cell was placed in the high temperature cavity, where heating up to 1000 ^{o}C is possible. The inlet gas was passed through the inner tube with the catalyst sample fixed in position at the bottom by small quartz wool plugs. The temperature was measured by a 1/16" chromel-constantan thermocouple placed on top of the catalyst sample. The SIM simulation software written by Weihe was used to extract numerical values of spin Hamiltonian parameters from the experimental EPR spectra [32].The relative spin concentrations were estimated by double integration of each spectrum, taking the temperature effect of the Boltzmann distribution into account, when comparing spectra at different temperatures.

2.12 High Resolution - Transmission Electron Microscopy

The principle of operation of the transmission electron microscope (TEM) is essentially the same as for the conventional light microscopy except that it uses electrons instead of light. Because of that, the electron microscope may reach the resolution of few Å. Electrons travel in a vacuum through electromagnetic lenses in order to form a very thin beam. When the beam hits the analyzed material, some electrons are scattered, but others pass through the sample and hit a fluorescent screen, where subsequently the image appears. The beam energy typically is high, it ranges between 100 and 400 keV and may easily damage the analyzed material. The element identification and quantification may be done, before the analysis of the diffraction patterns, using the X-ray energy dispersive spectrometry (EDS) or electron energy loss spectrometry (EELS). As for the other X-ray techniques they base on differences in energy levels.

The bulk VPO catalyst was analyzed with HR-TEM using TEM/STEM (JEOL 2100F) operating at 200 kV with a Field Emission Gun (point resolution of 0.19 nm). The system was coupled with an EDX detector (INCA x-sight by Oxford Instruments). The sample was suspended in ethanol using ultrasonic waves. Thin section of particles transparent for the electron beam was obtained. The suspension was dispersed onto a thin foil, and placed in the microscope for analysis. Few images were taken of each spot in order to examine the possible damage of the sample, which might have been caused by the electron beam. The phase of the analyzed spot was determined with EDX.

2.13 Raman Spectroscopy

Spectroscopic techniques are considered to be the most powerful for determination of structure-activity relationships. Raman spectroscopy is one of these tools, since it enables analysis at elevated pressures and temperatures above 1000 ^{o}C without gas-phase interference. It may use any excitation wavelength from UV to IR. Heterogeneous or homogenous materials can be easily examined but also experiments in liquid phase or under supercritical conditions are possible. However, quantification is still difficult since it depends on radiation scattering. This can only be done in the presence of an internal standard.

The Raman effect is a two-photon event related to the change in polarizability of the molecule with respect to its vibrational motion. The molecule is excited after an interaction with a photon, while different kinds of relaxation may occur. The Rayleigh scattering (elastic scattering) relates to most of the scattered radiation. In this case, the excited molecule returns to its original state, so that no changes in the frequency radiation occur. The Raman scattering (inelastic scattering) takes place when the scattered radiation possesses different energy than the impinging radiation. Stokes scattering takes place when the Raman scattered photon is emitted with lower energy than impinging ones. In contrast the anti-Stokes scattering is due to scattered photon emission of higher energy [33].

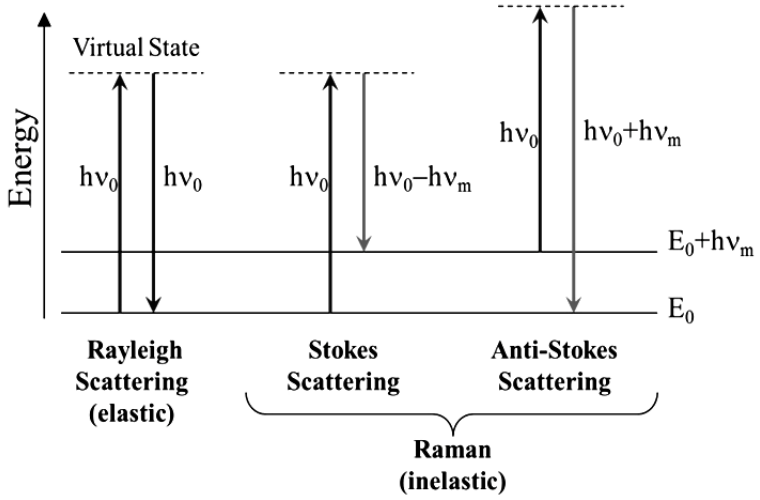

Figure 2.10 Energy transitions for Rayleigh and Raman scattering

The elastic scattering radiation (Rayleigh) is more than six orders of magnitude more intense that the inelastic one (Raman). It is removed by laser-line filtering using monochromators and filters (Notch or Edge types) to make Raman signal measurement possible preventing detector damage by saturation.

Raman spectroscopy is a bulk technique with a depth analysis of ca. 1000 nm [34]; despite this, Raman spectroscopy is a useful tool for analysis of supported metal oxides, since most of the supports exhibit only weak Raman transitions. Amorphous phases and crystals not detectable for XRD (< 4 nm) can be

analysed by Raman spectroscopy; and, thus the structure of nanocrystallites can be determined. Raman spectroscopy is also sensitive to crystallization progress, phase transformations and the coordination of the metal oxide sites. The determination of reaction mechanisms may be performed by Raman oxygen isotopic studies. However, it happens that Raman spectra of some surface species cannot be obtained because of a very small molecular scattering cross-section and low concentration (i.e. in case of supported metal oxide catalysts where the support posses very high surface area). The solution in this case appears to be the surface-enhanced Raman scattering effect. Laser damage and fluorescence are the typical limitations of Raman spectroscopy. In case of laser heating, the spectra may no longer be representative because of loss of water, reduction or other degradation phenomena. The laser heating effect depends on the colour of the sample, power and wavelength of the laser beam (UV>Vis>IR). Such an effect may be reduced by applying low laser power (<1 mW) in combination with edge or notch filters since these would not decrease the intensity of Raman bands. The other limitation of Raman spectroscopy is the fluorescence. Its intensity is 10000-fold more intense than the Raman signal, which typically overwhelms the Raman bands. It is often caused by organic deposits, basic -OH groups, proton superpolarizability or reduced transition metal ions, which can be resonantly excited. The solution includes change of the excitation frequency, use of UV or IR excitation or calcination for burning off the organic contaminants. Also *black-body* radiation can significantly overlap with the Raman spectrum. Such a phenomenon is increasingly important as the excitation wavelength grows longer. No blackdody radiation interference is expected for UV excitation , even for processes occurring above 1000 ºC, since UV radion would be emitted at ca. 10000 ºC, well above any experimental condition.

Raman spectra performed at the Institute of Catalysis and Petroleum Chemistry in Madrid were obtained with a single monochromatic Renishaw Raman System 1000 equipped with a thermoelectrically cooled CCD detector (-73 ^{o}C) and Edge filter. The samples were excited with the 488 or 514-nm Ar line (detailed description in figures captions), Spectra Physics, 163-C4210 (output power of 20 mW, power on sample, ≤1 mW). The lasers were focused on the samples with a confocal microscope equipped with a 20X long working distance objective (Olympus ULWD MSPlan20). Spectra at elevated temperatures were obtained in an *in situ* cell (Linkam TS-1500, cooled with a circulating water) under certain conditions. The dehydration process was performed at 400 ^{o}C in a flow of N_2 for

1 hour with a temperature ramp of 10 ^{o}C min^{-1}. The spectral resolution was 3 cm^{-1}, and the spectrum acquisition for most of the cases was 300 s for each sample.

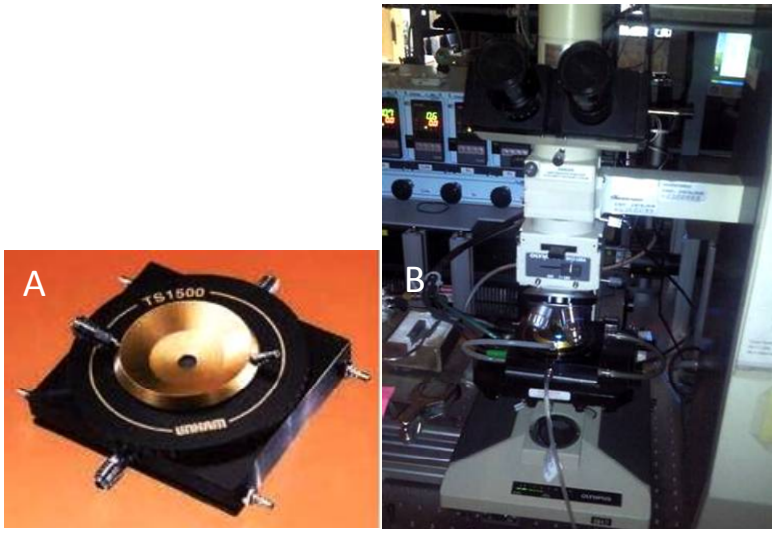

Figure 2.11 Linkam cell (A) during *in situ* Raman experiment (B) performed *Catalytic Spectroscopy Laboratory* (ICP)

A number of Raman spectra were performed at the *Operando Molecular Spectroscopy and Catalysis Laboratory* at Lehigh University (Bethlehem, PA, the USA). The Raman spectra were obtained with a high resolution, dispersive Raman spectrometer system, Horiba-Jobin Yvon LabRam HR equipped with a holographic notch filters (Kaiser Super Notch) and cooled CCD detector (Horiba-Jobin Yvon CCD-3000V). Samples were excited using the visible laser at 532 nm generated by a Coherent Compass 315M-150, Nd:YAG double diode pumped laser (output power of 150 mW, sample power of 10 mW) and the UV laser at 325 nm generated by a He-Cd laser (Kimmon, model IK5751I-G; (output power of 30 mW, sample power of 7 mW). The lasers were focused on the samples with a confocal microscope equipped with a 50X long working distance objective (Olympus BX-30-LWD) for the visible lasers and 15X objective (OFR LMU-15X-NUV) for the UV laser. Ca. 50 mg of the sample powder were placed in a Harrick cell (Harrick, HVC-DR2) with a quartz

window, cooled with a circulating water. The dehydration process was performed at 450 ^{o}C (temperature ramp of 10 ^{o}C min^{-1}) in 10% O_2 in Ar flow (30 ml min^{-1}) with 1 hour of holding atime at 450 ^{o}C. The spectral resolution was ca. 2 cm^{-1}, and the spectrum acquisition was ca. 50 s for the visible laser and ca. 1800s for the UV laser.

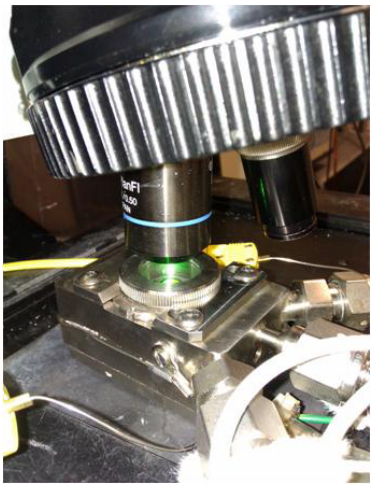

Figure 2.12 Harrick cell during *in situ* Raman experiment performed at *Operando Molecular Spectroscopy and Catalysis Laboratory* (Lehigh University)

2.14 Infrared Spectroscopy

Raman and infrared spectroscopy (IR) complement each other and give similar information for the study of molecular vibrations. They are complementary techniques for supported oxide catalysts characterization, but in case of IR spectroscopy an interference of support bands with the bands of surface species often appears. Raman bands depend on molecular polarizability change or the amount of electron cloud. In contradistinction, the IR absorption depends on the change of the dipole moment caused by rotations or vibrations corresponding to discrete energy levels and in this case give a strong IR signal for bonds possessing ionic character. Only those transitions corresponding to vibrations with variation of the dipole moment are active in IR Spectroscopy, so IR

stretching vibrations are only possible with asymmetric molecules. However, simple molecules have no dipole, but may be detected with IR spectrometry since energy may be absorbed by vibrations like bending or rocking. Vibrations in molecules are excited by absorption of IR radiation. When the IR photon hits a molecule the radiation can be absorbed by an oscillator (if their frequencies are equal). This leads to increase in vibrational energy level of the molecule, while the difference in energy is equal to the energy of the photon. The IR technique is very useful for determination of adsorbed species, as well as surface active sites or functional groups, and thus it is widely used for determination of reaction mechanisms. The procedure follows determination of adsorbed reactants, reaction intermediates and adsorbed final reaction products. IR spectroscopy also plays an extremely important role in determination of the acidity of examined materials. This study includes examination of adsorption sites and adsorption strength of probe molecules.

The IR experiments were performed both, by the transmission mode, where the IR beam reaches the detector after passing through a sample (usually a self-supporting disc) and by the diffused reflectance mode, where light diffused from the powder surface of analyzed material is collected. The diffuse reflectance IR spectroscopy is an alternative method when the transmission through the sample it too low to obtain a good spectra (typically <10% of transmission), and when it cannot be diluted with KBr, CsI or other "IR transparent" substances. Dilution is not possible if the analyzed material reacts with the diluting compound or if the adsorption process of a probe molecule or reactants is being studied (adsorbents interact with the sample and with the diluting agent). The diffuse reflectance spectroscopy follows the Kubelka Munk theory (see chapter 2.5) and the radiation diffused from a powder sample is collected by a spherical or an ellipsoidal mirror. Thus the quantification becomes difficult since the band intensities depend on particle size of the analyzed material, temperature and reaction conditions [[35]]. Nevertheless, this technique is convenient on account of simplified sample preparation and high sensitivity.

The catalyst acidity was examined using the *in-situ* FTIR Spectroscopy at *Laboratory of Catalysis and Spectrochemistry* (LCS) in Caen, France during a short time stay in a group of prof. Marco Daturi. The samples were pressed ($\sim 10^8$ Pa) into self-supported disks (2 cm^2 area, ca. 20 mg cm^{-2}) and placed in an *in-situ* quartz cell equipped with KBr windows connected to a grease free gas manipulation and evacuation lines ($P_{residual} \approx 10^{-3}$ Pa under secondary vacuum). A movable quartz sample holder permits to adjust the pellet in the infrared beam

for spectra recording (at room temperature) and to displace it into a furnace in the upper part of the cell for thermal treatment. The addition of known doses of gases in the cell is possible via a calibrated volume connected to a pressure gauge for the control of the gas pressure. Before spectra acquisition, the samples were activated by evacuation at 400 ^{o}C for 1 hour. The IR spectra were recorded by a Nicolet Nexus Fourier Transform spectrometer equipped with a Mercury Cadmium Telluride (MCT) cryodetector and a KBr beam splitter, in the 4000-650 cm^{-1} range. The resolution of the spectra was 4 cm^{-1}, and 64 scans were accumulated for each spectrum. The spectrum of activated sample was subtracted from spectra with adsorbed probe molecule.

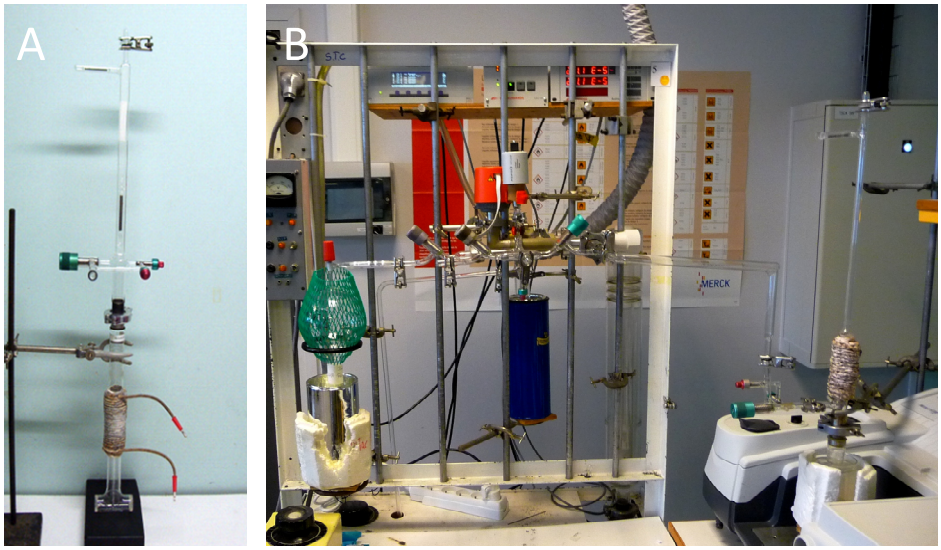

Figure 2.13 *In situ* IR cell (A) and the system for *in situ* IR analyses (B)

Study of propylene oxidation reaction mechanism was performed using *in situ* Diffuse Reflectance Fourier Transform IR Spectroscopy at *Operando Molecular Spectroscopy and Catalysis Laboratory* at Lehigh University (Bethlehem, PA, the USA). The spectra were obtained with a Thermo Nicolet 8700 FT-IR spectrometer equipped with a Harrick Praying Mantis attachment (model DRA-2). Ca. 50 mg of the catalyst was placed in a Harrick cell (model HVC-DR2 with a CaF_2 windows, the same cell was used for propane/propylene oxidation

reaction analyzed with Raman spectroscopy). The catalyst was subsequently dehydrated at 450 ^{o}C for 1 hour in presence of O_2 (10% O_2 in He, 20 ml min^{-1}). Propylene was preadsorbed on the activated catalyst for ca. 40 min. at 125 ^{o}C (5 ml min^{-1}). Then 20 ml min^{-1} of helium was fed for 20 minutes in order to remove gas phase and physisorbed propylene. This step was followed by propylene desorption at 125 ^{o}C for 20 min in different gas compositions and successively the temperature was increased to 400-475 ^{o}C.

The spectra resolution was 4 cm^{-1} for all experiments and 34 scans were accumulated for each spectrum. During propylene desorption spectra were collected every 20 seconds. The spectrum of activated sample was showed for reference (it was not subtracted from spectra with adsorbed propylene).

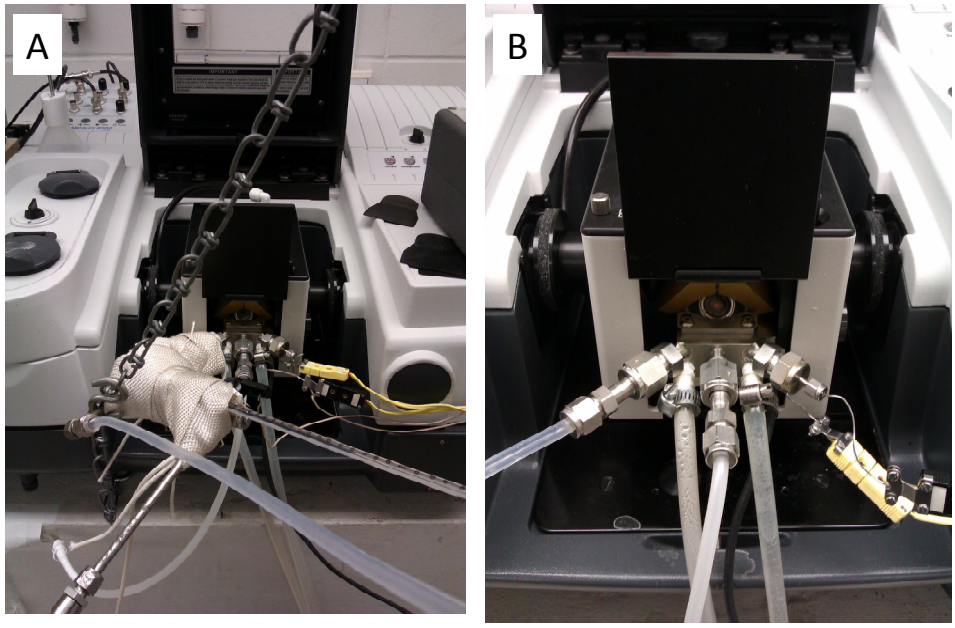

Figure 2.14 System for *in situ* DRIFTS experiments performed in presence of moisture (A) and in absence of moisture (B)

2.15 Catalytic testing

Catalysts were tested in selective propane oxidation reactions (oxidation and ammoxidation) under conditions determined previously in our group as optimal. Reactions were run in a conventional fixed bed quartz reactor of 9 mm of the external diameter and 7 mm of the internal diameter for the catalytic bed and of 6 mm of the external diameter and 4 mm of the internal diameter for the gas outlet. This design aims to minimize the death space in the reactor and to avoid contributions from non catalyzed reactions. Ca. 200 mg of catalyst particles with 0.125 – 0.250 mm particle size range were loaded in the reactor on a small amount of a quartz wool, thus minimizing rate limitations due to internal diffusion effects. The amount of catalysts and total flow were adjusted in order to avoid internal and external diffusion contributions. The temperature of the catalytic bed was controlled with a type K thermocouple connected to the temperature controller FC11 ICP. The thermocouple was placed in a quartz tube with a dimension appropriate to fill the extant death volume of the catalytic bed.

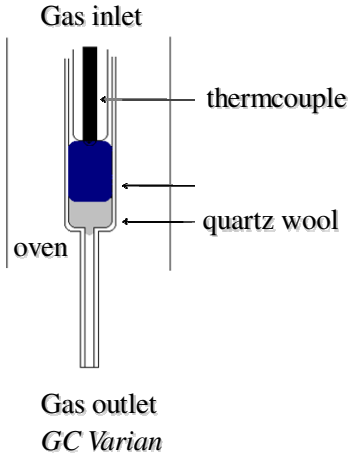

Figure 2.15 Reactor design for catalytic tests of propane selective oxidation reactions

The reaction feed controlled by Bronkhorst Hi-TEC flow controllers was supplied to the reactor as a preheated up to 200 ^{o}C mixture. In case of reactions carried out in presence of water vapor, the moisture was supplied by use of a syringe pump and kept at min. 150 ^{o}C. The product stream was analyzed by gas chromatography (Bruker CP 3800) equipped with a molecular sieve (5A)

column for analysis of O_2, CO and CO_2 and with a Porapak Q packed column for analysis of methane, ethane, ethylene, propane, propylene, acrolein, acetone, acetonitrile, acrylonitrile, acrylic acid and acetic acid. The temperature of the injector was adjusted to 250 ^oC, while the oven was heated from 50 to 220 ^oC at 10 ^oC min^{-1}. The flame ionization (FID, 300 ^oC) and thermal conductivity (TCD, 150 ^oC) detectors were used for analysis of the outgoing reaction stream. Gases used as a reaction feed were supplied by AIR LIQUIDE (Propane N35, B10, ALPHAGAZ; Ammonia N36, B10, ALPHAGAZ; certified gases at ICP: oxygen 99.9 % and helium 99.99 %). Yields and selectivities of products were determined on the basis of the moles of propane fed and products, considering the number of carbon atoms in each molecule.

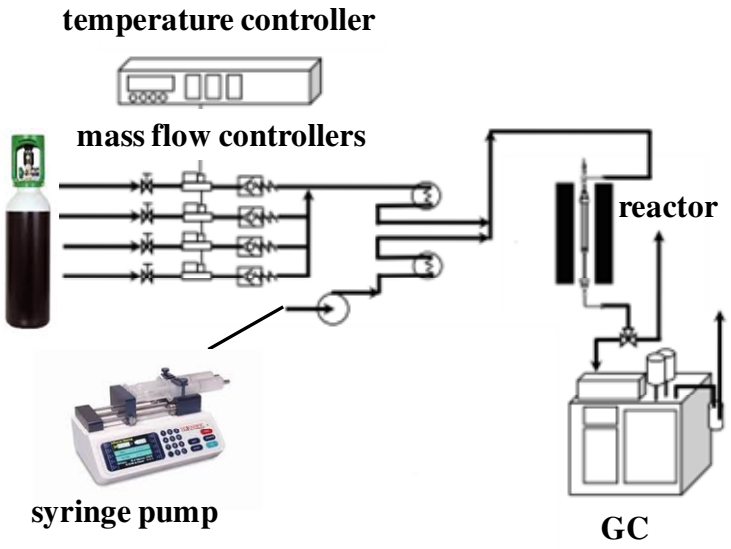

Figure 2.16 Reaction system for propane selective oxidation reactions

The correctness of the analytical determinations was checked for each test by carbon balance verification (based on the propane converted), which was within the cumulative mean error of the determinations of ±10%. Propane conversion, selectivity to products and product yields were calculated as follows:

Propane conversion:

$$X_j = \frac{(\sum_i y_i n_i)}{(y_j n_j + \sum_i y_i n_i)} \quad \text{(eq. 2.13)}$$

Selectivity to products:

$$S_i = \frac{y_i n_i}{\sum_i y_i n_i} \quad \text{(eq. 2.14)}$$

Yields to products:

$$Y_i = \frac{X_j S_i}{100} \quad \text{(eq. 2.15)}$$

Where, y_i states for number of moles of the products (with carbon atoms), y_j for number of moles of propane, n_i for number of carbon atoms in a product molecule, and n_j for number of carbons in propane molecule.

2.15.1 Experimental procedure for propane ammoxidation reaction

Ammoxidation reactions were carried out in a fixed-bed quartz reactor described above. O_2, NH_3, C_3H_8 and He feed, preheated up to 200 ^oC, was supplied by Bronkhorst flow controllers. The total flow was 20 ml min^{-1} (GHSV: 3000 h^{-1} approximately) corresponding to 25% of O_2; 9.8% of C_3H_8; 8.6% of NH_3 and 56.6% of He. Catalyst particles (0.125 – 0.250 mm size, 200 mg) were loaded in the reactor. Unless otherwise stated, the catalyst was activated previously by calcination in N_2 at 400 ºC and tested in the 350 to 500 ^oC temperature range. The product stream was analyzed as described above.

2.15.2 Experimental procedure for propane oxidation reaction

The propane oxidation reaction was carried out in a fixed-bed quartz reactor described above. Reaction feed preheated to 200 ^{o}C controlled by Bronkhorst flow controllers was supplied. The total flow was 40 ml min^{-1} (GHSV: 4800 h^{-1} approximately) corresponding to 20.4% of O_2; 12.5% of C_3H_8; and from 0 to 15.9% of steam in He. Catalyst particles were loaded in the reactor and activated by thermal treatment in N_2 at 400 ^{o}C. The product stream was analyzed by gas chromatograph (Bruker CP 3800, packed column – Porapak Q) equipped with a FID detector for analysis of ethane, ethylene, propane, propylene, acetic acid, acrolein and acrylic acid (formation of maleic anhydride was not studied with the GC test) and with a TCD detector for analysis of CO, CO_2, O_2, and H_2O. Trapped reaction products were injected to another gas chromatograph (Varian 3400, capillary column CP-Sil-5 CB) for confirmation.

2.16 *Operando* methodology

2.16.1 *Operando* Raman Studies of propane ammoxidation reaction

The importance of operando techniques was proved in Chapter 1. Propane ammoxidation reaction over supported vanadium and phosphorus oxide catalysts was studied using *operando Raman* methodology to assess the relevance of various VPO phases on the activity of these catalysts. Catalysts studied in this reaction typically contain loading of two V+P monolayers, so that effects such as crystallization, thermal broadening and interaction between supported species and nanocrystallites were considered. The structure-activity relationships were determined as follows.

Operando Raman studies were carried out at ICP with the above-mentioned Raman system (Section 2.13). A homemade *operando* reaction cell [36] was fitted to the Raman system. The *operando* cell is a fixed-bed reactor in which the catalyst is loaded with the same mesh and weight as in a conventional fixed-bed reactor, and the reaction conditions and residence time are identical to those used in the fixed-bed reactor. This reactor behaves exactly as the conventional fixed-bed reactor and allows for simultaneous spectroscopic measurements [37]. The activity was measured simultaneously with and on-line gas chromatograph, Bruker CP 3800, equipped with a flame-ionization and thermal-conductivity

detectors. O_2, NH_3, C_3H_8 and He feed, preheated up to 200 ^oC, were supplied using Bronkhorst flow controllers. The total flow was 20 ml min^{-1} (GHSV: 3000 h^{-1} approximately) corresponding volumetrically to 25% O_2; 9.8% C_3H_8; 8.6% NH_3 balanced in He. Tests were made using 0.2 g of catalyst with particle size between 0.125 – 0.250 mm. The fresh precursor containing catalyst and the pretreated in N_2 catalyst were heated stepwise up to 500 °C. The catalyst was heated in the reactor up to 350 ^oC at 20 ºC min^{-1} in the propane ammoxidation reaction feed. Thereafter it was held 30 minutes and heated stepwise to 500 ºC, every 30 minutes in steps of 25 ^oC. Observation of catalytic activities and simultaneous acquisition of Raman spectra were done during the last 300 seconds of each temperature. These runs were doubled-checked with the Ar^+ 514 nm excitation line and also with the Ar^+ 488 nm excitation line. Only the data obtained using the 514 nm excitation line is presented. After reaching operation temperature, 500 ^oC, the system was kept running for 60 hours, recording Raman spectra and GC analyses every 38 minutes.

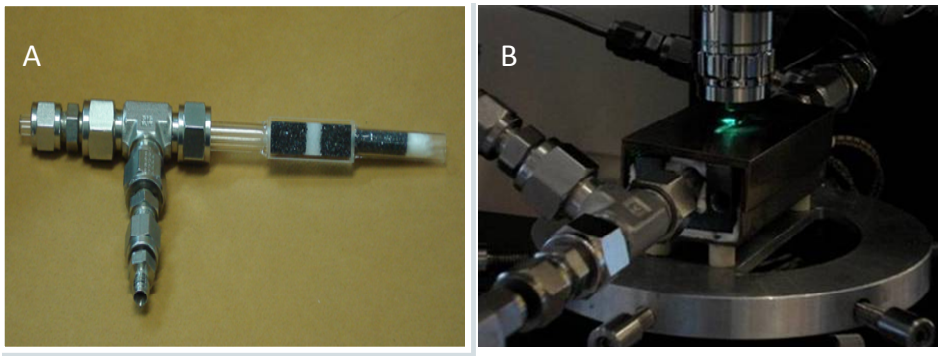

Figure 2.17 Quartz reactor for *operando* Raman study (A) and *operando* Raman system in operation (B)

2.16.2 *Operando* IR studies of propane oxidation reaction

Influence of water vapor on propane oxidation reaction was evaluated using *operando* IR Spectroscopy. The most interesting catalysts for this reaction are phosphorus doped alumina or titania-supported vanadium catalyst. IR spectroscopy is a very sensitive technique for evaluation of reaction intermediates and its interaction with the catalyst surface or with other species as

dopants or moisture. The reaction mechanism was widely studied by *in situ* DRIFT methodology (described in Section 2.14), which is more sensitive than the FTIR study by transmittance mode. The catalytic properties were related to the dynamic changes occurring on the catalyst surface in presence or absence of water vapor.

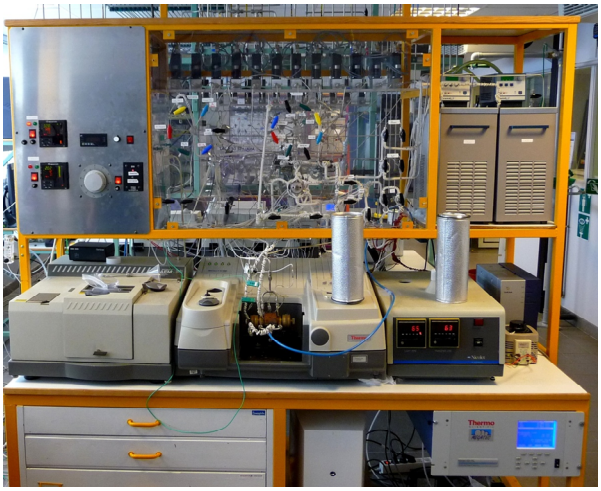

Figure 2.18 O*perando* IR system at LCS Caen, France

These experiments were run in a group of prof. Marco Daturi at *Laboratory of Catalysis and Spectrochemistry* (LCS) in Caen, France. The current LCS operando system is connected to a flow set-up with lines heated at 60 ^{o}C. Two gas mixtures, the so-called activation and the reaction flow can be controlled by mass flow controllers and sent independently to the reactor. The samples were pressed (~10^{8} Pa) into self-supporting disks (2 cm^{2} area, ca. 20 mg cm^{-2}) and placed in a homemade transition reactor-cell with a CaF_2 windows. A principal sketch of the IR reactor cell is shown in Figure 2.19. It consists of a cylindrical reaction chamber of ca. 1.3 cm size surrounded by an electronically controlled oven and crossed by a probe channel where the IR beam goes through the reactor and the catalyst pellet. The reactor-cell is cooled by circulating air system. The catalyst was activated at 100 ^{o}C in Ar flow for 3 hours. Subsequently the reaction flow was introduced to the reactor. The total flow was

5 ml min^{-1} corresponding to 20.4 % O_2, 12.5 % C_3H_8, and between 5 and 8 % of H_2O balanced in He, the same test was run in absence of water. The temperature was increased to 350 ^oC and held at this temperature for ca. 2.5 hours. The IR spectra were acquired in 50 ^oC or 10 min steps. The surface of the catalyst was examined by a Thermo Scientific Nicolet 6700 FTIR spectrometer, equipped with a MCT detector, while catalytic activity was determined by gas phase IR spectroscopy (Thermo Fisher Scientific, model: GC Interface) and the Quadrupole Mass Spectrometer: Pfeiffer OmniStar, GSD 301.

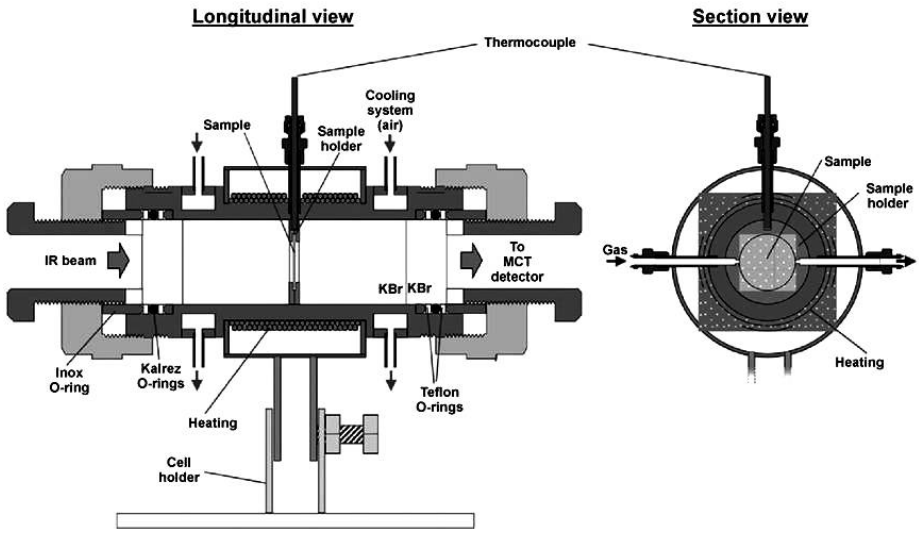

Figure 2.19 Home-made transition reactor for *operando* IR study used at LCS Caen, France [38]

References

[1] G. Hausinger, H. Schemlz, H. Knözinger, *Appl. Catal*. 39 (1988) 267

[2] C. Martín, V. Rives, *J. Mol. Catal.* 48 (1988) 381

[3] R. Y. Saleh, I. E. Wachs, S. S. Chan, C. C. Chersich, *J. Catal*. 98 (1986) 102

[4] G. C. Bond, S. F. Tahir, *Appl. Catal*. 71 (1991) 1

[5] E. Bordes, R. M. Contractor, *Topics. Catal.* 3 (1996) 365

[6] R. M. Contractor, A. W. Sleight, *Catal. Today* 1 (1987) 587

[7] H. Taheri*, US Patent* 5.011.945 (1991)

[8] G. J. Hutchings, *Appl. Catal*. 72 (1991) 1

[9] J. M. C. Bueno, G. K. Bethke, M. C. Kung, H. H. Kung, *Catal. Today* 43 (1998) 101

[10] K. Inumaru, T. Okuhara, M. Misono, *Chem. Lett.* 10 (1992) 1955

[11] R. M. Contractor, H. E. Bergna, H. S. Horowitz, C. M. Blackstone, B. Malone, C. C. Torardi, B. Grifiths, U. Chowdry, A. W. Sleight, *Catal. Today* 1 (1987) 49

[12] V. Cortés Corberan, S. Vic Bellón (Eds.), R. M. Contractor, D. I. Garnett, H. S. Horowitz, H. E. Bergena, G. S. Patience, J. T. Schwartz, G. M. Sisler, *New Development in Selective Oxidation II*, Elsevier, Amsterdam (1994)

[13] N. F. Dummer, W. Weng, C. Kiely, A. E. Carley, J. K. Bartley, C. J. Kiely, G. J. Hutchings, *Appl. Catal.* 376 (2010) 47

[14] S. Brunauer, P. H. Emmet, E. Teller, *J. Am. Chem. Soc.* 60 (1938) 309

[15] S. Brunauer, L. S. Deming, W. S. Deming, E. Teller, *J. Am. Chem. Soc.* 62 (1940) 1723

[16] E. L. Lee, I. E. Wachs, *Silica Silicates Modern Catal*. (2010) 375

[17] A. Escobedo Morales, E. Sánchez Mora, U. Pal, *Rev. Mex. Fis*. 53 (2007) 18

[18] S. V. Merzlikin, N. N. Tolkachev, L. E. Briand, T. Strunskus, C. Woll, I. E. Wachs, W. Grunert, *Surf. Sci.* 602 *(*2008) 755

[19] S. V. Merzlikin, N. N. Tolkachev, L. E. Briand, T. Strunskus, C. Woll, I. E. Wachs, W. Grunert, *Angew. Chem., Int. Ed.* 49 (2010) 8037

[20] M. Heber, W. Grünert, *J. Phys. Chem. B* 104 (2000) 5288

[21] S. Merzlikin, *Dissertation: Depth profiling by X-ray photoelectron Spectroscopy*, Ruhr-University, Bochum, Germany, 2007

[22] S. Tanuma, C.J. Powell, D.R. Penn, *Surf. Interface Anal.* 21 (1994) 165

[23] S. Tanuma, C.J. Powell, D.R. Penn, *J. Electron Spectrosc. Relat. Phenom.* 62 (1993) 325

[24] S. Tanuma, C.J. Powell, D.R. Penn, *Surf. Interface Anal.* 25 (1997) 25

[25] C.J. Powell, A. Jablonski (Eds.), *Electron Inelastic-Mean-Free-Path Database*, Version 1.1 (2000)

[26] W.N.Delgass, G.L.Haller, R.Kellerman, J.H.Lunsford, *Spectroscopy in Heterogeneous Catalysis,* Academic press, New York (1979)

[27] *H. Brongersma, Unique opportunities for new insight in the outer surfaces and interfaces by Low Energy Ion Scattering (LEIS)*, Lehigh University Surface Analysis Symposium Lectures (2011), http://www.lehigh.edu/operando/symposium.html (May 5th 2012)

[28] William Andrew (Ed.), P. M. Marin, *Handbook of Deposition Technologies for Films and Coatings: Science, Application and Technology*, Oxford : Elsevier Science, Norwich, N.Y (2009)

[29] J. W. Niemantsverdriet, *Spectroscopy in Catalysis: An Introduction*, Wiley-VCH, Wienheim, Germany (2000)

[30] *H. Brongersma, Unique opportunities for new insight in the outer surfaces and interfaces by Low Energy Ion Scattering (LEIS)*, Lehigh University Surface Analysis Symposium Lectures (2011), http://www.lehigh.edu/operando/hiddelecture.pdf (May 5th 2012)

[31] M. Ruitenbeek, *Dissertation: Characterisation of vanadium based oxidation catalysts*, Utrecht University, The Netherlands (1999), ISBN 90-393-2051-9

[32] Glerup, J. and Weihe, H. *Acta Chem. Scand*. 45 (1991) 444

[33] H. S. Nalva (Ed.), M. A. Bañares, *In situ Spectroscopy of Catalysts,* Chapter 4, *Raman Spectroscopy,* American Scientific Publishers (2004)

[34] I. E. Wachs, J.-M. Jehng, G. Deo, B. M. Weckhuysen, V. V. Guliants, J. B. Benziger, *Catal. Today* 32 (1996) 47

[35] H. S. Nalva (Ed.), J. Saussey, F. Thibault-Starzyk, *In situ Spectroscopy of Catalysts,* Chapter 1, *Infrared Spectroscopy: Classical Methods,* American Scientific Publishers (2004)

[36] M. Martínez-Huerta, *Dissertation*, Universidad Autónoma de Madrid, Madrid, Spain (2001)

[37] S. J. Khatib, R. Guil-López, M. A. Peña, J.L.G. Fierro, M. A. Bañares, *Catal. Today* 118 (2006) 353

[38] I. Malpartida, E. Ivanova, M. Mihaylov, K. Hadjiivanov, V. Blasin-Aubé, O. Marie, M. Daturi, *Catal. Today* 149 (2010) 295

3

Characterization of industrial bulk VPO catalyst

3.1 INTRODUCTION

An industrial bulk VPO catalyst, encapsulated in a porous silica shell in order to improve the attrition resistance of the catalyst particles, was supplied by DuPont. This modification might change the catalyst nature by modification of its surface. The vanadyl pyrophosphate phase may be reached by the reacting molecules through the pores of SiO_2, but also the VPO phase may decorate the outer side of the porous silica shell. In the latter case the SiO_2 may play the role of a support for the active phase. In order to evaluate the nature of the modified bulk VPO catalyst (bulk or VPO/SiO_2) the catalyst was characterized using bulk and surface-sensitive techniques. The catalyst structure was examined by XRD, TEM and Raman studies. Vanadium oxidation states were determined using HR-XPS (1-3 nm analysis depth), while the catalyst surface was studied by HS-LEIS. Acidity of the catalyst surface was determined by NH_3 adsorption/desorption *in situ* FT-IR experiments.

3.2 BET Surface Area

The industrial VPO catalyst possesses relatively high BET surface area (37 m^2 g^{-1}) when compared to standard bulk oxide catalysts. It is largely mesoporous with an average pore size of 2 nm. However, macroporosity also appeared to be present.

3.3 Powder XRD Patterns

Diffraction patterns of bulk (calcined) VPO catalyst and its precursor are shown in Figure 3.1. The catalyst precursor shows diffraction lines at 15.58 (16), 19.70 (16), 24.29 (18), 27.19 (29), 28.70 (13), 30.49 (100), 32.05 (13), 34.06 (9), 37.48 (13), 40.42 (6), 44.31 (4), 47.88 (9), 49.44 (18), 51.92 (5), 56.42 (5) and 63.26 (8) 2θ. The resulting XRD pattern is due to $(VO)_2H_4P_2O_9$, the precursor of the vanadyl pyrophosphate catalyst, widely used in the *n*-butane oxidation reaction to maleic anhydride. The calcined bulk VPO catalyst generates a diffraction pattern with peaks at 2θ: 14.18 (5), 18.58 (9), 22.95 (47), 28.48 (100), 29.96 (53), 33.75 (14), 37.02 (12), 43.32 (28), 46.95 (7), 49.53 (13), 56.11 (7), 57.69 (7), 58.63 (17), 63.57 (10), 67.92 (7) and at 72.59 (3). This pattern can be completely assigned to the vanadyl pyrophosphate phase, such that no significant additional phases were detected. The perfect match in both cases suggests that the XRD technique does not demonstrate presence of SiO_2 shell neither in the calcined VPO catalyst neither in its precursor. It is principally related to the fact that a silica fume (amorphous silicon dioxide) is used in the coating process to improve surface and mechanical properties of the VPO catalysts that does not generate a diffraction pattern. Nevertheless, for calcined VPO, the low intense XRD line at 26.35 is probably due to crystalline SiO_2. Although one peak is not enough for phase characterization, this indicates, that some other low intense XRD reflections of crystalline silicon or silicon oxide may be overlapped by reflections of the VPO phases.

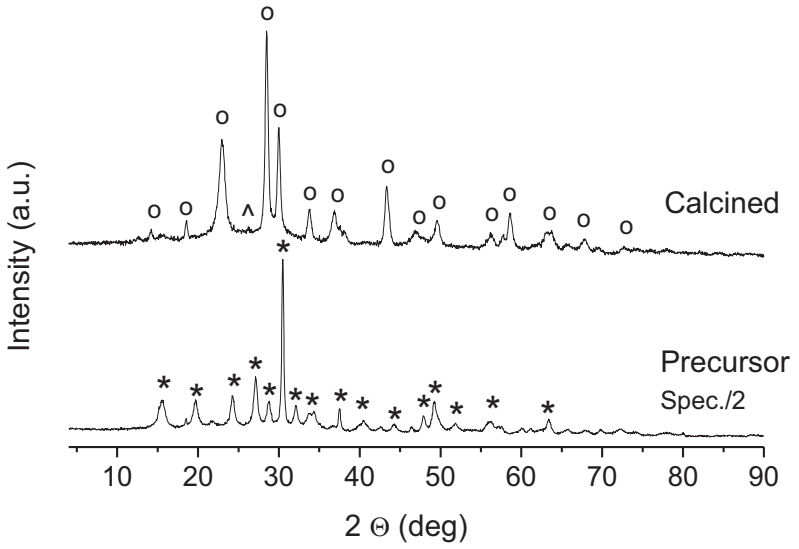

Figure 3.1 XRD patterns of calcined bulk VPO catalyst (top) and its precursor (bottom); (o) $(VO)_2P_2O_7$, (∗) $(VO)_2H_4P_2O_9$, (^) SiO_2. The diffractogram of the catalyst precursor was divided by 2 for graphical reason

3.4 Raman Spectroscopy

Figure 3.2 illustrates Raman spectrum of bulk VPO catalyst. The spectrum of catalyst precursor could not be acquired because of strong fluorescence effects probably coming from the organic medium used during synthesis. The Raman spectrum of bulk VPO exhibits Raman bands at 1184m, 1135m, 1024w, 994w, 927s, 794w, 700w, 651w, 576w, 539w, 476w, 427w, 401w, 361w, 312w, 310w, 284w, 223w, 190w, 149w, where "s" means strong, "m" medium, and "w" weak Raman band. This spectrum profile is essentially that of $(VO)_2P_2O_7$ [1]. Additionally, Raman bands at 1024, 994, 700, 539, 284 and 149 cm^{-1} may be assigned to species containing V^{5+} [2]. Raman features at 994, 700, 539, 284 and 149 cm^{-1} match V_2O_5 phase. Oxidized phases were not detected by XRD, which indicates that the size of V_2O_5 crystallites is smaller than 4Å. It proves that Raman Spectroscopy is more sensitive for phase determination. The intensity of Raman bands characteristic of V_2O_5 suggests very low amounts of this phase,

since the Raman section of crystalline V_2O_5 is very high [3]. Additionally, the dehydration process at 400 °C in presence of oxygen leads to increase of relative intensity of V_2O_5 bands. In contrast, treatment in reductive environment of propane ammoxidation reaction at 500 °C causes the complete disappearance of the V^{5+} containing phases (see Figure 3.3).

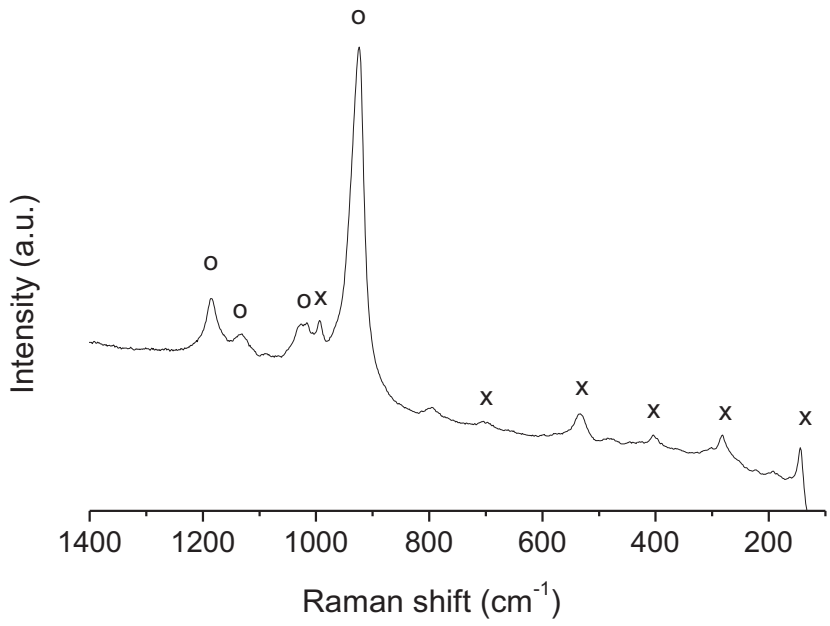

Figure 3.2 Raman spectrum of the calcined bulk VPO catalyst; (o) $(VO)_2P_2O_7$, (x) V_2O_5. Ar excitation line: 514 nm

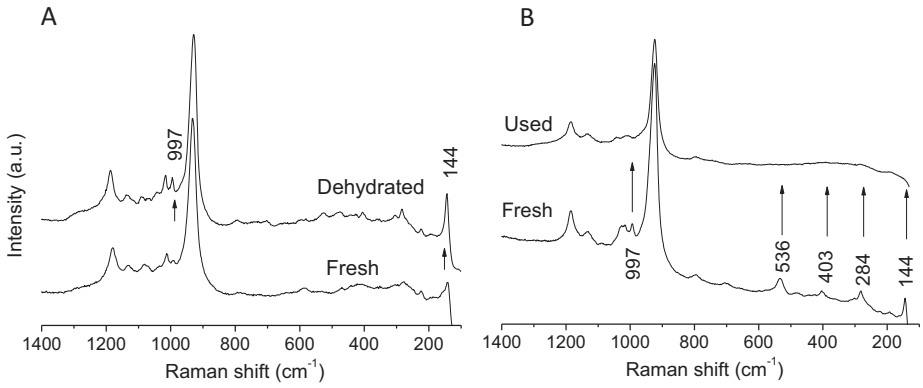

Figure 3.3 Formation of V_2O_5 on the bulk VPO catalyst after dehydration process in air at 400 ^oC (A) and decomposition of V_2O_5 after testing in propane ammoxidation reaction at 500 ^oC (B). All spectra were taken at 50 ^oC in air flow using 514 nm laser

The facility of formation and decomposition of vanadium pentoxide in oxidizing or reductive atmosphere suggest that V_2O_5 crystallites are present on the surface of the vanadyl pyrophosphate catalyst. Exposure to high temperatures may cause a dispersion of V_2O_5 crystallites over the exposed support, which can be either solid $(VO)_2P_2O_7$ or the amorphous SiO_2. However, this is rather unlikely in our case, since V_2O_5 Raman bands were observed at elevated temperatures (300-350 ^oC) during the heating and cooling processes (see Figure 3.4). This implies that the V^{5+} content on the support probably exceeds one monolayer.

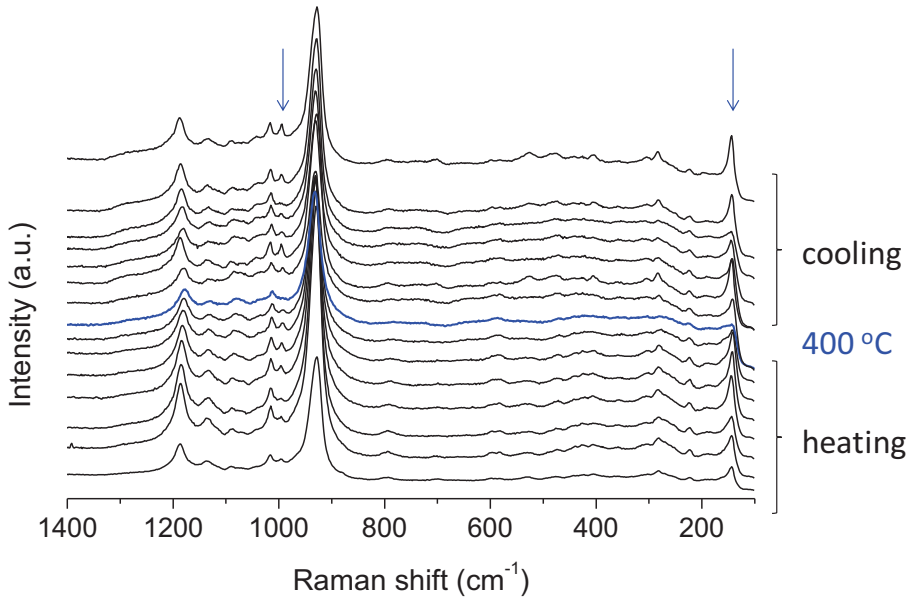

Figure 3.4 Raman spectra of the VPO catalyst acquired with 50 °C step during a dehydration process in air. Ar excitation line: 514 nm

3.5 High Resolution XPS Study

The XPS technique is widely applied in studies of VPO catalysts for the determination of an average oxidation state of vanadium (V_{AOS}) [4,5,6,7,8]. The oxidation state of vanadium ions in bulk vanadyl pyrophosphate catalysts ranges between 4.00 and 4.30 [9,10,11]. It is usually determined either by curve fitting methods or using the formulas proposed by Clouston et al. [12], which rely on the fact that the energy difference between the O1s and $V2p_{3/2}$ levels relates to the vanadium oxidation state:

$$V_{AOS} = 13.82 - 0.68\,(O1s - V2p_{3/2}) \qquad \text{eq. 3.1}$$

The values obtained using the XPS technique are often considered to give information about the surface layers of the bulk material. However, the lowest

escape depth of XPS analyses is usually between 1-3 nm, so the results from this technique obviously includes an interference of the bulk phase. Nevertheless, the oxidation state of vanadium in bulk vanadyl pyrophosphate is rather congruent and indicates that it possess mainly V^{4+}, but the presence of small amounts of V^{5+} cannot be excluded. Somehow more controversial is the reported P/V atomic ratio of the bulk vanadyl pyrophosphate phase, which ranges from 1.5 to 3 [13,14,15,16]. These values are much higher in comparison to the stoichiometric P/V=1 of bulk $(VO)_2P_2O_7$. This phenomenon is explained by surface enrichment in phosphorus ions caused by the addition of excess of phosphorus during the synthesis of VPO catalysts. It is assumed that an excess of phosphorus, which does not form vanadyl pyrophosphate, must be present at the catalyst surface. However, the value of P/V ratio obtained from XPS depends strongly on the calculation method, mainly on sensitivity factors. When VPO glasses were used for determination of the experimental sensitivity factors, assuming that there is no difference in P/V ratio between the bulk and the surface, the calculated P/V ratio of vanadyl pyrophosphate catalysts was P/V=1.1 [17].

Figure 3.5 represents the HR-XPS spectrum of the bulk VPO catalyst. The $V2p_{3/2}$ peak appears at 517.01 eV and is fitted into two peaks at 516.7 eV for V^{4+} and at 517.8 eV for V^{5+}. These values are in a good agreement with binding energies previously reported in literature [18,19,20]. The O1s peak was found at 531.32 eV. The curve fitting method indicates that this catalyst possesses mainly V^{4+} (77%), but some V^{5+} was also detected (23%). The vanadium average oxidation state (V_{AOS}) according to Clouston's formula equals 4.09, which is in accordance to the literature. These data combined with P/V, O/V, Si/V and C/V atomic ratios are presented in table 3.1.

Table 3.1 HR-XPS measurements on bulk VPO catalyst; V_{AOS} was calculated according to Cloustos's formula

Catalyst	V^{4+} (%)	V^{5+} (%)	V_{AOS}	P/V	O/V	Si/V	C/V
VPO	77	23	4.09	2.7	11.6	0.6	1.5

Excess of phosphorus was detected. The P/V=2.7 ratio, although high, is in accordance with the literature. Also the O/V atomic ratio is much higher compared to the stoichiometric vanadyl pyrophosphate phase (O/V=4.5). The O/V ratio of ca. 6.4 was previously reported in literature [21]. If we assume that in our case about 45% of oxygen comes from the oxygen associated to phosphorus, as it was calculated from the deconvolution of the oxygen peak, the oxygen not associated to PO_x gives an O/V ratio of 6.4. Carbon was detected at C/V=1.5 ratio. This indicates that the catalyst is contaminated with remnants of carbonaceous species, probably the organic compounds used in the preparation method. The low Si/V ratio suggests that extensive amounts of vanadium are available in the first 3 nm of the bulk phase.

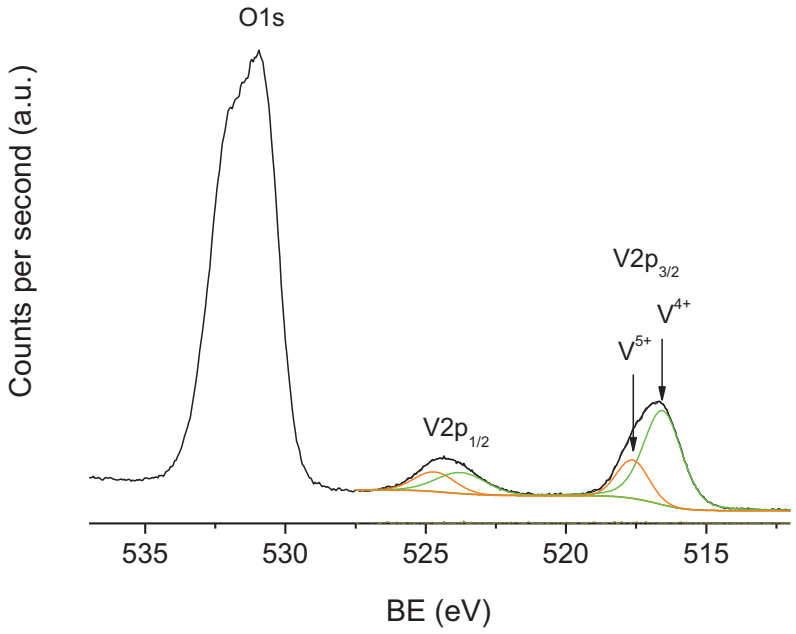

Figure 3.5 O1s and V2p regions of HR-XPS spectrum of bulk VPO catalyst

3.6 High Sensitivity LEIS Spectroscopy

Even though bulk VPO catalysts were widely studied during last four decades, still, the actual surface structure and composition are poorly known. The LEIS

technique provides valuable information about the nature of the outermost layer of bulk catalysts, while the composition depth-profile may provide complementary information. Very limited number of LEIS studies on vanadyl pyrophosphate catalysts is available in the literature [5,21,22,23]. Thus, HS-LEIS study was performed at Lehigh University in order to examine the surface of bulk VPO catalyst. Figure 3.6 shows clearly visible and nicely separated peaks arising from oxygen, silicon, phosphorus and vanadium. It implicates that even though the vanadyl pyrophosphate phase was encapsulated in the silica shell, vanadium and phosphorus are present at the outermost layer. However, presence of silica peak suggests that SiO_2 is not completely covered with vanadium and phosphorus but probably some clusters of these elements are embedded on the silica shell. Taking into account that the transformation of the vanadyl hydrogen phosphate precursor encapsulated in the silica shell to vanadyl pyrophosphate takes place during the calcination process at 390 ^{o}C, surface enrichment in phosphorus and vanadium may be expected, since the temperature of the treatment is well above the Tamman temperatures of vanadium and phosphorus oxides (Tamman T_{V2O5} = ca. 200 ^{o}C; Tamman T_{P2O5} = ca. 30 ^{o}C). However, LEIS spectrum of the precursor catalyst was not acquired, so that the presence of vanadium and phosphorus clusters on the silica shell before calcination process cannot be ruled out.

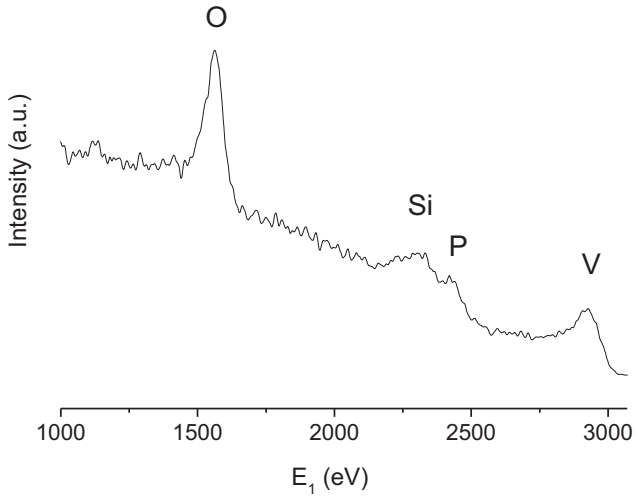

Figure 3.6 LEIS $^{4}He^{+}$ spectrum of the industrial VPO catalyst. Surface composition of vanadyl pyrophosphate encapsulated in silica shell

Depth profile has been obtained due to sputtering effect. Spectra were taken at a total ion dose of $3.8 \cdot 10^{16}$ Ar^+ ions cm^{-2}, which is equal to depth analysis of ca. 40 monolayers.

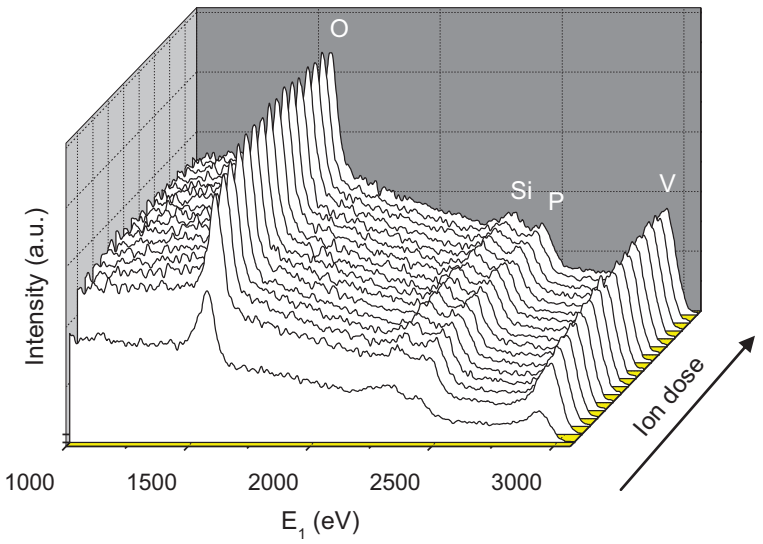

Figure 3.7 LEIS Ar^+ spectra during sputtering process of subsequent layers of the industrial VPO catalyst. The first dose was made with $^4He^+$

The sputtering process induces changes of the areas of vanadium, phosphorus and oxygen peaks, while the area of the silicon peak is stable (see Figure 3.8). The depth profile includes only about the first 10 nm of the bulk phase. Since the thickness of silica shell is ca. 2 μm [24] it was not possible to reach the core of vanadyl pyrophosphate. Thus, we are examining the spreading effect of the active vanadyl pyrophosphate phase on and in the silica shell.

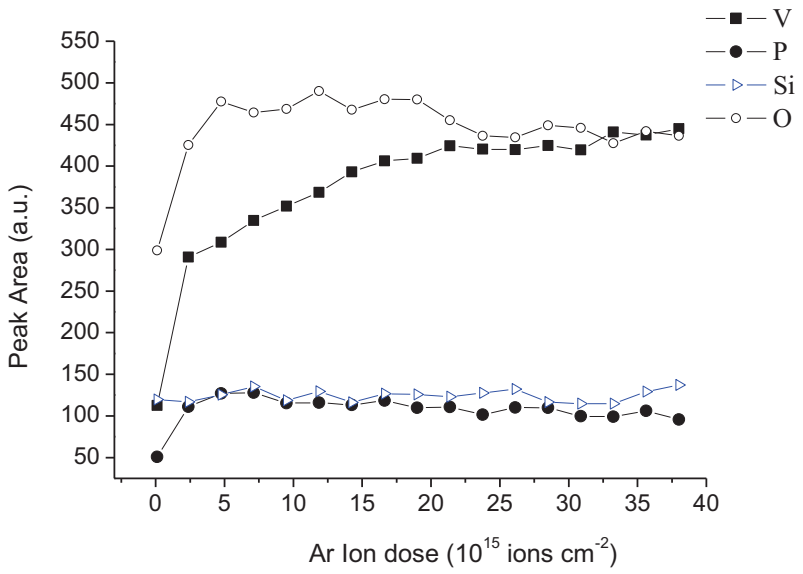

Figure 3.8 Changes in V, P, Si and O peak areas as sputtering effect during LEIS analysis

During LEIS analysis, the first dose was made with $^4He^+$ ions and subsequent doses with Ar^+. The intensity of peak areas of vanadium, phosphorus and oxygen increases rapidly after the first Ar ion dose. One Ar^+ dose removes ca. 20 times more material (about 3 Å) than was removed during the LEIS analysis performed with $^4He^+$ ions. Thus, the increase in peak intensities is probably related to removal of adsorbed contamination, which shields these elements during examination of the outer layer. Shielding effects are also related to the lower intensity of the first LEIS spectrum in the Figure 3.7. The surface of vanadyl pyrophosphate terminates with V=O, V-OH, P=O or P-OH groups. This leads to shielding effect of vanadium and phosphorus by oxygen and is related to high area of the oxygen peak. However, other contaminants, like moisture, carbon, or some hydrogen containing species [25] are expected since also the oxygen peak was shielded. Carbon was not detected by LEIS, because the sensitivity of $^4He^+$ is low for elements of relatively low atomic numbers [26]; furthermore, the total amount of carbon is low in the system, unlike oxygen. Presence of carbon in the industrial bulk VPO catalyst is obvious, since it was prepared in organic medium, and adventitious carbon is present on the surface of catalysts. This method probably leads to higher carbon contamination in

comparison to aqueous preparation method. Moreover, the XPS analysis has confirmed presence of carbon in the industrial VPO catalyst. The stable area of the silicon peak implicates that it is not affected by contamination (only VPO clusters), so that it is fully exposed during sputtering process or that the surface is V, P and O deficient, which is the reason of increase in peak areas of these elements during sputtering of subsequent layers.

The surface P/V ratio was not calculated, since the LEIS analyses need to be performed with both, $^{4}He^{+}$ and $^{3}He^{+}$ in order to get the quantitative information using the dual-isotope surface composition (DISC) method [27]. However, Figure 3.9 shows that the P/V ratio decreases continuously. It may be related to the surface enrichment in phosphorus, but this scenario does not seem fundamental, since the peak area of phosphorus decreases only slightly (see. Figure 3.8) in contrast to the area of vanadium peak. The mass difference between vanadium and phosphorus might cause higher sputtering yield of phosphorus, this would lead to a decrease of the phosphorus signal with an opposite effect for vanadium, due to the preferential removal of phosphorus. Moreover, the difference in *a* slopes of linear functions $f(P_{area})$ and $f(V_{area})$, when both are increasing equals $a(P_{area})$ - $a(V_{area})$ = -3.31, which indicates that the area of vanadium peak changes significantly during sputtering in contrast to the area peak of phosphorus. The first points were not considered as they were related to removal of gaseous contamination or to the surface deficiency. Thus, vanadium is probably the preferential site for the contaminants or another effect, like e.g. surface vanadium deficiency needs to be related to the increase of the vanadium peak area during the depth profile.

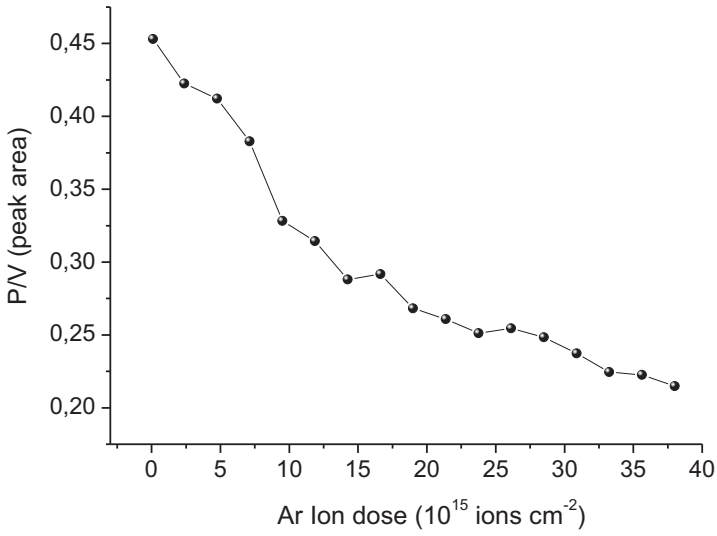

Figure 3.9 Changes in P/V atomic ratio during the depth profile analysis

Delichére et. al reported that the carbonaceous contaminants are preferentially adsorbed on Lewis acid vanadium sites [21]. This would explain an intense increase of the vanadium peak area as a function of ion dose. Additionally presence of vanadium Lewis acid sites not shielded by oxygen, together with high atomic number of vanadium would explain much higher vanadium peak areas in comparison to areas of phosphorus peak.

3.7 High Resolution TEM Study

TEM images of bulk VPO catalyst are present in Figure 3.10. The energy dispersive analysis of X-rays (EDAX) was performed in order to determine the elemental composition. Figures 3.10A and B clearly show that the crystalline particles posses an amorphous layer. Significant changes were observed when a second TEM image was taken on the same spot (see Figure 3.10C). The sample has lost its crystallinity probably due to high energy of the electron beam. The EDAX studies show that at the same time the atomic percentage of silicon increases significantly. This may suggest that the crystalline VPO clusters are damaged during analysis and that the amorphous layer can be determined as the

silica shell. However, the dynamic changes that occurred during TEM imaging prevent detailed analysis and make the EDAX study questionable.

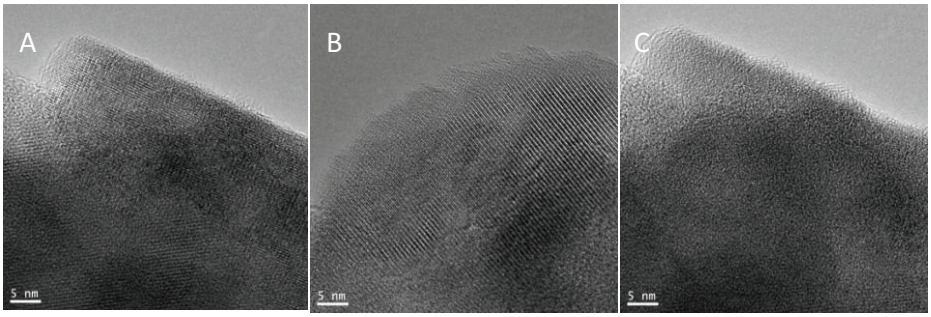

Atomic %	A	B	C
Si	0.9	9.9	33.4
P	41.0	43.6	33.9
V	58.0	46.5	32.7

Figure 3.10 TEM images of bulk VPO catalyst and atomic percentage of Si, P and V atoms detected by EDAX

TEM analysis became more complicated in case of the VPO catalyst precursor. No crystalline phase was detected, and the sample was damaged when exposed to the electron beam. The blue arrow in the Figure 3.11A shows catalyst particles, which are clearly out of focus due to the dynamic changes caused by the analysis. EDAX analysis induces further changes, shown in Figure 3.11B making the sample highly macroporous.

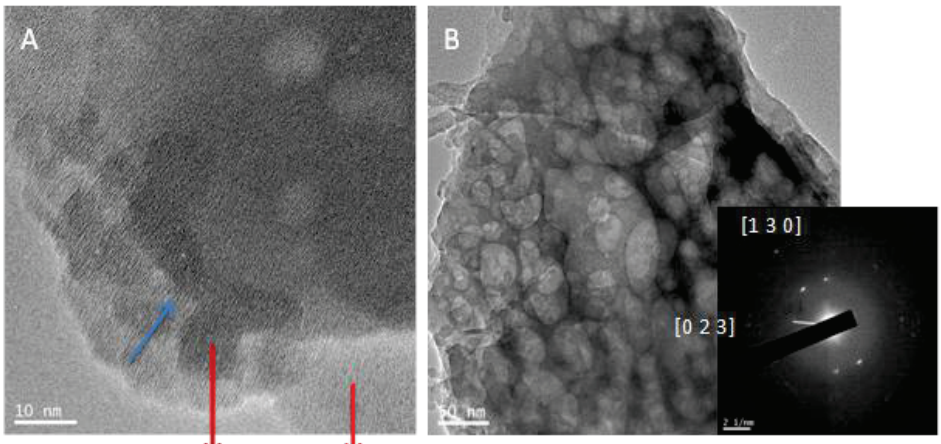

Atomic %	A		B
Si	9.0	5.6	10.3
P	49.0	51.1	47.1
V	42.0	43.3	42.6

Figure 3.11 TEM images of bulk VPO catalyst precursor and atomic percentage of Si, P and V atoms detected by EDAX. Selected area electron diffraction (SAED, right)

The selected area electron diffraction (SAED) analyses performed at the end of the experiment indicate that the catalysts possess crystalline phases. Moreover, [1 3 0] and [0 2 3] planes mach perfectly the *d*-spacing (0.30 nm) of the previously presented $(VO)_2H_4P_2O_9$ XRD pattern, but other planes like [0 0 1] seem to be distorted with difference in *d*-spacing of 0.03 nm (0.54 instead of 0.57 nm) according to the $(VO)_2H_4P_2O_9$ phase.

3.8 *In situ* FT-IR Study

The acidity of the bulk VPO catalyst was examined by ammonia adsorption/desorption studies followed by *in situ* FT-IR spectroscopy. Before running the experiment the catalyst was activated in vacuum at 400 ^{o}C for 1 hour. The spectrum of the activated sample was subtracted from presented spectra. Figure 3.12A shows an evacuation process of adsorbed species formed on the bulk VPO catalyst surface by contact with NH_3 at room temperature. The band at 1611 is due to $\delta_{as}(NH_3)$ modes of chemisorbed ammonia, while the bands at 1676 and 1433 cm^{-1} are characteristic of $\delta_s(NH_4)$ and $\delta_{as}(NH_4)$

ammonium cations, respectively [28,29]. These features evidence presence of both Lewis (coordinatively unsaturated vanadium cations) and Brønsted (acidic hydroxyls) acid sites. The band at ca. 1230 cm^{-1}, characteristic of $\delta_s(NH_3)$ modes of chemisorbed ammonia (Lewis acid site) was not detected because of the skeletal pyrophosphate absorption and the energy cut-off. The ammonium cations disappear during evacuation between 300-400 ^oC, indicating a medium-weak acid strength of the Brønsted sites. The desorption of ammonia coordinated on Lewis acid sites (1611 cm^{-1}) occurs at the same temperature range as for Brønsted sites (300-400 ^oC).

Adsorption of small doses of ammonia (0.02-0.50 torr) at room temperature on VPO catalyst showed that ammonia preferentially adsorbs on Lewis acid sites ($\delta_{as}(NH_3)$ at ca. 1611 cm^{-1}). Brønsted sites appear at ca. 0.20-0.50 torr of ammonia gas introduced to the *in situ* IR cell (see Figure 3.12B).

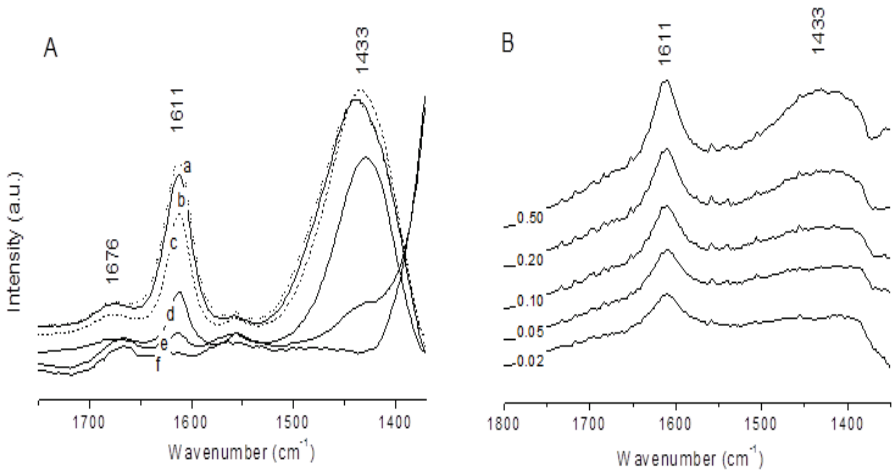

Figure 3.12 FT-IR Spectra of NH_3 desorption from the VPO surface (A), after evacuation at room temperature (a), at 50 ^oC (b), at 100 ^oC (c), at 200 ^oC (d) at 300 ^oC (e) and at 400 ^oC (f). FT-IR Spectra of adsorption of small doses of NH_3 (0.02-0.50 torr) at room temperature (B), formation of Lewis and Brønsted acid sites

3.9 SUMMARY

The industrial bulk VPO catalyst was analyzed using bulk and surface-sensitive techniques. The HR-XPS measurements indicate that the catalysts contain mainly V^{4+}, although V^{5+} was also detected. Presence of V^{5+} containing phases in fresh VPO catalyst was also confirmed using Raman spectroscopy. The P/V ratio calculated from the XPS data is high (P/V=2.7), but still in accordance to data previously reported in literature. However, there is a debate in literature about the correctness of the sensitivity factors used for these calculations, and it is stated that values obtained are rather questionable. Nevertheless, the HS-LEIS study confirms that P/V ratio decreases within the depth profile, but it is related rather to the surface deficiency of vanadium, and not to the surface enrichment in phosphorus. Moreover, the LEIS analysis shows that vanadium, phosphorus, silicon and oxygen are present on the catalyst surface. This suggests that the VPO clusters are embedded on the silica shell. Presumably vanadium and phosphorus migrate to the SiO_2 surface during the calcination process forming VPO crystallites due to their relatively low Tamman temperature. *In situ* FT-IR study shows that bulk VPO possesses medium-weak Brønsted and Lewis acid sites, but the Lewis sites are preferentially occupied by chemisorbed ammonia.

References

[1] F. B. Abdelouahab, R. Olier, N. Guilhaume, F. Lefebvre, J. C. Volta, *J. Catal*. 134 (1992) 151

[2] R. M. Feng, X. J. Yang, W. J. Ji, Y. Chen, C. T. Au, *J. Catal*., 224 (2007) 166

[3] S. Xie, E. Iglesia, AT Bell, *Langmuir* 16 (2000) 7162

[4] L. M. Cornaglia, E. A. Lombardo, *Appl. Catal*., 127 (1995) 125

[5] F. Richter, H. Papp, G. U. Wolf, Th. Götze, B. Kubias, *Fresenius J. Anal Chem*., 365 (999) 150

[6] K. Aït-Lachgar, A. Tuel, M. Brun, J.M. Herrmann, J.M. Krafft, J.R. Martin, J.C. Volta, M. Abon, *J. Catal*, 177 (1998) 224

[7] Y. Suchorski, L. Rihko-Struckmann, F. Klose, Y. Ye, M. Alandjiyska, K. Sundmacher, H. Weiss, *Appl. Surf. Sci*., 249 (2005) 231

[8] L.K. Rihko-Struckmann, Y. Ye, L. Chalakov, Y. Suchorski, H. Weiss, and K. Sundmacher, *Catal. Lett*., 109 (2006) 89

[9] M. Abon, J. C. Volta, *Appl. Catal. A*, 157 (1997) 173

[10] F. Cavani, F. Trifiro, *Chem. Tech*., 24 (1994) 18

[11] S. Luciani, Dissertation: *Structural changes and dynamic behavior of vanadium oxide-based catalysts for gas-phase selective oxidations*, Bologna University, Italy (2009)

[12] G. W. Clouston, E. A. Thompson, N. Herron, *J. Catal.*, 163 (1996) 122

[13] L.M. Cornaglia, C. Caspani, E.A. Lombardo, *Appl. Catal*. 74 (1991) 15

[14] G. Centi, F. Trifiró, J. R. Ebner, V. M. Franchetti, *Chem, Rev*. 88 (1988) 55

[15] H. Morishige, J. Tamaki, N. Miura, N. Yamazoe, *Chem. Lett*. (1990) 513

[16] F. Garbassi, J. Bart, R. Tassinari, G. Vlaic, P. Labarde, *J. Catal*. 98 (1986) 317

[17] T. Okuhara, M. Misono, *Catal. Today,* 16 (1993) 61

[18] N. Harrouch-Batis, H. Batis, A. Ghorbel, J.C. Vedrine, J.C. Volta, *J. Catal*. 128 (1991) 248

[19] T.P. Moser, G.L. Schrader, *J. Catal*. 104 (1987) 99

[20] S. Albonetti, F. Cavani, F. Trifiro, P. Venturoli, G. Calestani, M. Lopez-Cranados, J.L.G. Fierro, *J. Catal*. 160 (1996) 52

[21] P. Delichére, K. E. Béré, M. Abon, *Appl. Catal.*, 172 (1998) 295

[22] W. P. A. Jenses, M. Ruitenbeek, A. W. Denier van der Gon, J. W. Geus, H. H. Brongersma, *J. Catal.*, 192 (2000) 379

[23] W. P. A. Jensen, Dissertation: *Insight in the outside of catalysts with LEIS*, Eindhoven University of Technology, The Netherlands (2002), ISBN 90-386-1535-3

[24] N. F. Dummer, W. Weng, C. Kiely, A. E. Carley, J. K. Bartley, C. J. Kiely, G. J. Hutchings, *Appl. Catal.*, 376 (2010) 47

[25] H. H. Brongersma, R. A. Van Santen (Eds.), H. H. Brongersma, G. C. Van Leerdam, *Fundamental Aspects of Heterogeneous Catalysis Studied by Particle Beam* (1991) 283

[26] M. Ruitenbeek, *Dissertation: Characterization of vanadium-based oxidation catalysts,* Utrecht University, The Netherlands (1999) ISBN 90-393-2051-9

[27] P. A. J. Ackermans, M. A. P. Creuwels, H. H. Brongersma, P. J. Scanlon, *Surf. Sci.* 227 (1990) 361

[28] G. Centi, S. Perathoner, *J. Catal*. 142 (1983) 84
[29] G. Busca, G. Centi, F. Trifiró, V. Lorenzelli, *J. Phys. Chem*. 90 (1986) 1337

4

Characterization of supported VPO catalysts

4.1 INTRODUCTION

Alumina-supported nanoscaled VPO catalysts were characterized in this chapter in order to better understand the role of amorphous phases at the surface of VPO domains. These catalysts were compared to alumina-supported vanadium catalysts to evaluate the function of phosphorus on the structure and on the reactivity of vanadium species. The V+P loading on alumina does not exceed 2 monolayers (a monolayer is ca. 8 atoms/nm^2), except for the 16V16PAl catalyst, which was synthesized with V+P loading of 4 monolayers for comparison. The low content of the active VPO phase prevents the formation of large VPO crystallites and enables the characterization of amorphous VPO phases or VPO nanocrystallites. Their nanoscale (less than 5 nm) triggers the surface-to-volume ratio, which permits characterizing nanoparticles without an overwhelming signal from the bulk phase. Particular attention was paid to the 8V9PAl catalyst, the alumina-supported counterpart of the bulk VPO catalyst. The structural features related to V^{5+} and V^{4+} species were analyzed using different complementary techniques, among these, Raman spectroscopy characterized essential V^{5+} and, to some extent, V^{4+} phases, while EPR studies are only sensitive to V^{4+} species. In addition, surface acid sites were studied using *in situ* FT-IR technique and probe molecules.

4.2 BET Surface Area

Table 4.1 summarizes BET surface area of the alumina-supported vanadium and phosphorus catalysts. In general, the BET areas of the supported catalysts were lower than that of the bare alumina support. BET area decreases with a V + P surface coverage, but it can be observed that the V/P atomic ratio has no significant effect on the surface area. All the samples possess mesopores in a 5-20 nm range (peak maxima at ca 10 nm). The dV/dlogD (cm^3/g nm) decreased with loading of the active phase. This suggests the pores are plugged with the active phase, which subsequently leads to decrease in surface area.

Table 4.1 BET Surface areas and P/V atomic ratio of alumina supported vanadium and phosphorus catalysts

Sample	Al_2O_3	4PAl	4V4PAl	8V8PAl	8V9PAl	16V16PAl	4VAl	8VAl
BET (m^2g^{-1})	194	138	149	130	135	113	168	141
P/V	-	-	1.0	1.0	1.1	1.0	-	-

4.3 Powder XRD Patterns

XRD patterns of alumina-supported catalyst pretreated in N_2 flow are shown in Figure 4.1. Except for the alumina support, no new crystalline phases are apparent, even for the 16V16PAl catalyst, which contains 4 monolayers of V+P on alumina. This indicates formation of amorphous phases, which is further confirmed in a rise of baseline of the diffractograms in a range of 2θ between 19 and 35^o.

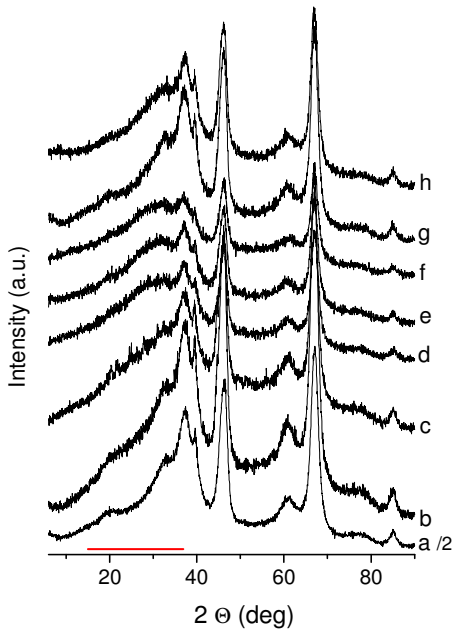

Figure 4.1 X-ray diffractograms of alumina supported vanadium and phosphorus oxide catalysts, Al_2O_3 (a), 4PAl (b), 4V4PAl (c), 8V8PAl (d), 8V9PAl (e), 16V16PAl (f) 4VAl (g), 8VAl (h). The XRD pattern of alumina support (a) was divided by 2 for graphical reasons

4.4 Raman Spectroscopy

Figures 4.2 and 4.3 illustrate Raman spectra of hydrated and dehydrated 8V9PAl and 8VAl, respectively. Both catalysts were calcined in air flow for 19 hours at 400 ^{o}C. It can be observed that the calcination process leads to formation of crystalline phases like γ-$VOPO_4$ for 8V9PAl and V_2O_5 for both 8V9PAl and 8VAl.

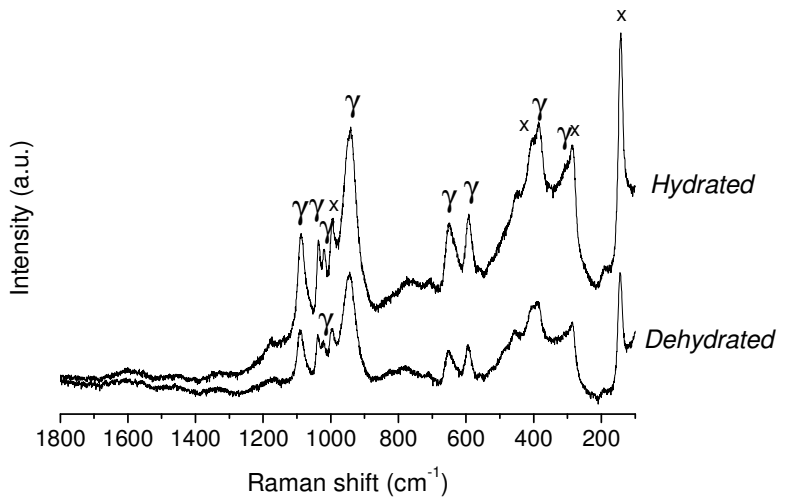

Figure 4.2 Raman spectra of ambient (hydrated, top) and dehydrated (bottom) fresh 8V9PAl catalyst calcined in air at 400 °C for 19 hours, x – V_2O_5, γ – γ$VOPO_4$. Spectra acquired in air flow at 50 °C. Raman laser: 532 nm

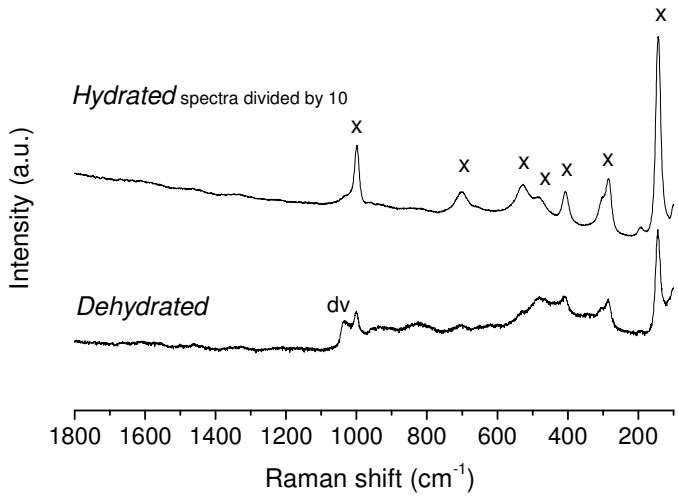

Figure 4.3 Raman spectra of ambient (top) and dehydrated (bottom) 8VAl catalyst calcined in air at 400 °C for 19 hours; x – V_2O_5, dv – dispersed vanadium. Spectra acquired in air flow at 50 °C. Raman laser: 532 nm

The γ-$VOPO_4$ phase shows characteristic Raman bands at 1188, 1096s, 1040s, 1022, 958, 951s, 656s, 596, 454, 390s, 334, 293 cm^{-1} (where "s" stands for "strong") [1], while V_2O_5 exhibits Raman bands at ca. 143s, 195, 286, 305, 406, 483, 530, 704 and 996s cm^{-1} [2,3,4]. The catalysts were prepared by impregnation of the alumina support with an aqueous solution, where V^{4+} is stabilized by formation of complexes with oxalic acid, $(COOH)_2$. Thus, the calcination process for catalysts analyzed in this section was replaced with a thermal treatment in N_2 flow in order to avoid the total oxidation of vanadium species and formation of oxidized crystalline phases.

Raman spectra of ambient (hydrated) and dehydrated supported vanadium and phosphorus oxide catalysts are shown in Figure 4.4. The catalysts were dehydrated at 400 ^oC for 1 hour in flow of N_2 in order to avoid formation of vanadium pentoxide crystallites or other oxidized phases, like $VOPO_4$. Spectra of the alumina support and of 4PAl were not acquired due to strong fluorescence. The fluorescence effect made the Raman spectra of γ-Al_2O_3, 4PAl and even 4V4PAl impossible to analyze neither after calcination process nor with spectra acquisition using the 785 nm excitation laser line. The Raman spectra of hydrated catalysts presented in Figure 4.4A exhibit Raman bands in the 988-1016 cm^{-1} range. These features are due to V=O stretching modes of vanadium surface species and shift to higher frequencies upon dehydration process (1000-1037 cm^{-1} range). It can be observed particularly from the Figure 4.4B that the Raman feature due to V=O stretching modes shifts to higher frequencies with increasing vanadium loading. This effect was widely reported in literature [5,6,7]. The broad band at ca. 940 cm^{-1} is due to V-O-M bonds, where M is either V or Al.

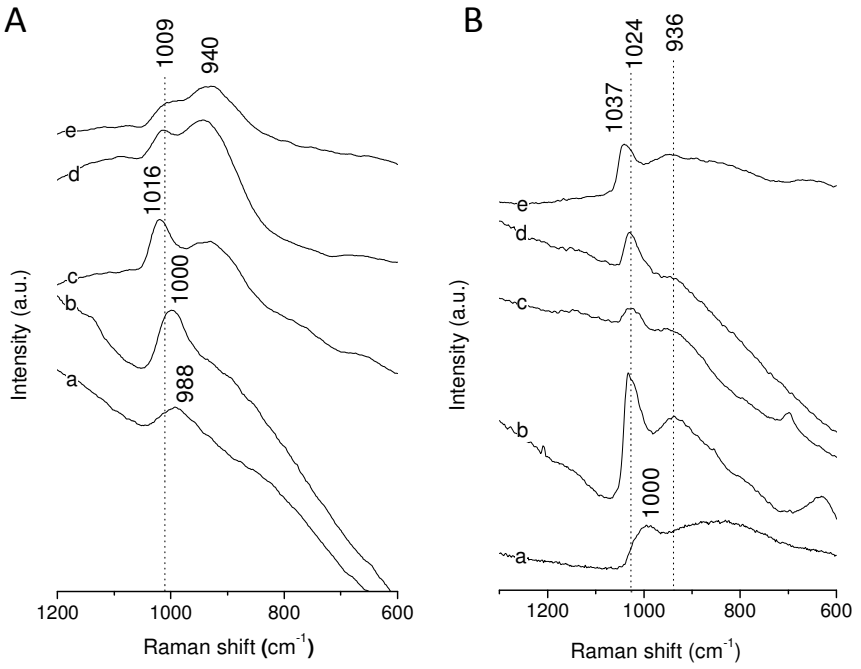

Figure 4.4 Raman spectra of hydrated catalysts (A) and catalysts dehydrated at 400 ^{o}C in N_2 flow (B); 4VAl (a), 8VAl (b), 8V8PAl (c), 8V9PAl (d), 16V16PAl (e). All the spectra were acquired at 50 ^{o}C using 514 nm laser

4.5 TPR Study

Figure 4.5 illustrates results of temperature-programmed reduction. Hydrogen consumption is noticeable at 100 ^{o}C for all examined samples, probably due to reaction with surface hydroxyl groups. Vanadium and phosphorus supported catalysts show a broad reduction profile of V^{5+} at the 400-600 ^{o}C interval and subsequently a well-defined reduction peak at about 890 ^{o}C. The first vanadium reduction peak suggests a broad distribution of surface vanadium oxide species, which typically reduce in this temperature range [8,9]. It was reported that P_2O_5 interacts with the surface vanadium oxide phase and that this interaction depends on the concentration of phosphorus additive and preparation method [10]. Different degrees of interaction with phosphorus may account for the broad distribution of vanadium surface species, which is further confirmed by the fact that the alumina-supported vanadium catalysts show a well-defined reduction

peak at this range. Moreover, only one reduction peak at 550 °C with a small shoulder at ca 350 °C was observed when phosphorus was not present at the catalyst surface. Assuming that the 8VAl catalyst mainly possesses V^{5+} species, an H/V ratio of 1 is expected for reduction process of V^{5+} to V^{4+} and an H/V of 2 is expected when V^{5+} is reduced to V^{3+} [11]. The H/V ratio for 8VAl was determined as 1.9, indicating that the reduction of vanadium species from V^{5+} to V^{3+} takes place. The H/V ratio for 8V9PAl catalyst equals 0.7. Such differences in TPR profiles with phosphorus-containing catalysts suggest that phosphorus would stabilize V^{4+} species, which is in accordance to the literature [12,13,14,15].

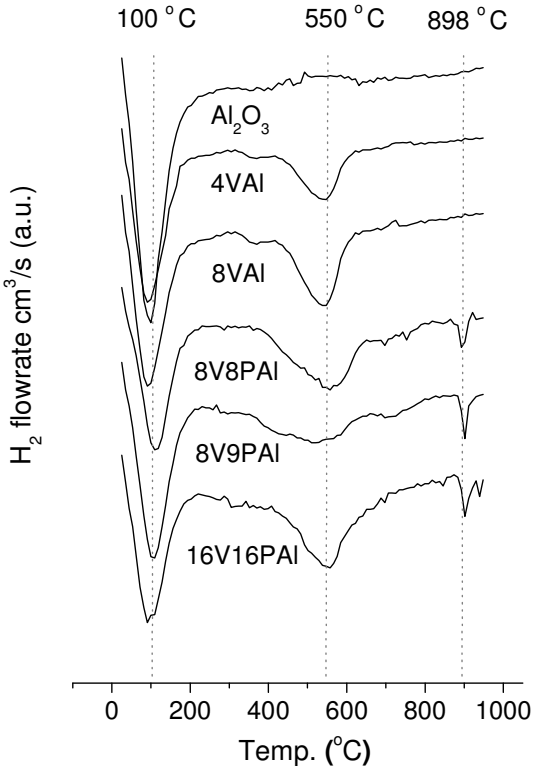

Figure 4.5 H_2-TPR profiles of alumina support and supported vanadium and phosphorus oxide catalysts. From the top: Al_2O_3, 4VAl, 8VAl, 8V8PAl, 8V9PAl and 16V16PAl

The XRD diffractogram of the 8V9PAl catalysts after H_2-TPR shows that vanadium phosphate oxide $V_2(PO_4)O$ forms on the alumina surface (see Figure 4.6). Reduction from V^{4+} to V^{3+} and in some extent to V^{2+} is probably reflected by the broad peak in 600-900 ^oC range as well as by the well defined reduction peak at ca. 900 ^oC.

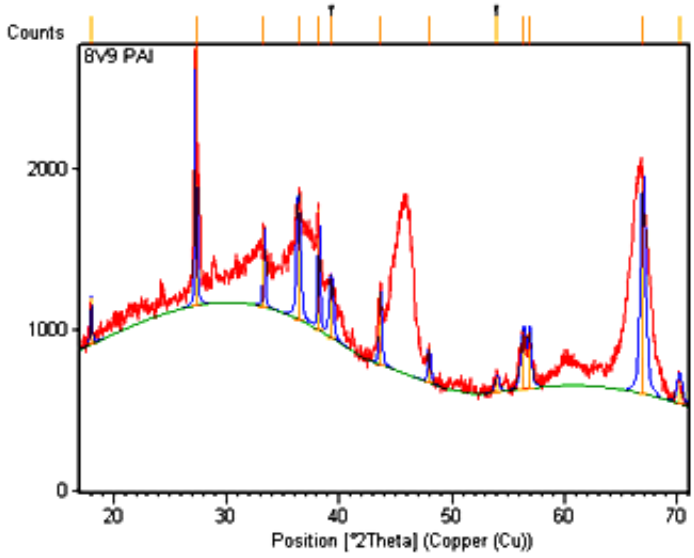

Figure 4.6 XRD diffractogram of 8V9PAl catalyst spent in the H_2-TPR analysis. Blue pattern states for the $V_2(PO_4)O$ phase

4.6 Characterization of 8V9PAl Catalyst

Extended characterization of the alumina-supported nanoscaled VPO catalyst was performed in order to examine the influence of the support on the surface VPO species. *In situ* Raman spectroscopy is more sensitive to surface V^{5+} species, while *in situ* EPR is sensitive to V^{4+} species. *In situ* FT-IR studies of NH_3 adsorption/desorption provides information about Brønsted and Lewis acid sites present on the catalyst surface.

4.6.1 *In situ* Raman Studies

8V9PAl precursor

Figure 4.7A illustrates representative Raman spectra during thermal treatment of the 8V9PAl precursor in N_2 flow. (Raman spectra of initial compounds, $(COOH)_2$ and NH_4VO_3, were plotted in the Figure 4.8 for comparative purposes). Under ambient conditions, hydrated 8V9PAl precursor exhibits a band near 990 cm^{-1}, characteristic of $VOHPO_4 \cdot 0.5H_2O$ since the absence of a sharper Raman band at 145 cm^{-1} rules out the presence of V_2O_5. Such compound decomposes near 300 ^oC. The Raman band at 1080 cm^{-1} was reported to be due to V-O-P bonds [16]; however, metaphosphate chains exhibit the P=O stretching modes at 1000-1200 cm^{-1} range [17,18]. When these groups are protonated a new Raman stretching mode appears in the 850-900 cm^{-1} region due to formation of P-OH groups [19,20,21]. Raman features at 931 and 878 cm^{-1} reflect remnants of ammonium metavanadate and oxalic acid, respectively. The Raman spectrum of the dehydrated sample near ambient conditions exhibit features suggesting the presence of an amorphous phase with a Raman band characteristic of dispersed vanadium species (1033 cm^{-1}) and a broad band at 1009-845 cm^{-1} due to V-O-support bonds or supported VO_x species and polyphosphoric acids. For supported vanadium catalysts Raman bands at ca. 900 cm^{-1} are usually characterized by V-O-V stretching modes of polymerized vanadia species, but the DFT calculations suggest that the V-O-support bonds appear at the same frequencies, and V-O-V bonds would appear at lower frequencies [22]. The TPO of 8V9PAl is illustrated in Figure 4.7B. Thermal treatment of 8V9PAl in the presence of oxygen forms V_2O_5.

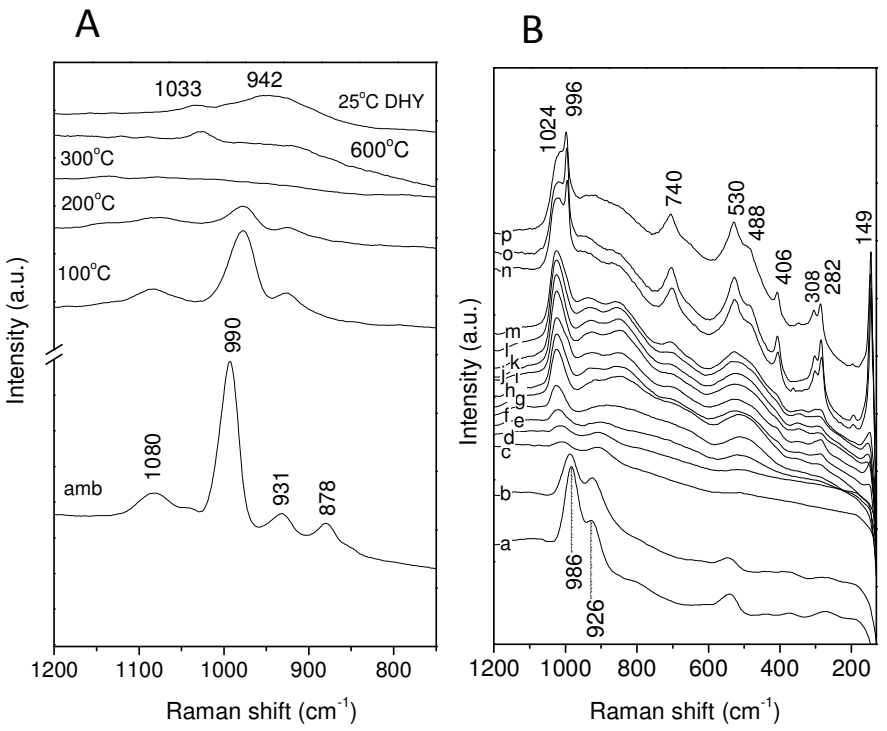

Figure 4.7 *In situ* Raman spectra of dehydration process of 8V9PAl precursor in N_2 flow (A) amb – ambient temperature, i.e., hydrated, DHY – dehydrated sample at ambient temperature and V_2O_5 formation during thermal treatment in dry air flow (B). Temperature increase from 50 °C to 400 °C (a-h) with step of 50 °C for spectrum recording, after 30 min at 400 °C (i), and cool down from 350 °C to 50 °C (j-p). Laser: 514 nm

Thermal treatment of the 8V9PAl precursor in an oxidizing environment i.e. synthetic air, first leads to the formation of dispersed vanadium oxide species, which vanadyl group exhibits a band near 1024 cm^{-1}. As the temperature increases, new Raman features become apparent at 149, 282, 08, 406, 488, 530 and 996 cm^{-1}, which evidence the formation of V_2O_5 crystallites. It should be noted that the Raman section of crystalline V_2O_5 is very high, and at least one order of magnitude higher than that of dispersed vanadium oxide (Raman band at 1024 cm^{-1}) [23]. Thus, V_2O_5 domains are not very large and their total amount will be low, since the vanadyl Raman mode of molecularly dispersed vanadia exhibit similar intensity. This is also supported by the frequency shift of the

sharper V_2O_5 bands from characteristic values at 990 and 145 cm^{-1} to 996 and 149 cm^{-1}, respectively. The size-effect on Raman modes frequency shift in nanoscaled materials is observed for many oxides [24,25]. It has been attributed to surface disorder/stress or quantum confinement phenomena that occur in nanoscaled particles [26,27,28,29].

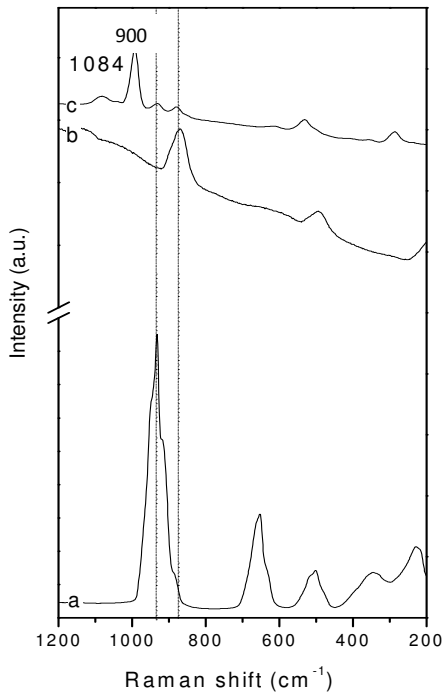

Figure 4.8 Raman spectra of a: NH_4VO_3, b: $(COOH)_2$, c: 8V9PAl precursor. Laser: 514 nm

Activated 8V9PAl catalyst

Figure 4.9A presents a dehydration process of the 8V9PAl catalyst (preactivated in N_2 flow as described in section 2.2.1). The Raman spectrum of the hydrated sample exhibits a broad feature near 976 cm^{-1}, which is characteristic of hydrated surface vanadium oxide species [30]. Its progressive dehydration is evidenced by the onset of a new Raman band at 1031 cm^{-1} and a broad band

characteristic of V-O-V or V-O-support bonds of vanadium surface species appears near 900 cm^{-1}. The Raman band of dehydrated vanadyl groups at ambient temperature shifts to lower frequencies, which suggests partial re-hydration of the sample. Formation of V_2O_5 (Figure 4.9B) was observed during the thermal treatment of 8V9PAl in the presence of air, while phase transformation occurs faster compared to its precursor, which uses the first oxygen doses for burning off $(COOH)_2$. This sample has already been exposed to a treatment in N_2. Thus, V_2O_5 formation is quicker, and V_2O_5 population appears higher since the intensity of its Raman bands is higher than that of the dispersed vanadium oxide, as compared to the previous sample. The redshift is also smaller than for the previous sample, which would indicate that V_2O_5 domains are larger. The following thermal treatment at 400 ^oC in N_2 does not influence the V_2O_5 phase.

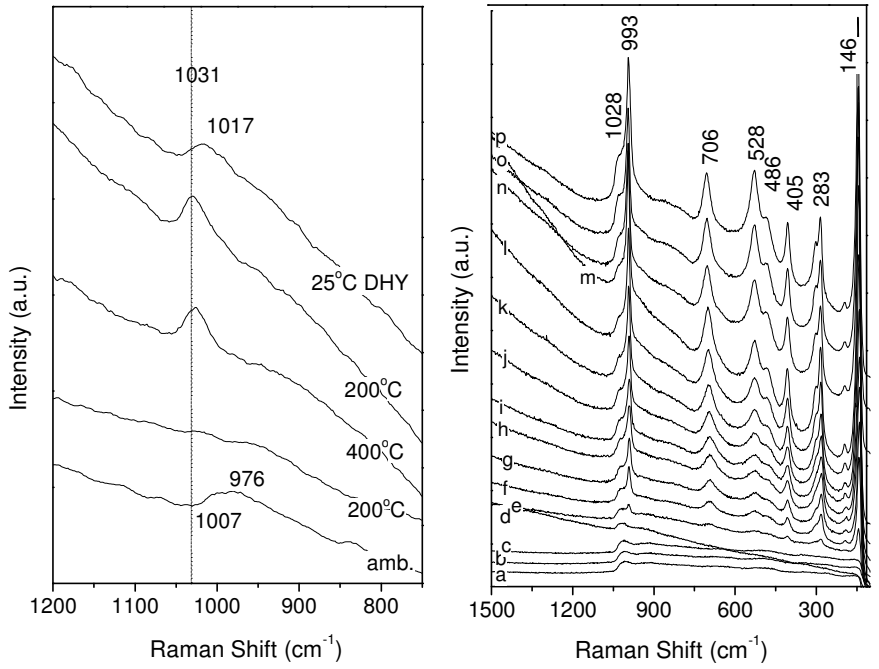

Figure 4.9 *In situ* Raman spectra of dehydration process of 8V9PAl in N_2 flow (A), amb – ambient temperature, DHY – dehydrated sample at ambient temperature, and V_2O_5 formation during thermal treatment dry air flow (B). Temperature increase from 50 ^oC to 400 ^oC (a-h) with step of 50 ^oC for spectrum recording, after 30 min at 400 ^oC (i), and cool down from 400 ^oC to 50 ^oC (j-p). Laser: 514 nm

4.6.2 *In situ* FT-IR Studies

Before running the experiment the catalysts were activated in vacuum at 400 ^{o}C for 1 hour. The spectrum of the activated sample was subsequently used as pseudo background, and thus the spectra are presented as difference spectra. For the alumina support both Lewis and Brønsted acid sites were detected by ammonia adsorption. Bands at 1619 and 1244 cm^{-1} were observed due to the $\delta_{as}(NH_3)$ and $\delta_s(NH_3)$ modes of chemisorbed ammonia coordinated to aluminum cations (Lewis acid sites) as well as bands at 1689, 1479 and 1394, which are characteristic of deformation modes of NH^{4+} formed by interaction of ammonia with Brønsted sites [31].

Figure 4.10A shows *in-situ* FTIR spectra of the evacuation process of adsorbed species formed on the surface of the 8V9PAl catalyst by simultaneous exposure to NH_3 and C_3H_8 at room temperature. C_3H_8 does not adsorb on the catalyst surface at room temperature as evidenced by the absence of strong vibrations in the 2900 cm^{-1} region (not shown in Figure 4.10B), even after evacuation at room temperature. Thus, the observed bands are exclusively due to ammonia and desorption process effectively becomes a desorption sequence of adsorbed ammonia species only.

The bands at 1613 and 1288 cm^{-1} are assigned to $\delta_{as}(NH_3)$ and $\delta_s(NH_3)$ modes of chemisorbed ammonia on vanadium respectively, while the bands at 1669 and 1442 cm^{-1} are characteristic of $\delta_s(NH_4)$ and $\delta_{as}(NH_4)$ bendings of ammonium cations. These features evidence the presence of both Lewis (coordinatively unsaturated vanadium cations) and Brønsted (acidic hydroxyls) acid sites. These band positions strongly depend on the support and on the oxidation state of the catalyst [32]. Furthermore, bands characteristic of ν_{NH} stretches are observed at 3388, 3351 3274, 3187, 2990 and 2825 cm^{-1} (not shown), which confirm the above assignment. The ammonium cations disappear during evacuation between 200 and 300 ^{o}C, indicating medium-weak acid strength of the Brønsted sites [33,34]. However, desorption of ammonia coordinated on Lewis acid sites (1613 and 1288 cm^{-1}) occurs already at 50 ^{o}C and the complete desorption takes place at the same temperature range as for ammonium species (200-300 ^{o}C).

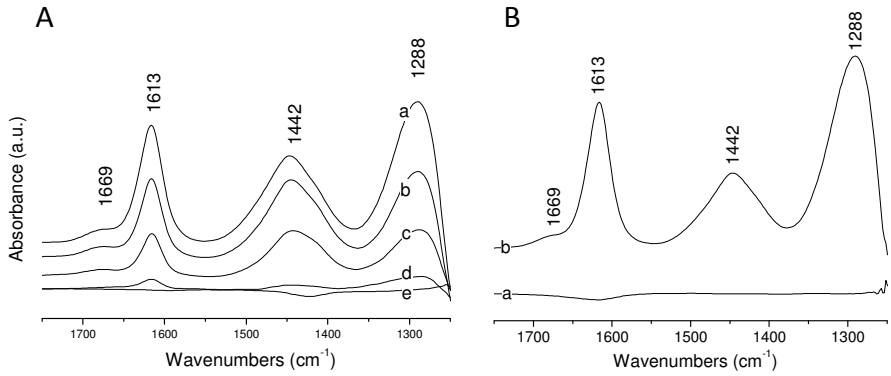

Figure 4.10 FTIR Spectra of (A) NH_3 and C_3H_8 adsorbed on 8V9PAl after evacuation at room temperature (a), at 50 ^oC (b), at 125 ^oC (c), at 200 ^oC (d) and at 300 ^oC (e) and (B) FTIR Spectra of C_3H_8 (a) and NH_3 (b) adsorbed on 8V9PAl after evacuation at room temperature

4.6.3 *In situ* EPR Studies

8V9PAl precursor

Figure 4.11 exhibits EPR spectra acquired during heating of the 8V9PAl precursor in He gas flow. Figure 4.11A shows the whole temperature range; thus the fresh precursor catalyst exhibits a clear EPR signal at 3470 Gauss (g = 1.966) at room temperature, with a line width of 82 Gauss, suggesting that the $(VO)_2P_2O_7$ precursor ($VOHPO_4 \cdot 0.5H_2O$) has been formed, as previously seen by Raman. This signal diminishes during heating. Up to 250 ^oC this species is still the only VO^{2+} compound present in the catalyst, but new phases begin to form at 480 ^oC. It is evident that the quantity of VO^{2+} is relatively low (<10% compared to original $VOHPO_4 \cdot 0.5H_2O$ concentration, even after temperature correction for the Boltzmann effect) at this stage. Figure 4.11B represents the amorphous phases present in these high temperature spectra in some more details. The appearance of some isolated VO^{2+} species is evident, due to the formation of the classic 16 line EPR spectra, characteristic of axial symmetric vanadyl in 5 or 6 folded coordination.

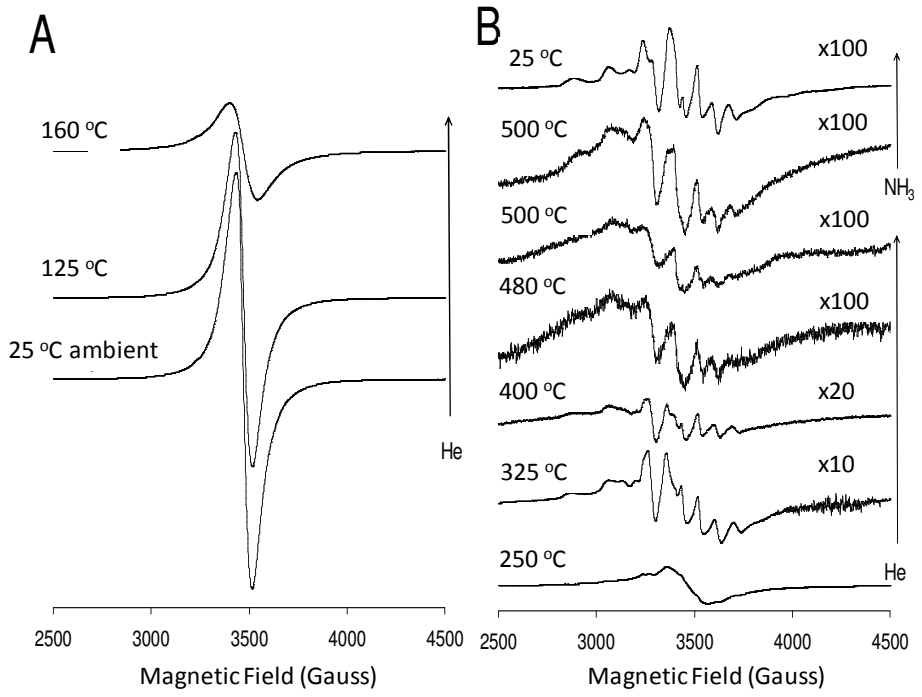

Figure 4.11 High-temperature EPR spectra acquired on 8V9PAl catalyst precursor during heating up in He, and subsequent reduction with 1% NH_3. Whole temperature range (A), and high temperature section (B)

A less spectacular, but none the less more significant, is the very broad underlying signal appearing at 480 °C and above. This probably originates from VO^{2+} units in dimeric or polymeric networks, whose spin-spin interactions provoke a line broadening effect causing the loss of spectral resolution of any hyperfine structure and anisotropy. This behavior is well known, in general for supported vanadia catalysts [35,36], but also specifically for vanadium-phosphate interactions on supported catalysts, where it can be attributed to the vanadyl pyrophosphate phase. No significant change of the monomeric VO^{2+} is observed during this heating sequence; suggesting that there is no change in the specific environment of the vanadyl unit.

The sample was exposed to a 1% NH_3/He gas mixture after acquiring the spectrum at 500 °C. As it can be seen, especially in Figure 4.11B, the reducing ammonia containing gas provokes a slight re-appearance of the VO^{2+} signal, probably combined with a slight decrease of the vanadyl pyrophosphate signal (broad underlying line) in the EPR spectra. Furthermore, a closer look at the new

spectrum reveals a shift in the line position of the parallel *g*-tensor, which can most clearly be observed as the shift to higher magnetic field values for the first hyperfine line from the *g*-tensor. A simulation of the spectrum (not shown) revealed that this change is due to a change in the parallel hyperfine structure constant (shifts from 173 to $158 \cdot 10^{-4}$ cm^{-1}). This suggests a shift in the coordination sphere of vanadium, due to reaction or complex formation with NH_3. The monomeric contribution to the spectrum maintains essentially the same magnetic properties after returning to room temperature and thus appears chemically unaltered. However, it is evident that the contribution from the broad polymeric (a non-crystalline VPP-like structure) signal appears significantly less dominant on the post mortem sample.

Activated 8V9PAl catalyst

Part of the catalyst sample was subjected to a 19 hours thermal treatment at 400 ^{o}C in a flow of N_2. The EPR spectra acquired during the subsequent (re-)heating sequence is plotted in Figure 4.12. The most striking feature at room temperature is the complete absence of the spectra from the $VOHPO_4 \cdot 0.5H_2O$ precursor compared to Figure 4.11. The pre-heating step probably provokes that the vanadium and phosphorus phases are present as frozen amorphous phases. Furthermore, it can also be seen that significantly more polymeric (amorphous vanadyl pyrophosphate like) vanadyl is present, probably since this sample has not been exposed to NH_3 at high temperature. Monitoring the rest of the heating procedure uncovers little changes. However, by comparing spin concentrations of spectra in Figures 4.11 and 4.12, it does seem like the monomeric phase and the VO^{2+} species have gained intensity during the pre-treatment step. The room temperature EPR spectrum in Figure 4.12, can be regarded as representative, and is compared to its simulated spectrum (see Figure 4.13). The $g_{\parallel}$ was found to be 1.937, while the $g_{\perp}$ was 1.976 and the hyperfine coupling constants were $A_{\perp} = 63.6 \cdot 10^{-4}$ and $A_{\parallel} = 173 \cdot 10^{-4}$ cm^{-1}.

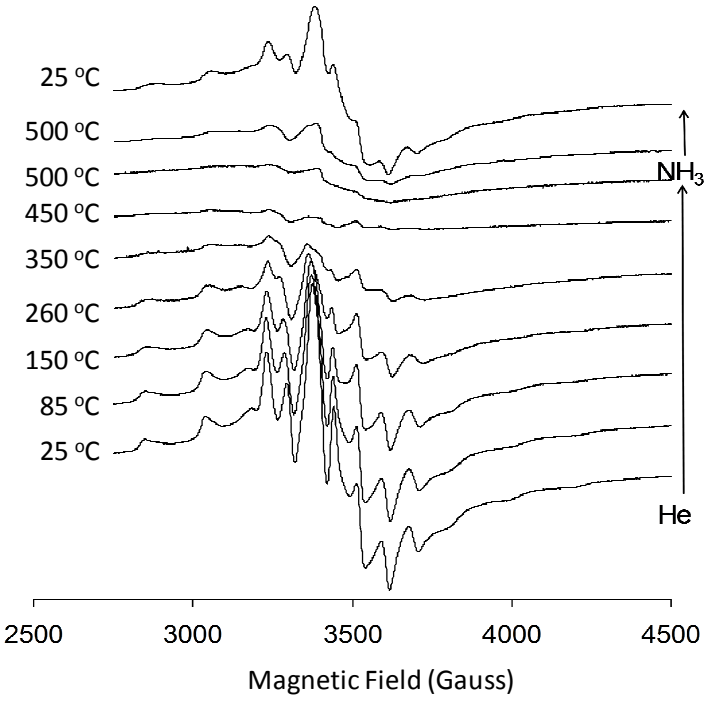

Figure 4.12 EPR Spectra during reheating process of 8V9PAl pretreated in N_2 flow

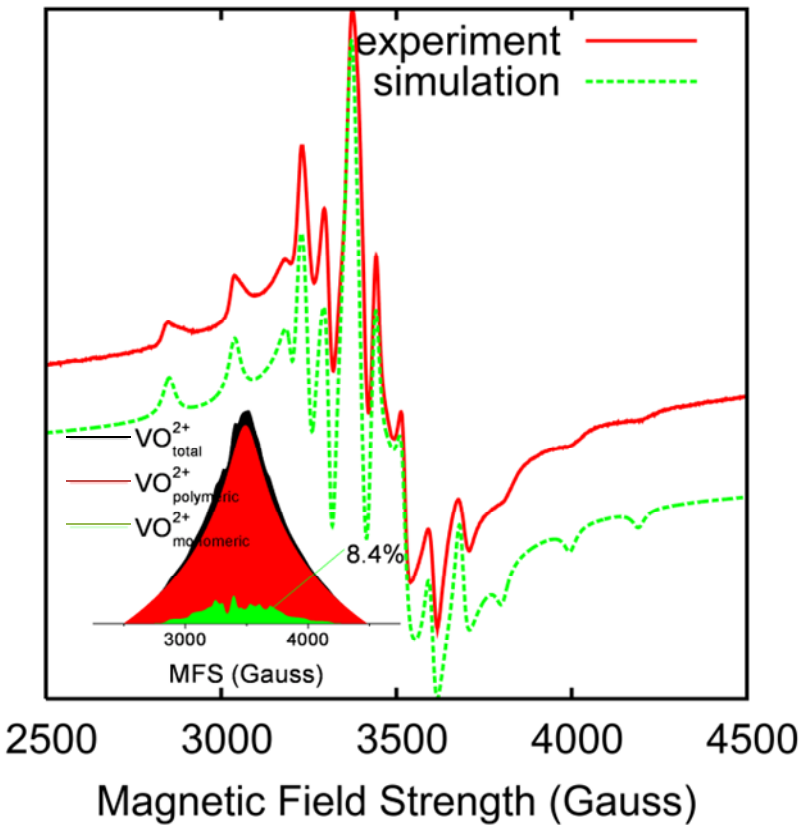

Figure 4.13 Experimental and calculated EPR spectra, and (inserted figure) relative quantitative distribution between monomeric and polymeric vanadyl (IV) phosphates

4.7 SUMMARY

Alumina-supported VPO-type catalysts were characterized using bulk analytical techniques like XRD, Raman and EPR. The surface acidity was examined by FT-IR studies of NH_3 adsorption/desorption. XRD patterns and Raman spectra show that no crystalline phase forms on the alumina support, when the catalyst precursors were pretreated in N_2 flow for 19 hours at 400 ^oC. However, the same thermal treatment in air flow leads to crystalline V^{5+}-containing phases. Formation of V_2O_5 was observed for alumina-supported vanadium catalyst, while the γ-$VOPO_4$ phase in combination with V_2O_5 was detected for 8V9PAl catalyst. TPO-Raman experiment of the 8V9PAl precursor shows that the

decomposition of the catalyst precursor leads, first to the formation of dispersed vanadium species and, then, V_2O_5 nanocrystallites at 150 ^oC after the calcination process. No γ-$VOPO_4$ phase was detected in this experiment, which indicates that formation of oxidized VPO phases requires longer treatment time. Both V^{4+} (EPR) and V^{5+} species (Raman) were detected on the support surface for 8V9PAl, which suggest that the V^{5+} species are stabilized by the alumina support. The main contribution to the EPR spectra originates from polymeric V-O-V entities and monomeric (isolated) VO^{2+} species. The polymeric signal exhibits a behavior that is concurrent with that of the important vanadyl pyrophosphate phase. The monomeric contribution is quantitatively less than 10% of the polymer. According to the literature, the spin Hamilton parameters [37] fit best to a six coordinated VO^{2+} hydrated defects in α-$VOPO_4$ crystals, as seen in the work of Ballutaud et al. [38]. They reported that the dehydrated α-$VOPO_4$ sample characteristically lacks hyperfine structure, similarly to V_2O_5-P_2O_5 type glasses. Judged from the spectra, which evidently contains a mixture of polymeric (ca. 92%) and monomeric (ca. 8%) vanadyl species, it therefore seems reasonable to conclude that the $VOPO_4$ phase derived from the vanadyl pyrophosphate pre-cursor forms scattered $VOHPO_4$ and $VOPO_4$ defects.

The spin Hamiltonian parameters obtained from the simulation in Figure 4.13 yields a $\Delta g_\perp/\Delta g_\parallel$ = 0.0653/0.0263 = 2.5 similar to a double layer VO_x/Al_2O_3 catalysts [39]. After exposure to ammonia containing gas the parallel hyperfine structure constant, $A_\parallel$, changes. Generally, nitrogen containing ligands like ammonia/ammonium ion form complexes with higher energy b_2 to e ($E_{xy} \rightarrow E_{zx,yz}$) and b_1 ($E_{xy} \rightarrow E_{x^2-y^2}$) transitions [40,41]. If this were the case, a significant change in the *g*-values should be observed. Based on this, it appears that ammonia would not be directly bound to the vanadyl unit, but rather indirectly, contributing to an increase of the vanadyl concentration by facilitating hydroxylation reactions such as [42]:

$$P—O—V=O + NH_3 \rightarrow P—NH_2 + HO—V=O \quad \text{eq. 4.1}$$

Centi and Parathoner [43] observed an increase of Brønsted and Lewis acid sites when NH_3 was adsorbed on VPO catalysts, which originate from the formation of coordinatively unsaturated V^{4+} ions [44]. The formation of such acid monomeric vanadyl sites could come from vanadyl pyrophosphate interaction

with ammonia according to eq. 4.1. This is partly supported by the existence of Brønsted and Lewis acid sites, as observed by *in-situ* FTIR in Figure 4.10. It can be seen that the IR bands representing the two types of acid sites, diminish significantly already at 300 ^{o}C. The IR analyses were performed in an evacuated *in-situ* cell, which facilitates desorption of ammonia at lower temperatures than in the atmospheric pressure *operando* studies. The results suggest that the influence of ammonia at reaction temperature would not be related to simple adsorption of NH_3 or NH_4^+, but instead related to a chemical reaction involving ammonia, one example being the equation outlined in eq. 4.1. However, the low pressure used in this experiment cannot deliver evidence of $–NH_2$ species.

References

[1] F. B. Abdelouahab, R. Olier, N. Guilhaume, F. Lefebvre, J. C. Volta, *J. Catal*. 134 (1992) 151

[2] H. Zhao, S. Bennici, J. Cai, J. Shen, A. Auroux, *Catal. Today* 152 (2010) 70

[3] C. V. Ramana, O. M. Hussain, B. Srinivasulu Naidu, *Matter. Chem. Phys.* 50 (1997)195

[4] Y. Iida, Y. Kaneko, Y. Kanno, *J. Matter. Proces. Tech*. 197 (2008) 261

[5] Z. Luan, P. A. Meloni, R. S. Czernuszkiewicz, L. Kevan, *J. Phys. Chem.* 101 (1997) 9046

[6] M. A. Vuurman, I. E. Wachs, *J. Phys. Chem.* 96 (1992) 5008

[7] P. C. Stair, *Advanc. Catal.*, 51 (1997) 75

[8] M. V. Martínez-Huerta, X. Gao, H. Tian, I. E. Wachs, M. A. Bañares, J. L. G. Fierro, *Catal. Today* 118 (2006) 279

[9] M. V. Martínez-Huerta, J. L. G. Fierro, M. A. Bañares, *Catal. Commun*. 11 (2009) 15

[10] G. Deo, I. E. Wachs, *J. Catal.146 (1994) 335*

[11] F. Close, T. Wolff, H. Lorenz, A. Seidel-Morgenstern, Y. Suchorski, M. Piórkowska, H. Weiss, *J. Catal.* 247 (2007) 176

[12] R. P. Singh, M. A. Bañares, G. Deo, *J. Catal.* 233 (2005) 388

[13] F. Castellino, S. B. Rasmussen, A. D. Jensen, J. E. Johnsson, R. Fehrmann, *Appl. Cat. B* 83 (2008)110

[14] H. S. Horowitz, C. M. Blackstone, A. W. Sleight, G. Teufer, *Appl. Catal.* 38 (1988) 193

[15] S. D. Jackson, J. S. J. Hargreaves (Eds.), J. K. Bartley, N. F. Dummer, G. J. Hutchings, *Metal Oxide Catalysis,* Wiley VCH Verlag GmbH & Co. KGaA, Weinheim, 1 (2009) 499

[16] Z-Y. Xue, G. L. Schrader, *J. Phys. Chem. B* 103 (1999) 9459

[17] H. H. Eysel, K. T. Lim, *J. Raman. Spetrosc.* 19 (1988) 535

[18] W. Bues, H.-W. Gehrke, *Z. Anorg. Allg. Chem*. 288 (1956) 307

[19] M. K. Cerreta, K. A. Berglund, *J. Cryst. Growth* 84 (1987) 577

[20] C. M. Preston, W. A. Adams, *J. Phys. Chem*. 83 (1979) 814

[21] E. Steger, K. Herzog, J. Klosowski, *Z. Anorg. Allg. Chem*. 432 (1977) 42

[22] V. Brazdova, M. V. Ganduglia-Pirovano, J. Sauer, *J. Phys. Chem. B* 109 (2005) 394

[23] S. Xie, E. Iglesia, A.T. Bell, *Langmuir* 16 (2000) 7162

[24] M. Grujic-Brojcin, M.J. Scepanovic, Z.D. Dohcevi-Mitrovic and Z.V. Popovic, *Acta Physica Polonica A* 116 (2009) 51

[25] P. Dehk, Z. Hajnal, M. Stutzmann, H. D. Fuchs, *Thin Solid Films* 255 (1995), 241

[26] M. X Gu, L. K Pan, B. K Tay, Chang Q Sun, *J. Raman Spectrosc*. 38 (2007) 780

[27] L.-Q. Mai, W. Chen, Q. Xu, J.-F. Peng, Q.-Y. Zhu, *Mater. Lett.* 62 (2008) 1458

[28] K. A. Alim, V. A. Fonoberov, and A. A. Balandina, *Appl. Phys. Lett.* 86 (2005) 053103

[29] L. H. Ai, *Powder Technol*. 195 (2009) 11

[30] M. A. Bañares, I. E. Wachs, *J. Raman Spectrosc*. 33 (2002) 359

[31] H. Zou, X. Ge, J. Shen, *Therm. Acta* 397 (2003) 81

[32] A.A. Davydov, A.A. Budneva, *Theor. Exp. Chem*. 19 (1983) 217

[33] G. Centi, F. Marchi, S. Perathoner, *Appl. Catal. A* 149 (1997) 225

[34] G. Busca, *Langmuir* 2 (1986) 577

[35] M.C. Paganini, L. Dall'Acqua, E. Giamello, L. Lietti, P. Forzatti, G. Busca, *J. Catal.* 166 (1997) 195

[36] J. Due-Hansen, S.B. Rasmussen, E. Mikolajska, M.A. Bañares, P. Ávila, R. Fehrmann, *Appl. Catal. B* 107 (2011) 340

[37] A. Davidson, M. Che, *J. Phys. Chem*. 96 (1992) 9909

[38] D. Ballutaud, E. Bordes, P. Courtine, *Mater. Res. Bull*. 17 (1982) 519

[39] V.K. Sharma, A. Wokaun, A. Baiker, *J. Phys. Chem*. 16 (1986) 2715

[40] P.E. Riley, V.L. Pecoraro, C.J. Carrano, J.A. Bonadies, K.N. Raymond, *Inorg. Chem*. 25 (1986) 154

[41] J.A. Bonadies, C.J. Carrano, *J. Am. Soc*. 108 (1986) 4088

[42] C. Janke, M. Schneider, U. Bentrup, J. Radnik, A. Martin, G. Scholz, A. Brückner, *J. Catal*. 277 (2011) 196

[43] G. Centi, S. Perathoner, *J. Catal*. 142 (1993) 84

[44] G. Busca, G. Centi, F. Trifiró, V Lorenzelli, *J. Phys. Chem*. 90 (1986) 1337

5

Comparison of bulk and supported VPO catalysts

5.1 INTRODUCTION

Bulk and alumina-supported VPO catalysts are compared in this chapter. Both catalysts were characterized by N_2 adsorption/desorption isotherms, TPR UV-Vis, XPS and XANES studies. Most of the analyses described in this chapter were performed using bulk analytical techniques, so that the signal from the bulk would significantly contribute to the readings if we deal with large particles. Such contribution is significantly diluted for alumina-supported nanoscaled VPO due to its very high surface-to-volume ratio. In particular, this would affect the relative signals of V^{4+} species inside VPO particles *vs.* that of V^{5+}species, preferably present on the surface. Thus, the goal of this chapter is not the direct comparison of vanadium oxidation states, but rather evaluation of the average oxidation state of the supported catalyst and the determination of any amount of V^{5+} species which could be present at the surface of the bulk VPO catalyst, as shown in section 3.4.

5.2 BET Surface Area

As shown in Chapters 3 and 4, the 8V9PAl catalyst possesses almost four times higher BET surface area than its bulk VPO counterpart. The supported catalyst contains ca. 50% of the VPO phase, and the relative higher surface area, compared to an expected linear combination of the alumina support and the bulk VPO material, is probably related to dispersion of nano-sized VPO clusters on the alumina surface. Both catalysts, as well as the alumina support exhibit type IV isotherm according to the BDDT and IUPAC classifications [1,2,3]. This isotherm is characteristic of mesoporous materials, and indeed, the alumina support and the catalysts possess pores in the 5-20 nm range, while this range is wider for the bulk VPO catalyst, even progressing into the region of smaller macropores.

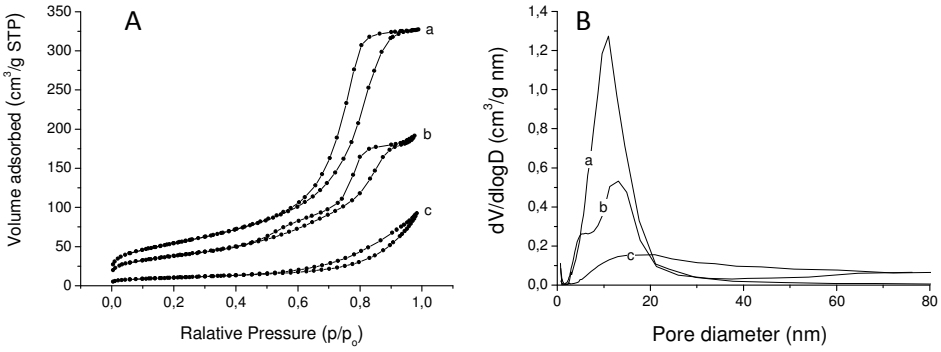

Figure 5.1 Adsorption isotherms (A), and pore distribution (B) for Al_2O_3 (a), 8V9PAl (b), VPO (c)

5.3 TPR and UV-Vis Studies

TPR profiles and UV-Vis spectra of VPO and 8V9PAl catalysts were acquired in order to determine the presence of V^{5+} and V^{4+} species. The TPR profile of bulk VPO catalyst shows strong H_2 consumption at ca. 795 ^oC due to reduction process of V^{4+} [4,5]. However, a small peak appears at ca. 500 ^oC. This temperature matches the reduction range of V^{5+} of the supported 8V9PAl; this is

attributable to the removal of lattice oxygen from V^{5+} [6,7,8]. The 8V9PAl catalyst also exhibits a broad peak at ca. 750 °C, which is probably related to further reduction of vanadium oxides. A well-defined peak at 904 °C may be due to the formation of V^{2+} species, as evidenced by the XRD pattern of this sample after TPR treatment (Figure 4.6).

The UV-Vis technique provides insight on the oxidation state and coordination geometry of vanadium oxide species [9,10,11]. The spectra presented in Figure 5.2B are consistent with the TPR profiles illustrating that the bulk catalyst possesses mainly reduced vanadium species in contrast to the supported catalyst, which shows a strong band characteristic of V^{5+} in a range typically observed for VO_4 and VO_6 ligand-to-metal change transfer. However, in case of the supported catalyst, absorption in the 600-800 nm range is observed indicating the presence of reduced vanadium species; while the bulk VPO catalyst also absorbs in a range characteristic of V^{5+}. These results indicate that both catalysts contain V^{4+} and V^{5+} but with different relative populations. Such differences would endow the catalytic systems with different activity and selectivity of hydrocarbon selective oxidation reactions.

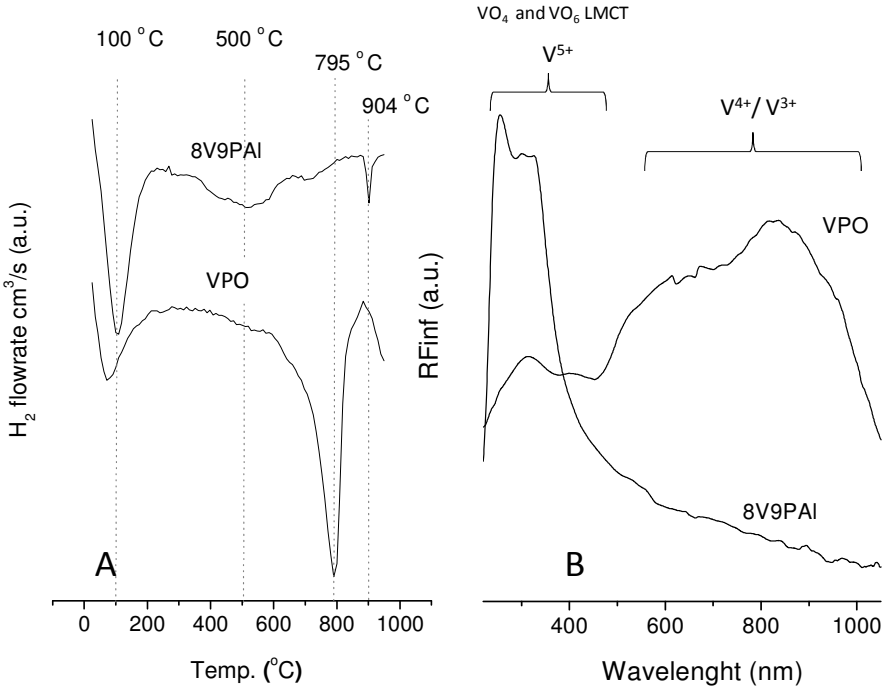

Figure 5.2 TPR profiles (A) and UV-vis spectra (B) of VPO and 8V9PAl catalysts

5.4 XPS and XANES Study

Figure 5.3 represents XP spectra of bulk and alumina-supported VPO catalysts. XPS studies provide detailed information about the oxidation state and chemical environment of the analyzed atom [12,13,14]; but the structural information is limited since XPS can hardly discriminate among vanadium species with different coordination numbers (VO_4, VO_5, VO_6) possessing the same oxidation state [15]. In general, the XPS spectrum of vanadium shows two peaks (V $2p_{3/2}$ and V $2p_{1/2}$) corresponding to a spin orbital with specific binding energies. The difference of binding energies between V $2p_{3/2}$ and V $2p_{1/2}$ for vanadium oxide is equal to 7.5 eV. However, from Figure 5.3 it can be observed that a strong interaction of O 1s satellite takes place, which causes difficulties of interpretation of the spectra. The strong O 1s satellite line appearing between V $2p_{3/2}$ and V $2p_{1/2}$ peaks challenges precise deconvolution of the V 2p peaks. Thus, the best fit in our case shows the differences of binding energies of 7.1 eV between V $2p_{3/2}$ and V $2p_{1/2}$ peaks of V^{5+} in the 8V9PAl XPS spectra, 6.7 eV for V^{4+} of the 8V9PAl and 7.8 eV for V^{4+} of the VPO catalyst. The O 1s satellite may be subtracted from the XPS spectra, but this process influences the V 2p peaks to the same extent as before subtraction. The bulk VPO catalyst shows presence of only V^{4+}. The thin orange line forms a peak at the binding energy related to V^{5+}, but it was not taken into consideration since the fit of corresponding V $2p_{1/2}$ peak was not possible. The XPS spectra of 8V9PAl show presence of both V^{4+} and V^{5+} surface atoms. Detailed information was presented in table 5.1. The V^{4+}/V^{5+} ratio of 8V9PAl, obtained by peak deconvolution, is 1 and seems to be relatively high for a supported "monolayer" type vanadium oxide catalysts. The reason of that may be that the catalyst is reduced by exposure to the ultra high vacuum [16]. However, V^{4+} in supported VPO catalyst was clearly seen by high temperature EPR studies (Chapter 4) and was detected by the UV-Vis spectroscopy (Chapter 5). For confirmation, the vanadium average oxidation state (V_{AOS}) was calculated using an empirical formula reported by Clouston [17]:

$$V_{AOS} = 13.82 - 0.68\ (O\ 1s - V\ 2p_{3/2}) \qquad \text{eq. 3.1}$$

The average oxidation state of vanadium atoms in 8V9PAl catalyst was equal to 4.27, which also indicates high amount of V^{4+} species. The average oxidation state of the bulk VPO catalyst was 3.61, which is relatively low. The Clouston's

equation is convenient, since correction of peak positions is not necessary. However, the spectral resolution for these analyses was 0.1 eV, which results in an error of 0.07. Moreover, the O 1s satellite lines seem to influence the V 2p peak positions. Thus, the same calculation was performed using the HR-XPS spectrum of bulk VPO catalyst presented in Chapter 3. That spectrum possesses no O 1s satellite line and the calculation gives a V_{AOS} value of 4.09. This value is already closer to that reported in literature (4.00 – 4.30) [18,19,20]. The vanadium oxidation state of 4.09 suggests the presence of small amounts of V^{5+}, nevertheless, caution should be taken, since it is close to the experimental error of the XPS measurements.

Table 5.1 XPS data of the bulk and supported VPO catalysts

Catalysts	Peak position (eV)	Area	FWHM (eV)	V-oxidation state	Percentage (%)
VPO	515.90	10320	2.44	V^{4+}	100
8V9PAl	516.20	25626	2.17	V^{4+}	50
	517.33	25608	1.94	V^{5+}	50

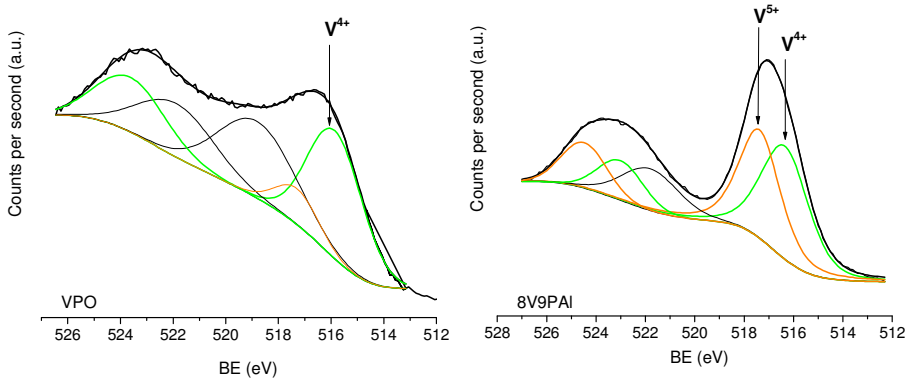

Figure 5.3 XPS spectra of bulk (left) and supported (right) VPO catalysts

XANES studies also provide information about the oxidation state of a given atom; but in contrast to the XP spectroscopy, it also delivers structural information, especially when combined with EXAFS [21,22,23,24]. Using XANES, the oxidation state of vanadium can be determined by examination of the K-edge position. It is connected to the energy of the core electron which decreases with higher valence and thus the K-edge shifts to higher energy [25]. Also the pre-edge of the given spectrum, which reflects transitions from K-shell to the empty bound *d*-level is used to determine the oxidation states. Additionally, the intensity of the pre-edge provides information of the coordination of the analyzed element. The pre-edge intensity of vanadium species with inversion symmetry, like regular octahedra is very low. Coordination with no inverse symmetry, like tetrahedra, result in high intensities of the pre-edge peak [26]. However, the intensity of the pre-edge peak of a distorted octahedron increases significantly due to the loss of the inverse symmetry caused by the disorder. In the present work, vanadium coordination and oxidation state will be determined using XANES. For this purpose the position and intensity of the pre-edge and position of the K-edge of the bulk and supported VPO catalysts is compared with V^{4+} and V^{5+} references. V_2O_5, NH_4VO_3 and $VOSO_4 * 3H_2O$ were used as references. However, since XANES is a bulk technique and the oxidation state and coordination of vanadyl pyrophosphate is well-known, this catalyst may also be considered as reference. XANES spectra of the catalysts and the references are presented in Figure 5.4.

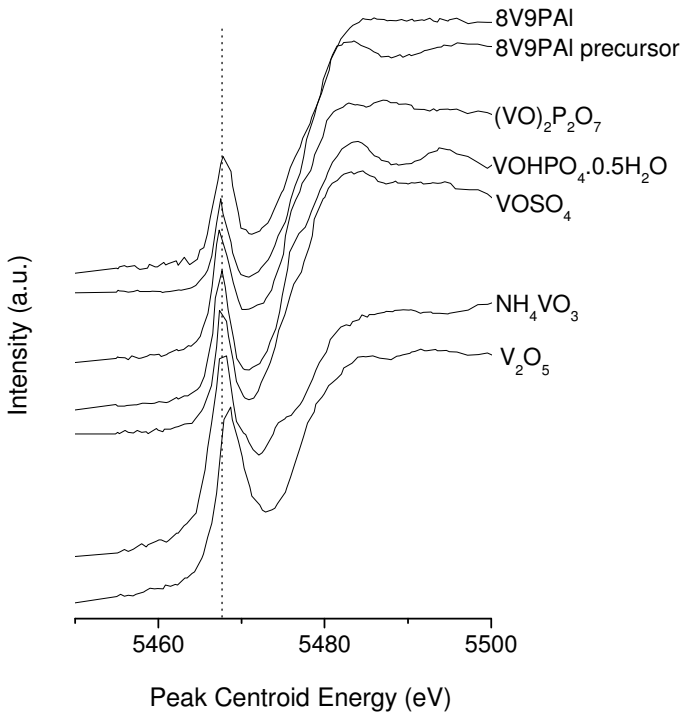

Figure 5.4 XANES spectra of bulk and supported VPO catalysts, their precursors and reference samples, under ambient conditions

V_2O_5 has a coordination of strongly distorted square pyramids of VO_5 [27], NH_4VO_3 has an almost regular tetrahedral coordination [28], while the coordination of $VOSO_4*3H_2O$ is a distorted VO_6 [29]. The coordination of supported vanadium species depends on the loading and on the vanadium oxidation state. Isolated VO_x species are present at very low loadings; two-dimensional polymerized vanadium surface species appear at higher loadings, while disordered (amorphous) V_2O_5 phase forms at loadings above monolayer coverage. Crystalline V_2O_5 forms at high vanadium loadings. Tetrahedrally coordinated vanadium species were found on alumina support in supported catalysts at monolayer coverage [30]. However reduced vanadium surface species (V^{4+}) typically possess octahedral coordination [31,32]. Table 5.2 shows positions and intensity of the vanadium pre-edge peak, main-edge position, oxidation states and coordination of examined samples. It is clearly seen that the main edge position of samples possessing V^{4+}, like $VOSO_4*3H_2O$, $VOHPO_4*0.5H_2O$

and $(VO)_2P_2O_7$ is near 5483.34 eV. This value is higher (5484.66 eV) in case of V^{5+}-containing samples (V_2O_5, NH_4VO_3). Also the pre-edge position shifts towards higher energy with increasing oxidation state of vanadium. Comparing these main-edge and pre-edge positions, it may be concluded that the 8V9PAl precursor contains essentially V^{4+} species, since its main-edge position is very low (5484.29 eV). Assignment of the oxidation state for the 8V9PAl catalyst is not as obvious as for its precursor. The intermediate value of the main-edge position suggests oxidation state of vanadium between +4 and +5, and it was calculated to be +4.8.

Table 5.2 XANES properties of the bulk and supported VPO catalysts, their precursors and reference compounds

Catalyst	Pre-edge peak position (eV)	Main-edge position (eV)	Pre-edge intensity (a.u.)	Oxidation state	Coordination
V_2O_5	5468.33	5484.66	0.78	+5	VO_5
NH_4VO_3	5467.79	5484.66	0.81	+5	VO_4
$VOSO_4*3H_2O$	5467.42	5483.33	0.51	+4	VO_6
$VOHPO_4*0.5H_2O$	5467.41	5483.34	0.55	+4	VO_6
$(VO)_2P_2O_7$	5467.42	5483.34	0.53	+4	VO_6
8V9PAl precursor	5467.43	5483.29	0.38	+4	VO_6
8V9PAl	5467.77	5484.37	0.45	<+5	VO_6

Comparing intensities of the pre-edge vanadium peaks, the geometry of vanadium species may be concluded (see Figure 5.5). As described above, the intensity of the pre-edge peak is high for compounds with inversed symmetry. It was reported that vanadyl pyrophosphate has a distorted VO_6 symmetry [33,34]. Its structure is build up by layers in which pairs of edge-sharing distorted VO_6 octahedra are connected by PO_4 tetrahedra. The octahedral coordination of $VOSO_4*3H_2O$ is also distorted, which explains very similar pre-edge peak intensities comparing to $(VO)_2P_2O_7$. The same scenario is observed for the precursor of the bulk VPO catalyst, and for 8V9PAl precursor. Lower intensity of the 8V9PAl precursor indicates less distorted VO_6 coordination. There are two reasons for the octahedral coordination in supported VPO catalysts: (1) the

loading of V+P is about two monolayers, which can explain the absence of tetrahedrally coordinated vanadium species, observed for the model supported vanadium oxide catalysts, due to higher loading of surface species; (2) these samples possess reduced vanadium species (especially 8V9PAl precursor), and the preferential coordination of reduced vanadium in supported monolayer type catalysts is octahedral. Distortion observed in the VO_6 coordination of the pretreated 8V9PAl catalyst may be due to higher V^{5+}/V^{4+} ratio. EPR studies have shown that the 8V9PAl contains mainly polymerized vanadium species, while UV-Vis spectra show presence of both, VO_4 and VO_6 coordinated vanadium species.

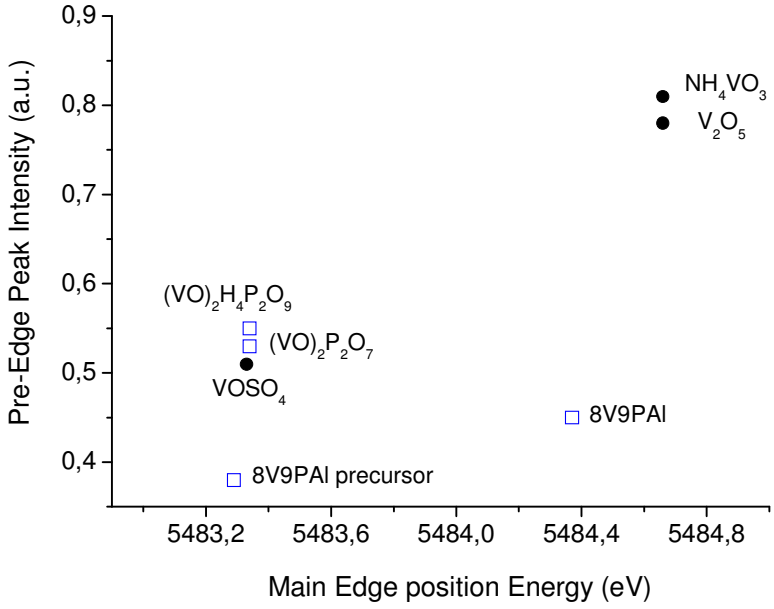

Figure 5.5 The position of main-edge energy *vs.* pre-edge peak intensity of bulk and supported VPO catalysts, their precursors and reference compounds

5.5 SUMMARY

The alumina-supported VPO catalyst possesses almost four times higher surface area than its bulk counterpart, even if it contains around half of the active VPO phase. This self assembling nano dispersion effect is an interesting phenomenon

considering the cost of the catalyst production. In addition, the higher available surface area may lead to a strong improvement of catalytic performance if the active sites are identical for bulk and supported catalysts. However, the support changes the nature of the catalyst by increasing V^{5+}/V^{4+} ratio. This may change activity and selectivity during hydrocarbon oxidation reactions; thus, it is important to examine the support effect on vanadium sites [35]. The UV-Vis spectra show that both catalysts contain reduced and oxidized vanadium species. The presence of V^{4+} & V^{5+} mixture in the alumina-supported VPO catalyst is confirmed by XPS and XANES study, but detection of V^{5+} species in bulk VPO catalyst was complicated because of the strong signal coming from the bulk of the catalyst. The O 1s satellite line in vanadium XP spectra caused additional difficulties. Thus the XPS data for bulk VPO catalyst obtained in this Chapter differ from those presented in section 3.5. Additionally different X-ray sources (different sensitivity factors) were used in these analyses. XANES study was used for evaluation of the oxidation state of 8V9PAl. It shows that the vanadium average oxidation state of the 8V9PAl precursor is +4, while the V^{5+}/V^{4+} population ratio increases for catalyst activated in N_2 flow. The 8V9PAl reveal vanadium oxidation state below +5, but still higher compared to that calculated from XPS data. The advantage of XANES is that this analysis does not require high vacuum conditions, so that in contrast to XPS there is no danger that the catalyst may be reduced during analysis. However, these data show at least half of vanadium species present on the alumina support are oxidized to V^{5+} in supported VPO catalyst. This is related to the effect of the support, which promotes vanadia dispersion and favors higher oxidation state of these vanadium species. The vanadium coordination in supported VPO catalyst was determined as octahedral with a geometry that is less distorted than the bulk VPO. The vanadium coordination in $(VO)_2P_2O_7$ is reported as distorted VO_6, but it is also quite often considered as edge-sharing VO_5 square pyramids bridged by PO_4 double tetrahedra [36,37,38]. The loading of two monolayers of V+P is enough to change the coordination of vanadium from tetrahedral, typical for alumina-supported vanadium monolayer type catalysts, to octahedral, typical for bulk vanadia phases or reduced vanadia species. However, quantification of VO_6 vs. VO_4 was not possible from the XANES spectra, but the UV-Vis spectra indicate that tetrahedrally coordinated vanadium species are also present on the alumina support.

References

[1] Brunauer, L. S. Deming, W. E. Deming and E. J. Teller, *J. Am. Chem. Soc*. 62 (1940) 1723

[2] IUPAC Recommendations, *Pure Appl. Chem.* 57 (1985) 603

[3] IUPAC Recommendations, *Pure Appl. Chem.* 66 (1994) 1739

[4] R.-M. Feng, X.-J. Yang, W.-J. Ji, Y. Chen, C.-T. Au, *J. Catal.* 246 (2007) 166

[5] X.-K. Li, W.-J. Ji, J. Zhao, Z.-B. Zhang, C.T. Au, *J. Catal.* 238 (2006) 232

[6] X.S. Wang, L.J. Xu, X. Chen, W.J. Ji, Q.J. Yan, Y. Chen, *J. Mol. Catal. A*, 206 (2003) 261

[7] C.Y. Xiao, X. Chen, Z.Y. Wang, W.J. Ji, Y. Chen, C.T. Au, *Catal. Today* 93 (2004) 223

[8] F. Close, T. Wolff, H. Lorenz, A. Seidel-Morgenstern, Y. Suchorski, M. Piórkowska, H. Weiss, *J. Catal.* 247 (2007) 176

[9] X.T. Gao, I.E. Wachs*, J. Catal*. 188 (1999) 325

[10] E.V. Kondratenko, M. Baerns, *Appl. Catal*. 222 (2001) 133

[11] B.M. Weckhuysen, I.P. Vannijvel, R.A. Schoonheydt, *Zeolites* 15 (1995) 482

[12] M. Wark, A. Brückner, T. Liese, W. Grunert, *J. Catal.* 175 (1998) 48

[13] M.A. Vuurman, I.E. Wachs, A.M. Hirt, *J. Phys. Chem*. 95 (1991) 9928

[14] M.A. Eberhardt, M. Houalla, D.M. Hercules, *Surf. Interface Anal*. 20 (1993) 766

[15] B. M. Weckhuysen, D. E. Keller, *Catal. Today* 78 (2003) 25

[16] Y. Suchorski, L. Rihko-Struckmann, F. Klose, Y. Ye, M. Alandjiyska, K. Sundmacher and H. Weiss, *Appl. Surf. Sci.* 249 (2005) 231

[17] G. W. Clouston, E. A. Thompson, N. Herron, *J. Catal.* 163 (1996) 122

[18] M. Abon, J. C. Volta, *Appl. Catal. A* 157 (1997) 173

[19] F. Cavani, F. Trifiro, *Chem. Tech*. 24 (1994) 18

[20] S. Luciani, Dissertation: *Structural changes and dynamic behavior of vanadium oxide-based catalysts for gas-phase selective oxidations*, Bologna University, Italy (2009)

[21] M. Ruitenbeek, F.M.F. de Groot, A.J. van Dillen, D.C. Koningsberger, *Stud. Surf. Sci. Catal*. 130 (2000) 3101

[22] T. Okuhara, K. Inumaru, M. Misono, N. Matsubayashi, H. Shimada, A. Nishijima, *Catal. Lett*. 20 (1993) 73

[23] R. Kozlowski, R.F. Pettifer, J.M. Thomas, *J. Chem. Soc., Chem. Commun*. (1983) 438

[24] R. Kozlowski, R.F. Pettifer, J.M. Thomas, *J. Phys. Chem*. 87 (1983) 5176

[25] J. Wong, F.W. Lytle, R.P. Mesmer and D.H. Maylotte, *Phys. Rev. B* 30 (1984) 5596

[26] G. Silversmit, J. A. van Bokhoven, H. Poelman, A. M. J. van der Eerden, G. B. Marin, M.-F. Reyniers, R. De Gryse, *Appl. Catal.* 285 (2005) 151

[27] H.G. Barnes, F.R. Ahmed, W.H. Barnes, *Z. Kristallogr*. 115 (1961) 110–131

[28] H.T. Evans Jr., *Z. Kristallogr*. 114 (1960) 257–277

[29] F. Théobald, J. Galy, *Acta Cryst. B* 29 (1973) 2732–2736

[30] J. Haber, A. Kozlowska and R. Kozlowski, *J. Catal*. 102 (1986) 52

[31] F. Lemoigno, E. Prouzet, Z.Y. Wu, P. Gressier and G. Ouvrard, *J. Phys. IV France* 7 (1997) 263

[32] M. Ruitenbeek, A.J. van Dillen, F.M.F. de Groot, I.E. Wachs, J.W. Geus, D.C. Koningsberger, *Top. Catal*. 10 (2000) 241–254

[33] V. V. Guliants, J. B. Bezinger, S. Sundaresan, I. E. Wachs, J.-M. Jehng, J. E. Roberts, *Catal. Today* 28 (1996) 275

[34] M. Witko, R. Tokarz, J. Haber, K. Hermann, *J. Mol. Catal. A* 166 (2001) 59

[35] I. E. Wachs, J-M. Jehng, G. Deo, B. M. Weckhuysen, V. V, Guliants, J. B. Benziger, S. Sundaresan, *J. Catal.* 170 (1997) 75

[36] S. Geupel, K. Pilz, S. van Smaalen, F. Büllesfeld, A. Prokofiev, Assmus W, *Acta Cryst. C* 58 (2002) 9

[37] B. Schioett, K. A. Joergensen, R. Hoffmann, *J. Phys. Chem.* 95 (1991) 2297

[38] P. A, Agaskar, L. Caul, R. K. Grasselli, *Catal. Letters* 23 (1994) 339

6

Influence of phosphorus on titania- and alumina-supported vanadia catalysts

6.1 INTRODUCTION

Titania- and alumina-supported vanadium and phosphorus oxide catalysts are studied in this chapter. It is known that doping often improves catalytic properties, but this effect is not well understood, mainly because the changes caused by very low amounts of an additive are difficult to follow by conventional analytical techniques. Thus, supported vanadium catalysts were compared to supported VPO-type catalysts and to phosphorus-doped titania- and alumina-supported vanadium oxide catalysts in order to evaluate the influence of high and low contents of the phosphorus additive.

6.2 BET Surface Area

Catalysts supported on titania anatase exhibit ca. 40 m^2g^{-1} less BET area than γ-alumina-supported catalysts due to the lower area of the titania support. The BET area decreases with V+P loading with the same factor for alumina and titania-supported samples. The alumina-supported catalysts possess pores in a range between 5-20 nm, with a maximum at 10 nm. The titania-supported catalysts possess wider range of pore diameters, with two maxima at 6 and 15 nm. The maximum of 15 nm pores becomes increasingly apparent with vanadium and phosphorus, loading, which is related to plugging of smaller pores. The maximum at 15 nm has a broad shoulder indicating the presence of mesopores up to 50 nm and macropores.

Table 6.1 BET surface area and theoretical P/V ratio of alumina- and titania-supported catalysts

Catalyst	TiO_2	8VTi	8V1PTi	8V9PTi	16V2PTi	Al_2O_3	8VAl	8V1PAl	8V9PAl
BET [m^2/g]	140	105	109	91	75	194	141	145	135
Theoretical P/V ratio	-	-	0.1	1.1	0.1	-	-	0.1	1.1

6.3 XRD Patterns

Figures 6.1 and 6.2 represent powder XRD patterns of N_2-pretreated titania- and alumina-supported vanadium and phosphorus oxide catalysts. The XRD patterns are dominated by TiO_2 anatase or γ-Al_2O_3 and generally no new crystalline phases form on the support.

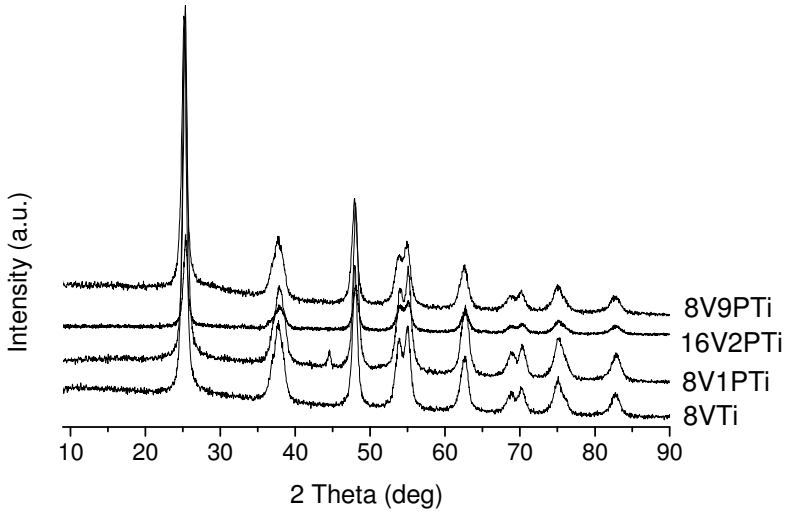

Figure 6.1 Powder XRD patterns of N_2-pretreated titania-supported vanadium and phosphorus oxide catalysts

An additional peak is observed for the fresh 8V1PTi near 44° 2Θ. It could be assigned to a V-Ti phase, like $V_{0.92}Ti_{0.8}O$, with XRD lines at 2Θ ca. 38.00, 44.06 and 68.20, but the information supplied by the observed peak is not sufficient for characterization of any additional phase. The XRD pattern of 8V9PAl shows increase of the baseline in the 20-35° 2θ range, which suggests formation of amorphous VPO phase on the alumina support.

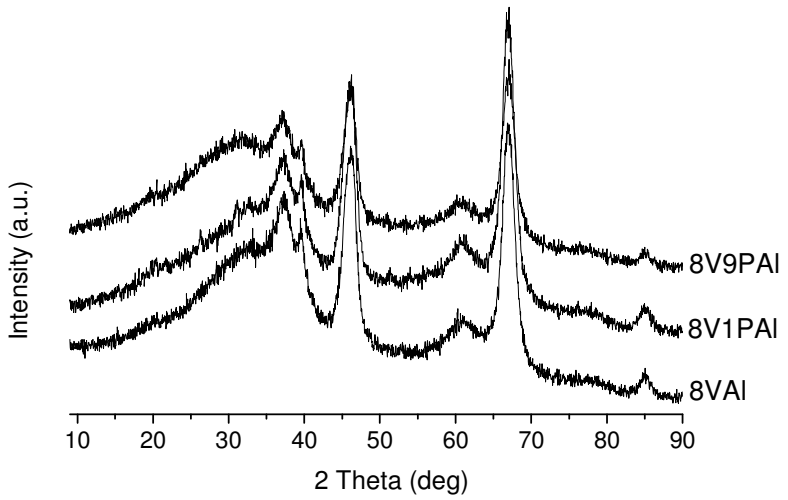

Figure 6.2 Powder XRD patterns of pretreated in N_2 alumina-supported vanadium and phosphorus catalysts

6.4 Raman Spectra

Representative Raman spectra of dehydrated catalysts supported over titania and alumina are presented in Figure 6.3. At least 10 Raman spectra were acquired at different spots for each sample in order to evaluate homogeneity of the catalysts. The samples were pretreated in N_2 flow for 19 hours at 400 ^{o}C. As it can be observed, no crystalline vanadia phases were detected for titania-supported catalysts. The Raman spectra exhibit bands characteristic of the terminal V=O bond of molecularly dispersed vanadia at 1029 cm^{-1} [1,2,3] and Raman features due to V-O-M bonds (M states for Ti, Al or V) at 910 cm^{-1} [4,5,6]. Titania support also exhibits strong Raman bands at frequencies < 800 cm^{-1}, characteristic of titania anatase phase, these bands may overlap with those of supported phases. The bands of titania anatase show up at 402, 515, 638 and at ca. 800 cm^{-1} in Figure 6.3A [7,8]. Figure 6.3B represents the Raman spectra of alumina-supported catalysts. All these catalysts show one Raman feature near 1013 cm^{-1}, which is characteristic of the stretching mode of its terminal V=O bond [9,10]. No crystalline phases were detected, except for the phosphorus-doped alumina-supported vanadium oxide catalyst (8V1PAl). This catalyst exhibits the V=O

stretching mode of dispersed vanadium oxide species (band at 1013 cm^{-1}) in addition to the Raman bands characteristic of V_2O_5 at 996, 704, 529, 482, 406, 303, 286, 195, and 144 cm^{-1} (not shown). Considering the high Raman section of crystalline V_2O_5 [11], it may be concluded that the V_2O_5 population is very little in 8V1PAl since its intensity is comparable to that of the Raman band of the molecularly dispersed vanadium oxide species. In addition, a very few spots were found possessing the Raman bands of V_2O_5.

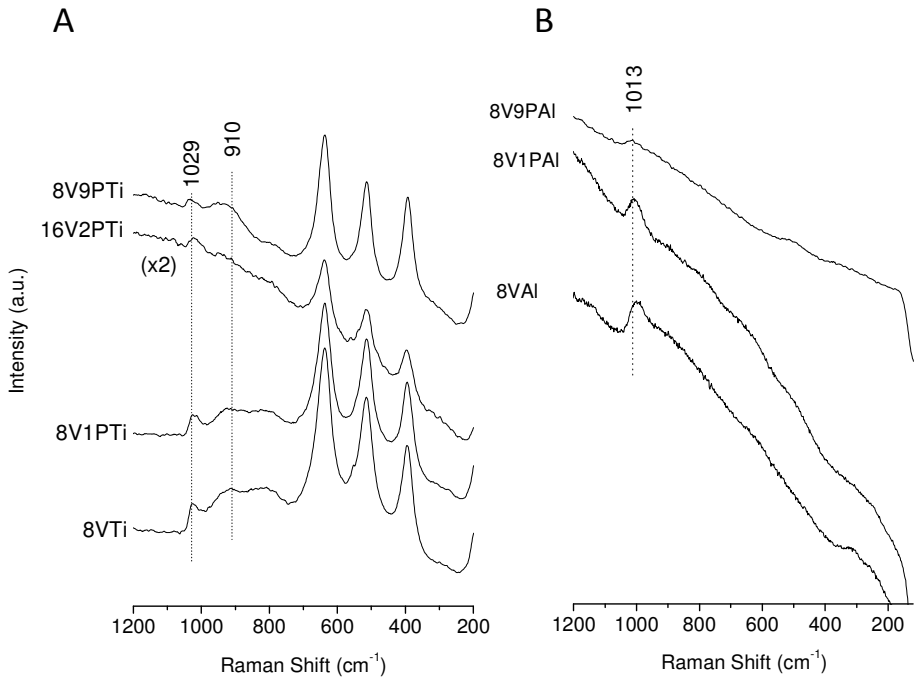

Figure 6.3 Raman Spectra of N_2 activated titania-supported catalysts under dehydrated conditions (A) and alumina-supported catalysts under dehydrated conditions (B). Spectrum of 16V2PTi was multiplied by factor of 2 for graphical reason.

6.5 H_2-TPR Profiles

H_2-TPR profiles of titania- and alumina- supported catalysts were obtained. Hydrogen consumption at ca. 100 ^oC is observed for all examined samples (see Figure 6.4), it is probably due to reaction of hydrogen with surface hydroxyl

groups. Another reduction peak is observed in a 480-600 ^{o}C range. Alumina-supported samples require slightly higher reduction temperature compared to titania-supported samples but this scenario relates only to samples with low phosphorus contents. It can be observed that with increasing amounts of phosphorus, the T_{max} of titania-supported catalysts shifts to higher temperatures, which suggests that vanadia sites are less reducible in phosphorus vicinity. This tendency is noticeable already for phosphorus-doped titania-supported vanadium catalyst. It was previously reported in literature that an increase of the vanadium content causes a similar effect shifting the vanadium reduction peak to higher temperatures [12,13]. This shift caused by increasing amount of phosphorus is not observed for the alumina-supported catalysts, but rather a broadening of the reduction peak at 506 ^{o}C is evident. Different degrees of interaction with phosphorus probably account for the broad distribution of vanadium surface species. The areas of the first reduction peaks were integrated for determination of hydrogen consumption. The H/V ratios are 1.9 for alumina-supported vanadium catalysts and 1.5 for titania-supported vanadium catalyst, which suggests a reduction of vanadium species from V^{5+} to V^{3+}. These data are in a good agreement with literature [14,15]. However, V^{3+} species form easier on the alumina support. The hydrogen consumption decreases with increasing phosphorus content [16,17]. The lower H/V ratio of 8V9PAl (0.7) and 8V9PTi (1.2) suggests that the presence of phosphorus decreases the reduction rate, probably by stabilization of V^{4+} species [18]. 8V9PAl and 8V9PTi catalysts show additional reduction peaks in the 600-905 ^{o}C range due to further reduction of vanadium sites. As reported in Chapter 4, the XRD pattern of 8V9PAl after H_2-TPR measurements exhibits presence of V^{3+} and V^{2+} species. No crystalline VPO phases were detected for the titania-supported 8V9PTi after H_2-TPR experiment.

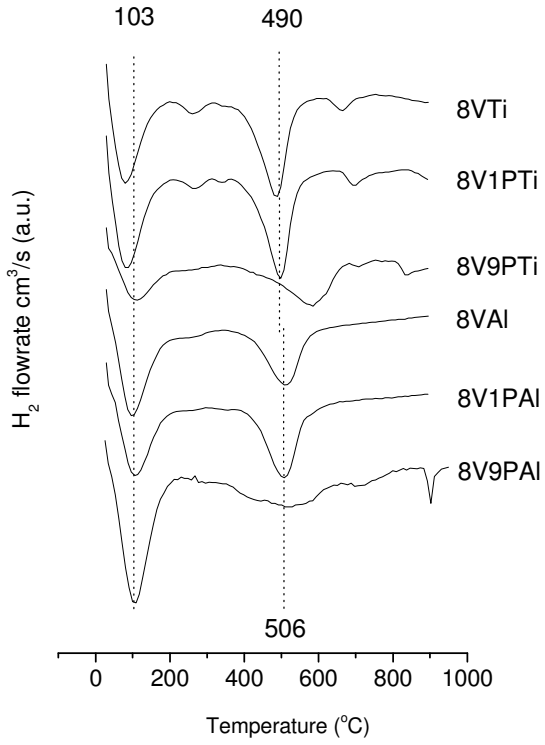

Figure 6.4 H_2-TPR profiles of titania- and alumina-supported vanadium and phosphorus catalysts

6.6 *In situ* FT-IR Studies

The catalysts were activated in vacuum at 400 °C for 1 hour prior to running the experiment. The spectrum of the activated sample was subtracted from presented spectra. Ammonia was adsorbed on the Lewis acid sites of the titania anatase support showing three bands at 1160, 1220 and 1601 cm^{-1} due to symmetric (1160 and 1224 cm^{-1}) and asymmetric (1600 cm^{-1}) NH deformation vibrations [19,20] (spectra not shown). No bands in the 1420-1460 cm^{-1} region characteristic of asymmetric deformation mode of the NH_4^+ cation adsorbed on Brønsted sites [21,22] were observed.

For the alumina support, both Lewis and Brønsted acid sites were detected by ammonia adsorption (spectra not shown). Bands at 1619 and 1244 cm^{-1} were observed due to $\delta_{as}(NH_3)$ and $\delta_s(NH_3)$ modes of chemisorbed ammonia

coordinated to aluminum cations (Lewis acid sites) and bands at 1689, 1479 and 1394, which are characteristic of deformation modes of NH_4^+ were formed by interaction of ammonia with Brønsted acid sites [23].

Figure 6.5 shows the evacuation process of adsorbed species formed on the titania-supported catalysts surface by contact with NH_3 at room temperature. For 8VTi, the bands at 1605 and 1235 cm^{-1} are due to $\delta_{as}(NH_3)$ and $\delta_s(NH_3)$ modes of chemisorbed ammonia respectively, while the bands at 1665 and 1425 cm^{-1} are characteristic of $\delta_s(NH_4)$ and $\delta_{as}(NH_4)$ ammonium cations [24]. These features evidence presence of both Lewis (coordinatively unsaturated vanadium cations) and Brønsted (acidic hydroxyls) acid sites. The ammonium cations disappear during evacuation between 200 and 300 °C, indicating a medium-weak acid strength of the Brønsted sites. However, the desorption of ammonia coordinated on Lewis acid sites (1605 and 1239 cm^{-1}) occurs already at 50 °C and the complete desorption takes place at the same temperature range as for Brønsted sites (200-300 °C).

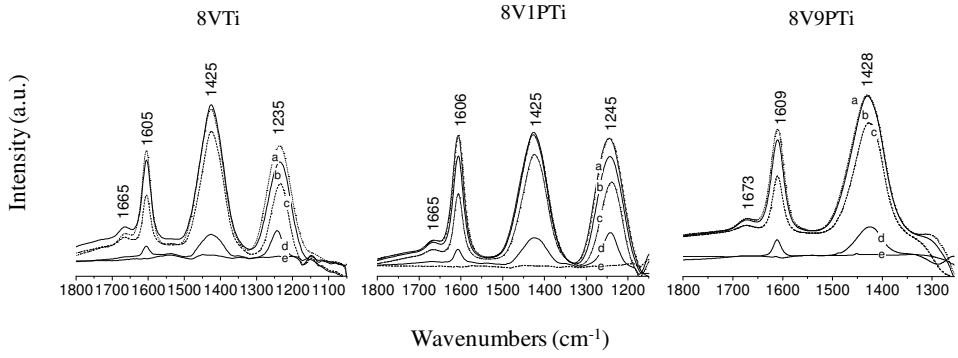

Figure 6.5 FT-IR Spectra of NH_3 adsorbed on 8VTi, 8V1PTi and 8V9PTi after evacuation at room temperature (a), at 50 °C (b), at 100 °C (c), at 200 °C (d) and at 300 °C (e)

The same scenario is observed for phosphorus doped titania-supported vanadium catalyst (8V1PTi), but a shift to higher frequencies is observed for the band at 1235 cm^{-1} (Lewis acid sites), which indicates a difference in the strength of the coordination bond. Moreover, higher amounts of phosphorus additive (8V9PTi) cause a general shift to higher frequencies of the bands characteristic of ammonia chemisorbed on Lewis acid sites and of ammonium cations on the

Brønsted sites. This is due to the higher electronegativity of phosphorus compared to vanadium, which causes the polarization of the V-(O-P) moiety and by an inductive effect, which enhances the Lewis acid strength of vanadium sites [25]. The band at ca. 1235 cm^{-1} was not detected because of the skeletal pyrophosphate absorption and the energy cut-off.

Desorption of adsorbed ammonia species from alumina-supported vanadium and alumina-supported vanadium and phosphorus catalysts is shown in Figure 6.6. The bands observed at ca. 1610 and 1200-1300 cm^{-1} are due to $\delta_{as}(NH_3)$ and $\delta_s(NH_3)$ modes of chemisorbed ammonia respectively (Lewis acid sites), while the Brønsted acid sites are represented by the bands at ca.1675 and 1430 cm^{-1} which are characteristic of $\delta_s(NH_4)$ and $\delta_{as}(NH_4)$ ammonium cations [26,27]. Similarly to titania-supported samples, both Brønsted and Lewis acid sites disappear during evacuation between 200 and 300 ^oC, indicating a medium-weak acid strength of these sites. The presence of phosphorus causes a positive shift of about 9 cm^{-1} for the bands at 1670, 1607 and 1425 cm^{-1} due to the higher electronegativity of phosphorus with respect to vanadium, while the band at 1252 cm^{-1} shifts 39 cm^{-1} which clearly indicates a difference in the strength of the coordination bond. This effect could not be observed for the previously presented 8V9PTi catalyst because of the skeletal pyrophosphate absorption and the energy cut-off in the region from 1300 cm^{-1}. However, as mentioned above, already a small addition of phosphorus (P/V=0.1) causes a shift of 10 cm^{-1} of the band at 1235 cm^{-1}.

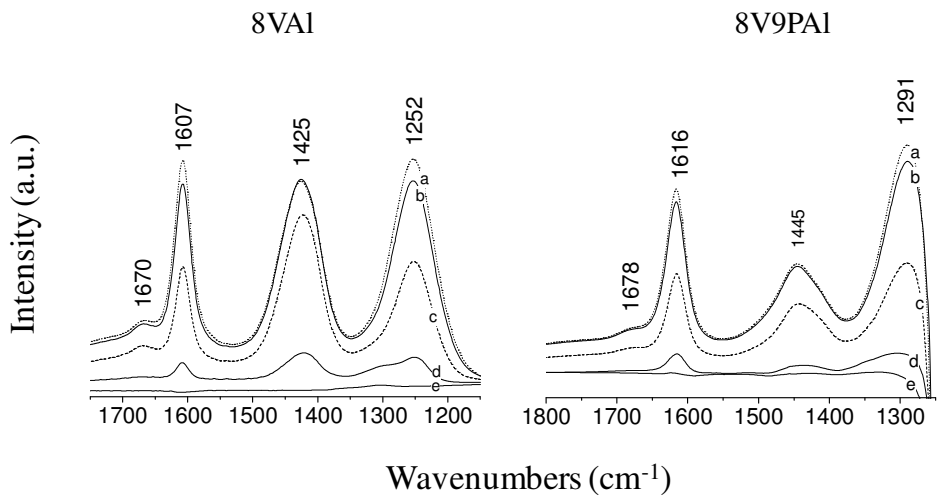

Figure 6.6 FT-IR Spectra of NH_3 adsorbed on 8VAl and 8V9PAl after evacuation at room temperature (a), at 50 ^oC (b), at 100 ^oC (c), at 200 ^oC (d) and at 300 ^oC (e)

Adsorption of small doses of ammonia (0.02-0.50 torr) at room temperature on the surface of 8V9PTi and 8V9PAl catalysts shows that the phosphorous addition favors ammonia adsorption on Lewis acid sites ($\delta_{as}(NH_3)$) while both Lewis and Brønsted acid sites ($\delta_{as}(NH_3)$ and $\delta_{as}(NH_4)$) are occupied in the case of the titania- and alumina-supported vanadium catalyst. The increase in strength of Lewis acid sites is already observed for phosphorus-doped catalysts (see Figure 6.8).

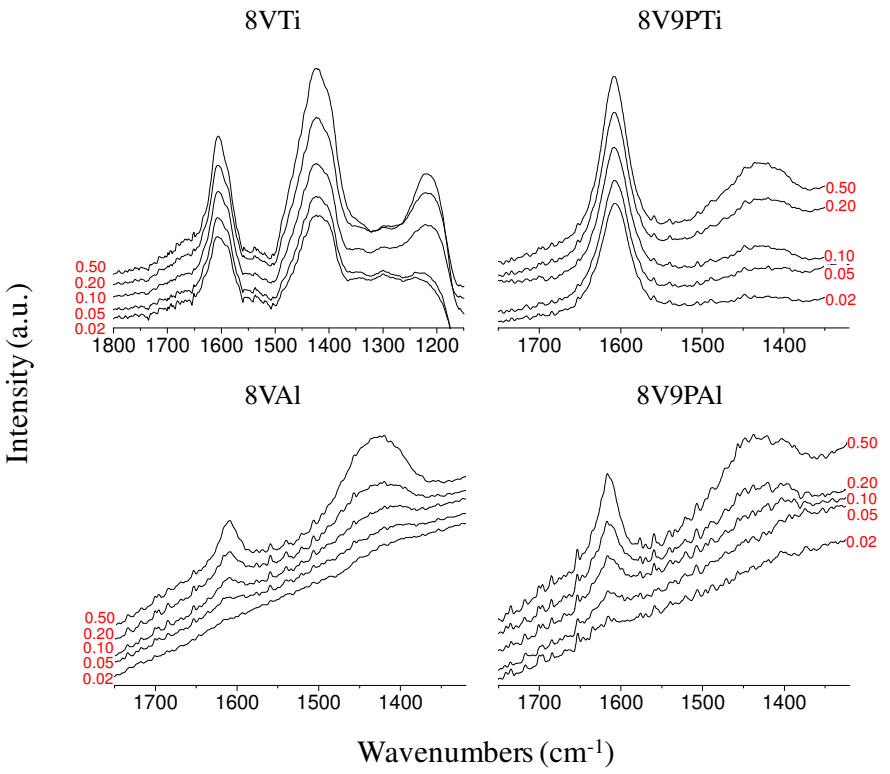

Figure 6.7 Adsorption of small doses of NH_3 (Torr indicated in the figure) on the surface of 8VAl, 8VTi, 8V8PAl and 8V8PTi

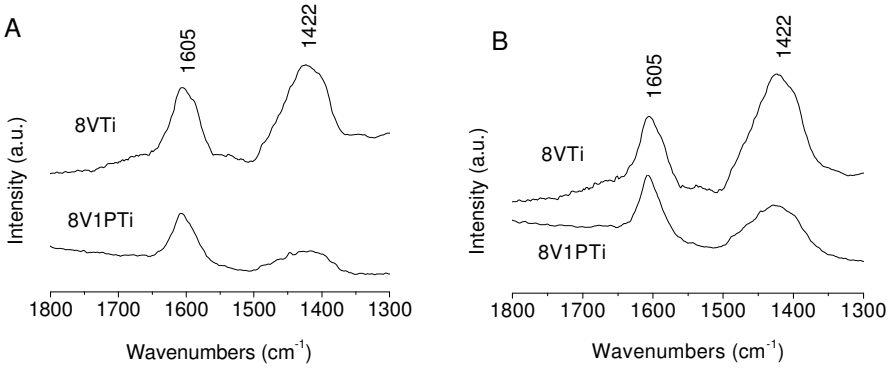

Figure 6.8 Adsorption of 0.1 (A) and 0.5 (B) Torr of NH_3 on the surface of 8VTi and 8V1PTi

Another effect caused by the presence of phosphorus in alumina- and titania-supported vanadium catalysts is a decrease of Brønsted acidity with respect to the Lewis acidity, which is related to the enhancement of the Lewis acid strength of vanadium in presence of phosphorus.

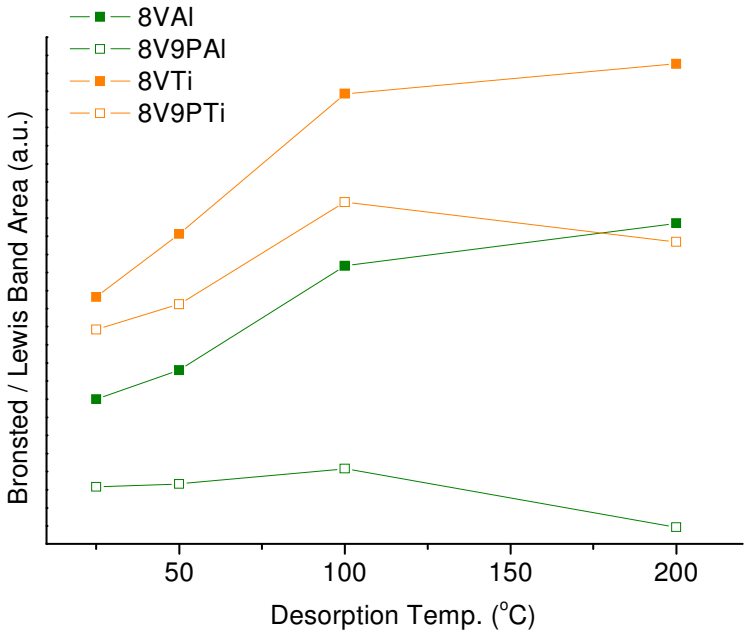

Figure 6.8 Decrease in Brønsted acidity in respect to Lewis sites as an effect of phosphorus addition and evacuation temperature

6.7 SUMMARY

Titania- and alumina-supported vanadium and phosphorus catalysts were characterized in this chapter. XRD and Raman show that in general no crystalline phases were detected on the catalysts support, and the H_2-TPR study confirms an interaction between vanadium and phosphorus moieties. The results show that phosphorus stabilizes V^{4+} species, moderating further reduction of vanadium species to V^{3+}. *In situ* FT-IR studies demonstrate that phosphorus has strong influence to the polarization of the V-(O-P) moiety, the coordination bond and the acidity of the catalysts surface. Moreover, the phosphorus effect was observed already for the samples with the P/V ratio of 0.1.

References

[1] J.-M. Jehng, I. E. Wachs, *Catal. Lett.* 13 (1992) 9

[2] J.-M. Jehng, G. Deo, B. M. Weckhuysen, I. E. Wachs, *J. Mol. Catal*. 110 (1996) 41

[3] I. E. Wachs, J-M. Jehng, G. Deo, B. M. Weckhuysen, V. V. Guliants, J. B. Benziger, *Catal. Today* 32 (1996) 47

[4] Z. Wu, P. C. Stair, S. Rugmini, S. D. Jackson, *J. Phys. Chem. C* 111 (2007) 16460

[5] D. E. Keller, F. M. F. de Groot, D. C. Koningsberger, B. M. Weckhuysen, *J. Phys. Chem.B* 109 (2005) 10223

[6] G. T. Went, L.-J. Leu, A. T. Bell, *J. Catal.* 134 (1992) 479

[7] T. Ohsaka, *J. Phys. Soc. Jpn*. 48 (1980) 1661

[8] G. N. Kryukova, G. A. Zenkovets, G. Mestl, R. Schlögl, *React. Kinet. Catal. Lett.* 80 (2003) 161

[9] Z. Wu, H.-S. Kim, P. C. Stair, S. Rugmini, S. D. Jackson, *J. Phys. Chem. B* 109 (2005) 2793

[10] A. Haoudi, P. Dhamelincourt, A. Mazzah, M. Drahe, P. Conflant, *Internat. J. Inorg. Mater*. 3 (2001) 357

[11] S. Xie, E. Iglesia, A.T. Bell, *Langmuir* 16 (2000) 7162

[12] M. V. Martínez-Huerta, J. L. G. Fierro, M. A. Bañares, *Catal. Commun.*11 (2009) 15

[13] P. Knotek, L. Čapek, R. Bulánek, J. Adam, *Topics Catal.* 45 (2007) 51

[14] R. P. Singh, M. A. Bañares, G. Deo, *J. Catal.* 233 (2005) 388

[15] F. Close, T. Wolff, H. Lorenz, A. Seidel-Morgenstern, Y. Suchorski, M. Piórkowska, H. Weiss, *J. Catal.* 247 (2007) 176

[16] L. Savary, J. Saussey, G. Costentin, M.M. Bettahar, M. Gubelmann-Bonneau, J.C. Lavalley, *Catal. Today* 32 (1996) 57

[17] R.A. Overbeek, P.A. Warringa, M.J.D. Crombag, L.M. Visser, A.J. van Dillen, J.W. Geus, *Appl. Catal. A* 135 (1996) 209

[18] F. Ben Abdelouahab, R. Olier, N. Guilhaume, F. Lefebvre, J.C. Volta, *J. Catal*. 134 (1992) 151

[19] G. Ramis, G. Busca, F. Bregani, P. Forzatti, *Appl. Catal. A* 64 (1990) 259

[20] S. Yamazoe, T. Okumura, Y. Hitomi, T. Shishido, T. Tanaka, *J. Phys. Chem*. 111 (2007) 11077

[21] G. Ramis, L. Yi, G. Busca, M. Turco, E. Kontur, R. J. Willey, *J. Catal*. 157 (1995) 523

[22] K. Hadjiivanov, *Appl. Surf. Sci*. 135 (1998) 331

[23] H. Zou, X. Ge, J. Shen, *Therm. Acta* 397 (2003) 81

[24] G. Centi, S. Perathoner, *J. Catal*. 142 (1983) 84

[25] G. Busca, G. Centi, F. Trifiró, V. Lorenzelli, *J. Phys. Chem*. 90 (1986) 1337.

[26] G. Centi, S. Perathoner, *J. Catal*. 142 (1983) 84

[27] G. Busca, G. Centi, F. Trifiró, V. Lorenzelli, *J. Phys. Chem*. 90 (1986) 1337

7

Propane ammoxidation reaction

7.1 INTRODUCTION

The TPR, XAS, UV-Vis and XPS analyses confirm the predominance of V^{5+} in supported VPO catalysts. This suggests that the interaction of VPO with alumina support results in a higher dispersion degree of V^{5+} species or that the surface of VPO materials is essentially constituted by V^{5+} species. The bulk VPO catalyst exhibits mainly V^{4+}species. However, since the analytical techniques for determination of the vanadium oxidation state in the industrial VPO are not surface selective, the evaluation of the surface vanadium oxidation state becomes complicated. The presence of V^{5+} species on fresh VPO catalysts was detected by Raman spectroscopy, but it was shown that these phases decompose rapidly upon use in propane ammoxidation reaction conditions. Low amount of V^{5+} in bulk VPO catalyst was also detected by HR-XPS technique (ca. 20%). Changes in vanadium oxidation state will significantly affect catalytic properties of the material. The VPO catalysts are attractive for selective oxidation processes, since they are active, inexpensive and relatively environmentally friendly. Supported VPO catalysts have already been studied for *n*-butane oxidation, as well as for ammoxidation of aromatic compounds. In this chapter the propane ammoxidation reaction over V-Al, P-Al, VP-Al and bulk VPO materials will be studied in order to determine the structure-activity relationships. *Operando* Raman-GC studies were performed on low-coverage supported VPO catalyst to follow the structural changes of the outermost VPO layers.

7.2 Performance of bulk and alumina-supported VPO catalysts in propane ammoxidation reaction

Bulk and alumina-supported VPO catalysts were studied for the conversion of propane into acrylonitrile, which is the main raw material for production of synthetic fibers, plastics, elastomers and polymers as styrene-acrylonitrile and acrylonitrile-butadiene-styrene. By polymerization of acrylonitrile with butadiene synthetic rubber is produced.

Figure 7.1 illustrates the catalytic performance of alumina, bulk VPO, P-Al, V-Al and VP-Al catalytic oxide materials in the propane ammoxidation reaction to acrylonitrile. The alumina support, as well as the individual phosphorus or vanadium supported on alumina, are hardly selective in acrylonitrile formation. However, when both, phosphorous and vanadium, are supported on alumina, the yield to acrylonitrile approaches 46 % at 500 ^{o}C. This indicates that the interaction between vanadium and phosphorus is necessary for acrylonitrile formation. Alumina-supported VPO is significantly more active than the bulk VPO, which is probably related to higher population of V^{5+} species stabilized by the alumina support, since V^{5+} species are responsible for activation of hydrocarbons [[1,2]]. Moreover, propane conversion decreases with increasing P/V ratio in VPO-type catalysts (8V8PAl = 16V16PAl < 8V9PAl < VPO). This is particularly observed at lower temperatures (<450 ^{o}C) and is probably related to the stabilization of V^{4+} species by phosphorus and a decrease in the population of V^{5+} surface species.

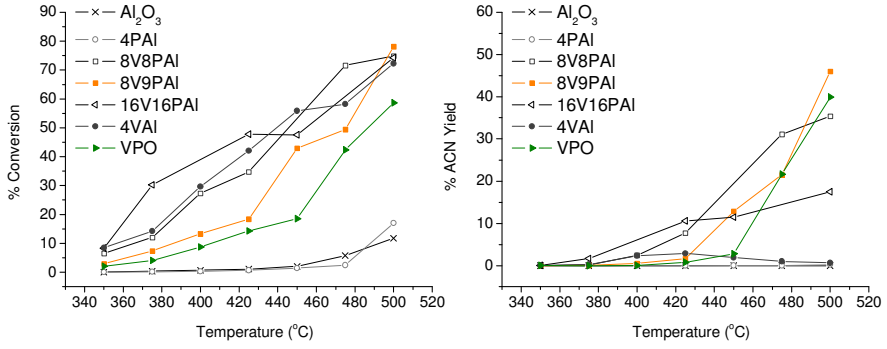

Figure 7.1 Propane conversion (left) and yield to acrylonitrile (right) for γ-Al_2O_3, VPO catalyst and alumina-supported vanadium and phosphorus catalysts. Total flow of 20 ml min^{-1}: 25% of O_2; 9.8% of C_3H_8; 8.6% of NH_3 and 56.6% of He, 0.2 g of catalyst

The 16V16PAl is the most active catalyst at lower temperatures, which is probably connected to higher number of active vanadium sites or lower V^{4+}/V^{5+} ratio.

The activity of bulk and supported VPO catalyst in the 350 to 500 °C temperature range is presented in Figure 7.2. As expected, propane conversion increases with reaction temperature and the yield shifts from propylene and acetonitrile (up to 450 ºC) towards acrylonitrile with the temperature increase (> 450 ºC). Bulk VPO catalyst is more selective to acrylonitrile. However, due to the lower propane conversion if compared to the alumina-supported VPO catalyst (8V9PAl), the yield to acrylonitrile is lower. Formation of acrylonitrile requires lower temperature in case of 8V9PAl catalyst, but more acetonitrile is formed indicating breaking of propane molecule, which is probably related to the higher activity of the supported VPO catalyst.

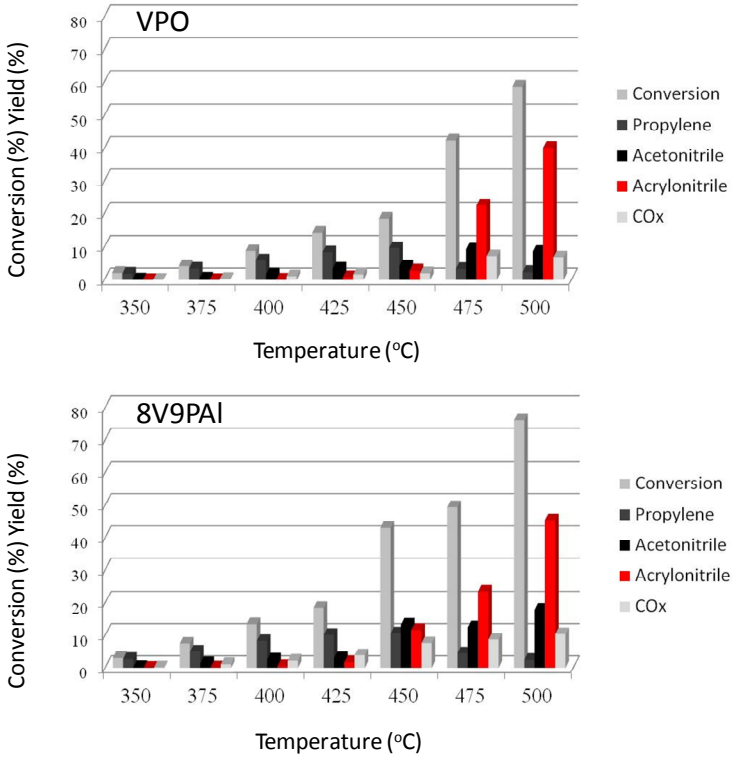

Figure 7.2 Catalytic properties of bulk and alumina-supported VPO catalysts in propane ammoxidation reaction. Total flow of 20 ml min^{-1}: 25% of O_2; 9.8% of C_3H_8; 8.6% of NH_3 and 56.6% of He, 0.2 g of catalyst

The catalytic properties of materials for propane ammoxidation reaction at 500 ^{o}C are presented in Figure 7.3. The 8V9PAl catalyst appears to be the best material for acrylonitrile production under current reaction conditions, even though it forms more by-products than the bulk VPO catalyst. Acetonitrile becomes the main reaction product in case of 4VAl (no phosphorus addition). This indicates that formation of acetonitrile is probably related to supported V^{5+} species and that no V-P interaction is required. In general, the increase of the P/V ratio causes a decrease in acetonitrile formation and higher yields of acrylonitrile are obtained. However, the 16V16PAl seems to be an exception of this case, which means that most likely another factor than P/V ratio (loading or V^{4+}/V^{5+} ratio) direct the reaction towards acetonitrile in this case. Thus, spent catalysts were analyzed by XRD and Raman spectroscopy in order to follow possible structural changes that may occur during reaction.

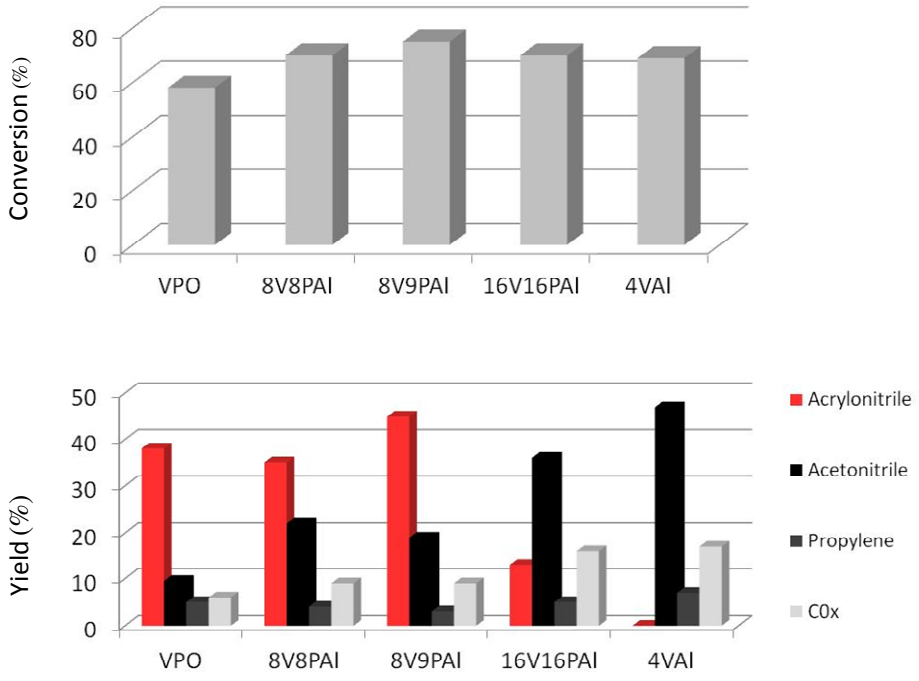

Figure 7.3 Catalytic properties of bulk VPO and alumina-supported vanadium and phosphorus catalysts in propane ammoxidation reaction at 500 ^{o}C (total flow of 20 ml min^{-1}: 25% of O_2; 9.8% of C_3H_8; 8.6% of NH_3 and 56.6% of He, 0.2 g of catalyst)

7.3 Characterization of catalysts used in propane ammoxidation reaction

The V+P loading effect on alumina-supported catalysts is presented in Figure 7.4. Formation of amorphous species was observed for fresh catalysts and a rise of baseline of the diffractogram in the 20 and 35^{o} 2θ range. However, the XRD patterns of spent catalysts after 4 hours running propane ammoxidation show that crystalline phases form for catalysts possessing V+P loadings of 2 or 4 monolayers. One monolayer of V+P was not enough for formation of XRD detectable crystalline phases. The X-ray diffractogram of 16V16PAl demonstrates formation of crystallites of vanadyl pyrophosphate. According to the peak intensity, two $(VO)_2P_2O_7$ phases with different cell volume were detected. The diffractograms of 8V8PAl shows an additional peak at ca. 26.5^{o} 2θ. Figure 7.5 demonstrates the X-ray diffractograms of fresh and used VPO and 8V9PAl catalysts. The formation of a new phase becomes apparent for 8V9PAl after use in the propane ammoxidation. The XRD pattern shows diffraction peaks near 2θ = 28.36^{o}, which is the most intense peak of vanadium pyrophosphate. Also, peaks at 2θ = 21.26^{o} and 22.35^{o} are characteristic for this phase, but with different cell volume. The broad peak at 2θ = 20.49 ^{o} may indicate formation of Al-P-V-O phases. Finally, the diffraction peak at 26.46 º along with the peak at 28.48 may be characterized as β-$V^{5+}OPO_4$ phase [3] or as vanadyl hydrogen phosphate phase ($V^{4+}OHPO_4$). This indicates complications for detailed peak assignment in case of supported VPO-type catalysts based only on XRD measurements, which is mainly due to the low number of the XRD lines, probably characteristic of various VPO phases. Moreover, a broad baseline is observed for spent supported VPO-type catalysts due to amorphous phases. Small size of crystallites as well as formation of distorted VPO phases on the alumina support may cause the above mentioned difficulties. Finally, no changes were evident in the diffractogram of used bulk VPO catalyst after 4 hours on stream.

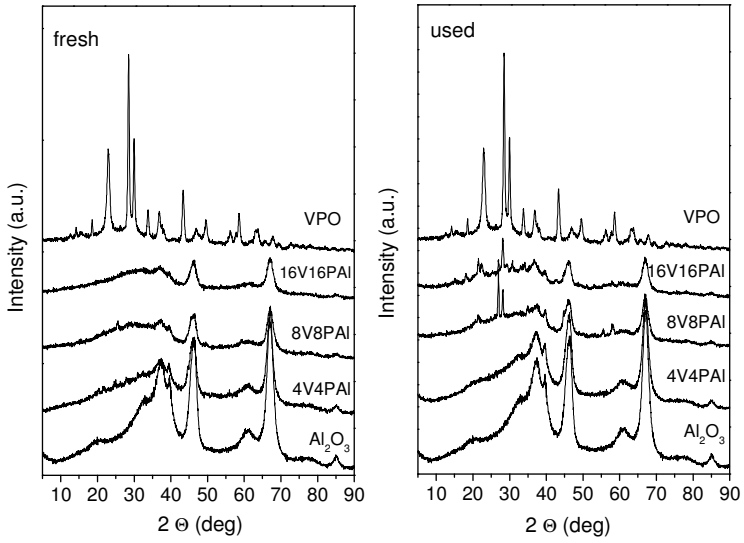

Figure 7.4 Formation of crystalline VPO phases on alumina support after propane ammoxidation reaction followed by XRD

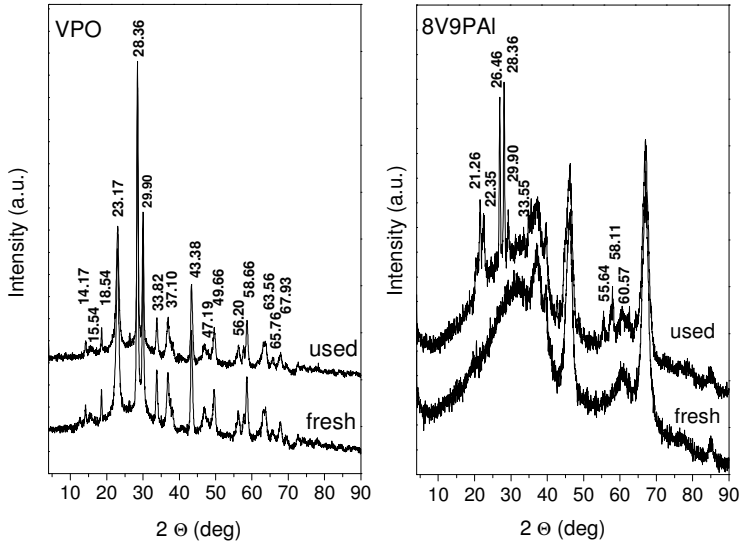

Figure 7.5 Powder XRD patterns of fresh and used VPO (left) and 8V9PAl (right) catalysts

The XRD technique is sensitive to crystallites larger than ca. 4Å, but formation of smaller crystallites or structural changes in amorphous V-P-O phases are expected as a result of exposure of the catalysts to the reaction conditions. Thus fresh and used catalysts were also characterized by Raman spectroscopy. According to literature, alumina-supported vanadium monolayer type catalysts exhibit Raman features below 400 cm^{-1}, which are due to the bending modes of V-O-V groups. The asymmetric and symmetric stretching modes of these bands appear in a 450-850 cm^{-1} range, while the terminal V=O bond may be found above 850 cm^{-1} [4]. The bending O-V-O bands were found at 340 cm^{-1} for $V_2O_5/AlO_x/SiO_2$ or V_2O_5/ZSM-5 catalysts [5,6]. The symmetric V-O-V stretch of polymerized VO_4 species existed at ca. 530 cm^{-1} and the asymmetric V-O-V appeared at ca. 835 cm^{-1}. A weak Raman bands at ca. 700 or 900 cm^{-1} would correspond to V-O-support modes, while the terminal symmetric V=O stretch was detected at ca. 1035 cm^{-1}. For characterization of phosphorus oxides by Raman spectroscopy the characteristic region of Raman spectra is usually restricted to 600-1500 cm^{-1} range. In the 300-600 cm^{-1} region low intense bands are observed due to complicated internal vibrations of phosphate chains or PO_3 deformation vibrations of pyrophosphate groups [7,8,9]. Phosphorus supported alumina catalysts exhibit Raman band between 1000-1200 cm^{-1} due to the terminal P=O stretch, while the bending P=O bond appears at 375-500 cm^{-1} range. However, the position of the P=O bond strongly depends on the structure of the phosphate compound. The P_4O_{10} possesses very short P=O bond and thus the Raman feature related to this stretch appears at ca. 1440 cm^{-1} [10]. The P=O bond of $Bi_{24}P_2O_{40}$ was detected at 905 cm^{-1} [11], while the metaphosphate chains of $NaPO_3$ or KPO_3 exhibit the P=O bond in a range between 1087-1285 cm^{-1} [12]. The Raman spectrum of $P_2O_7^{4-}$ (aq) ions has a strong P=O stretch at 1020 cm^{-1} and two weaker modes at 1097 and 1128 cm^{-1} [13]. Finally, the P-OH bonds may be found at ca 800-900 cm^{-1} [14,15,16], the P-O stretch at 615-763 cm^{-1} and P-O-P bending modes at ca. 200-350 cm^{-1}. Vanadium and phosphorus containing glasses were also characterized by Raman spectroscopy [17,18]. It was reported that for these amorphous materials, a broad Raman band at 1257 cm^{-1} is due to the terminal P=O stretch. The P-O-P symmetric stretching vibrations appear at ca. 670 cm^{-1} and the band at 1173 cm^{-1} was assigned to O-P-O symmetric stretching vibrations with non bridging oxygen (Q^2 symmetry) [19].The band at 997 cm^{-1} was reported to be due to P-O-P bonds of $(P_2O_7)^{4-}$ or to the V=O terminal vibration, while bands at 422 and 490 cm^{-1} were characterized as bending modes of VO_4 and PO_4 respectively [20]. When V_2O_5 is added to phosphate glasses more ionic V-O-P bonds are expected to form as a result of depolymerization of phosphate chains [21]. Thus, due to the progressive

depolymerization of the phosphate network Raman bands at ca. 665 and 997 were assigned to P-O-P of $(PO_4)^{3-}$ or $(P_2O_7)^{4-}$ respectively.

Figures 7.6 and 7.7 show Raman spectra of dehydrated fresh and used catalysts. As described in Chapter 3, decomposition of V_2O_5 is observed after propane ammoxidation reaction for bulk VPO catalyst. The alumina-supported VPO are presented in figure 7.7. Fresh catalysts exhibit Raman bands at 1120, 1021, 935, 490 and 350 cm^{-1}. The Raman band at 1120 cm^{-1} is probably due to P=O terminal stretch. The band at 1021 cm^{-1} is characteristic of terminal V=O vibration of vanadium surface species, while the band at 935 cm^{-1} may be due to V-O-M bonds, where M is either V or Al overlapping with polyphosphoric acid [22]. The bands at 490 and 350 cm^{-1} are characteristic of bending modes of PO_4 and VO_4 respectively. From the Figure 7.7B it may be observed that crystalline phases form as a result of propane ammoxidation reaction. Aged alumina-supported VPO-type catalysts exhibit new Raman bands, essentially a sharper band at 927 cm^{-1}, which is due to the vanadium pyrophosphate phase; in particular, Feng et al. have assigned Raman band at 928 cm^{-1} to asymmetric P-O-P vibrations of $P_2O_7^{2-}$ of vanadium pyrophosphate phase [23]. Additionally the 8V8PAl and 8V9PAl exhibit Raman features at 1295, 1100, 850 and 360 cm^{-1}. The bands at 1295 and 1100 are probably due to the terminal P=O stretch. A low intense band at 1020 cm^{-1} is also detected, which may be characteristic of the terminal V=O vibration. However, more likely, this band along with the broader band at 1100 cm^{-1}, which probably consists of bands at ca. 1097 and 1128 cm^{-1} are due to the terminal P=O bond of pyrophosphate species. The band at 850 cm^{-1} may be characterized as P-OH vibration modes and the band at 360 cm^{-1} as P=O or O-V-O bending modes.

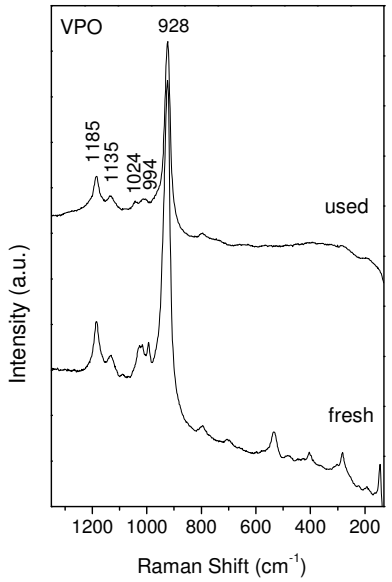

Figure 7.6 Fresh (bottom) and used in propane ammoxidation reaction (top) VPO catalyst. Excitation Ar line: 514 nm

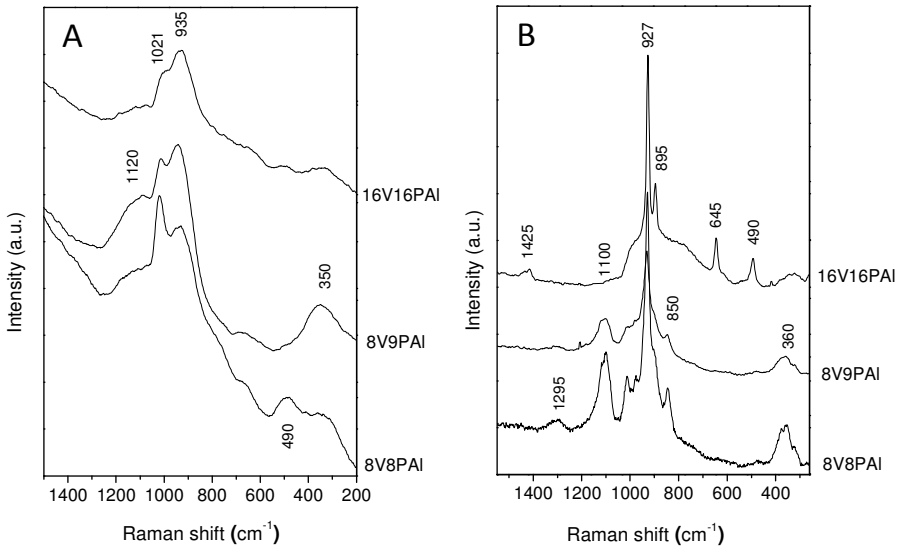

Figure 7.7 Raman spectra of fresh (A) and used in propane ammoxidation reaction (B) alumina-supported VPO catalysts. Excitation Ar line: 514 nm

The Raman spectrum of 16V16PAl differs from those of 8V8PAl and 8V9PAl probably due to higher V+P loading. No Raman band at 1100 cm^{-1} is observed, but a new band at 1425 cm^{-1} appears. This band is probably still characteristic of the P=O bond, but its shift to higher frequencies indicates that it is significantly shorter compared to those of 8V8PAl and 8V9PAl. Probably a phase closer to P_4O_{10} is formed. Bands at 895 and 645 cm^{-1} may be due to P-OH and P-O-P or V-O-V modes respectively, while the band at 490 cm^{-1} is probably characteristic of the PO_4 bending modes. However, the latter three bands may indicate formation of distorted $VOPO_4$ phases (i.e. β-$VOPO_4$) evidencing presence of V^{5+} species. These bands were not observed for catalysts containing two monolayers of V+P, which would be in agreement with their higher selectivity to acrylonitrile if compared to the 16V16PAl catalyst.

Recently, Cavani et al. reported that the divergence in the literature related to VPO catalysts is due to the fact that *ex-situ* measurements are not only a function of the VPO nature, but also of the reaction conditions [[24]]. The supported 8V9PAl catalyst was chosen for evaluation of reaction conditions, specifically of the activation process. Conventional activation process by calcination in inert (preactivated 8V9PAl) was compared with activation during reaction conditions (precursor 8V9PAl). The structural differences of the surface species caused by the different activation procedures are shown in Figure 7.8. Raman spectra of the preactivated and the precursor 8V9PAl obtained at the end of the time-on-stream measurements at 500 ^oC after 60 h demonstrate essentially the same Raman features at 870, 933, 1022, 1036 and 1136 cm^{-1}, but their relative intensity is different (see Figure 7.8B). The difference in intensity of Raman spectra acquired under reaction conditions seems to be important since the Raman spectra of the used preactivated 8V9PAl and precursor 8V9PAl catalysts differ significantly. These spectra were taken at different spots in ambient conditions after the catalytic test, so that the spent catalysts were exposed to air. Representative Raman spectra of the used catalysts are shown in figure 7.8A and C. Different Raman spectra were obtained for the same catalyst when taken on stream or after the catalytic test.

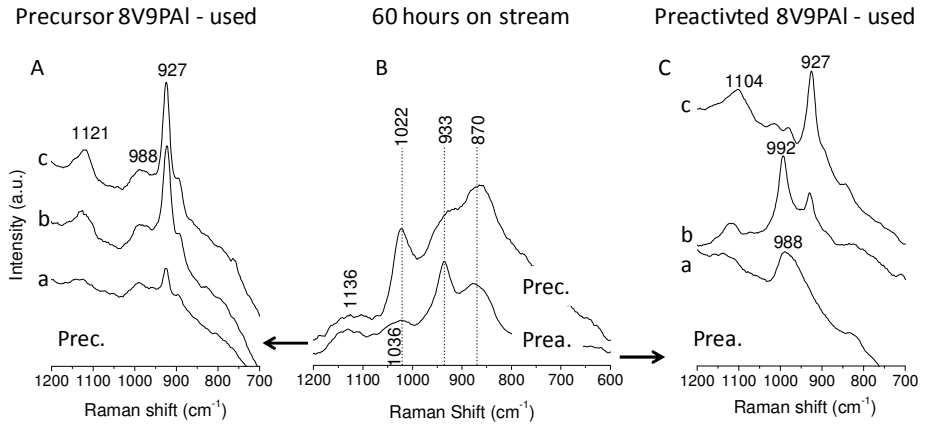

Figure 7.8 Raman spectra of precursor 8V9PAl (Prec.) and preactivated 8V9PAl (Prea.) acquired during propane ammoxidation reaction at 500 ^{o}C after 60 hours on stream (B), and representative Raman spectra of precursor 8V9PAl (A) and preactivated 8V9PAl (C) taken under ambient conditions (sample exposed to air at room temperature) after the catalytic test. Excitation Ar line: 514 nm, reaction conditions: total flow of 20 ml min^{-1}: 25% of O_2; 9.8% of C_3H_8; 8.6% of NH_3 and 56.6% of He, 0.2 g of catalyst

The Raman spectra at three representative spots of used precursor 8V9PAl show essentially one Raman feature at 927 cm^{-1} characteristic of $(VO)_2P_2O_7$, which presence during reaction is unclear (Figure 7.8A). Fig. 7.8C shows three representative spots of used preactivated 8V9PAl, which is significantly less homogeneous than its counterpart. Spectrum 7.7Ca shows a broad Raman feature at 988 cm^{-1}, probably due to the amorphous $V^{+4}OHPO_4$ phase. The Raman band at 993 cm^{-1} in spectrum 7.8Cb with no Raman band at 143 cm^{-1} (not shown) rules out the possible presence of crystalline V_2O_5. Thus, this band is probably due to a slightly crystalline $VOHPO_4$ phase, which would be in agreement with the XRD patterns of the used catalyst (see Figure 7.9B). Some $(VO)_2P_2O_7$ is also apparent at this spot. The Raman spectrum 7.8Cc is similar to those presented for precursor 8V9PAl with characteristic bands of $(VO)_2P_2O_7$.

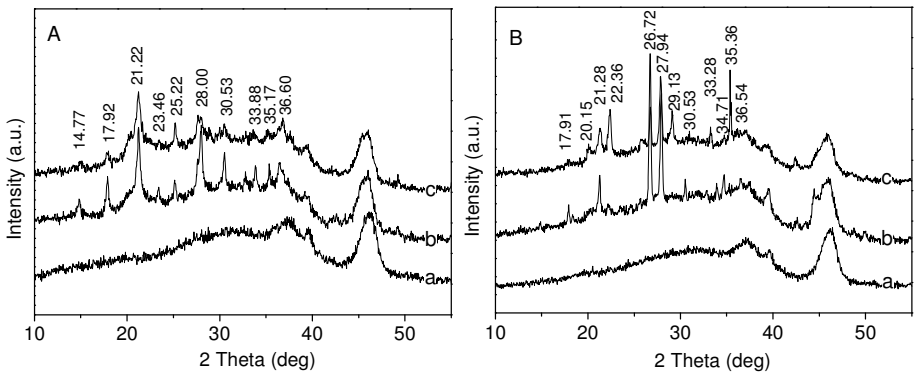

Figure 7.9 XRD patterns of precursor 8V9PAl (A) and preactivated 8V9PAl (B): fresh (a), after 4 hours on stream (b), after 60 hours on stream at 500 ^{o}C (c). Total flow of 20 ml min^{-1}: 25% of O_2; 9.8% of C_3H_8; 8.6% of NH_3 and 56.6% of He, 0.2 g of catalyst

Figure 7.9 illustrates the XRD patterns of the precursor and preactivated 8V9PAl catalysts, fresh, after use in reaction, and after extended use in reaction. The diffractograms of the precursor 8V9PAl in Figure 7.9A show that the pattern of the fresh catalyst is dominated by the alumina support. Formation of a new phase becomes apparent after use in propane ammoxidation, even for a short reaction time. The XRD pattern shows mainly diffraction peaks at 2θ near 14.77 (11), 17.92 (26), 21.22 (59), 28.00 (100), 30.53 (31), 33.88 (22) and 36.60 (32), characteristic of two similar vanadyl pyrophosphate phases differing in unit cell volume. After 60 hours on stream at 500 ^{o}C the same sample exhibits essentially the same diffraction peaks but less intense. The absence of crystalline phases in the XRD pattern of the fresh preactivated 8V9PAl (Fig. 7.9B) suggests formation of amorphous species on the alumina support, while the pattern of the catalyst after use in the ammoxidation reaction exhibits diffraction peaks at 17.91 (10), 21.28 (24), 26.72 (100), 27.94 (70), 30.53 (9), 33.28 (6), 34.71 (12), 36.54 (7). The two main diffraction peaks at 26.72 and 27.94 2θ are probably characteristic of $VOHPO_4$, while the peaks at 17.91, 21.28, 27.94, 30.53, 33.28 and 36.54 2θ are due to the $(VO)_2P_2O_7$ phase. The vanadyl pyrophosphate phase became more apparent after extended exposure to reaction conditions demonstrating diffraction peaks at 17.91, 21.28, 22.36, 27.94, 29.13, 33.28, and 36.54 2θ. However, some slight shifts and intensity changes confirm the inherent diversity of the supported vanadyl pyrophosphate phase. Moreover, the support

seems to be affected, since the peak at 20.15 2θ is characteristic of Al–V–P–O phases and the diffraction line at 2θ = 35.36 suggests presence of corundum.

These results indicate that indeed, the *ex-situ* measurements are not relevant to the structure-activity relationships. Raman spectra and XRD patterns of spent catalysts show phases that are not observed under reaction conditions, i.e. crystalline $VOHPO_4$ for preactivated 8V9PAl or $(VO)_2P_2O_7$ for the 8V9PAl precursor. The absence of crystalline phases may be due to the thermal broadening, but this effect relates only to the preactivated 8V9PAl catalyst by increase in intensity of the band at 927 cm^{-1} with temperature decrease under reaction conditions. The precursor 8V9PAl does not show appearance of sharp bands during cooling down to room temperature on stream (spectra not shown). Thus alumina-supported VPO catalysts were tested using the *operando* Raman-GC methodology, which is very convenient to fully understand the structure and reactivity of VPO-like catalysts [25].

7.4 Structure-activity Relationships

Raman spectroscopy is a powerful technique to study structure changes during reaction, but some constrains apply for solid bulk catalysts. It is essentially a semi-bulk technique, and the surface structure cannot be directly evaluated in the presence of an overwhelming signal from the bulk. One approach to obtain surface-relevant information from bulk systems is to stabilize nanoscaled bulk oxides on a support [26,27]. Then the signal from the surface can be analyzed due to the significant decrease of the bulk signal. Typically, VPO loadings slightly above monolayer coverage on a support, will lead to incipient VPO particles (nanoscaled), and thus significantly enhance the surface-to-volume ratio. The support interaction stabilizes such particles, minimizing their sintering into larger particles during reaction. In turn, the support increases the population of molecularly dispersed V^{5+} species, which may be in equilibrium with (partially reduced) lattice vanadium sites in the nanoscaled phase. This is observed for alumina-supported nanoscaled $SbVO_4$ catalysts for propane ammoxidation [28] where this approach uncovered details on the redox cycle of vanadium species during propane ammoxidation. Bulk and supported VPO catalysts have been used for the ammoxidation of propane into acrylonitrile [29] but, to our knowledge, no *in-situ* or *operando* spectroscopic studies have been done yet to understand this process and the nature of active sites. Thus, in this chapter, we

report *operando* and *in situ* studies of alumina-supported nanoscaled VPO catalysts during propane ammoxidation reaction.

Figure 7.10 exhibits *operando* Raman-GC data of the precursor 8V9PAl while heating in reaction feed. The Raman feature at 1022 cm^{-1}, corresponding to the V=O stretch of the supported V^{5+} species, is observed in all of the temperature range investigated. A shoulder near 990 cm^{-1} appears at 475 ^{o}C and is replaced at 500 ºC by a Raman band near 923 cm^{-1}, which is probably due to P-O-P vibrations of the vanadium pyrophosphate phase [30]. The catalyst undergoes further transformation after 30 minutes at 500 ^{o}C, which triggers off the formation of a new broad band near 860 cm^{-1}, probably consisting of two features at 877 and 855 cm^{-1}. The appearance of a broad Raman band at 990 cm^{-1} (which cannot be assigned to crystalline V_2O_5 due to the absence of a stronger phonon near 145 cm^{-1}) results in a significant decrease in acrylonitrile selectivity, while the rearrangement into new Raman bands at 923 cm^{-1} and subsequently at 860 cm^{-1} restores acrylonitrile selectivity. This change in catalytic performance appears related to the rearrangement of vanadium and phosphorous species; the vanadium pyrophosphate (923 cm^{-1}) and the phase associated with the Raman band near 860 cm^{-1} (V_2O_7 [31] or the stretching vibrations or $P(OH)_2$ groups [22] according to the literature) promote acrylonitrile formation (selectivity raises to 40-50%). It is worth noting, that during early stages, at 425-450 ºC, acrylonitrile formation reaches appreciable selectivity. Acrylonitrile was formed already at 425 ^{o}C with rather high selectivity (ca. 40%), which is probably influenced by the presence of $(COOH)_2$ in the precursor catalyst. The DTA-TGA analysis in N_2 flow showed that the decomposition of oxalic acid is apparent in the 200-450 ^{o}C temperature range. These results suggested that the structure of supported VPO catalysts was stabilized at about 450 ^{o}C where no thermal or weight changes were apparent. The selectivity changes below 450 ^{o}C, may be related to the process of burning off the oxalic acid, even though no structural changes were observed by Raman spectroscopy. After reaching 500 ^{o}C, the catalyst was held on stream at this temperature for 60 hours. No new Raman bands were observed during the following 59 hours at 500 ^{o}C and the catalytic performance was also stable.

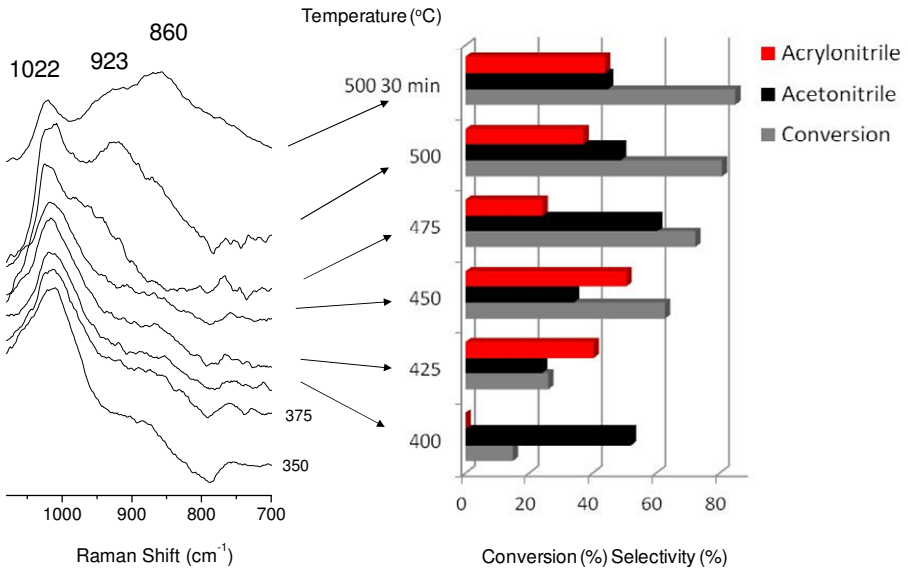

Figure 7.10 *Operando* Raman-GC study with product selectivities and propane conversion of precursor 8V9PAl catalyst during propane ammoxidation (total flow of 20 ml min^{-1}: 25% of O_2; 9.8% of C_3H_8; 8.6% of NH_3 and 56.6% of He, 0.2 g of catalyst, excitation Ar line: 514 nm)

Figure 7.11 shows the *operando* Raman-GC data of the thermally pretreated catalyst, 8V9PAl, as the reaction temperature increases. Raman spectra up to 475 ºC show essentially a band at 1022 cm^{-1} corresponding to the V=O bond, along with broad Raman features near 923 and 880 cm^{-1}. The former band is characteristic of the $(VO)_2P_2O_7$ phase or to V-O-Al vibrations, while the latter has been assigned to pyrovanadate moieties (V_2O_7) or to the stretching vibrations of P-OH groups, as mentioned before. At 500 ºC the Raman band at 1022 cm^{-1} decreases significantly in intensity and the Raman band at 923 cm^{-1} increases during time on stream. The selectivity towards nitriles increases with increasing temperature; it reaches ca. 50% acrylonitrile selectivity at ca. 70% propane conversion. Propylene is an intermediate in acrylonitrile formation from propane [32] so the catalyst transformations lead to a more efficient system for the reaction pathway; propane to propylene and its subsequent conversion to acrylonitrile. It should be noted that the selectivity to acetonitrile remains essentially unchanged (near 30% selectivity), so this side reaction is not directly affected by these structural changes of the catalyst. Thus, the selectivity to

products shifted from acetonitrile to acrylonitrile at 475 °C, just before the vanadyl pyrophosphate phase became apparent.

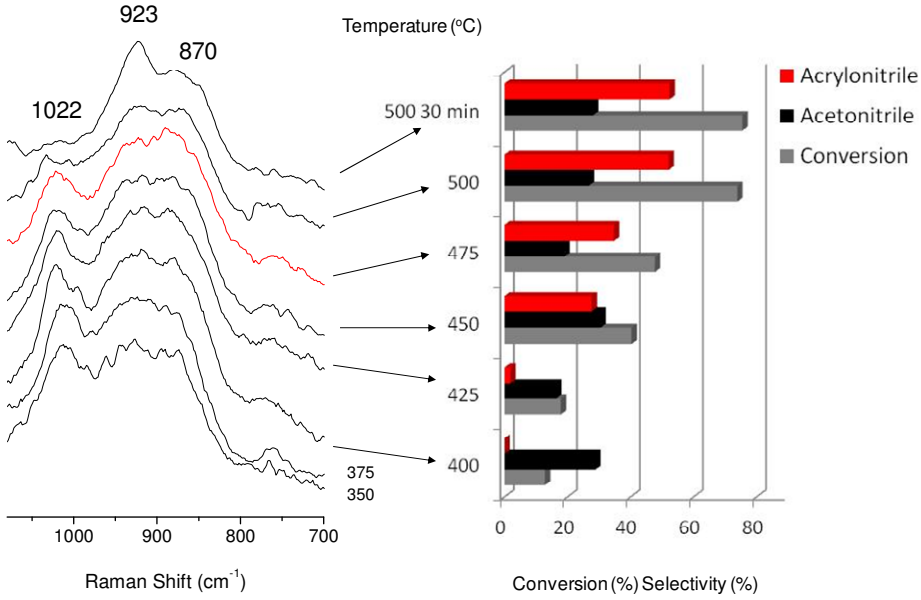

Figure 7.11 *Operando* Raman-GC study with product selectivities and propane conversion of preactivated 8V9PAl catalyst during propane ammoxidation (total flow of 20 ml min^{-1}: 25% of O_2; 9.8% of C_3H_8; 8.6% of NH_3 and 56.6% of He, 0.2 g of catalyst, excitation Ar line: 514 nm)

Figure 7.12 illustrates 60 h time-on-stream *operando* Raman-GC data of the preactivated 8V9PAl catalyst after it reaches 500 ºC in reaction, as described in Figure 7.10. Close to the end of the catalytic test the Raman band at 923 cm^{-1}, characteristic of vanadyl pyrophosphate becomes broader and shifts to 933 cm^{-1}, which may suggest coexistence of $VOPO_4$ phases. This is supported by the fact that traces of acrylic acid were detected at the same time, indicating NH_3 deficiency and, thus, lower reduction ability. The oxygen conversion at 500 °C was about 70%. Also, the intensity of the vanadyl pyrophosphate band changes, reaching its maximum in the 760-1500 minutes time range. These structural

transformations do not have much effect on the catalytic performance. Propane conversion remains essentially constant at 70-80% during 60 hours on stream. However, the selectivity to acrylonitrile slightly decreases.

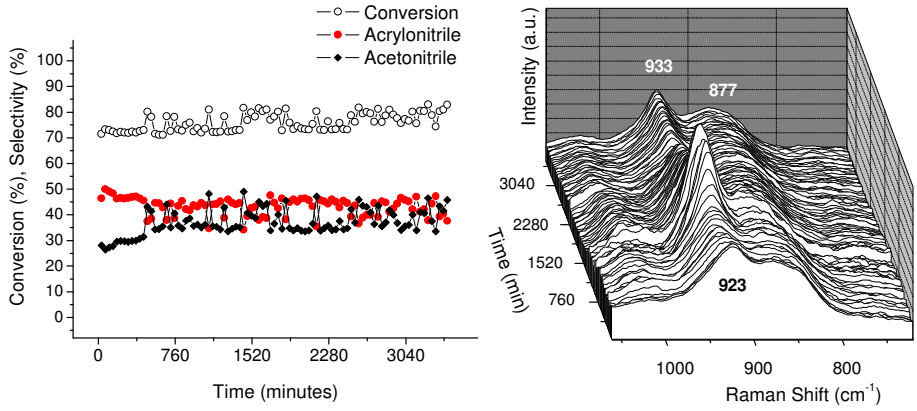

Figure 7.12 60 h time-on-stream at 500 °C *operando* Raman-GC study with selectivities to products and propane conversion of preactivated 8V9PAl catalyst during propane ammoxidation (total flow of 20 ml min^{-1}: 25% of O_2; 9.8% of C_3H_8; 8.6% of NH_3 and 56.6% of He, 0.2 g of catalyst, excitation Ar line: 514 nm)

To further assess the relevance of the reductive environment, the structural transformations of the precursor of 8V9PAl in reductive and oxidative atmosphere are shown in Figure 7.13. The experimental conditions are similar to those described in section 2.16.1 with the exception that the spectrum acquisition time was reduced to 150 seconds in order to increase the time-resolution. Heating to 500 °C at 20 °C min^{-1} in propane ammoxidation reaction feed generates two Raman features near 927 and 877 cm^{-1}. The former band increased in intensity in relation to the latter when the feed is switched to synthetic air at 300 °C (Figure 7.13c and d). The Raman band near 877 cm^{-1} disappears after ca. 30 min exposure to air at 300 ºC, while the intensity of the band characteristic of vanadyl pyrophosphate phase concomitantly increases.

Returning to the propane ammoxidation reaction feed at 300 ºC, has no significant effect on the catalyst structure, as determined by Raman spectroscopy. The band near 877 cm^{-1} is only restored after reaching 500 ºC as illustrated by the Raman spectrum in Figure 7.13g, which resembles that in Figure 7.13a. These results demonstrate that the Raman feature near 877 cm^{-1} appears in highly reductive atmosphere, while oxygen supply restores $(VO)_2P_2O_7$. This trend and its transformation into vanadyl pyrophosphate phase upon exposure to air (oxidizing conditions) suggest that this feature may be somehow related to a phase containing reduced V^{3+}. As a matter of fact, the formation of V^{3+} during catalytic cycles in bulk and alumina-supported VPO catalysts has already been reported for other ammoxidation reactions by Martin and co-workers [33,34].

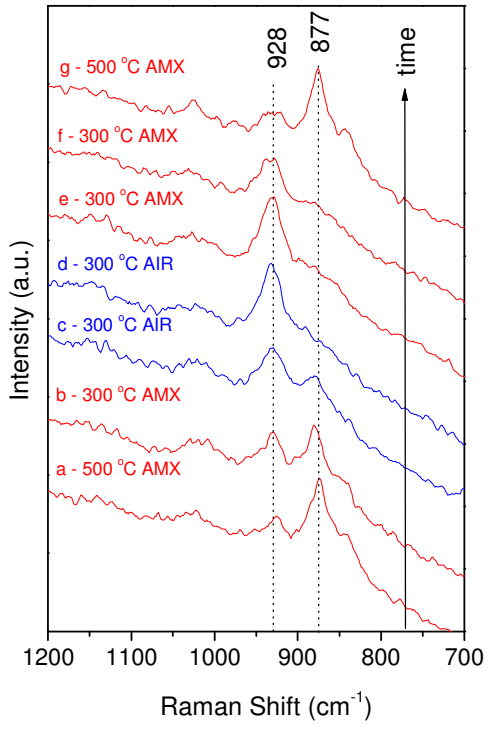

Figure 7.13 Raman spectra of precursor 8V9PAl during ammoxidation reaction and reoxidation process in the *operando* Raman cell. Structural transformations in reductive (AMX) and oxidative (AIR) atmosphere. Ammoxidation reaction conditions as indicated in Figure 7.12

The oxidation test was repeated at 500 ^{o}C and the relationships between structure and activity were studied. Figure 7.14 illustrates that the selectivity to acetonitrile and acrylonitrile stabilizes on stream at ca. 40%, when the Raman feature at 877 cm^{-1} is observed (Figure 7.14a). The sample is then oxidized in air flow at 500 ^{o}C for 30 minutes. Reoxidation at 500 ^{o}C does not lead to formation of the band at 927 cm^{-1}, but to overoxidation of the catalyst and formation of V_2O_5. After 30 min in air flow, the feed was switched back to the propane ammoxidation; crystalline V_2O_5 (spectrum b) is apparent; but also dispersed vanadium oxide species were detected. Only dispersed vanadium oxide species were present on the catalyst surface after 30 minutes under ammoxidation reaction conditions (Figure 7.14c). The selectivity to nitriles changed dramatically upon catalyst reoxidation (Fig 7.14 b, c). The oxidized sample was much more selective to acetonitrile than to acrylonitrile. The difference in selectivity became even stronger when no crystalline V_2O_5 was detected. When V_2O_5 crystallites are present on the surface, the conversion decreases according to lower accessibility of the active sites [35].

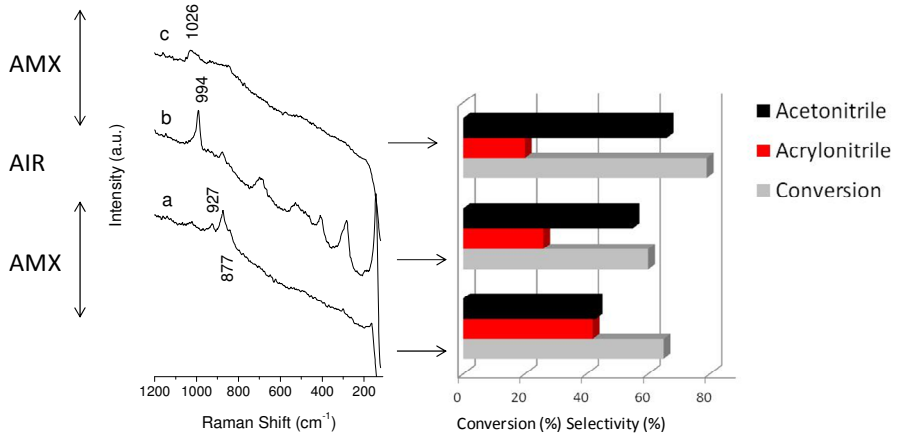

Figure 7.14 Left: *Operando* Raman-GC of propane ammoxidation reaction over the catalyst activated on stream at 500 ^{o}C (a) and subsequently oxidized in air at 500 ^{o}C for 30 min (b and c), laser: 514 nm. Right: Acrylonitrile selectivity and its relation to the formation of the active phase, (total flow of 20 ml min^{-1}: 25% of O_2; 9.8% of C_3H_8; 8.6% of NH_3 and 56.6% of He, 0.2 g of catalyst)

As it can be observed from Figures 7.10, 7.11, 7.12 and 7.14, the band at ca. 877 cm^{-1} may be related to acrylonitrile formation, since it is usually observed in Raman spectra when high selectivities to acrylonitrile are obtained. Deconvolution of Raman spectra of Figure 7.11 was done in order to suggest a relationship between transformations of surface species in reaction feed (see Figure 7.15). The deconvolution is depicted in the right panel of Figure 7.15, and their areas *vs*. reaction temperature are depicted in the left panel along with the simultaneously recorded conversion/selectivity data. The area of the Raman band at 1022 cm^{-1}, due to surface V^{5+} species, decreases with increasing reaction temperature during ammoxidation. This runs parallel to the decrease in propylene formation, and it is consistent with the relevance of molecularly dispersed vanadium oxide for propane oxidative dehydrogenation to propylene [[36,37]]. The loss of dispersed vanadium oxide species initially runs parallel to the formation of vanadyl pyrophosphate (927 cm^{-1}). The Raman band near 877 cm^{-1} exhibits an area trend complementary to that of vanadyl pyrophosphate, so that they are clearly interconnected and bound to the critical phase for propane ammoxidation. This phase transformation is bound to a clear selectivity shift from propylene formation to acrylonitrile formation. These trends also indicate that acetonitrile formation must follow a reaction pathway different to that for propylene and acrylonitrile, or it would not be affected by the above-mentioned structural transformations. The nature of the Raman band near 877 cm^{-1} is not clearly established, but a similar band has been observed in a study concerned reduced vanadium alumina catalysts [[38]]. In this work, Stair at al. reported that UV Raman is more powerful than conventional visible Raman for studies of reduced metal oxide catalysts. Authors assigned a band centered at ca. 870 cm^{-1}, observed with UV Raman during reduction by hydrogen of θ-Alumina-supported vanadium catalysts to V-O-V bonds of reduced V^{3+} species. The assignment was made basing on UV and visible Raman spectra of bulk VO_x references (V_2O_5, V_6O_{13}, VO_2 and V_2O_3). However, this band was not observed in visible Raman spectra, except for V_6O_{13}, which resulted in a feature at ca. 875 cm^{-1}.

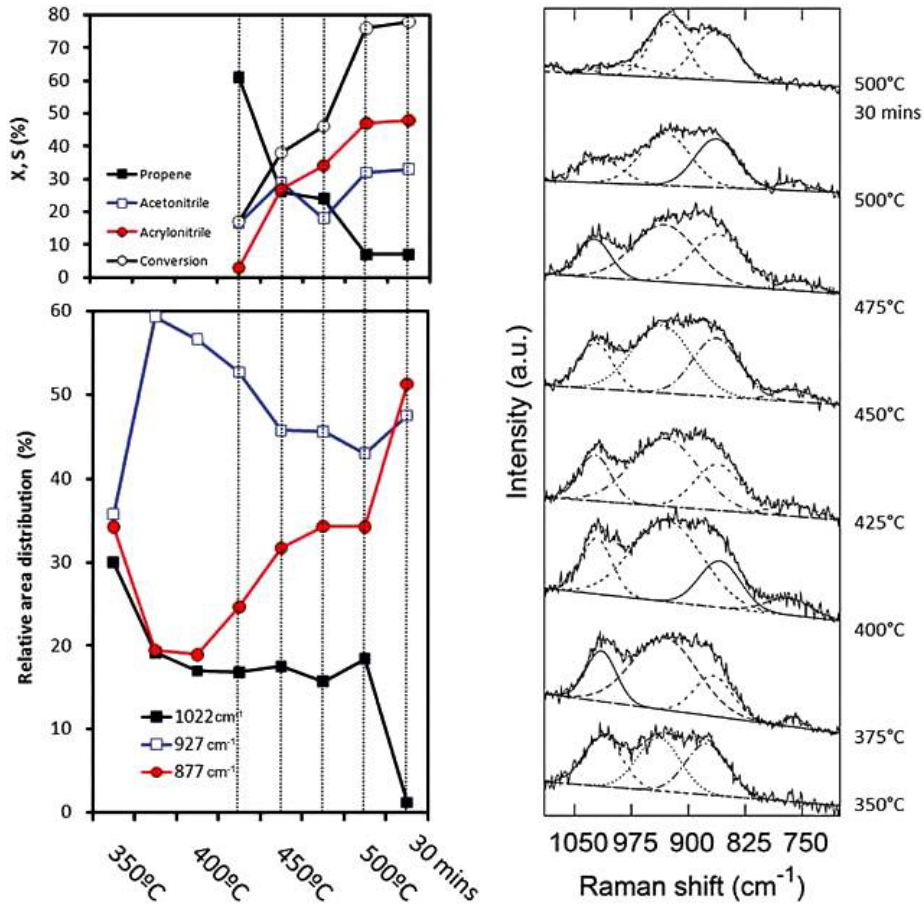

Figure 7.15 Deconvolution of 8V9PAl Raman spectra of an *operando* Raman-GC study during reaction and relation between Raman bands at 1022, 923 and 877 cm^{-1} with increasing temperature in propane ammoxidation flow (total flow of 20 ml min^{-1}: 25% of O_2; 9.8% of C_3H_8; 8.6% of NH_3 and 56.6% of He, 0.2 g of catalyst, excitation Ar line: 514 nm)

The laser excitation in the UV range is used to avoid fluorescence limitations [39,40,41]. Interestingly, the UV Raman spectra appear to be more sensitive not only to reduced vanadium species but also to the out-of-plane bending and symmetric stretching vibrations of bridging oxygen species (M-O-M), while the visible Raman spectra are more sensitive to the terminal oxygen vibrations (V=O) [6]. In order to obtain more complete characterization of the surface species of the 8V9PAl precursor under reaction conditions *in situ* UV Raman

experiment of propane ammoxidation reaction was performed at the *Operando Molecular Spectroscopy and Catalysis Laboratory* at Lehigh University. The nature of species related to the Raman feature at ca. 877 cm^{-1} was evaluated by comparison of the UV and visible Raman spectra.

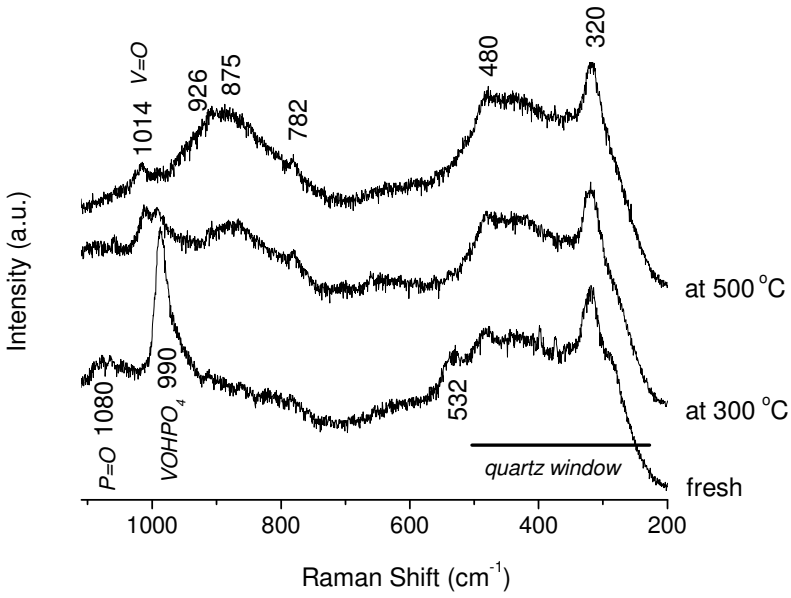

Figure 7.16 UV Raman spectra of precursor 8V9PAl catalyst under propane ammoxidation reaction conditions (UV excitation line: 325 nm, total flow of 36 ml/min: 4% O_2, 8% NH_3, 3% C_3H_8, 50 mg of catalyst)

The UV Raman spectra show essentially the same Raman features as the visible Raman spectra (1080, 1014, 926, 875 cm^{-1}), but the band at ca. 875 cm^{-1} is more intense. The increase in intensity of the band at ca. 875 cm^{-1} (and decrease in intensity of the band at 1014 cm^{-1}) suggest that it may be related to the M-O-M (where M is V, P or Al) bonds in polymeric surface species. However, no information about reduction state of vanadium was obtained by comparison of spectra acquired in UV or visible Raman, but the participation of reduced vanadium species in formation of polymeric moieties cannot be excluded.

The band at ca. 875 cm^{-1} was proposed to be characteristic of P-OH vibrations. Since the vibrational modes of atoms in a molecule can be described as harmonic oscillators associated with appropriate effective force constant and effective masses the approximate band positions of V-OH and P-OH were calculated using equations, which base on "mass effects" and isotopic substitutions [42]. For a simple diatomic molecule, the vibrational wavenumber is given by the equation 7.1:

$$\nu' = \frac{1}{2\pi c}\sqrt{\frac{K}{\mu}} = \frac{\nu}{c} = \frac{1}{\lambda} = \frac{\Delta E}{hc} \qquad \text{eq. 7.1}$$

where K is the force constant, μ is the reduced mass, c is the velocity of light, ν is the frequency, λ is the wavelength, h is Plank's constant, and ΔE is the energy difference between two states. For masses $m1$ and $m2$, the reduced mass, μ, is equal to $(m1 \cdot m2)/(m1 + m2)$, of the atoms involved. When one atomic species is substituted by another species of a different chemical nature, the ratio of the new to the old wavenumber is approximately equal to the square root of the inverse ratio of the reduced masses [43]. Thus, an increase in mass leads to decrease in wavenumber of the band position according to equation 7.2:

$$\frac{\tilde{\nu}}{\bar{\nu}'} = \sqrt{\frac{\mu\prime}{\mu}} \qquad \text{eq. 7.2}$$

The equation 7.2 was used for assignment of P-OH and V-OH bands positions. The Si-OH band was used as a reference, since its Raman position in 970-980 cm^{-1} range is well established in literature [44,45]. According to the equation 7.2 the P-OH bond may be expected at ca. 953 cm^{-1}. This value is higher to these reported in literature (850-900 cm^{-1}). The V-OH band should appear at ca. 886 cm^{-1}, which is close to 875 cm^{-1}. Thus, another *in situ* Raman experiment was performed in order to evaluate the possible assignment of the band at 877 cm^{-1} to V-OH or P-OH vibtations. In this case D_2O was introduced to the reaction cell during propane ammoxidation reaction at 530 ^oC. The catalyst was heated up to 530 ^oC in propane ammoxidation flow and held for 1 hour at this temperature.

Subsequently D_2O was introduced to the reaction flow for 2.5 hours and Raman spectra were taken every 5 minutes. If M-OH bands were present, a shift of Raman bands is expected due to substitution of M-OH by M-OD. However, no Raman shifts due to M-OD formation were observed even after 2.5 hours in D_2O flow indicating that no M-OH bands are present under these conditions.

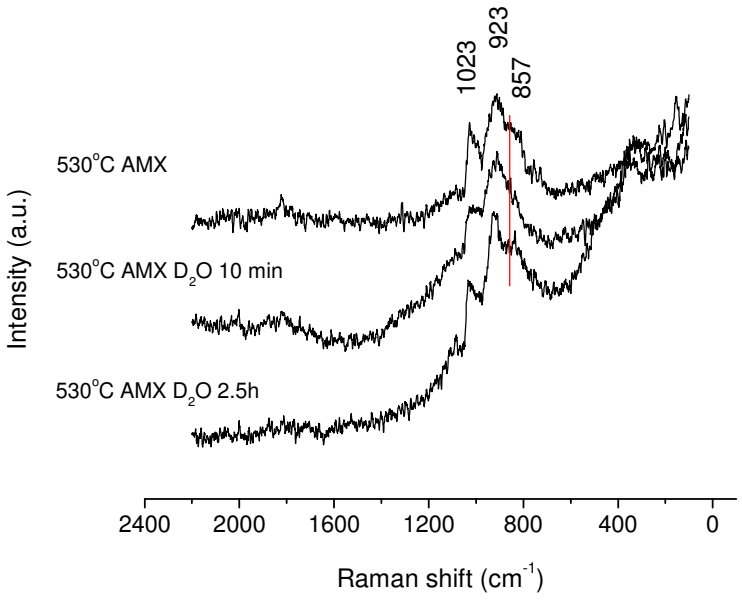

Figure 7.17 Raman spectra of precursor 8V9PAl catalyst under propane ammoxidation reaction at 500 °C (top) and after introduction of D_2O to the reaction flow for 10 min (middle) and for 2.5 hours (bottom). (Ar excitation line: 532 nm, total flow of 36 ml/min: 4% O_2, 8% NH_3, 3% C_3H_8, D_2O 1.5 ml h^{-1}, 50 mg of catalyst)

7.5 SUMMARY

High selectivities to acrylonitrile were obtained over analyzed catalysts for the propane ammoxidation reaction. The alumina support in supported VPO-like catalysts triggers off the presence of V^{5+} species, which upon interaction with phosphorus transform into V^{4+}-containing phases during the ammoxidation reaction. The dispersed vanadium oxide phase as well as the oxidized catalyst is selective to acetonitrile. This indicates that V^{5+} probably is responsible for the acetonitrile formation and that no P-V interaction is required for this (side-) reaction. This is further confirmed by the fact, that no $V^{5+}OPO_4$ phases form after reoxidation, but V_2O_5 was detected, which suggest separation of VO_x and PO_x phases. XRD patterns and Raman spectra of the fresh and used samples demonstrate that active phases were formed on stream and, subsequently, restructured. Catalyst activation in reaction flow leads to the formation of $(VO)_2P_2O_7$. This phase decomposes with time on stream. On the other hand, the $VOHPO_4$ phase initially predominates in preactivated 8V9PAl, and $(VO)_2P_2O_7$ forms along run time. It should be remarked that *ex situ* studies do not reveal the actual state of the working catalyst. *Operando* and *in situ* techniques were used to understand the nature of the supported VPO-type catalysts and to deduce the active sites for acrylonitrile formation. These show that no crystalline VPO phases are necessary for acrylonitrile formation in propane ammoxidation reaction, but that the presence of phosphorus is essential for stabilization of V^{4+}. However, the increase in the V^{4+}/V^{5+} atomic ratio leads to decrease of the propane conversion. The *operando* Raman-GC analyses reveal phase transformations in the catalysts during reaction. *Operando* Raman spectra of the pretreated 8V9PAl sample show that V^{5+} reduces to V^{4+} at 500 ^oC and the V^{5+}=O feature at 1022 cm^{-1} decreases in intensity, while a band due to $(V^{4+}O)_2P_2O_7$ appears at 923 cm^{-1}. This suggests a combination of dispersed vanadium oxide and phosphorous into such VPO phases during reaction. The intensity of the latter band changes during the 60 hours on stream. This is probably related to the existence of redox cycles that would induce additional changes. The selectivity to acrylonitrile increases with increasing reaction temperature, shifting from acetonitrile to acrylonitrile just before the Raman band characteristic of $(VO)_2P_2O_7$ appears. This is probably caused by an increase of the amount of amorphous V^{4+}, which cannot be detected by Raman spectroscopy. For the catalyst precursor, the Raman band characteristic of dispersed V^{5+} oxide species is present in the whole investigated temperature range. Above 475 ^oC, phase transformations occur leading to $(VO)_2P_2O_7$ formation, and a new broad Raman band near 850–880 cm^{-1} after 38 minutes at 500 ^oC. This new band is not

characteristic of any VPO phase. High selectivity to acrylonitrile was reached at low temperatures for the precursor 8V9PAl, which might be caused by the fact that originally the precursor contains mainly V^{4+} species. Simultaneous calcination of the $(COOH)_2$ precursor ligands during the first reaction steps would have an effect on the reaction equilibrium. It has to be noted that even if $(COOH)_2$ decomposition causes a catalyst mass decrease of approx. 20%, the activity remains higher compared to the preactivated 8V9PAl, which underlines its higher activity per V+P site. However, no clear band associated to vanadyl pyrophosphate phase was observed in Raman spectra of the 8V9PAl precursor after 30 min on stream at 500 °C. The bulk $(VO)_2P_2O_7$ forms by dehydration of $VOHPO_4 * {}^1/_2\ H_2O$ passing through an amorphous phase; which might be stabilized by the support. Simultaneously, the alumina support would also promote that some vanadium could be dispersed and stabilized as V^{5+} surface species. In a similar fashion, the formation of $(VO)_2P_2O_7$ in the supported VPO-type catalysts requires reduction of surface vanadium species to V^{4+}. Since the precursor 8V9PAl operates under oxygen-limiting conditions at high reaction temperatures (oxygen conversion >90% at 500 °C), the over-reduction could be the factor limiting the presence of $(VO)_2P_2O_7$. The V^{4+} containing $(VO)_2P_2O_7$ phase was formed first at 500 °C, before the Raman feature at 850–880 cm^{-1}, which is lost upon exposure of the used catalyst to air and the $(VO)_2P_2O_7$ phase is restored. The *in situ* UV Raman experiment under propane ammoxidation reaction generates an intense band at ca. 875 cm^{-1}. However, the fact that this band was also observed in visible Raman spectra makes the assignment of this Raman feature to V^{3+} species rather complicated. Other *ex-situ* analytical techniques are not useful in this case, since used catalysts show presence of only V^{4+} containing phases. Thus, based on the UV Raman experiment the band at ca. 875 cm^{-1} would be associated with M-O-M bonds in polymeric species.

References

[1] H. Golińska, E. Rojas, R. López-Medina, V. Calvino-Casilda, M. Ziółek, M. A. Bañares, M. O. Guerrero-Pérez, *Appl. Catal. A* 380 (2010) 75

[2] P. Concepción, P. Botella, J. M. López Nieto, *Appl. Catal. A* 278 (2004) 45

[3] F. B. Abdelouahab, R. Olier, N. Guilhaume, F. Lefebvre, J. C. Volta, *J. Catal*. 134 (1992) 151

[4] G. Deo, I. E. Wachs, *J. Phys. Chem.* 95 (1991) 5889

[5] E. L. Lee, I. E. Wachs, *Silica Silicates Modern Catal*. (2010) 375

[6] Y. T. Chua, P. C. Stair, I. E. Wachs, *J. Phys. Chem*. 105 (2001) 8600

[7] J. Koo, B. Bae, H. Na*, J. Non-Cryst. Solids* 212 (1997) 173

[8] J. J. Hudgens, R. K. Brow, D. R. Tallant, S. W, Martin, *J. Non-Cryst. Solids* 223 (1998) 21

[9] S. T. Reis, D. L. A. Faira, J. R. Martinelli, W. M. Pontuschka, D. E. Day, C. S. M. Partiti, J. *Non-Cryst. Solids* 304 (2002) 188

[10] C. M. Preston, W. A. Adams, *Can. J. Spectrosc*. 22 (1977) 125

[11] M. Devalette, J. Darriet, M. Couzi, C. Mazeau, P. Hagenmuller, *J. Solid State Chem*. 43 (1982) 45

[12] W. Bues, H.-W. Gehrke, *Z. Anorg. Allg. Chemie* 288 (1956) 307

[13] H. H. Eysel, K. T. Lim, *J. Raman Spetrosc*. 19 (1988) 535

[14] M. K. Cerreta, K. A. Berglund, *J. Cryst. Growth* 84 (1987) 577

[15] C. M. Preston, W. A. Adams, *J. Phys. Chem*. 83 (1979) 814

[16] E. Steger, K. Herzog, J. Klosowski, *Z. Anorg. Allg. Chem*. 432 (1977) 42

[17] K. Nagamine, T. Honma, T. Komatsu, *J. American Ceramic Soc*. 91 (2008) 3920

[18] I. Ardelean, D. Rusu, C. Andronache, V Ciobotă, *Matter. Lett*. 61 (2007) 3304

[19] R. K. Brow, *J. Non-Cryst. Solids*, 263 and 264 (2000) 1

[20] R. N. Bhargava, R. A. Condrate, *Appl. Spectrosc*. 31 (1977) 230

[21] V. Dimitrov, T. Komatsu, *Phys. Chem. Glasses* 47 (2006) 638

[22] A. Caldarelli, F. Cavani, F. Folco, S. Luciani, C. Cortelli, R. Leanza, *Catal. Today* 157 (2010) 204

[23] R. M. Feng, X. J. Yang, W. J. Ji, Y. Chen, C. T. Au, *J. Catal*. 224 (2007) 166

[24] N. Ballarini, F. Cavani, C. Cortelli, M. Ricotta, F. Rodeghiero, F. Trifiró, C. Fumagalli, G. Mazzoni, *Catal. Today* 117 (2006) 174

[25] M. A. Bañares, G. Mestl., *Adv. Catal*. 52 (2009) 43

[26] M. A. Bañares, *Adv. Mater*. (2011) (doi: 10.1002/adma.201101803) in press

[27] M. A. Bañares, *Catal. Today* 100 (2005) 71

[28] M. O. Guerrero-Pérez, M. A. Bañares, *J. Phys. Chem.* 111 (2007) 1315

[29] G. Centi, F. Trifiró, J. R. Ebner, V. M. Franchetti, *Chem. Rev*. 88 (1988) 55

[30] Z.Q. Zhou, H.Y. Xu, W.J. Ji, Y. Chen, *Catal. Letters* 96 (2004) 221

[31] M. Sanati, A. Andersson, L. R. Wallenberg, B. Rebenstorf, *Appl. Catal. A* 106 (1993) 51

[32] M. O. Guerrero-Pérez, M. A. Peña, J. K. G. Fierro, M. A. Bañares, *Ind. Eng. Chem. Res*. 45 (2006) 4537

[33] V. Narayana Kalevaru, B. Lücke and A. Martin, *Catal. Today* 142 (2009) 158
[34] A. Martin and B. Lücke, *Chem. Eng. Technol*. 21 (1999) 294
[35] Ch. Zhao, I. E. Wachs, *Catal. Today* 118 (2006) 332
[36] A. Khodakov, B. Olthof, A. T. Bell and E. Iglesia, *J. Catal*. 181 (1999) 205
[37] R. Nilsson, T. Lindblad and A. Andersson, *Catal. Lett*. 29 (1994) 409
[38] Z. Wu, P.C. Stair, S. Rugmini, S.D. Jackson, *J. Phys. Chem*. C, 111 (2007) 16460
[39] S. A. Asher, C. R. Johnson, *Science* 225 (1984) 311
[40] C. Li, P. C. Stair, *Catal. Today* 33 (1997) 353
[41] S. L. Liu, G. X. Xiong, W. S. Yang, L. Y. Xu, G. Xiong, C. Li, *Catal. Lett*. 63 (1999) 167
[42] R. A. Meyers (Ed.), M. A. Bañares, I. E. Wachs, *Encyclopedia of Analytical Chemistry*, John Wiley & Sons Ltd (2010)
[43] I. R. Lewis, H. G. M. Edwards, Marcel Decker (Eds.), D.C. Smith, C. Carabatos-Nédelec, *Handbook of Raman Spectroscopy,* New York, (2001)
[44] X. Gao, I. E. Wachs, *J. Catal*. 192 (2000) 18
[45] T. Woignier, C. Fernandez-Lorenzo, J. L. Suavajol, J. F. Schmidt, J. Phalippou, R. Sempere, *J. Sol Gel Sci. Tech*. 5 (1995) 167

8

Partial oxidation of propane

8.1 INTRODUCTION

Selective oxidation reactions of alkanes are receiving an increasing interest. The low selectivity to partial oxidation products is the main reason why, despite great efforts, new effective catalysts are still required. Most catalysts used for propane oxidation are based on vanadium, which exhibits both redox and acidic properties. As shown in Chapter 6, the phosphorus additive has a strong influence on the acidity of the catalyst surface as well as on the environment of vanadium sites *via* the V-O-M bonds (M = P, V, Ti or Al), which are considered as the active bonds for selective oxidation reactions. Thus, phosphorus-doped titania- and alumina-supported vanadium catalysts were tested in propane oxidation reaction and compared to titania- and alumina-supported vanadia and VPO catalysts.

8.2 Performance of titania- and alumina-supported vanadium and phosphorus oxide catalysts in comparison to the industrial VPO for propane oxidation reaction

VPO, V-Ti, VP-Ti and VP-Al catalysts were tested for propane oxidation to acrylic acid between 325 and 400 ^{o}C. The best performance was observed at 350 ^{o}C. Propane combustion dominates above such temperature, and the selectivity to partial oxidation products becomes negligible, indicating a very narrow temperature operation range. The time-on-stream propane selective oxidation for titania- and alumina-supported catalysts at 350 ^{o}C are presented in Figures 8.1-8.4. Propane conversion and selectivities to the products (propylene, acrylic acid and CO_x) are reported. Traces of ethane, acrolein and acetone were also detected during catalytic tests. The presence of acetone would suggest that some acetic acid forms (see section 1.4.1 and references [1,2]). Probably the acetic acid was not detected, because it was not separated from acrylic acid due to fast temperature ramp of the packed column during analysis. However, slower temperature ramp leads to the significant elongation of the analysis time and subsequently to poor time resolution during the measured four hours on stream. Thus, the acetic acid, which was not detected during reaction, was separated from acrylic acid by injection of the trapped reaction products to the gas chromatograph with a capillary column

8.2.1 Titania-supported series

Figure 8.1 shows that the vanadium monolayer catalyst on titania is hardly active in this reaction, delivering 5-10% propane conversion. CO_x is the main reaction product, significant amounts of propylene are also formed, but neither acrylic nor acetic acid formation was apparent.

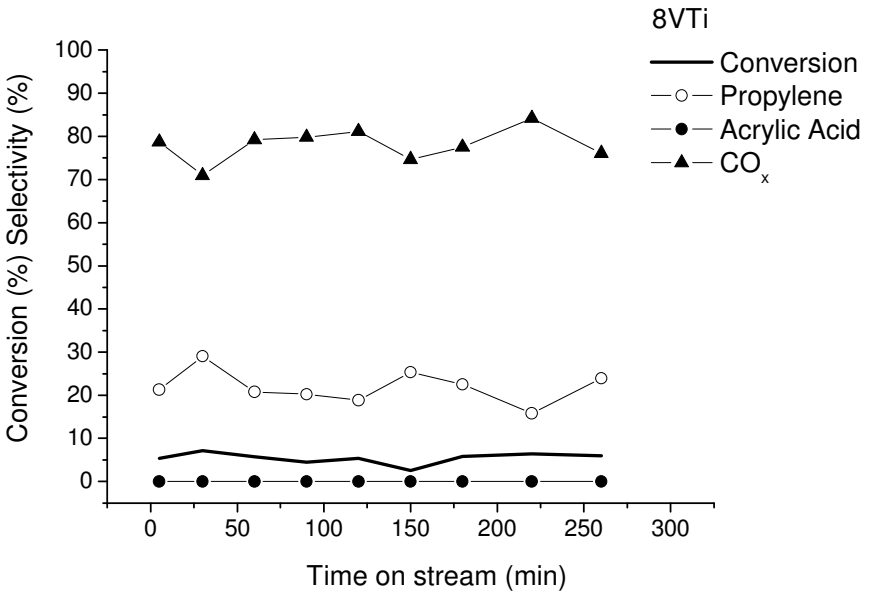

Figure 8.1 Time-on-stream propane selective oxidation at 350 ^{o}C on 8VTi (reaction conditions: total flow: 40 ml min^{-1}; 20.4% of O_2; 12.5% of C_3H_8; and 15.9% of steam in He)

Figure 8.2 shows that doping the above-mentioned sample with phosphorus (P/V = 0.1) dramatically changes the catalytic performance. The catalyst was activated on stream heating from 100-350 ^{o}C (temperature ramp: 20 ^{o}C/min). There is an intense activation in the initial time-on-stream, propane conversion increases to 55% after ca. 30 min at 350 ^{o}C. Selectivity to propylene and to CO_x decreases, while the selectivity to carboxylic acids reaches ca. 65% for 8V1PTi (Figure 8.2A). Formation of ca. 30% of acetic acid, which was not detected during reaction, was confirmed by the gas chromatography of the trapped reaction products. This suggests that the actual selectivity to acrylic acid would be ca. 35%.

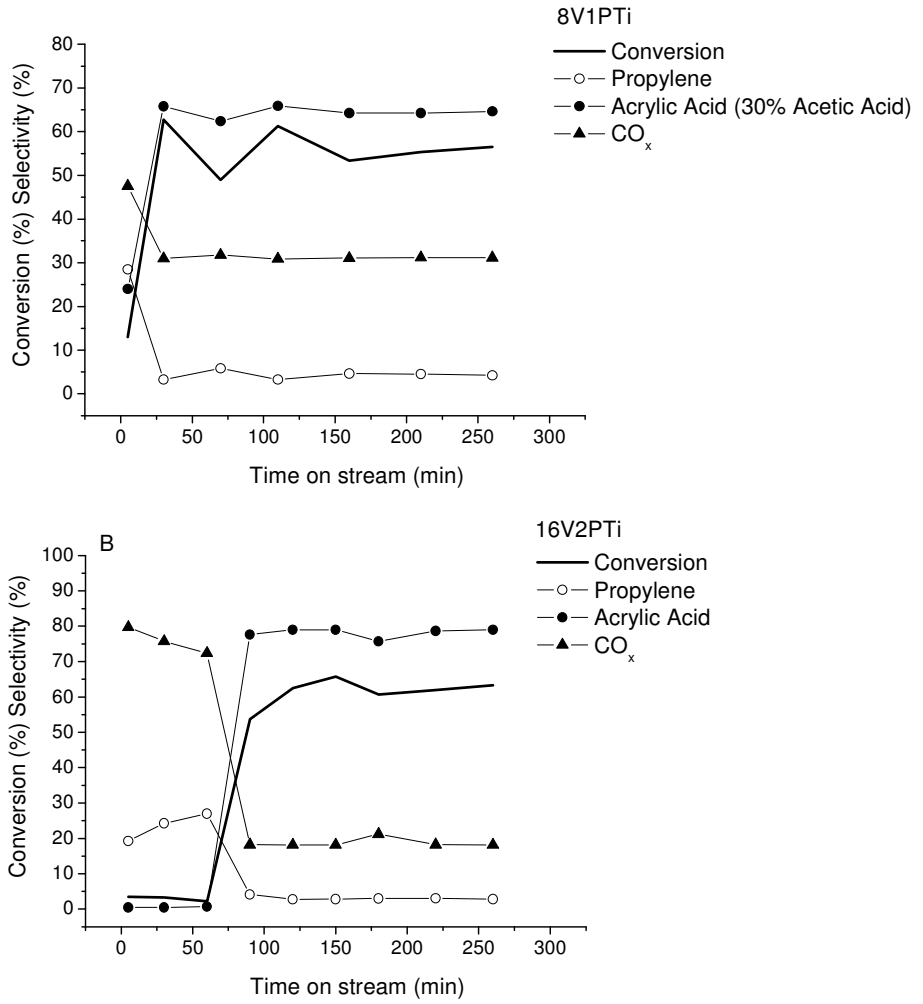

Figure 8.2 Time-on-stream propane oxidation at 350 ºC on 8V1PTi (A) and 16V2PTi (B) (reaction conditions: total flow: 40 ml min^{-1}; 20.4% of O_2; 12.5% of C_3H_8; and 15.9% of steam in He)

An interesting activity profile was obtained for 16V2PTi (Figure 8.2B), which possesses two monolayers of vanadium oxide on titania. During the first hour on stream its performance resembles that of the undoped catalyst (8VTi). The conversion is low and the catalyst is selective to CO_x and propylene. After ca. 70 min on stream (activation as for the 8V1PTi), a radical change occurs and the activity profile now approaches that of the phosphorus-doped titania-supported vanadia catalyst, 8V1PTi. However, the conversion is higher, reaching ca. 60%, probably as a result of the increased amount of the active phase.

Figure 8.3 illustrates the time-on-stream propane conversion and selectivities for propane oxidation on 8V9PTi. The higher P/V ratio does not appear to promote low-temperature propane oxidation. Propane conversion decreases continuously and the initial selectivity to acrylic acid shifts to CO_x after ca. 200 min on stream.

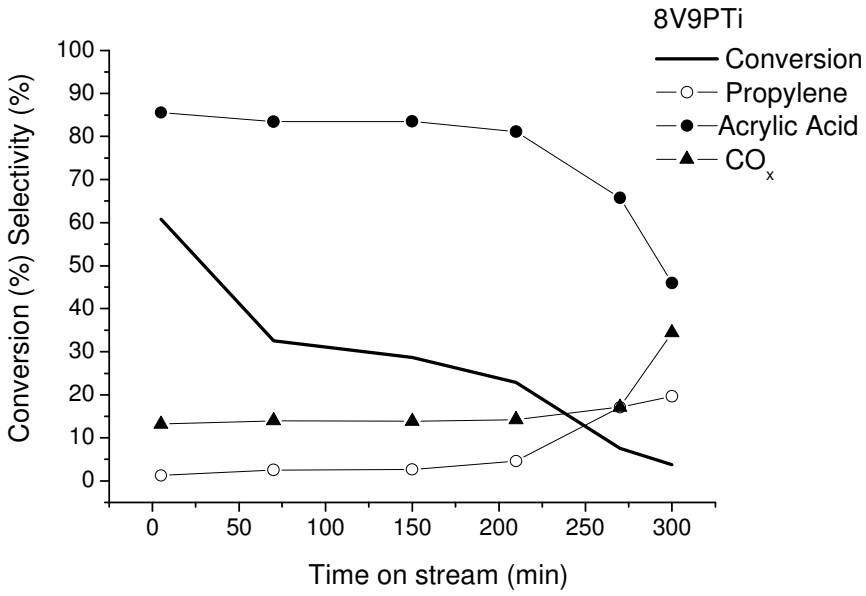

Figure 8.3 Time-on-stream propane oxidation at 350 ºC on 8V9PTi (reaction conditions: total flow: 40 ml min^{-1}; 20.4% of O_2; 12.5% of C_3H_8; and 15.9% of steam in He)

8.2.2 Alumina-supported series

Figure 8.4 shows time-on-stream propane oxidation at 350 ^oC on the phosphorus-doped alumina-supported vanadium catalyst (8V1PAl). Its performance is similar to that of the corresponding titania-supported catalyst (8V1PTi). This suggests that the support does not influence the catalytic properties of the phosphorus doped near monolayer catalysts.

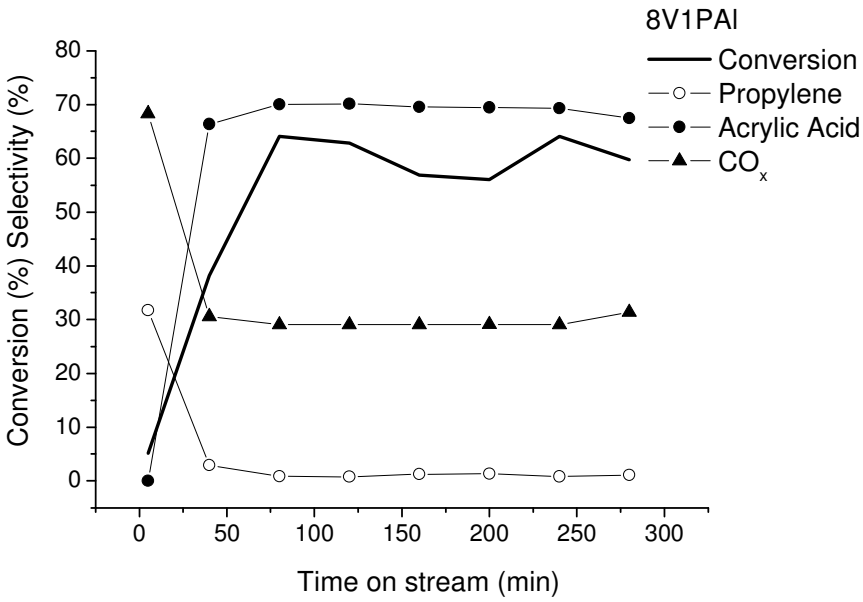

Figure 8.4 Time-on-stream propane oxidation at 350 ºC on 8V1PAl (reaction conditions: total flow: 40 ml min^{-1}; 20.4% of O_2; 12.5% of C_3H_8; and 15.9% of steam in He)

Neither 8V9PAl (P/V = 1.1 atomic) nor bulk VPO were active for propane oxidation at 350 ^oC. Both catalysts afford propane conversion close to 1% during 5 hours on stream. It is reported that bulk VPO catalysts are active for acrylic acid production, but at higher reaction temperatures (ca. 400 ^oC) [3]. Moreover, they require long activation time. Thus, probably the reaction temperature, contact time or the time-on-stream were not high or long enough for the activation of these catalysts.

The transient activity leading to acrylic or acetic acid formation may be related to a progressive V-P interaction. The spent catalysts were analyzed by XRD and Raman spectroscopy in order to follow possible structural changes that may occur under reaction conditions.

8.3 Characterization of catalysts used in propane oxidation reaction

Figure 8.5 presents the X-ray diffractograms of fresh and used titania-supported vanadium and phosphorus catalysts, respectively. The XRD patterns are dominated by titania anatase and generally no new phases are observed upon use in catalysis.

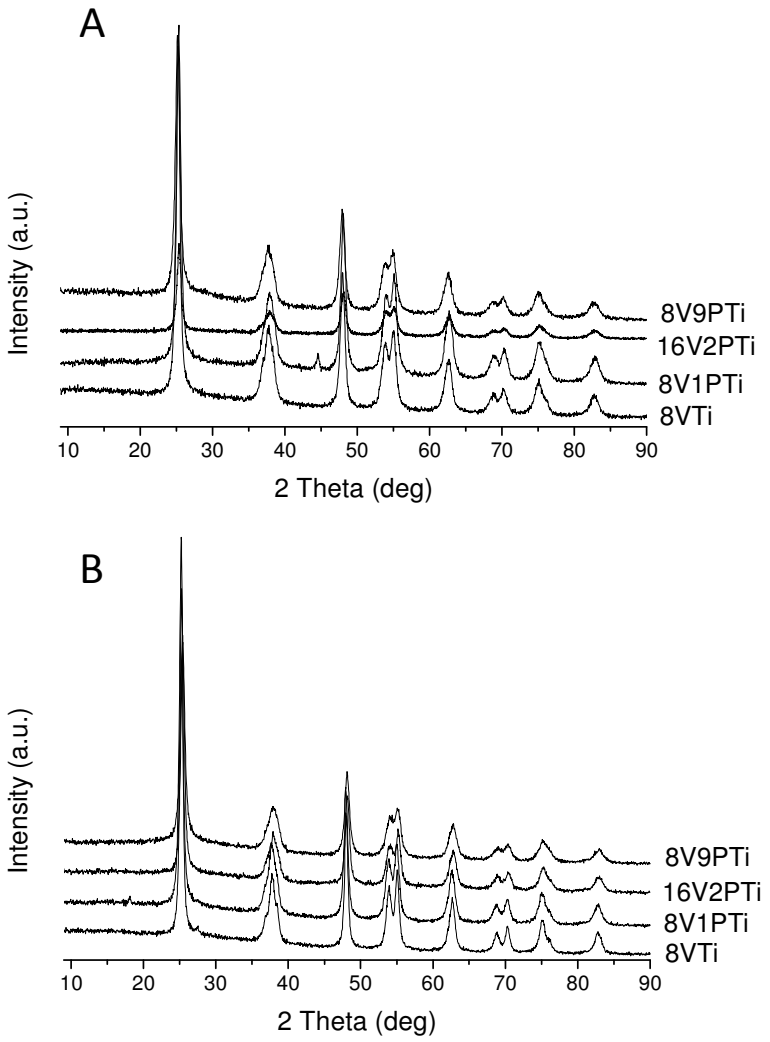

Figure 8.5 X-Ray diffraction patterns of fresh (A) and used (B) titania-supported vanadium and phosphorus catalysts

The X-ray diffractograms of alumina-supported vanadium and phosphorus oxide catalysts are shown in Figure 8.6. An amorphous phase is observed for fresh and used 8V1PAl. However, some very weak peaks are present. The peaks in fresh 8V1PAl may be assigned to various structures of Al_2O_3 , while those in used 8V1PAl match both alumina oxides and vanadium oxide phases. Used 8V9PAl exhibit new reflections, but the detailed assignment becomes complicated due to formation of mixed phases, probably distorted by the alumina support and low number of the XRD lines with a multiple-match in the ICDD database of the X-Pert High Score Plus software (i.e. AlPO, V_2O_5, $VOPO_4$, $VHOPO_4$, $(VO)_2P_2O_7$ phases). However, the reflections at 2Θ of 26.11, 28.05, 29.09 ^{o} may be characteristic of β-$V^{5+}OHPO_4$ phase [4], while the reflections below 25 ^{o}2Θ may be due to AlPO phases [5,6].

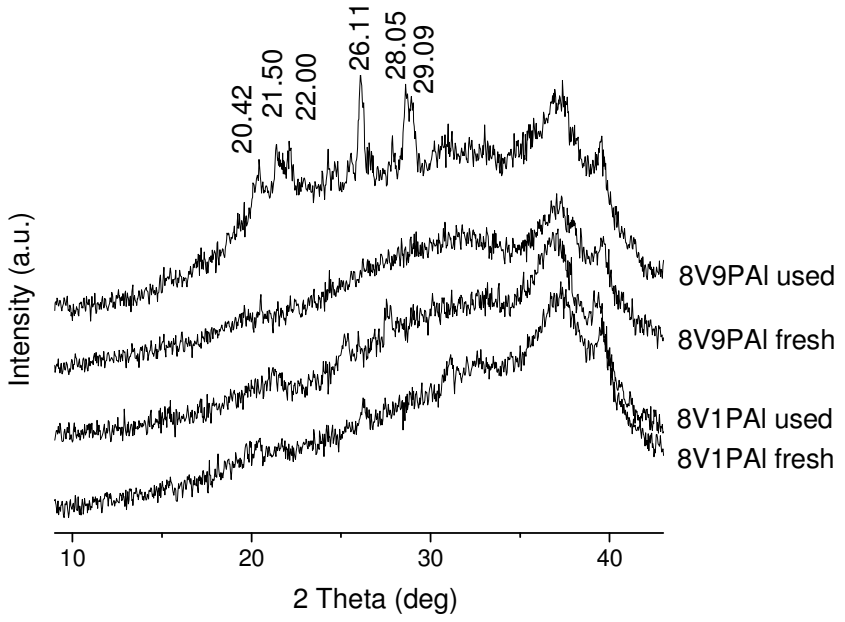

Figure 8.6 X-Ray diffraction patterns of fresh and used alumina-supported vanadium and phosphorus catalysts

Figure 8.7 illustrates the Raman spectra of dehydrated titania-supported catalysts. These samples were homogenous so that only the representative

spectra were plotted. No remarkable changes in the spectra are observed for the spent catalysts. This is in agreement with the XRD data and indicates that no new phase formation occurred after reaction and that the structural changes would relate only to the amorphous phase. Fresh samples exhibit Raman bands at 1029 and 910 cm^{-1} due to V^{5+}=O and V-O-M stretching modes respectively (where M stands for V, P or Ti). Comparing the Raman spectra of fresh and used catalysts it seems that the ratio of 1029/910 cm^{-1} bands increases for catalysts exposed to reaction conditions. It might be caused by formation of oxygen vacancies in V-O-M bonds, provoked by presence of steam [7].Used 16V2PTi exhibit Raman bands at 996, 698 and 282 cm^{-1}, characteristic of V_2O_5, but since the Raman section of crystalline V_2O_5 usually at least an order of magnitude larger than that of dispersed vanadia [8], its actual concentration is negligible.

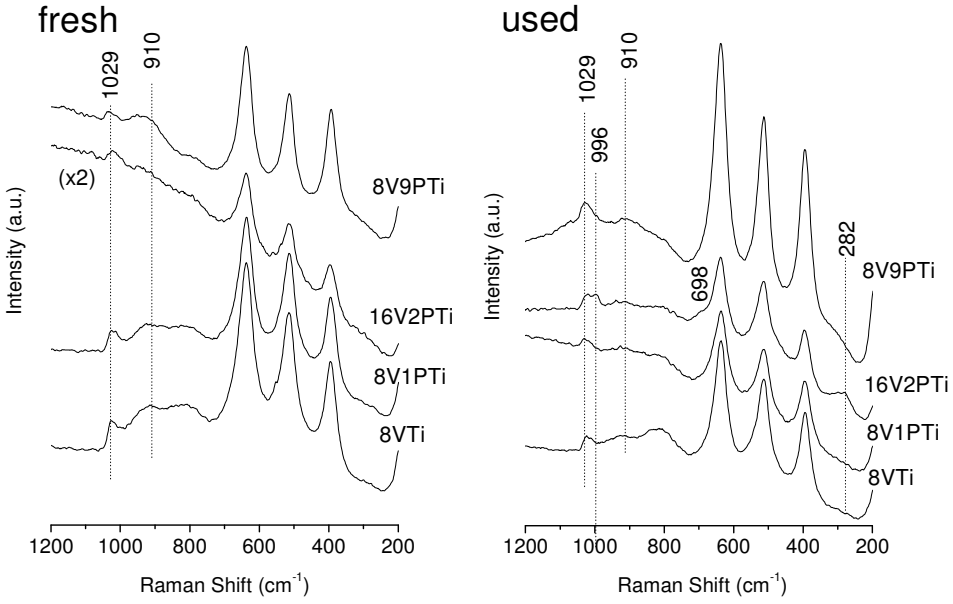

Figure 8.7 Raman spectra of dehydrated fresh and used titania-supported vanadium and phosphorus catalysts. Spectra were acquired at 50 ^{o}C in N_2 flow. Ar excitation line: 514 nm

Samples supported on alumina exhibit a different trend. Figure 8.8 presents Raman spectra of 8V1PAl. The catalyst surface is not homogenous and spectra

show a Raman band at 1013 cm^{-1}, due to dispersed vanadium surface species (V^{5+}=O) [9,10], or bands at 996, 704, 529, 482, 406, 303, 286, 195, and 144 cm^{-1}, characteristic of crystalline V_2O_5 [11,12,13]. The sample used in propane oxidation reaction mostly contains ill-defined crystals of V_2O_5.

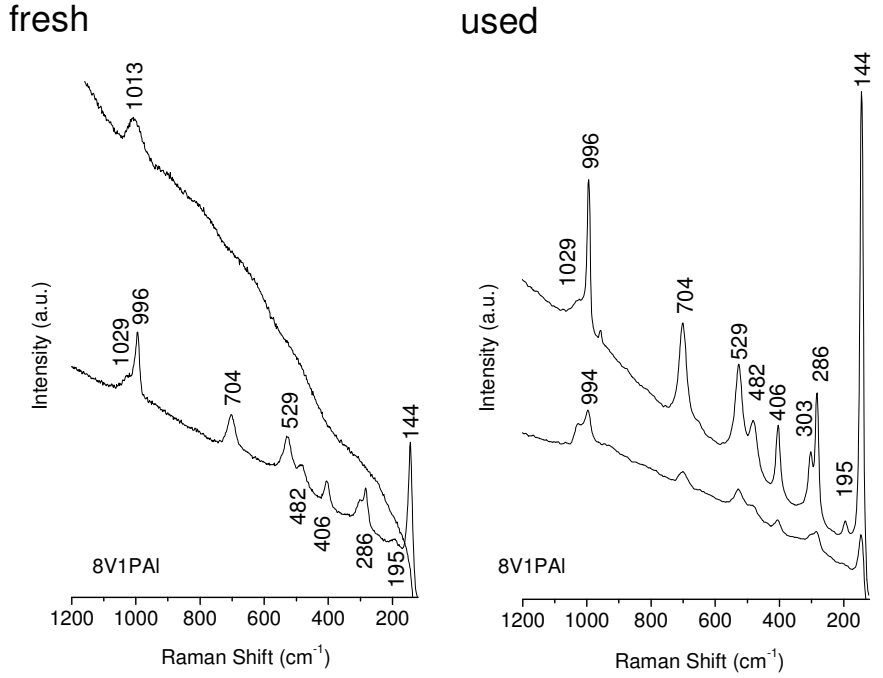

Figure 8.8 Raman spectra of dehydrated fresh and used 8V1PAl catalysts. Spectra were acquired at 50 ^oC in N_2 flow. Ar excitation line: 514 nm

The Raman spectra of alumina-supported fresh 8V9PAl (P/V = 1.1), exhibits the Raman vibration due to V^{5+}=O bond of vanadia surface species (see Figure 8.9). Three representative Raman spectra of used 8V9PAl evidence the presence of V_2O_5 and β-$VOPO_4$ phases. This indicates that the reaction conditions lead to entanglement of the vanadium and phosphorous species. The V_2O_5 and β-$VOPO_4$ phases contain V^{5+}, just like the fresh catalyst. It is in contradiction to the data obtained for propane ammoxidation, where the vanadyl pyrophosphate phase (V^{4+}) was formed on stream (Chapter 7 and references [14,15]). A strong tendency to crystallization is apparent for the alumina-supported series, which may be associated to presence of moisture in reaction flow. However, this

susceptibility is inhibited for the titania-supported samples. The *ex-situ* characterization does not supply information about the influence of phosphorus doping on the structure of supported vanadium oxide catalysts and thus, about the structure-activity relationships of the catalysts showing the best catalytic performance.

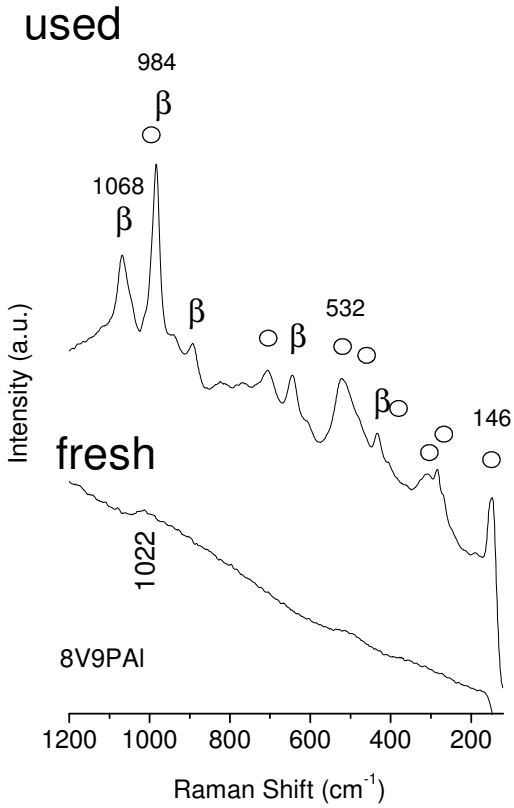

Figure 8.9 Raman spectra of dehydrated fresh 8V9PAl and three representative Raman spectra of used 8V9PAl catalyst; β – β-$VOHPO_4$ and ○ – V_2O_5. Ar excitation line: 514 nm

8.4 The role of steam in propane oxidation to acrylic acid

The influence of water vapor on activity and selectivity of 8V1PTi in propane oxidation reaction was evaluated. Figure 8.10 shows the catalytic performance

of the 8V1PTi catalyst in absence and in ca. 6 and 16% of steam in the reaction feed. It can be observed, that moisture plays a key-role in this reaction. The selectivity shifts from carbon oxides in absence of steam to carboxylic acids in presence of moisture. The selectivity to acrylic acid increases with increasing steam concentration.

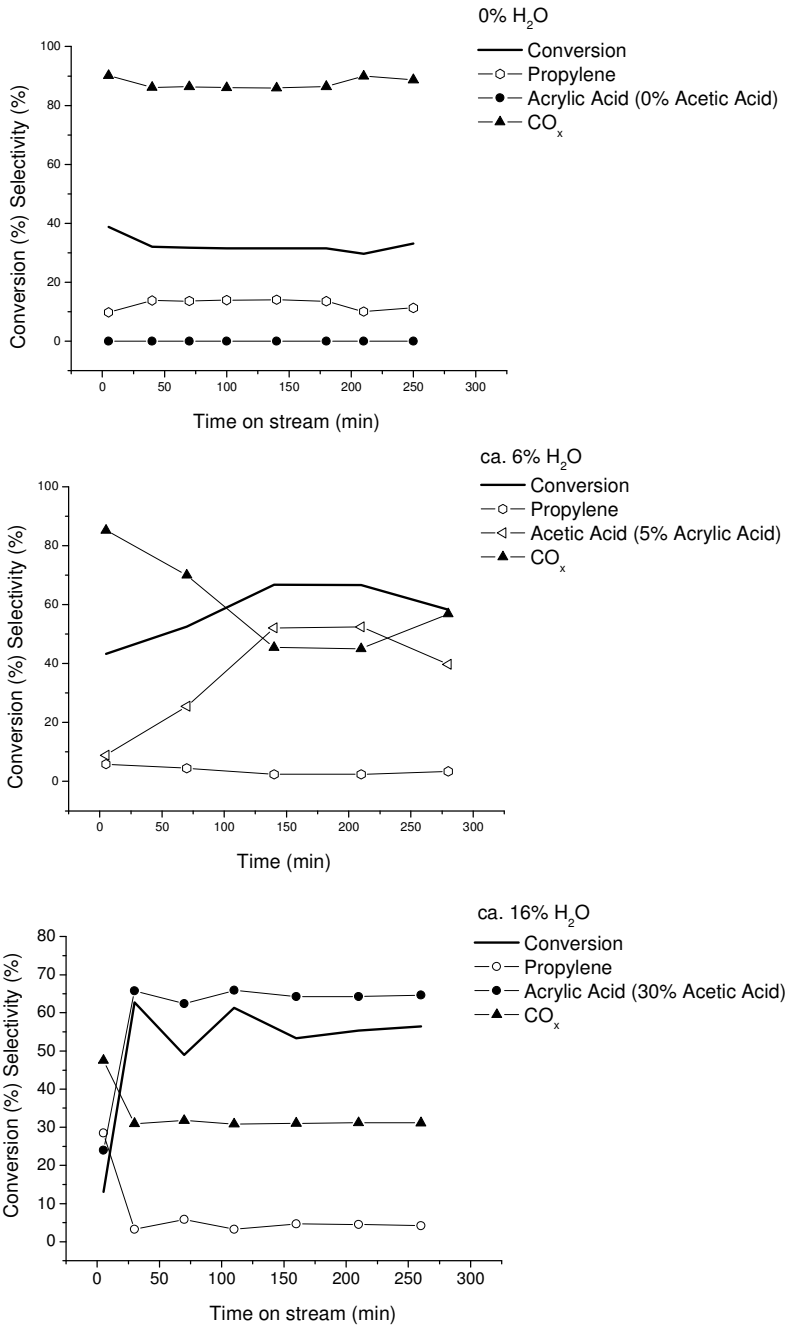

Figure 8.10 Time-on-stream propane oxidation reaction on 8V1PTi at 350 ^{o}C. Reaction conditions: total flow: 40 ml min^{-1}; 20.4% of O_2; 12.5% of C_3H_8; and X% of steam in He; X = 0% (A), X= 6% (B) X= 16% (C)

The Raman spectra presented in Figure 8.11 show that even though water vapor has a strong influence on the catalytic properties, no structural changes caused by exposure to steam are observed for the phosphorus doped titania-supported vanadium catalyst.

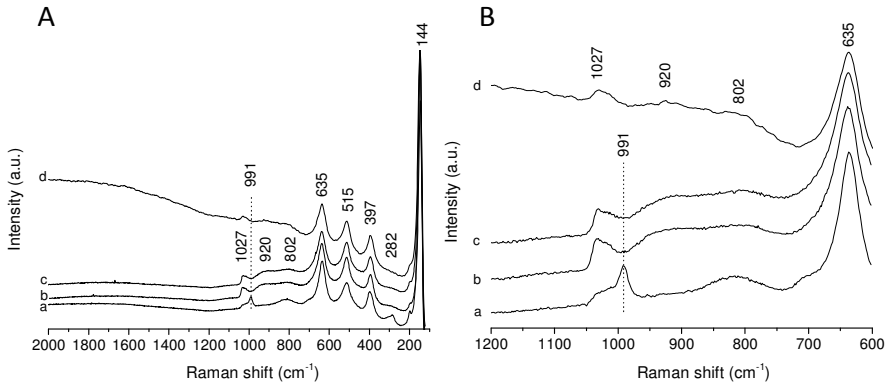

Figure 8.11 Influence of water vapor on the structure of 8V1PTi (A), zoom in 600-1200 cm^{-1} region (B) Representative Raman spectra of the dehydrated 8V1PTi after exposure to reaction conditions at 350 ^{o}C for ca. 5 hours in absence of steam (a and b) and in presence of ca. 6% (c) and ca. 16% of H_2O (d). Spectra were acquired at 50 ^{o}C in N_2 flow using the Ar 514 nm excitation line

Moisture may interacts with the catalysts surface or it may affect the gas phase, i.e. change of the reactants partial pressures. However, both, the water vapor and the phosphorus play a crucial role in formation of acrylic acid.

8.5 *In situ* and *operando* IR study during propane oxidation reaction

The *ex-situ* structural characterization of the used catalysts is not consistent with the activity profiles and does not provide information about the active phases. Moreover, titania-supported vanadium catalyst exhibits a Raman spectrum similar to that of phosphorus-doped titania-supported vanadium catalyst but in contrast to the 8V1PTi it does not deliver satisfying catalytic performance. No changes caused by doping with phosphorus were detected by Raman or XRD in

the structure of supported vanadium oxide catalysts and thus, *In situ* IR spectroscopy studies were performed in order to determine the role of phosphorus doping and moisture on the supported phosphorus and vanadium oxide catalysts in propane oxidation reaction and to relate the nature of these catalysts with their structure-activity relationships. DRIFTS studies of titania- and alumina-supported vanadium and phosphorus oxide catalysts were performed at the *Operando Molecular Spectroscopy and Catalysis Laboratory* at Lehigh University for the study of the mechanism of propylene oxidation reaction and for evaluation of the role of phosphorus and water vapor. Propylene was used in these analyses due to low adsorption of propane. The spectrum of the activated sample is shown as reference, but was not subtracted from spectra with adsorbed propylene.

The Figure 8.12 shows DRIFT spectra of the 8V1PTi. The catalyst precursor was previously treated in N_2 stream at 400 ^oC for 19 hours, and subsequently activated at 450 ^oC in presence of oxygen (10% in He). Figure 8.12r represents spectrum of the activated 8V1P Ti. This spectrum shows a band at ca. 2045 cm^{-1} characteristic of the first overtone of V=O stretching bond [16,17]. The spectrum "a" of the Figure 8.12 illustrates 8V1P Ti after propylene adsorption for 40 min at 125 ^oC. This spectrum is characteristic of gas phase propylene (see the reference spectrum on the Figure 8.13). The gas phase propylene was subsequently removed by flowing He for 20 min at 125 ^oC (Figure 8.12b). The spectrum acquired after the purging step shows IR features characteristic of propylene adsorbed on the catalyst surface. Sharp bands are evident in the 2800-3000 cm^{-1} range, characteristic of symmetric CH_2 and CH_3 bending modes. The band at 1670 cm^{-1} is due to ν(C=O) [18], while the band at 1570 cm^{-1} is due to asymmetric stretching of a $^-$O-C=C/O=C-C$^-$ anionic system [19]. These bands are often observed for acetone adsorbed on supported vanadium oxide systems, which suggests that propylene adsorbs on the catalysts surface undergoing an electrophilic attack by a proton of surface OH groups [20]. This leads to formation of isopropoxide species, which are not observed, because the dehydrogenation process of an isopropyl alcohol to acetone occurs already at 100 ^oC [19]. Oxygen (10 % in He; 20 ml/min) was introduced to the Harrick cell and desorption was performed during 20 minutes at 125 ^oC. No changes in the spectra (Figure 8.12c) were observed in comparison to the spectra acquired after purging of the gas phase propylene in He flow, suggesting that no reaction occurs between oxygen and adsorbed propylene at 125 ^oC.

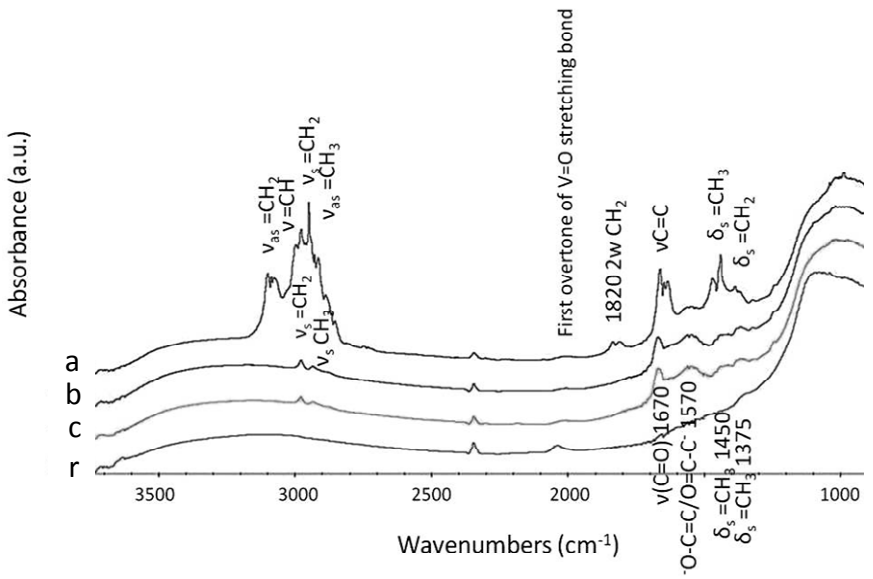

Figure 8.12 DRIFT reference spectrum of activated 8V1PTi (r), after C_3H_6 adsorption (a), after C_3H_6 purging step in He (b) and after desorption process at 125 ^oC in O_2 flow (c). All spectra were acquired at 125 ^oC

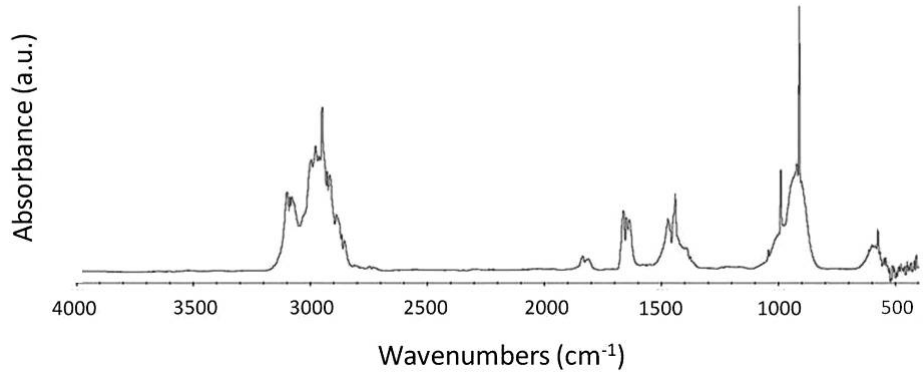

Figure 8.13 FT-IR spectrum of reference gas phase propylene

The desorption process in oxygen flow is shown in Figure 8.14. It may be observed that the band at 1670 cm^{-1} due to ν(C=O) disappears at ca. 300 ^oC.

New bands appear at 250 °C near 1870 cm^{-1}, 1790 cm^{-1}, 1530 cm^{-1} and 1435 cm^{-1}. The bands at 1530 and 1435 cm^{-1} are characteristic of carboxylate species (acetates or acrylates) [21], while bands at 1870 and 1790 cm^{-1} are due to the symmetric and asymmetric C=O bonds of cyclic anhydrides, probably to maleic anhydride [22]. In contrast to the bands of carboxylate species, IR features at 1870 and 1790 cm^{-1} are observed even after the temperature is increased to 400 °C. A strong band near 1135 cm^{-1} appears at 300 °C. This band increases in intensity and shifts to higher wavenumbers with increasing temperature (1260 cm^{-1} at 400 °C). At this region C-O single bonds of alcohols (1040-1200 cm^{-1}), ethers (1120-1260 cm^{-1}), carboxylic acids (1250-1300 cm^{-1}) and other C-O single bond containing compounds may be found, as well as vibrational modes characteristic of phosphates groups (900-1260 cm^{-1}) [23,24,25]. This band remains stable during treatment in O_2 flow at 450 °C for 1 hour, but it disappears rapidly when switched to He flow at 450 °C. This indicates that this band is present only at elevated temperatures in presence of O_2 (see Figure 8.15A and B). Bands characteristic of C-O may be excluded, since the appearance of the band was also observed during dehydration process of 8V1PTi in O_2 at 450 °C.

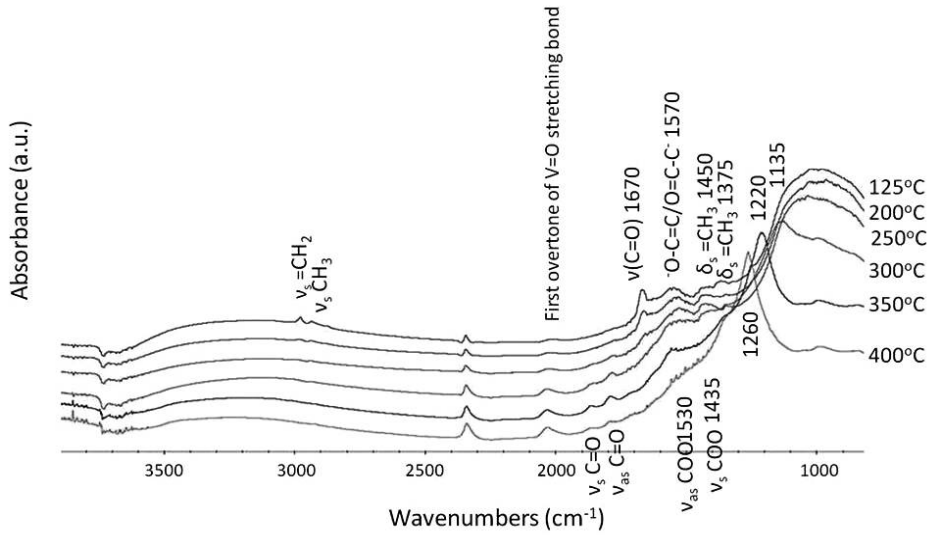

Figure 8.14 DRIFT spectra of propylene desorption in O_2 flow from the 8V1PTi surface

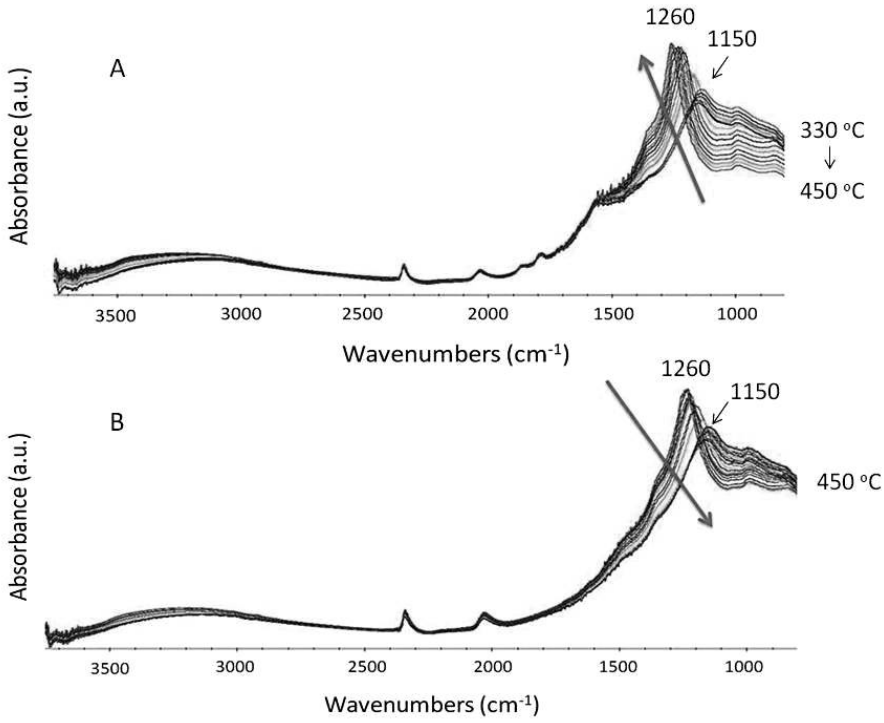

Figure 8.15 DRIFT spectra of the 8V1PTi. An increase in intensity of the band at ca. 1130 cm^{-1} and its shift to higher wavenumbers with increasing temperature in presence of O_2 (A); decrease in intensity of the band at ca. 1260 cm^{-1} and its shift to lower wavenumbers during treatment at 450 ^oC in He flow (B).

An *in situ* Raman experiment was performed. The 8V1PAl catalyst was heated to 450 ^oC in oxygen flow, held for 1 hour under these conditions and subsequently for 30 minutes in helium flow. No changes in Raman spectra were observed.

8.5.1 Influence of water vapor

Figure 8.16 shows IR spectra during propylene desorption from the 8V1PTi surface in O_2 (10% in He) and H_2O stream. Moisture was introduced to the reactor with a syringe pump. After 20 min of the desorption process at 125 ^oC in presence of moisture the IR bands characteristic of the adsorbed propylene decreases in intensity, while a band at ca. 1615 cm^{-1} due to adsorbed water is

observed. This suggests weaker interaction of propylene with the catalyst surface in presence of water vapor. The temperature increase in presence of O_2 and H_2O leads to desorption of water to the gas phase, no bands characteristic of carbonaceous intermediates were observed (see Figure 8.17).

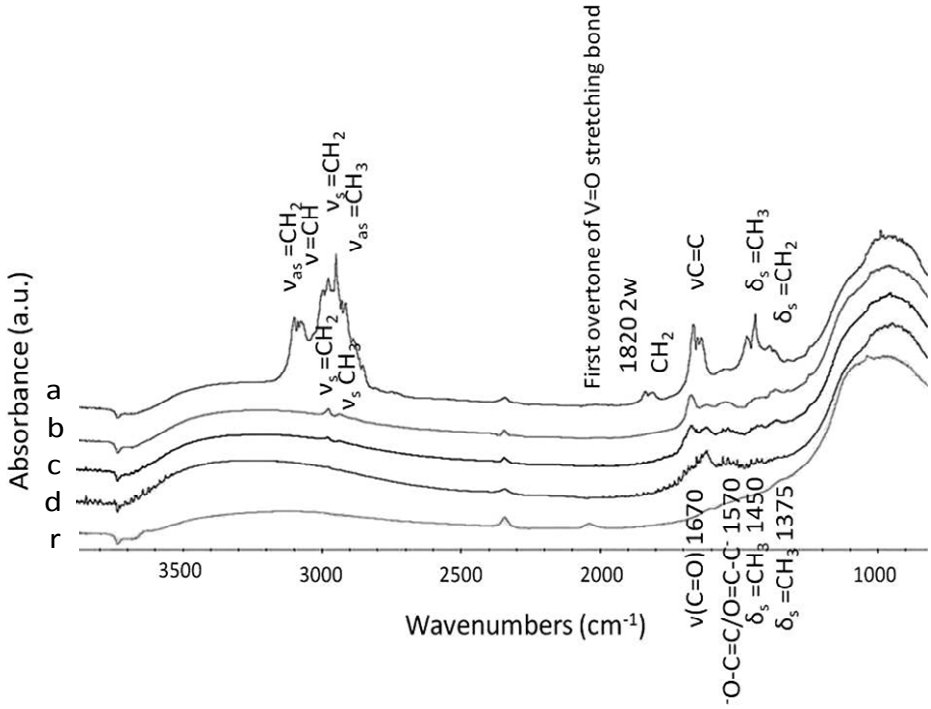

Figure 8.16 DRIFT reference spectrum of activated 8V1PTi (r), after C_3H_6 adsorption (a), after C_3H_6 purging step in He (b), after 10 minutes (c) and 20 minutes (d) of desorption process at 125 ^oC in O_2 (10% in He, 20 ml/min) and H_2O flow (1 ml/h). All spectra were acquired at 125 ^oC

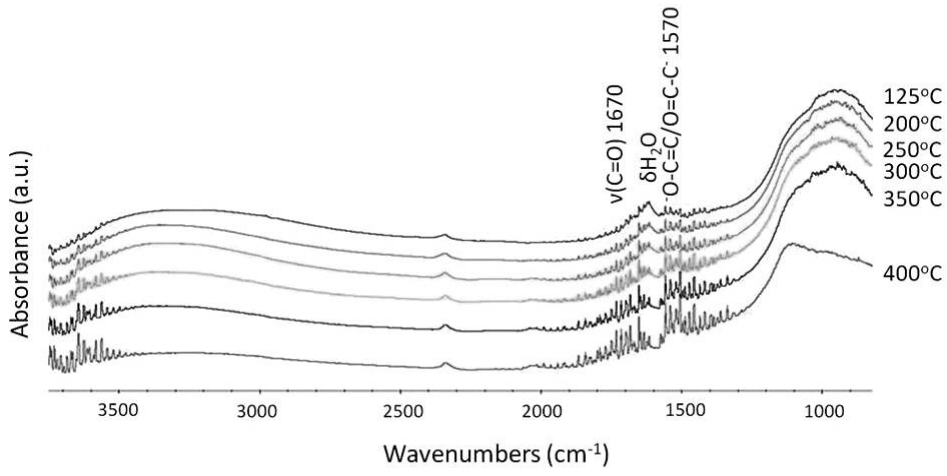

Figure 8.17 Desorption process from the 8V1PTi surface in presence of O_2 and H_2O

In order to verify the lower interaction of propylene with the catalyst surface in presence of water vapor a set of experiments with preadsorbed water was performed. Figure 8.18 compares spectra acquired during propylene adsorption at 125 ^{o}C on the dehydrated 8V1PTi surface and on the catalyst with preadsorbed water (hydrated 8V1PTi).

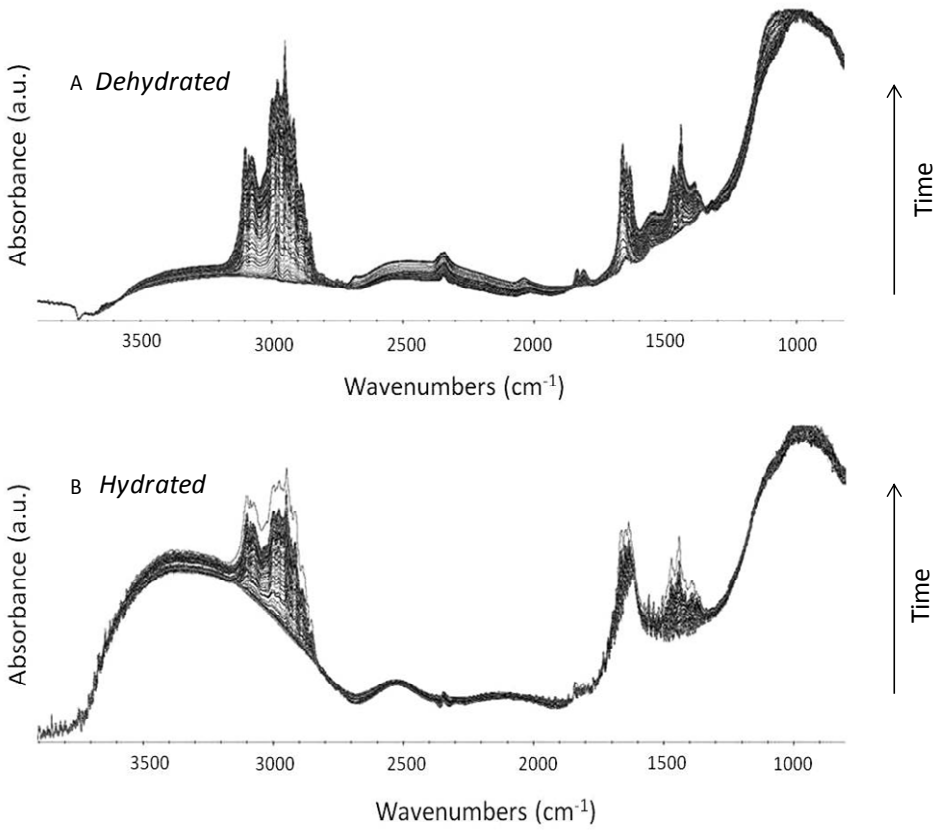

Figure 8.18 Propylene adsorption on the dehydrated 8V1PTi (A) and on the 8V1PTi surface with preadsorbed H_2O, hydrated 8V1PTi (B). Spectra acquired every 20 seconds

The weak interaction of propylene on hydrated 8V1PTi is confirmed by subsequent purging in He flow at 125 ^{o}C. Such a treatment leads to complete desorption of adsorbed propylene species from the surface in less than 30 min (see Figure 8.19).

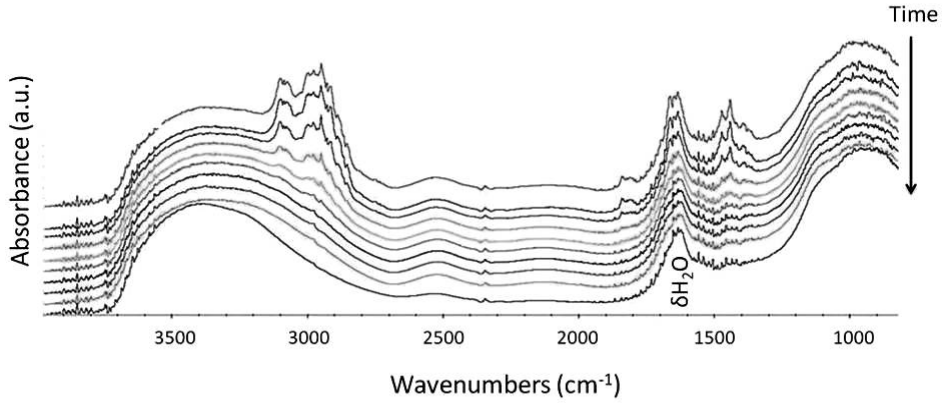

Figure 8.19 Purging process (125 °C, 30 minutes in He flow) of propylene adsorbed on the 8V1PTi surface with preadsorbed water

Only the IR bands of water vapor are apparent after ca. 15 minutes of purging. Figure 8.12 show that surface species originating from adsorbed propylene remain present on the dehydrated surface after ca. 20-40 minutes of the purging process at 125 °C in absence of steam. This proves that moisture facilitates the propylene desorption process.

8.5.2 Propane adsorption/desorption on alumina supported catalysts. The influence of phosphorus

Propane adsorption/desorption DRIFTS experiments on alumina-supported vanadium catalysts with varying P/V = 0, 0.1 or 1.1 help understanding the role of phosphorous additive. These catalysts were previously calcined for 19 hours in air at 450 °C, and subsequently activated in O_2 flow (10% in He) at 450 °C for 1h.

Figure 8.20 presents spectra of dehydrated activated 8V1PAl, which band at 2045 cm^{-1} corresponds to the first overtone of V=O stretching mode. This band shifts to 2025 cm^{-1} after propylene adsorption suggesting the existence of an interaction between vanadium and the adsorbed hydrocarbon. A broad band in the 3000-3700 cm^{-1} range is due to -OH groups characteristic of adsorbed water. The spectrum "a" in Figure 8.20 illustrates 8V1PAl after 40 min of propylene adsorption at 125 °C. This spectrum is characteristic of gas phase propylene,

which was subsequently removed by purging in He during 20 min at 125 °C (Figure 8.20b). In general, it can be observed that the adsorbed propylene forms the same species for phosphorus doped alumina- or titania-supported vanadium oxide catalysts.

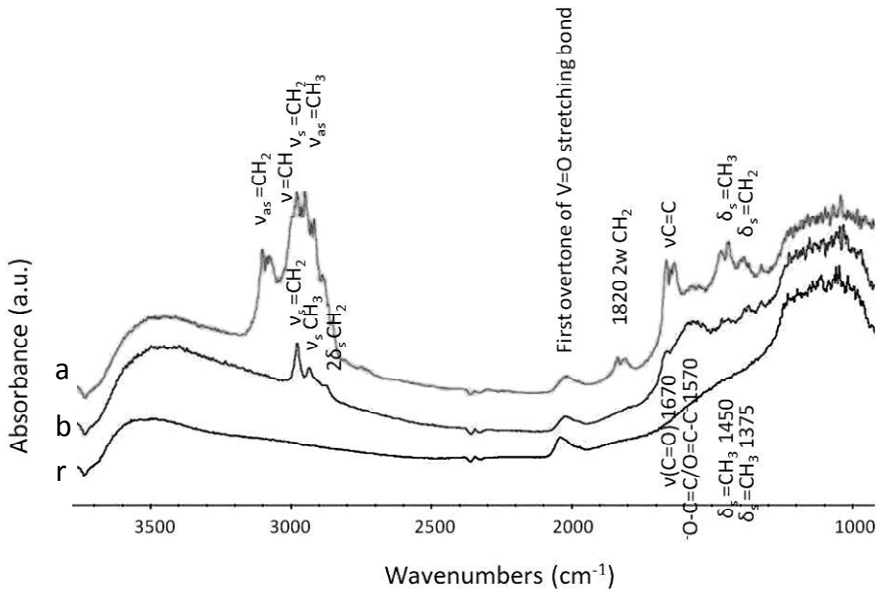

Figure 8.20 DRIFT reference spectrum of activated 8V1PTi (r), after 40 min C_3H_6 adsorption (a), after 20 min C_3H_6 purging step in He (b). All spectra were acquired at 125 °C

Figure 8.21 illustrates desorption of propylene species in oxygen flow. The band at 1670 cm^{-1} disappears already at 250 °C, while the shape of the bands at 1560 cm^{-1} and at 1450 cm^{-1} resembles those characteristic of carboxylate species (acetates or acrylates). The bands due to the cyclic anhydride become apparent at ca. 370 °C. The surface intermediates are no longer detected at 425 °C. The formation of the oxygenate species (mainly cyclic anhydrides) is also observed when propylene was desorbed in oxygen-free conditions (helium flow). This suggests that such species form by incorporation of the lattice oxygen (see Figure 8.22) and that the gas phase would, thus, be required for regeneration of the active site. This indicates that the Mars-van-Krevelen mechanism is operative for the propane oxidation to maleic anhydride, but the formation of

acetates or acrylates is rather unclear due to very low intensity of its IR bands 250-370 °C). The IR band at 1570 cm^{-1} is present even at 450 °C in anaerobic conditions, while that at 1670 cm^{-1} decreases. A very weak band at 1630 cm^{-1} appears along with two weak bands at 1870 and 1790 cm^{-1} at 350-400 °C. The band at 1630 cm^{-1} may be characteristic of the C=C bond of acrylate species (along with ν_{as} and ν_s COO bands at ca. 1570 and 1440 cm^{-1}) or of the allyl alcoholate species. The two latter bands are characteristic of symmetric and asymmetric C=O stretching of the cyclic anhydride system (O=C-O-C=O).

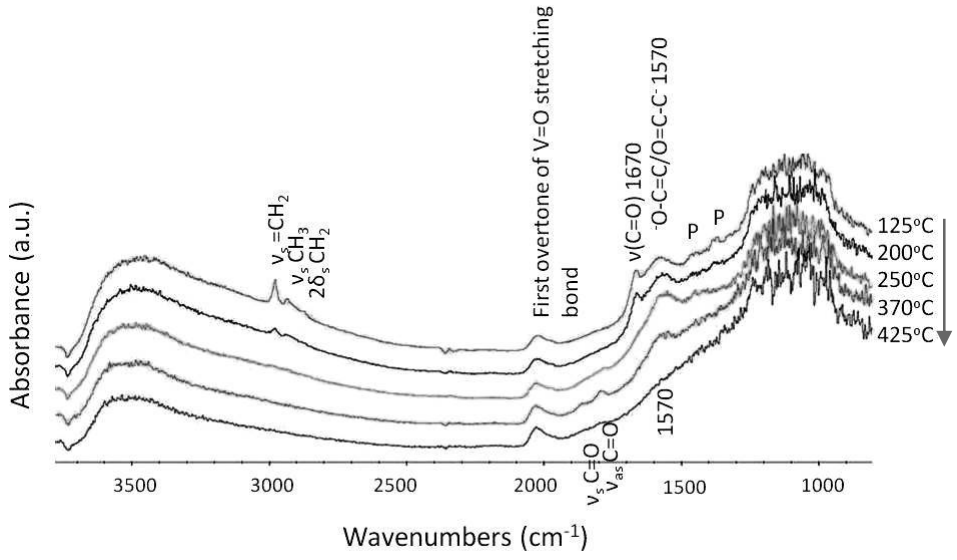

Figure 8.21 DRIFT spectra of the propylene desorption process in presence of oxygen from the surface of 8V1PAl (10% O_2 in He, flow: 20 ml/min), P: CH_3 and CH_2 modes of adsorbed propylene

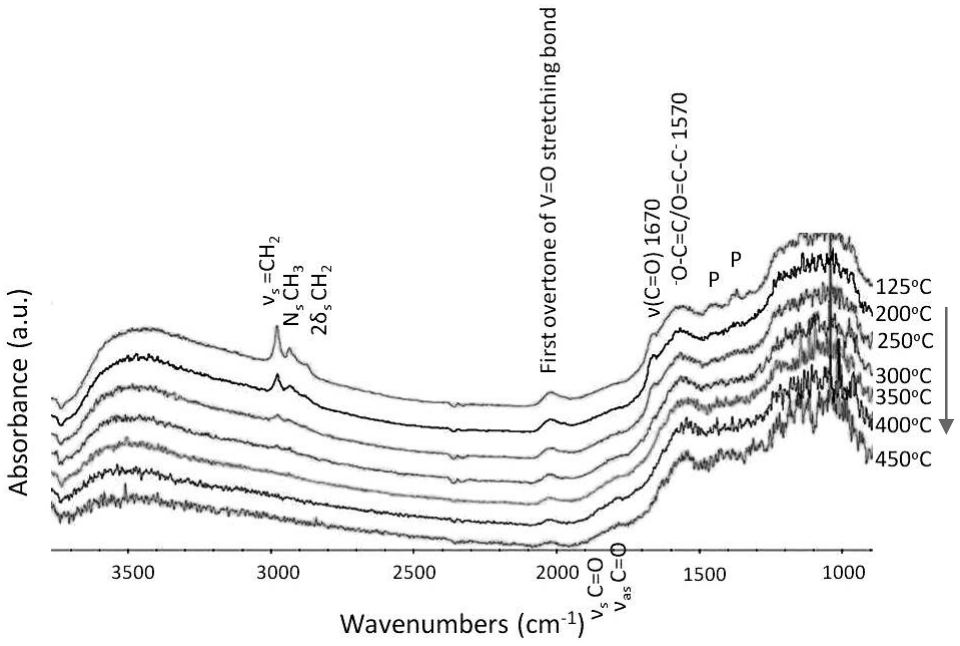

Figure 8.22 DRIFT spectra during propylene desorption process in absence of oxygen (He flow, 20 ml/min) from the surface of 8V1PAl, P: CH_3 and CH_2 modes of adsorbed propylene

For evaluation of the role of phosphorus, the same experiment was performed using catalysts with 0 and 1.1 P/V atomic ratio. DRIFT spectra of propylene desorption in O_2 flow from alumina-supported vanadium and phosphorus catalyst (8V9PAl) show the same trend observed for phosphorus doped alumina-supported vanadium catalyst (8V1PAl). However, a strong IR band at 1260 cm^{-1} due to the P=O stretch is apparent. This band strongly resembles that observed for 8V1PTi in presence of oxygen at 450 ^{o}C. Its intensity slightly decreases in the 300-350 ^{o}C temperature range. At the same time, IR bands due to reaction products (carboxylic species, cyclic anhydride species and CO_2) develop.

DRIFT spectra of propylene desorption in O_2 flow from the surface of alumina-supported vanadium oxide catalyst (8VAl) show the formation of carboxylate species at 250 ^{o}C. Intense IR bands at 1870 and 1790 cm^{-1} are observed in a temperature range between 300-400 ^{o}C. These bands are due to symmetric and asymmetric C=O stretchings of the cyclic anhydride and are much more intense comparing to the IR spectra of the phosphorus containing catalysts. According to literature, formation of the cyclic anhydride suggests that an allyl intermediate is

formed on Lewis acid sites by hydrogen abstraction from propylene. The allyl intermediate can dimerize with another propylene molecule and consequently, the product may be oxidized into maleic anhydride [19].

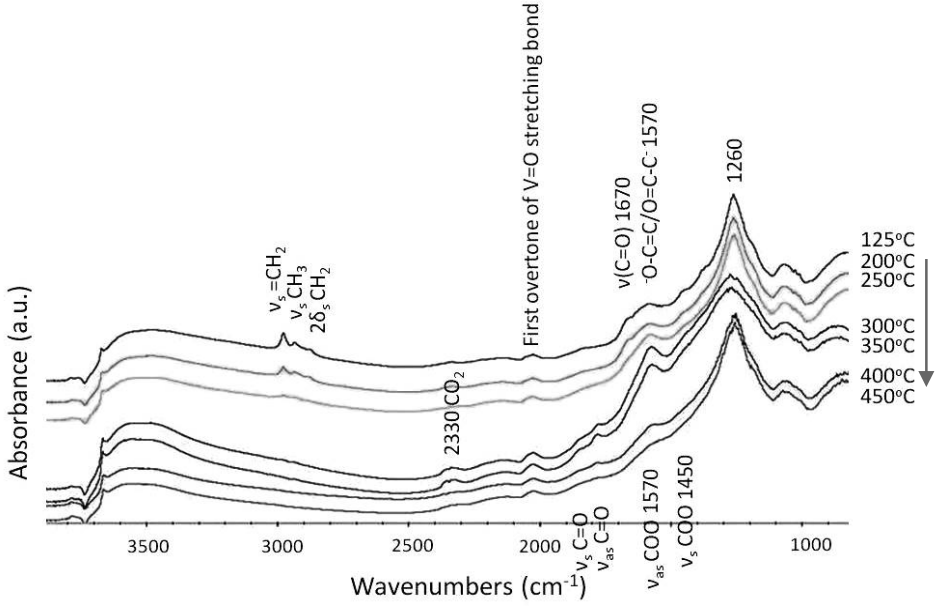

Figure 8.23 DRIFT spectra of the propylene desorption process in presence of oxygen from the surface of 8V9PAl (10% O_2 in He, total flow: 20 ml/min)

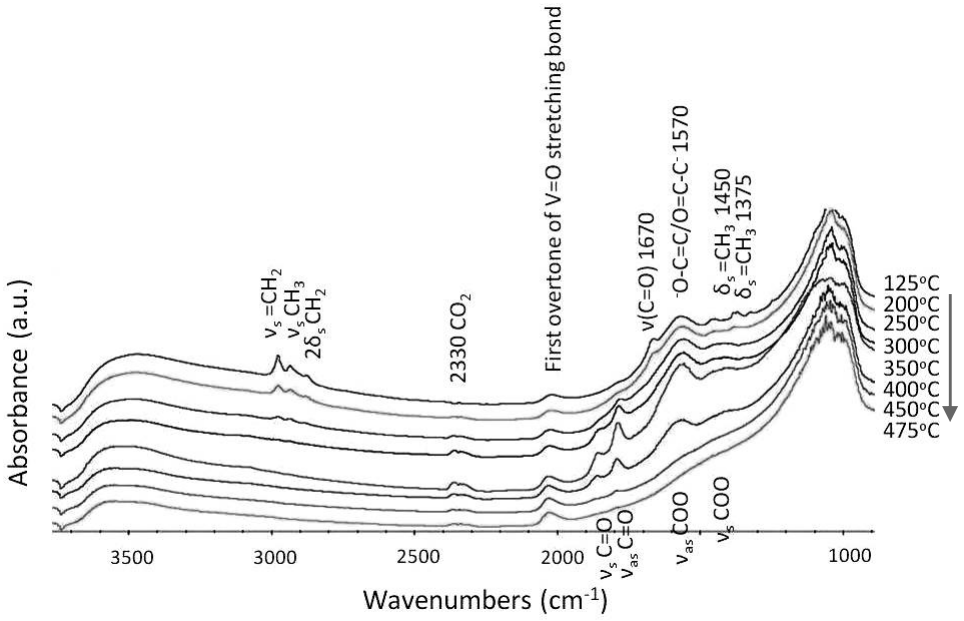

Figure 8.23 DRIFT spectra of the propylene desorption process in presence of oxygen from the surface of 8VAl (10% O_2 in He, total flow: 20 ml/min)

It was reported that phosphorus doping probably enhances the propane as well as propylene chemisorption on the vanadia surface sites, which leads to the formation of acrylic or acetic acids [[26]]. From our DRIFT studies it may be observed that propylene was easily adsorbed on the catalyst surface in the presence or in the absence of phosphorus. Strong chemisorption of reaction intermediates may deteriorate the catalytic performance. In the absence of phosphorus on the catalyst surface, formation of the cyclic anhydride seems to be favored over formation of acetate or acrylate species. This would suggest that phosphorus hinders dimerization of the allyl intermediate.

8.5.3 *Operando*-IR study of propane oxidation reaction over 8V1PTi

Propane oxidation in the presence of low concentration of water vapor on 8V1PTi at 100-350 ^{o}C was studied in details at *Laboratorie Catalyse et Spectrochimie (ENSICAEN)* in Caen using the *operando* FT-IR-MS methodology. The catalyst was pressed into self-supporting disc (ca. 20 mg, 16 mm diameter) and activated in Ar at 100 ^{o}C for 3 hours. Subsequently propane oxidation flow was introduced into the reactor. Formation of carboxylic intermediates was observed in the 250-350 ^{o}C temperature range, while the gas phase analysis performed with the IR Spectrometer shows consumption of

propane (2800-3100 cm^{-1}) and formation of reaction products. Formation of acetic acid in presence of low concentrations of water vapor was confirmed. Reference FT-IR spectrum of gas phase propane is shown in Figure 8.24.

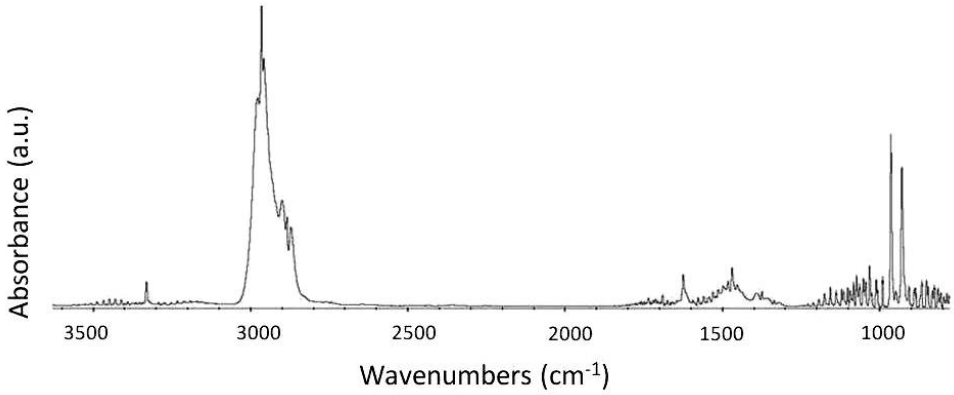

Figure 8.24 Reference FT-IR spectrum of gas phase propane

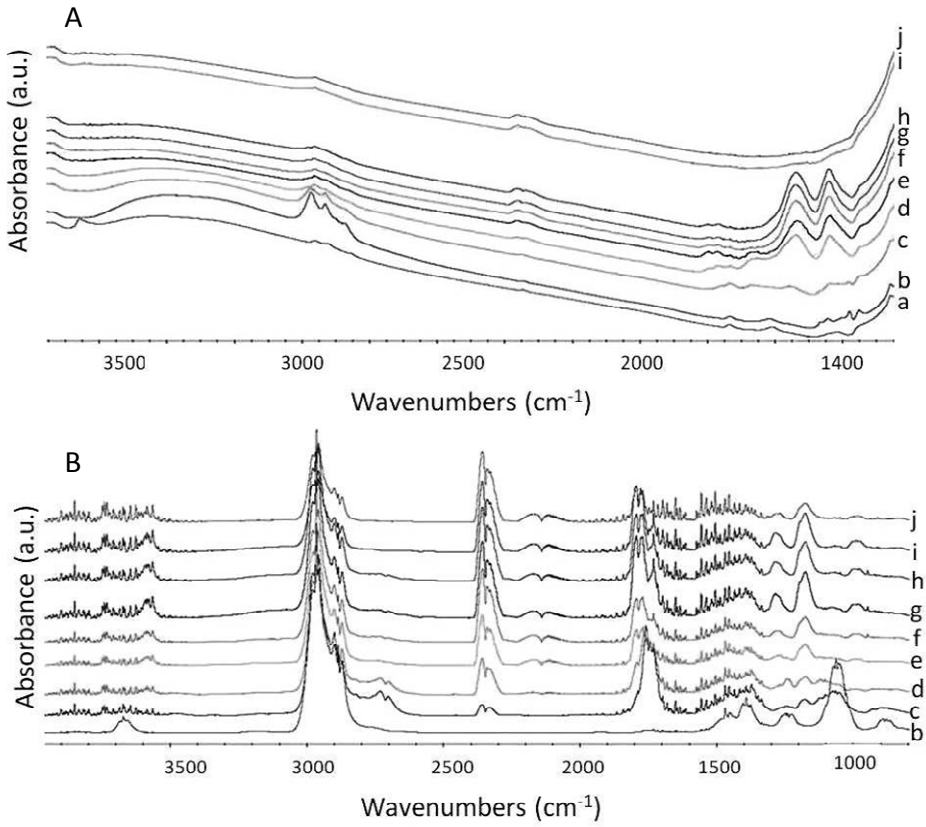

Figure 8.25 Propane oxidation in presence of steam. *Operando* FT-IR spectra of surface intermediates (A) and reaction gas phase (B); activated 8V1PTi (a), propane oxidation at 100 ^{o}C (b), 200 ^{o}C (c), 250 ^{o}C (d), 300 ^{o}C (e), 350 ^{o}C (f), 350 ^{o}C 10 min (g), 350 ^{o}C 30 min (h), 350 ^{o}C 60 min (i), 350 ^{o}C 90 min (j). Total flow: 5 ml min^{-1}; 20.4% O_2, 12.5% C_3H_8 and ca. 5-8% H_2O in He

The gas phase contains a mixture of propanol and propane at 100 ^{o}C. However, the IR band at ca. 1400 cm^{-1} suggests that also ethanol is formed at this temperature. The IR bands due to acetaldehyde are shown in the spectrum acquired at 200 ^{o}C, while at higher temperature acetic acid forms. Bands characteristic of CO_2 (2300-2400 cm^{-1}) and CO (2100-2200 cm^{-1}) are observed already at 200-250 ^{o}C as well as an increase in intensity with temperature. This suggests that propane molecule is cracked in presence of 5-8% of water vapor at 100-200 ^{o}C during oxidation conditions.

Comparison of the gas phase spectra acquired at 200 and 350 ^{o}C with acetic acid, acrylic acid and acrolein references from a database (NIST) is shown in

Figure 8.22. Spectrum “b” from the Figure 8.22 shows bands characteristic of the remnant of propylene, of CO, CO_2, acetic acid and probably acrolein.

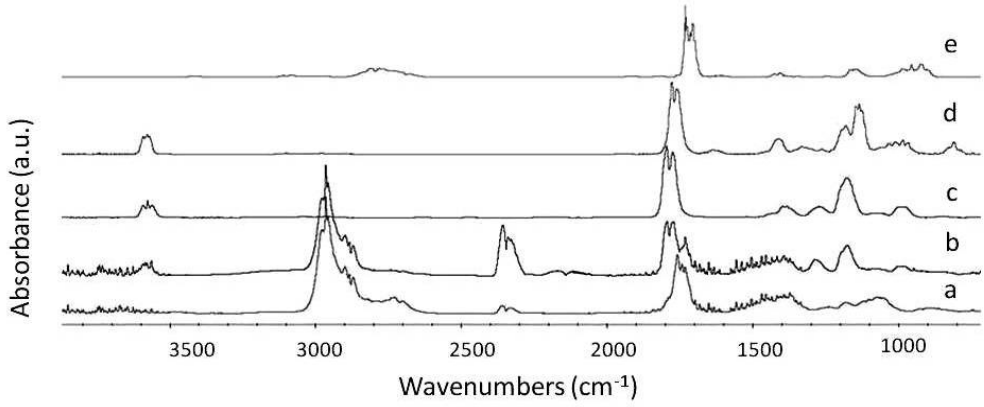

Figure 8.22 *Operando* FT-IR spectrum of 8V1PTi under propane oxidation conditions at 200 ^{o}C (a), after 10 min at 350 ^{o}C (b) and references: acetic acid (c), acrylic acid (d), and acrolein (e)

The same experiment was performed in absence of water vapor. Figure 8.23 shows the *operando* FT-IR spectra of reaction intermediates (A) and the spectra of the reaction gas phase (B). Propane conversion is low and the only products of this reaction at 350 ^{o}C were CO and CO_2, which is in accordance with the chromatographic analyses. Two IR bands at 1620 and 1660 cm^{-1} are observed in Figure 8.23A at 100 and 300 ^{o}C. The band at 1660 cm^{-1} is due to ν(C=O), while the band at 1620 cm^{-1} was observed already after the activation process and might suggest the presence of some impurities. Both bands disappear at 350 ^{o}C, and low intense bands characteristic of carboxylate species are observed along with surface CO_2 species. The absence of acetic or acrylic acids in the gas phase suggests that carboxylate compounds are formed even in absence of water vapor, but they are burned to CO_x before desorption from the catalyst surface. This would be related to very strong interaction of reaction intermediates with the catalyst active site. The slow desorption process would explain the combustion of propylene as well as low its low degree of conversion.

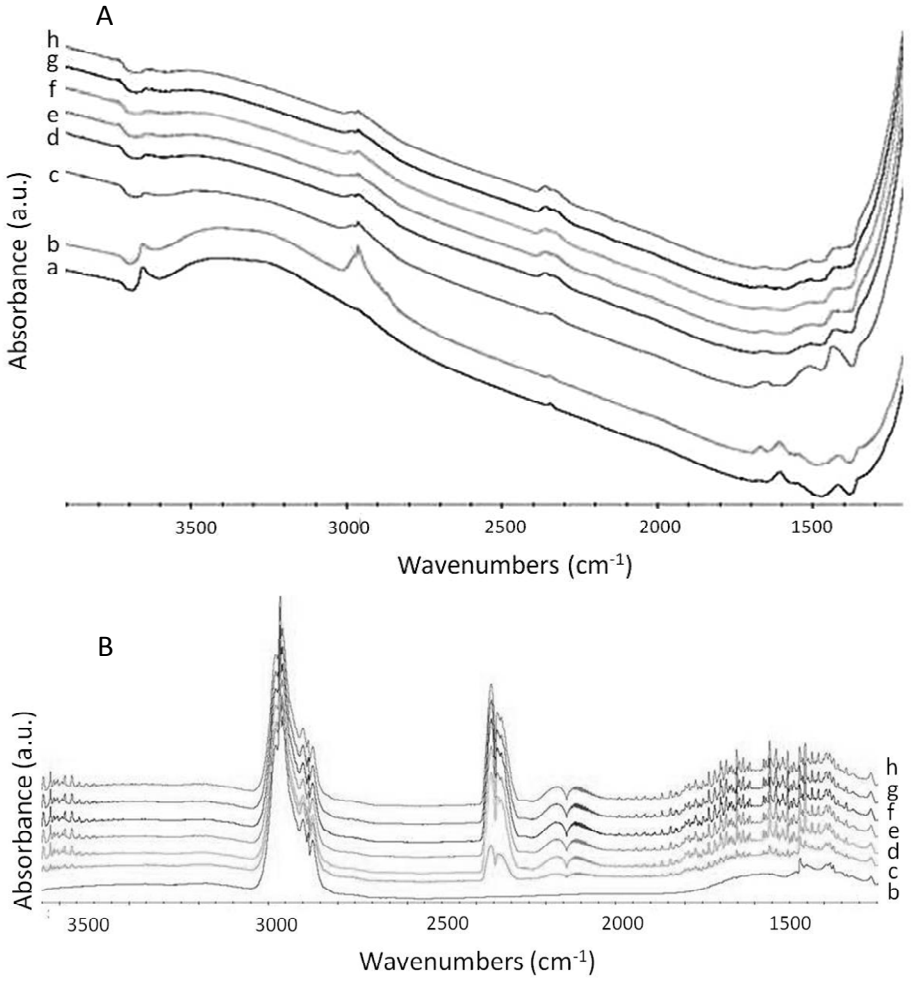

Figure 8.23 Propane oxidation reaction in the absence of water vapor. *Operando* FT-IR spectra of surface intermediates (A) and reaction gas phase (B); activated 8V1PTi (a), propane oxidation reaction at 100 ^{o}C (b), 300 ^{o}C (c), 350 ^{o}C (d), 350 ^{o}C 10 min (e), 350 ^{o}C 30 min (f), 350 ^{o}C 60 min (g), 350 ^{o}C 90 min (h). Total flow: 5 ml min^{-1} corresponding volumetrically to 20.4% O_2, 12.5% C_3H_8 in He

8.6 SUMMARY

Phosphorus-doped titania- and alumina-supported vanadium oxide catalysts are effective in low temperature propane oxidation reaction in presence of moisture. The catalyst is active in the absence of water vapor. However, in the presence of moisture, the activity increases, while the acrylic acid/acetic acid product ratio strongly depends on the water vapor partial pressure. Acetic acid and CO_x are the main products at low water concentrations (ca. 5-8%), while acrylic acid becomes the main reaction product at higher water concentration values (ca. 16%). This indicates that the higher concentration of steam prevent breaking of the propane molecule. In situ spectroscopic studies were performed to understand the rational of the promoting effect of water.

8.6.1 Surface species, competitive adsorption of water and propylene

DRIFTS experiments indicate that propylene undergoes transformations with increasing temperature according to the proposed path:

$$\text{Propylene} \rightarrow (\text{Isopropyl alcohol}) \rightarrow \text{Acetone} \rightarrow \text{Carboxylic species} \rightarrow CO_x$$

Where the parenthesis indicates a possible intermediate. This suggests that propylene adsorbs on the surface of supported vanadium and phosphorus oxide catalysts undergoing an attack, probably at its C_2 position, by a proton of surface -OH groups introducing the oxygen to the reacting molecule. DRIFTS experiments performed in the presence of water vapor indicate competitive adsorption of water and propylene on the surface. Water adsorption is stronger than that of propylene. This may significantly facilitate the desorption process of the reaction products and could avoid their overoxidation. Faster desorption also leads to higher reaction rates and to an increase of the propane/propylene conversion. A weak interaction of the adsorbed propylene molecule with the catalysts surface in presence of higher steam concentrations may avoid cracking of the propylene molecule leading to the formation of acrylic acid instead of acetic acid.

Aerobic and anaerobic reaction conditions deliver oxygenated reaction products in the absence of moisture. Despite that the band intensity of reaction intermediates was low when no oxygen was supplied, this experiment indicates that the molecular oxygen is not necessary for the cyclic anhydride formation.

8.6.2 Propane dimerization to cyclic products. The role of phosphorus additive

Formation of a cyclic anhydride was observed during the propylene oxidation reaction over titania- and alumina-supported catalysts in absence of water vapor. The IR bands due to the cyclic anhydride were also present during *operando* FT-IR studies of propane oxidation in presence of moisture. This suggests propylene

dimerization, probably through formation of an allyl intermediate on vanadium Lewis acid sites. However, the IR bands of such an intermediate were not detected; thus, this mechanism remains unverified. Moreover, phosphorus addition (already at P/V = 0.1) seems to hinder the formation of the cyclic products. Thus, the formation of the cyclic anhydride would not be related only to Lewis sites since Chapter 6 demonstrated that the Lewis/Brønsted acid sites ratio increases upon phosphorus addition.

An interesting scenario was observed during propylene desorption from the 8V1PTi in O_2 flow (10% in He). An IR band appears at 1135-1260 cm^{-1} at elevated temperatures. It is only detected in the presence of oxygen and disappears when the feed is switched to helium. This band was not observed for the phosphorus-doped at low P/V ratios (8V1PAl), but it was present at higher P/V ratios in supported VPO catalyst (8V9PAl). This suggests that it might be due to the P=O stretch of phosphate species. It was shown that the crystallization process occurs more easily on the alumina support. The V_2O_5 crystallites may conceal the IR P=O features. The formation of crystallites of V_2O_5 was not apparent on titania-supported samples. The Tamman temperature is lower for phosphorus oxide than for crystalline vanadium oxide (ca. 30 ^oC for P_2O_5 *vs*. ca. 200 ^oC for V_2O_5) and the oxygen, in contrast to inert gases, favors the agglomeration process, which subsequently leads to crystallization. Thus, possibly some dynamic changes occur on the surface of the 8V1PTi catalyst at high temperatures and in presence of oxygen leading to an inverse aglomeration of phosphorus species on the catalyst surface.

References

[1] M. Ai, *J. Catal*. 101 (1986) 389

[2] M. Ai, *J. Mol. Catal*. A 114 (1996) 3

[3] G. Landi, L. Lisi, G. Ruso, *J. Mol. Catal*. A 239 (2005) 172

[4] F. B. Abdelouahab, R. Olier, N. Guilhaume, F. Lefebvre, J. C. Volta, *J. Catal.* 134 (1992) 151

[5] N. Venkatathri, S. G. Hegde, V. Ramaswamy, S. Sivasanker, *Microporous Mesoporous Mater.* 23 (1998) 277

[6] S. Devika, M. Palanichamy, V. Murugesan, *J. Mol. Catal*. A 351 (2011) 136

[7] Z.-Y. Xue and G. L. Schrader, *J. Phys. Chem*. B, 1999, 103, 9459

[8] S. Xie, E. Iglesia, A.T. Bell, *Langmuir* 16 (2000) 7162

[9] Z. Wu, H. S. Kim, P. C. Stair, S. Rugmini, S. D. Jackson, *J. Phys. Chem.* 109 (2005) 2793

[10] X. Gao, J. Xu, *Appl. Clay Sci*. 33 (2006) 1

[11] H. Zhao, S. Bennici, J. Cai, J. Shen, A. Auroux, *Catal. Today* 152 (2010) 70

[12] C. V. Ramana, O. M. Hussain, B. Srinivasulu Naidu, *Matter. Chem. Phys.* 50 (1997)195

[13] Y. Iida, Y. Kaneko, Y. Kanno, *J. Matter. Proces. Tech*. 197 (2008) 261

[14] E. Mikolajska, E. Rojas Garcia, R. Lopez Medina, A. E. Lewandowska, J. L. G. Fierro, M. A. Bañares, *Appl. Catal.* A, 404 (2011) 93

[15] E. Mikolajska, S.B. Rasmussen, A.E. Lewandowska, M.A. Bañares, *Phys. Chem. Chem. Phys.* 14 (2012) 2128

[16] G. Busca, *Mater. Chem. Phys*. 19 (1988) 157

[17] G. Ramis, G. Busca, V. Lorenzelli, *J. Chem. Soc., Faraday Trans*. 90 (1994) 1293

[18] G. Delle Piane, J. Overend, *J. Spectrochim. Acta* 22 (1966) 593

[19] W. O. George, V. G. Mansell, *Spectrochim. Acta* 24 (1968) 145

[20] V. Sanchez Escribano, G. Busca, V. Lorenzelli, *J. Phys. Chem*. 94 (1990) 8939

[21] N. T. Sheppard (Ed.), A. Davydov. *Molecular Spectroscopy of Oxide Catalyst Surfaces*, John Willey & Sons Ltd. (2003) ISBN: 0-471-98731-X

[22] L. J. Bellamy, B. R. Connelly, A. R. Philpotts, R. L. Z. Williams, *Electrochem*. 64 (1960) 563

[23] M. Bosacka, *Therm. Acta* 523 (2011) 137

[24] S. K. Arora, T. R. Trivedi, A. T. Oza, V. A. Patel, *Acta Mater*. 49 (2001) 2103

[25] A. John, D. Philip, K. R. Morgan, S. Devanarayanan, *Spectrochim. Acta* 56 (2000) 2715

[26] R. K. Grasselli, C. G. Lugmair, A. F. Volpe Jr., A. A. Andersson, J. D. Burrington, *Catal. Today* 157 (2010) 33

9

Discussion and concluding remarks

9.1 INTRODUCTION

A summary of the results described in this Thesis is presented in the following chapter. Characterization of bulk and supported vanadium and phosphorus oxide catalysts will be discussed with emphasis on the use of bulk and surface-sensitive analytical methods. Structure-activity relationships of bulk and supported VPO-type catalysts for propane (amm)oxidation reactions will be considered as well as the influence of the phosphorus additive on vanadium-based catalysts and the role of moisture in propane oxidation reactions.

9.2 Discussion

The main objective of this dissertation is to analyze the structure of bulk and supported vanadium and phosphorus oxide catalysts, their activity in selective propane (amm)oxidation reactions and to determinate a relationship between them. Many factors must be considered in order to find an active and selective catalytic system. They relate not only to the conditions of the catalytic process, but also to the nature of the catalyst, its composition and applied preparation method. A series of alumina- and titania-supported vanadium and phosphorus oxide catalysts were synthesized using an incipient wetness impregnation method. These catalysts were compared to an industrial bulk VPO catalyst, which was commercially encapsulated in a porous silica shell in order to improve the attrition resistance of the catalyst particles. Characterization of catalysts, fresh and under catalytic process plays a very important role in catalytic design. It is a key-factor to understand the nature of the active sites. As reported in section 1.2 a careful selection of analytical techniques is necessary, especially for characterization of bulk catalysts. Thus, the catalysts were characterized by application of bulk and surface-sensitive analytical techniques for the purpose of identification of their active sites. The structure of supported VPO catalysts may be analyzed using conventional spectroscopic methods due to low loading of the active phase on the support and hence, higher surface-to-bulk ratio. Characterization of supported VPO-type catalysts is described in Chapters 4 and 5. Formation of the $V^{4+}OHPO_4 \cdot 0.5H_2O$ (vanadyl pyrophosphate precursor) for as-prepared supported VPO-type catalyst was confirmed by Raman and EPR studies. The Raman data has shown that calcination process (in presence of oxygen) leads to formation of γ-$V^{5+}OPO_4$ and V_2O_5 phases on the alumina surface. Temperature treatment of the catalyst precursor performed in inert atmosphere prevents the overoxidation of vanadium species and formation of crystalline phases. Therefore, these catalysts possess only amorphous phases on the alumina support, even at higher loading of four (V+P) monolayers.

According to XRD and Raman data the bulk structure of the industrial VPO catalyst was determined as vanadyl pyrophosphate phase. However, even though the surface science plays a key-role in understanding of the catalytic properties of the analyzed material, the surface of VPO catalysts is still poorly known [1]. Thus, the High Sensitivity LEIS analysis was applied for study of the surface structure and composition of the VPO catalyst (see Chapter 3). It was shown that vanadium, phosphorus, silicon and oxygen are present at the catalyst surface. This confirms that the VPO phase is embedded on the silica shell. However, the SiO_2 is also exposed, which suggests that bigger crystallites of VPO phases form

on the silica shell, probably due to low dispersion limit of the SiO_2. This is confirmed by low Si/V and Si/P ratios determined from the HR-XPS spectra. Thus, we suspect that the V_2O_5, which was observed by Raman study of the fresh industrial VPO catalyst, was formed on the exposed SiO_2, and that its low dispersion limit loading prevents dispersion of V_2O_5 crystallites at high temperatures in oxidizing atmosphere. The sputtering process during LEIS studies shows that after first doses of Ar^+ ions, the peak areas of vanadium, phosphorus and oxygen increase. As described in Chapter 3, this effect is probably due to removal of contaminants present on the catalyst surface. Peak areas of oxygen and phosphorus stabilize after ca. 5 Ar^+ doses, while peak area of vanadium increases continuously. This suggests that contaminants adsorb preferentially on vanadium sites. An additional explanation of this phenomenon might be a surface deficiency of vanadium, which would explain the continuous increase of vanadium amount up to 40 ion doses. High P/V atomic ratio, from 1.5 to 3, was reported in literature according to XPS studies of bulk VPO catalysts [2,3,4,5]. In our case the P/V = 2.7 was detected. It is believed that that the surface of bulk VPO catalysts is enriched in the extent of phosphorus used during synthesis. The $(VO)_2P_2O_7$ structure was determined by XANES and EXAFS study as edge-sharing VO_5 square pyramids bridged by PO_4 double tetrahedra [6,7,8]. However, since these are bulk techniques the surface enrichment in phosphorus was not taken into account. Considering P/V, O/V and Si/V atomic ratios, the following structure of VPO phase present at the 12 outermost layers may be proposed:

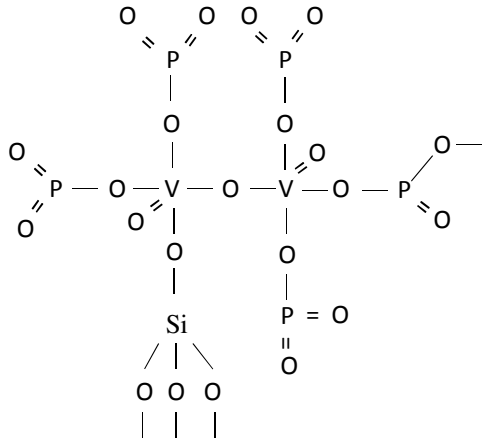

Figure 9.1 Structure of VPO phase designed according to HR-XPS data

However, the LEIS analyses show that *de facto*, the P/V atomic ratio increases during sputtering of subsequent layers from VPO catalyst, but this effect is rather related to the deficiency of vanadium in the outer layers or it is caused by the shielding effect of gaseous contaminants adsorbed on vanadium sites. It is supported by the fact that the slight decrease of the phosphorus peak area is not related to the increase of the vanadium peak area, as would be expected in case of surface phosphorus enrichment. Thus, according to results obtained from the LEIS studies, the followed scenario is proposed for the industrial VPO catalyst encapsulated in the silica shell:

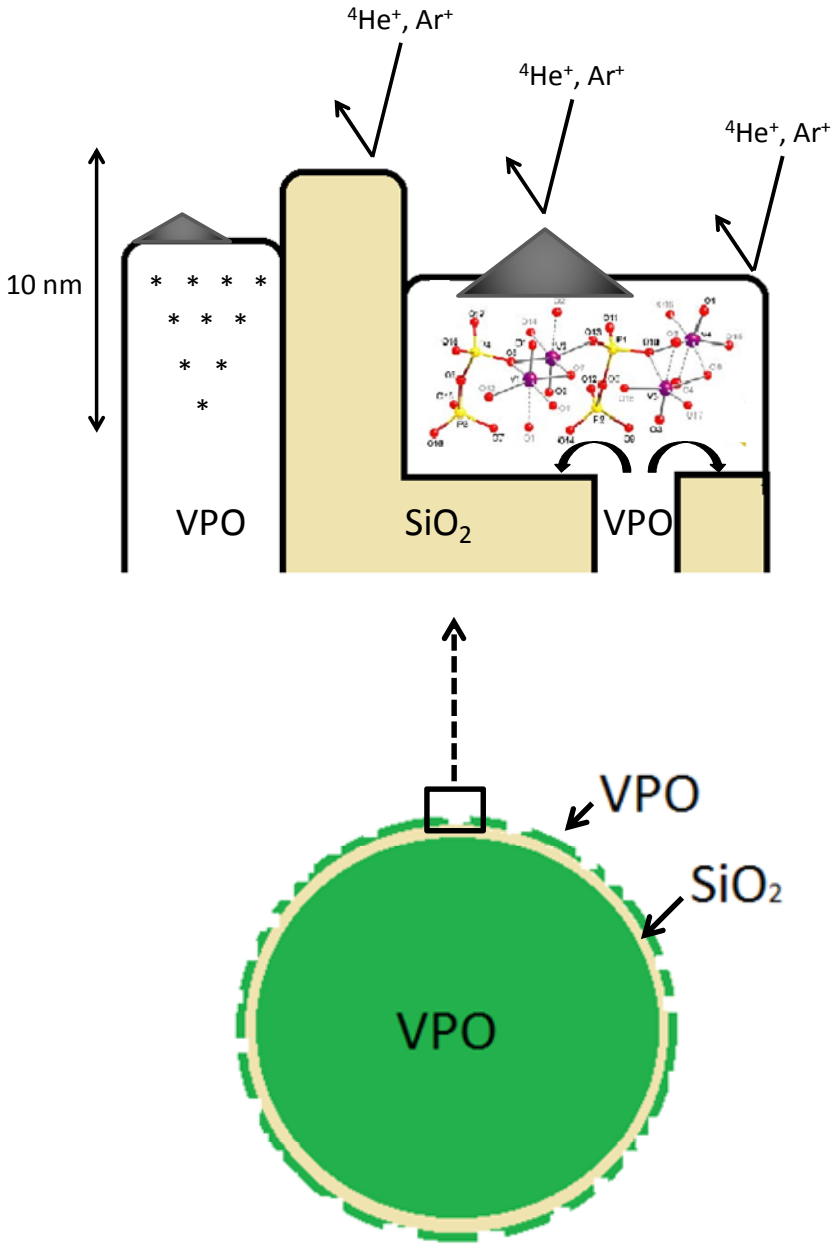

Figure 9.2 Structure proposed for the encapsulated in silica shell industrial VPO; (*) – vanadium vacancies and grey triangles – gaseous contamination. The structure of vanadyl pyrophosphate, where violet bolls stay for vanadium, yellow bolls for phosphorus and red bolls for oxygen was reprinted from a work published by O. F. Ikotun et. al [9]

As reported in Chapters 3 and 5, the XPS, TPR, UV-vis and XANES techniques show that the bulk VPO catalyst contains essentially V^{4+} species. However, all these techniques are considered as bulk ones, so that the signal from the bulk significantly contributes to the reading. The HR-XPS study is the most representative technique for evaluation of the oxidation state of the vanadium surface species. Assuming the escape depth of 3 nm it provides information about first 12 monolayers approximately. In this case the percentage of V^{5+} species determined by curve fitting and Clouston's formula relates to ca. 1-3 monolayers (assuming that 12 monolayers of vanadium species were analyzed). Only up to 25% of vanadium analyzed possesses +5 oxidation state. These species may be present on the silica shell or on the topmost layers of vanadyl pyrophosphate phase. The XPS, TPR, UV-vis and XANES analyses of alumina-supported VPO catalyst presented in Chapters 4 and 5 show that the alumina support stabilizes V^{5+} species. This catalyst consists of 2 monolayers of V+P, so that the contribution of the bulk phase does not take place in this case. The average oxidation state of vanadium determined by XPS using the curve fitting method and the Clouson's formula is between ca. +4.3 and +4.5. However, as mentioned in Chapter 5, the O 1s satellite line in vanadium XP spectra challenges the determination of the vanadium oxidation state with a satisfying precision. Thus taking the TPR and XANES data for further consideration, we propose the average oxidation state of the alumina-supported VPO catalyst in a range between $+4.5 \leq V_{AOS} \geq +4.8$, which gives 50-80% of V^{5+} surface species. It was reported that phosphorus addition is responsible for an increase of V^{4+}/V^{5+} ratio in vanadium and phosphorus oxide catalysts [10,11,12,13]. Our TPR studies have shown that under reductive environment phosphorus stabilizes V^{4+} species. The hydrogen consumption was calculated from the reduction peak observed at ca. 550 ^{o}C showing the H/V ratio 1.9 for alumina-supported vanadium oxide catalyst (8VAl) and 0.7 for alumina-supported vanadium and phosphorus oxide catalyst (8V9PAl). These results indicate that in contrast to 8V9PAl, in absence of phosphorus reduction from V^{5+} to V^{3+} occurs. The EPR spectroscopy was used for study of V^{4+} species in alumina-supported VPO catalysts. The contribution to the EPR spectra originates from polymeric V-O-V and monomeric VO^{2+} species, while the monomeric contribution is quantitatively less than 10% of the polymer. The polymeric signal exhibits a behavior that is concurrent with that of the vanadyl pyrophosphate phase, while the signal of monomeric vanadium species according to literature may originate from scattered $VOHPO_4$ and $VOPO_4$ defects [14,15]. Catalyst characterization provides important information about the nature of catalysts. This knowledge is necessary for the design of catalytic materials endowed with the required properties.

However, even though the catalyst does not appear itself in the products of the catalytic process, it may still undergo transformations – structural changes leading to activation or deactivation of the catalytic material. Thus, for fully understanding of the structure-activity relationships the catalyst structure should be also investigated under working conditions [16,17]. Alumina-supported VPO-type catalysts were studied for propane ammoxidation reaction to acrylonitrile. The results obtained from the conventional catalytic tests and *operando* Raman-GC studies are presented in Chapter 7. It was shown that the activity decreases with increasing P/V ratio. The bare alumina support as well as the individual phosphorus oxide supported on alumina is hardly active in this reaction. However, the V-P interaction is required for acrylonitrile production. The alumina-supported vanadium oxide catalyst even though it is active in propane ammoxidation reaction, is not selective to acrylonitrile. When both, P+V are supported on alumina, the yield to acrylonitrile reaches ca. 45 % at 500 ^{o}C. This value is similar to that obtained for the bulk VPO catalyst (ca. 40 % at 500 ^{o}C), however, an unquestionable economical advantage comes from the fact that the supported catalyst contains only ca. 50 w% of the active phase comparing to the industrial VPO catalyst. The good catalytic performance of the supported VPO catalysts is probably related to higher BET area, and thus higher accessibility of the active sites as well as to higher population of V^{5+} species stabilized by the alumina support, since V^{5+} species are responsible for activation of hydrocarbons [18,19]. Higher selectivity of the supported VPO catalyst to acetonitrile if compared to the industrial VPO catalyst, suggests that V^{5+} species are responsible for acetonitrile formation. It is supported by the fact that acetonitrile becomes the main reaction product for the alumina-supported vanadium catalyst (no phosphorus addition). Participation of V^{5+} species in acetonitrile formation was also confirmed by *operando* Raman-GC studies presented in Chapter 7 (Figure 7.14). It was shown that the selectivity to acetonitrile increases significantly after oxidation of the working catalysts in air flow at 500 ^{o}C for 30 min. In turn, higher selectivity of the industrial VPO catalyst to acrylonitrile suggests that the vanadyl pyrophosphate phase or V^{4+} species are required for acrylonitrile formation. *Operando* Raman-GC studies were performed in order to evaluate the structural transformations of the alumina-supported VPO-type catalyst with higher population of V^{5+} surface species and of its precursor containing mainly V^{4+} species. The 8V9PAl precursor shows high selectivity to acrylonitrile already at low temperature range, 425 – 450 ^{o}C, which is probably related to $(COOH)_2$ decomposition. At this temperature range, the Raman feature at 1022 cm^{-1}, corresponding to the V=O stretch of the supported V^{5+} species, is observed. Considering the fact that

the fresh 8V9PAl precursor consists of the $V^{4+}OHPO_4 \cdot 0.5H_2O$ phase it may be concluded that this crystalline phase undergoes decomposition under reaction conditions which leads to exposure of V^{5+} surface species (as confirmed by Raman), while the amorphous phases containing V^{4+} species are not detected by Raman spectroscopy. At a higher temperature range (475-500 ^oC), new Raman features are observed at 860 and 923 cm^{-1}. Raman spectra of the preactivated 8V9PAl obtained at 500 ^oC demonstrate essentially the same Raman features at 870, 923 and 1022 cm^{-1}, but their relative intensity is different. With increasing reaction temperature the Raman band at 1022 cm^{-1} decreases significantly in intensity, while the Raman band at 923 cm^{-1} increases, which reflects a combination of dispersed vanadium oxide and phosphorous into such VPO phase during reaction. The 8V9PAl pretreated in nitrogen atmosphere is more selective to acrylonitrile than its precursor. According to previously drew conclusion it indicates higher population of V^{4+} species in the pretreated catalyst. It is further supported by presence of the Raman band at 1022 cm^{-1} at 500 ^oC for the 8V9PAl precursor. During 60 hours time on stream the band at 923 cm^{-1} observed for the pretreated 8V9PAl shifts to 933 cm^{-1}, which may suggest coexistence of $V^{5+}OPO_4$ phases. This is probably related to redox cycles that would induce additional changes. At the same time the selectivity to acetonitrile slightly increases. Time-on-stream *operando* Raman-GC tests prove the stability of both catalysts for propane ammoxidation during at least 60 hours on stream at 500 ^oC. The observed stability of the activity of the catalyst after activation combined with the simultaneous fluctuations of the 923 cm^{-1} band, might suggest that the $(VO)_2P_2O_7$ phase is "only" indirectly related to the propane ammoxidation reaction. Thus, a deconvolution of Raman spectra was done in order to suggest a relationship between transformations of species in reaction feed. These results are presented in Figure 7.15 in Chapter 7. It was shown that The Raman band near 877 cm^{-1} seems to be related to the critical phase for propane ammoxidation. This band was assigned to V_2O_7 [20] or the stretching vibrations of $P(OH)_2$ groups [21] according to the literature. However, the *in situ* Raman experiment performed with D_2O as a probe molecule excluded presence of M-OH bands under reaction conditions, since no shift of Raman bands was observed. Thus, for the sake of the relation of this band to the selectivity to acrylonitrile an attempt of the band assignment was performed using UV Raman spectroscopy. The UV Raman spectra appear to be more sensitive to the out-of-plane bending and symmetric stretching vibrations of bridging oxygen species (M-O-M). The increase in intensity of the band at ca. 875 cm^{-1} (and decrease in intensity of the band at 1014 cm^{-1}) if compared to the experiment performed with visible Raman spectroscopy suggest that it may be related to the V-O-M

(where M states for V,P or Al) bonds in polymeric surface species. However, the UV Raman was reported to be a powerful tool also for characterization of reduced vanadium species [22]. The Raman spectra of 8V9PAl in reductive and oxidative atmosphere (shown in Figure 7.13) indicate that the Raman feature near 877 cm^{-1} appears in highly reductive conditions, while the reoxidation at 300 ^{o}C recovers the Raman band characteristic of vanadyl pyrophosphate phase. This could suggest presence of highly reduced vanadium species, already proposed in literature [23,24]. However, bands associated to V^{3+} were not observed with visible Raman spectroscopy. The fact that the 877 cm^{-1} band was acquired with 514 nm Ar excitation line, combined with the results obtained using the 325 nm excitation line suggests that this band might be assigned to mixed valence V-O-M bonds. Considering the catalytic performance of the 8V9PAl catalyst ($+4.5 \leq V_{AOS} \geq +4.8$) and its precursor (essentially V^{4+} species) it may be concluded that these catalysts reach a specific V^{4+}/ V^{5+} equilibrium under reaction conditions, while some extent of reduction to V^{3+} cannot be excluded.

Alumina- and titania-supported vanadium and phosphorus oxide catalysts and the industrial VPO catalyst were tested in propane oxidation reaction to carboxylic acids in a 325-400 ^{o}C temperature range in presence of water vapor. Influence of phosphorus addition and the role of moisture were determined. Present of water in propane oxidation reaction mixture is convenient [25], although its role is not fully understood yet. Bulk and supported VPO catalysts were not active in low temperature propane oxidation reaction, while alumina- and titania-supported phosphorus doped vanadium oxide catalysts (P/V = 0.1) has shown the best catalytic performance in low temperature propane oxidation reaction in presence of moisture. It was shown that acrylic acid/acetic acid ratio of products strongly depends on the water vapor partial pressure. Acetic acid and CO_x are the main products at low water concentrations (ca. 5-8%), while the selectivity to acrylic acid increases at higher water concentration values (ca. 16%). Titania-supported phosphorus doped vanadium oxide catalyst (8V1PTi) is also active in the absence of water vapor, but propane combustion to CO_x occurs.

Characterization of fresh and used catalysts is reported in Chapters 6 and 8. The conventional *ex-situ* characterization was not relevant to the activity data. No crystalline phases were formed on the alumina and titania supports after treatment of the supported vanadium and phosphorus oxide catalysts in N_2 flow at 400 ^{o}C for 19 hours. Formation of β-$VOHPO_4$ and V_2O_5 was observed for alumina-supported vanadium and phosphorus oxide catalysts used in propane

oxidation reaction in presence of water vapor, while crystallization did not occur in case of titania-supported catalysts. Taking into consideration the fact that already the phosphorus doping (P/V = 0.1) changes diametrically the catalytic properties (selectivity shifts from CO_x to acetic and acrylic acids), characterization of the active site and determination of the phosphorus role becomes rather challenging. Conventional characterization methods like Raman or XRD spectroscopy are not sensitive to such a small amounts of additives. Thus, the *in situ* and *operando* IR spectroscopy was used for evaluation of the nature of the phosphorus doped catalysts.

The FT-IR spectra of NH_3 adsorption/desorption on supported vanadium and phosphorus oxide catalysts has shown, that already a phosphorus doping causes differences in the strength of the coordination bond. This is confirmed by a shift to higher frequencies of the band at 1235 cm^{-1} (Lewis acid sites). Moreover, higher amounts of phosphorus additive (P/V = 1.1) causes the polarization of the V-(O-P) moiety and an inductive effect due to the higher electronegativity of phosphorus compared to vanadium, which enhances the Lewis acid strength of vanadium sites [[26]]. This scenario was observed by a shift to higher frequencies of the bands due to ammonia chemisorbed on Lewis acid sites and to ammonium cations on the Brønsted sites and by a decrease of Brønsted acidity with respect to the Lewis acidity. An increase of the Lewis acid strength of vanadium sites was also confirmed by adsorption of small doses of ammonia (0.02-0.50 torr) at room temperature on the surface of supported vanadium and phosphorus oxide catalysts. It was shown that the phosphorous addition favors ammonia adsorption on Lewis acid sites ($\delta_{as}(NH_3)$), which was observed already for phosphorus doped catalyst (P/V = 0.1). Further investigation of supported vanadium and phosphorus oxide catalysts was performed using *in-situ* DRIFTS studies. Temperature programmed propylene adsorption and reaction under diverse reaction conditions was performed in order to evaluate the nature of propylene intermediates. Subsequently moisture was introduced to the reaction feed in order to evaluate its role in propane oxidation mechanism. As described in Chapter 8, at 125 ^oC propylene adsorbs on the surface of alumina- and titania-supported vanadium and phosphorus catalysts forming acetone intermediates (characteristic bands observed at 1375, 1440, 1570, 1670 cm^{-1}). This process does not depend on the P/V ratio, since the same intermediates were observed for supported vanadium oxide catalyst and for the supported VPO-type catalysts. It indicates that propylene undergoes an electrophilic attack, at its C_2 position, by a proton of surface -OH groups. Desorption in oxygen atmosphere leads to formation of carboxylic species, probably acetates (bands at 1440 and 1530 cm^{-1}) at ca. 250-350 ^oC. As reported in section 1.4.1 oxidation of propane/propylene

on vanadium based catalysts leads to formation of acrolein as an intermediate and its further transformation to acrylic acid, or to formation of isopropyl alcohol, then acetone and its subsequent cracking to acetic acid and CO_x [27]. Performed DRIFTS experiments indicate that propylene undergoes transformations with increasing temperature in oxygen atmosphere according to the proposed path:

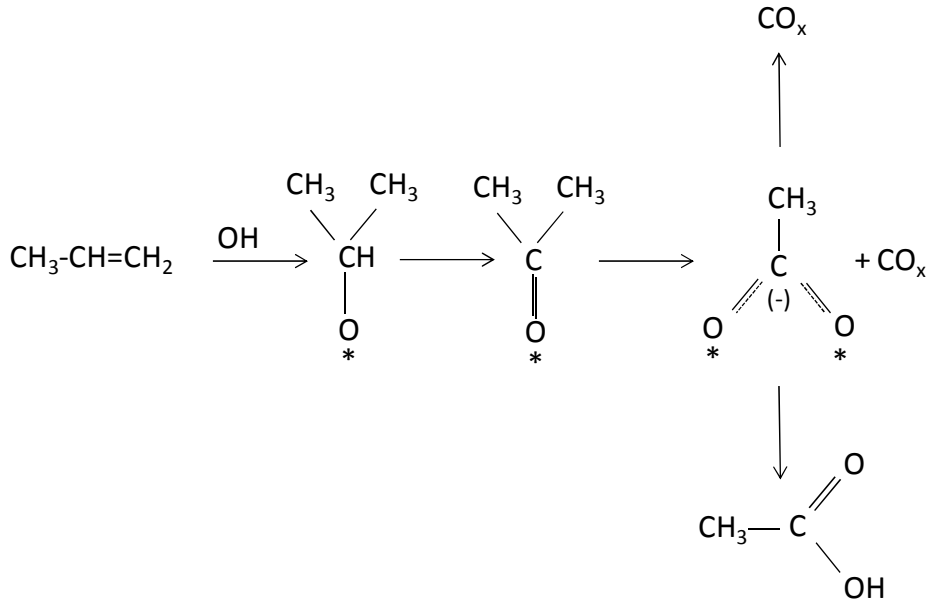

Figure 9.3 Propylene transformation on a surface of vanadium based catalysts

Bands characteristic of acrolein were not detected during propylene reaction with oxygen, thus it may be concluded that the propylene molecule cracks to acetic acid and CO_x under applied conditions. Additionally, the GC test shows that in absence of water vapor the propane combustion to CO_x occurs, since no carboxylic acids were detected. These results indicate that acetic acid is not desorbed from the catalysts surface, but it is burned to CO_x before desorption.
Formation of maleic anhydride (1590, 1790, 1870 cm^{-1}) is observed at higher temperature range (ca. 250-400 ^oC). This indicates that propylene dimerization

process takes place probably through formation of an allyl intermediate on Lewis acid sites [25,[28]]. This leads to formation of a cyclic anhydride according to Figure 9.4:

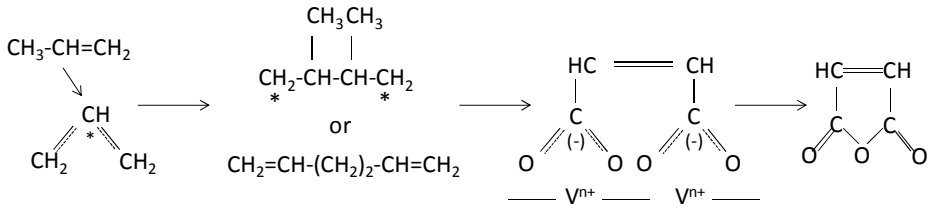

Figure 9.4 Maleic anhydride formation over vanadium based catalysts

IR bands of the allyl intermediate were not detected, so that this mechanism cannot be confirmed. Probably a low temperature propylene adsorption experiments would provide more information about this mechanism. As it was concluded above, phosphorus addition increases the ratio of Lewis/Brønsted acid sites; this, according to the above-proposed mechanism should facilitate the formation of maleic anhydride on the surface of phosphorus containing catalysts. However, the temperature programmed propylene reaction studies on alumina-supported vanadium oxide catalyst (8VAl) have shown, that phosphorus addition (already P/V = 0.1) seems to hinder the formation of cyclic products. Thus other mechanism, related to presence of phosphorus must influence the maleic anhydride formation. DRIFTS study was also used for determination of the role of moisture in propane/propylene oxidation reactions. It was shown (see Chapter 8), that propylene interaction with the catalyst surface diminishes in presence of water vapor. It is probably due to a competitive adsorption of water and propylene on the surface of vanadium based catalysts. In absence of water vapor in the reaction feed CO_x were formed. This suggests a strong interaction of surface intermediates detected by DRIFTS studies (carboxylic species) with the catalysts surface and their combustion. At low concentration of water vapor in the reaction feed (ca. 8%) acetic acid was formed. This suggests that the carboxylic intermediates are not burned to CO_x on the catalyst surface, probably due to weaker interaction of the surface intermediates with the active sites, but low concentration of moisture does not hinder cracking of propylene molecule to

acetic acid. However, at higher water vapor concentrations (ca. 16%) the selectivity shifts to acrylic acid. Due to weak interaction of propylene with the catalyst surface in presence of moisture propylene molecule is oxidized to acrylic acid. It was reported that in this reaction σ-allyl intermediate is transformed to acrolein, which is further oxidized to acrylic acid [29]. In the first step a dissociative chemisorption of gas phase O_2 on the catalyst surface occurs, which leads to formation of reactive surface O* species. Then, propylene is dissociated and chemisorbed as surface CH_2CHCH_2* and the surface oxygen is used to convert the surface H* species to HO* intermediates (Langmuir-Hinshelwood mechanism). The next step involves C-H bond breaking of the surface allyl intermediate and a simultaneous O* insertion according to Mars van Krevelen mechanism [30]. Thus a formation of σ-allyl intermediate or eventually, of a dynamic allyl intermediate is required for propane oxidation to acrylic acid. The dynamic allyl intermediate is a feature, which structure is related with π- and σ-allyl intermediates as presented in the figure 9.5:

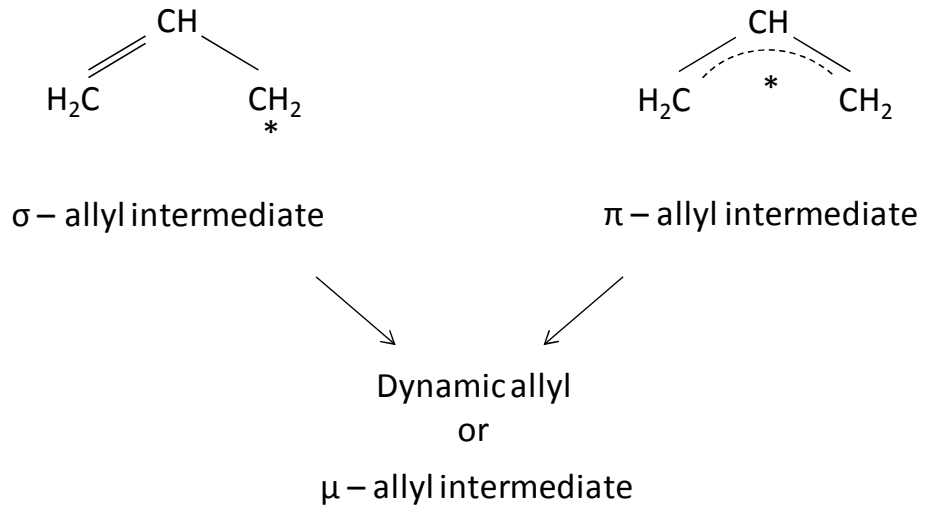

Figure 9.5 Structures of propylene allyl intermediates

Their presence may avoid propylene oxidation at its C_2 position and lead to formation of acrolein and its further transformation to acrylic acid. However, formation of these intermediates was not observed during propylene adsorption

and reaction in presence of oxygen and moisture due to high concentration of the latter. *Operando* study of propane oxidation reaction in presence of low concentration of water vapor was performed in order to confirm the mechanism of propane oxidation to acetic acid. FT-IR spectra of surface intermediates and reaction gas phase are presented in Figure 8.25. It was shown that carboxylic intermediates form in a 250-350 ^{o}C temperature range on the catalyst surface, while the IR study of the gas phase reaction products confirm that acetic acid is produced in the same temperature range. The operando IR experiment performed in absence of water vapor confirms propane combustion to CO_x.

9.3 SUMMARY

It may be concluded that phosphorus additive stabilizes V^{4+} species and it induces changes in the chemistry of vanadium oxide catalysts already at low phosphorus concentration (P/V = 0.1) by changing the strength of the coordination bond and by increasing the strength of Lewis acid sites. These slight changes are required for propane oxidation reaction to carboxylic acids, while higher amount of phosphorus is convenient for propane ammoxidation reaction to acrylonitrile due to an increase in the V^{4+}/V^{5+} ratio, which causes the selectivity shift from acetonitrile to acrylonitrile. No crystalline VPO phases are necessary for acrylonitrile formation in propane ammoxidation reaction, but essentially V^{4+}-O-M bonds in amorphous or crystalline phase are required. Presence of water vapor in the reaction feed for propane oxidation to carboxylic acids avoids the overoxidation of surface intermediates to CO_x by weakening of the interaction of reaction intermediates with surface active sites. Acetic acid forms by an electrophilic attack of propylene on surface –OH groups, while formation of acrylic acid probably involves formation of a weakly bonded σ-allyl intermediate.

References

[1] M. Ruitenbeek, *Dissertation: Characterization of vanadium-based oxidation catalysts,* Utrecht University, The Netherlands (1999) ISBN 90-393-2051-9

[2] L. M. Cornaglia, C. Caspani, E.A. Lombardo, *Appl. Catal.* 74 (1991) 15

[3] G. Centi, F. Trifiró, J. R. Ebner, V. M. Franchetti, *Chem, Rev*. 88 (1988) 55

[4] H. Morishige, J. Tamaki, N. Miura, N. Yamazoe, *Chem. Lett*. (1990) 513

[5] F. Garbassi, J. Bart, R. Tassinari, G. Vlaic, P. Labarde, *J. Catal*. 98 (1986) 317

[6] S. Geupel, K. Pilz, S. van Smaalen, F. Büllesfeld, A. Prokofiev, W. Assmus, *Acta Cryst. C* 58 (2002) 9

[7] B. Schioett, K. A. Joergensen, R. Hoffmann, *J. Phys. Chem.* 95 (1991) 2297

[8] P. A, Agaskar, L. Caul, R. K. Grasselli, *Catal. Letters* 23 (1994) 339

[9] O. F. Ikotun, N. Marino, P. E. Kruger, M. Julve, R. P. Doyle, *Coordination Chem. Rev*. 254 (2010) 980

[10] R. P. Singh, M. A. Bañares, G. Deo, *J. Catal.* 233 (2005) 388

[11] F. Castellino, S. B. Rasmussen, A. D. Jensen, J. E. Johnsson, R. Fehrmann, *Appl. Catal. B* 83 (2008)110

[12] H. S. Horowitz, C. M. Blackstone, A. W. Sleight, G. Teufer, *Appl. Catal.* 38 (1988) 193

[13] S. D. Jackson, J. S. J. Hargreaves (Eds.), J. K. Bartley, N. F. Dummer, G. J. Hutchings, *Metal Oxide Catalysis,* Wiley VCH Verlag GmbH & Co. KGaA, Weinheim, 1 (2009) 499

[14] A. Davidson, M. Che, *J. Phys. Chem*. 96 (1992) 9909

[15] D. Ballutaud, E. Bordes, P. Courtine, *Mater. Res. Bull*. 17 (1982) 519

[16] B. C. Gates, H. Knözinger (Eds.), M. A. Bañares, G. Mestl, *Adv. Catal.* 52 (2009) 43

[17] M. A, Bañares, *Adv. Mater.* 23 (2011) 5293

[18] H. Golińska, E. Rojas, R. López-Medina, V. Calvino-Casilda, M. Ziółek, M. A. Bañares, M. O. Guerrero-Pérez, *Appl. Catal. A* 380 (2010) 75

[19] P. Concepción, P. Botella, J. M. López Nieto, *Appl. Cat. A* 278 (2004)45

[20] M. Sanati, A. Andersson, L. R. Wallenberg, B. Rebenstorf, *Appl. Cat*. A, General106 (1993) 51

[21] A. Caldarelli, F. Cavani, F. Folco, S. Luciani, C. Cortelli, R. Leanza, *Cat. Today* 157 (2010) 204

[22] Z. Wu, P.C. Stair, S. Rugmini, S.D. Jackson, *J. Phys. Chem*. C 111 (2007) 16460

[23] V. Narayana Kalevaru, B. Lücke, A. Martin, *Cat. Today* 142 (2009) 158

[24] A. Martin, B. Lücke, *Chem. Eng. Technol*. 1999, **21**, 294

[25] G. Landi, L. Lissi, J-C. Volta, *J. Mol. Catal. A*, 222 (2004) 175

[26] G. Busca, G. Centi, F. Trifiró, V. Lorenzelli, *J. Phys. Chem*. 90 (1986) 1337.

[27] M. Ai, *Catal. Today*, 42 (1998) 297

[28] A. Davydov, *Molecular Spectroscopy of Oxide Catalyst Surfaces*, John Wiley & Sons, Ltd, cop. 2003

[29] V. S. Escribano, G. Busca, V. Lorenzelli, *J. Phys. Chem*., 94 (1990) 8939

[30] C. Zhao, I. E. Wachs, *J. Phys. Chem. C* 112 (2008) 11363

Conclusions

1. Reliable structure-activity relationships study requires *operando* spectroscopy since, both, structure and reactivity, are determined simultaneously on the same sample.

2. Phosphorus addition changes the chemistry of vanadium supported catalysts already at low P/V atomic ratio.

3. Surface $V^{5+}O_x$, responsible for propane activation, is selective to acetonitrile in propane ammoxidation reaction, while higher population of V^{4+} species shifts the selectivity from acetonitrile to acrylonitrile.

4. Crystalline VPO phases are not necessary for acrylonitrile formation in propane ammoxidation reaction.

5. The oxidation state equilibrium balance (V^{5+}/V^{4+}) reached under reaction conditions is controlled by catalyst activation.

6. Phosphorus doping improves significantly the activity and the selectivity to carboxylic acids of supported vanadium oxide catalysts in propane oxidation reaction in presence of moisture.

7. The ratio between acetic and acrylic acids strongly depends on water vapor partial pressure present in the reaction flow.

8. Presence of water vapor in the reaction feed for propane oxidation to carboxylic acids avoids the overoxidation of surface intermediates to CO_x by weakening of the interaction of reaction intermediates with surface active sites.

Conclusiones

1. Los estudios fiables sobre la relación estructura-actividad requieren análisis del tipo *operando* ya que la estructura y actividad son determinados simultáneamente para una misma realidad.

2. La presencia de fósforo cambia la química de los catalizadores soportados de oxido de vanadio, incluso a bajas relaciones atómicas P/V.

3. Las especies $V^{5+}O_x$, responsables de la activación del propano, son selectivas para acetonitrilo en la reacción de ammoxidación del propano, sin embargo en presencia de grandes poblaciones de especies V^{4+} la selectividad cambia de acetonitrilo hacia acrilonitrilo.

4. Las fases cristalinas VPO no son necesarias para la formación de acrilonitrilo durante la reacción de ammoxidación del propano.

5. El balance en el estado de oxidación (V^{5+}/V^{4+}) alcanzado en las condiciones de reacción, está controlado por la activación del catalizador.

6. El dopaje con fósforo mejora significativamente la actividad y la selectividad de ácidos carboxílicos de catalizadores soportados de óxido de vanadio, en la reacción de oxidación del propano en presencia de vapor de agua.

7. La relación entre ácido acético y ácido acrílico depende fuertemente de la presión parcial del vapor de agua presente en el flujo de la reacción.

8. La presencia de vapor de agua en la reacción contribuye con la oxidación del propano hacia ácidos carboxílicos, evitando así la sobre-oxidación de los intermediarios de la superficie hacia CO_x mediante el debilitamiento de las interacciones existentes entre los intermediarios de la reacción con los sitios activos de la superficie.